

https://dspace.org/

Indirect adaptive control of an unmanned receiver and tanker system during aerial refuelling

Panday, Aarti

2024
https://hdl.handle.net/10539/37384

Downloaded from a DSpace repository. https://dspace.org/

Indirect Adaptive Control of an Unmanned Receiver and Tanker System During Aerial Refuelling

Name: Aarti Panday
Supervisor: Prof. Jimoh O. Pedro
Student Number: 0003149T

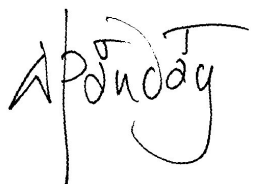
A thesis submitted to the Faculty of Engineering and the Built Environment, University of the Witwatersrand, Johannesburg, in fulfilment of the requirements for the degree of Doctor of Philosophy.

Johannesburg, November 2022

Declaration

I declare that this thesis is my own, unaided work, except where otherwise acknowledged. It is being submitted for the degree of Doctor of Philosophy in the University of the Witwatersrand, Johannesburg. It has not been submitted before for any degree or examination at any other university.

Signed this 25th day of November 2022



Name: Aarti Panday
Supervisor: Prof. Jimoh O. Pedro
Student Number: 0003149T

This thesis is dedicated to the 1860 Indians.

In November 1860, after a month-long journey at sea, the SS Truro arrived at the Port of Natal, South Africa. Three hundred and forty-two indentured labourers disembarked, the first of 200,000 that would eventually arrive, who were to work the sugar cane plantations of Natal.

I have often wondered what your journey must have been like. Were you filled with dreams of hope, or apprehension about your soon-to-be new lives in South Africa? Were your thoughts fixed on the immediate logistics of travel, or did you attempt to envisage what life we, your descendants, would encounter, generations later?

Many thought you arrived with nothing, not perceiving the riches you carried. The spirit of your holy mountains, sacred rivers and hallowed temples lived on in you. In books of history, you are remembered for your hard labour but we, your descendants, know you for this spirit which you passed on to us. No number of adversities could break your resilient resolve to fulfil your duties – to work, to live, to fight, to love.

I dedicate this thesis to you, my ancestors.
Please accept this humble offering at your feet.

Acknowledgements

I would like to express gratitude to Prof Jimoh O. Pedro, for the continuous support of my Ph.D study and related research, for his patience, motivation, and immense knowledge. His guidance helped me over the duration of this research and writing of this thesis. I could not have imagined having a better supervisor and mentor for my Ph.D study.

I would like to thank the Department of Science and Innovation for the bursary awarded to me in 2016 and 2017, which made my sabbatical and completion of this research possible.

Finally, I would like to acknowledge the support of my family, friends and colleagues during the completion of my research.

Abstract

Unmanned aerial vehicles (UAVs) have evolved in design, complexity and have seen increasingly diverse roles within the past five decades of its adoption as an essential aviation tool. The lack of an in-flight-refuelling capability is one of the major practical limitations of UAVs. In a successful automated aerial refuelling (AAR) manoeuvre, the refuelling receiver aircraft must maintain an accurate position relative to the tanker aircraft. Without the presence of a skilled pilot in the cockpit, control systems must be developed to meet the stringent performance and safety requirements of the AAR manoeuvre, while requiring stability and performance robustness. The aim of this study was to address the development of stable control laws by synthesising techniques in nonlinear and intelligent control. The objectives included system model development, optimisation of controller designs using evolutionary algorithms coupled with Lyapunov stability theory, and system simulation both with and without disturbances. The research objectives were addressed in three phases using numerical simulation in the MATLAB environment: establishing a baseline case in phase 1 where proportional-integral-derivative (PID) control was used, followed by the development of a Lyapunov-based feedback linearisation controller in phase 2 and lastly, the development of a dynamic neural network-based control scheme in phase 3. An aerial refuelling system model was developed, inclusive of the tanker-receiver engagement, where the receiver aircraft dynamics was framed as a variable-mass system subject to a wind field as inherent to the process. Three controllers were designed for the system. The nonlinear system model was used directly in the development of a benchmark controller case using PID control for the aerial refuelling manoeuvre. A single set of controller gains, applicable throughout all phases of the refuelling manoeuvre, was as found through manual tuning, eliminating the need for gain scheduling. Lyapunov stability theory was extended to the aerial refuelling system, where mechanical energy of the variable-mass system was increased as fuel was added to the receiver aircraft. Stability was established for the system throughout refuelling, including the post-refuelling phase, where the receiver aircraft would remain on station and mechanical energy would be conserved. The stability theorem was incorporated into a cost function, whose minimisation using evolutionary algorithms, would lead to optimisation of controller gains that would ensure system

stability. The manually-tuned controller gains for the benchmark PID controller were optimised using particle swarm optimisation and genetic algorithms (GAs). It was found through the minimisation routine, that there is a minimum energy threshold that must not be exceeded in the system for performance and stability to be maintained. The minimum energy was found to be related to the ratio of mass increase to total aircraft mass. Two disturbance cases were defined: decreased, asymmetric refuelling and turbulence, to test the robustness of the designed controller. The second controller designed was based on feedback linearisation (FBL). FBL was incorporated in the inner loop, while a pseudo-backstepping scheme in the command inversion loop converted the reference command signals into desired dynamics. PID tracking control was used to close the outer loop to give effect to controller tracking objectives. Controller gains were selected through manual tuning and were then optimised with the Lyapunov-based GA routine developed earlier. The third controller design was the synthesised nonlinear intelligent controller, which used dynamic neural networks (DNNs) in an indirect adaptive FBL control scheme in the inner loop, while the outer loop remained the same as the FBL controller without the DNN. System identification was performed in order to obtain the DNN models to estimate the plant dynamics. Controller gains were selected through manual tuning and were then optimised with the Lyapunov-based GA routine developed earlier. Dynamic simulation results showed that the system was sensitive in the lateral-directional states in the presence of disturbances. The benchmark PID control was the least robust to disturbances, but its performance was improved when the Lyapunov-based GA gains were applied. The manually-tuned FBL controller exhibited damped oscillatory behaviour in the lateral-directional states during refuelling, however, application of the Lyapunov-based GA gains led to these behaviours being eradicated from the system state-variable trajectories. The DNN-based FBL controller with Lyapunov-based GA-optimised gains performed the best from all designed controllers. Transient behaviour with maximum deviation of 0.004% from nominal in the longitudinal and vertical separation was observed in the DNN-based FBL controller prior to refuelling commencing, but this very quickly settled to nominal. Application of the Lyapunov-based optimisation gave improved controller performance compared to the manually-tuned control gains in all instances, and the system was able to return to its nominal or desired values when subjected to disturbances. For the AAR manoeuvre, the synthesis of nonlinear and intelligent control techniques was able to produce stable control which showed good robustness characteristics when subjected to disturbances.

Scope and Contribution

- The first principles development of a variable-mass system dynamic model subject to a wind-field to serve as the integrated nonlinear system model to be controlled and identified using the dynamic neural network (DNN).
- The extension of Lyapunov stability theory to the aerial refuelling problem, where the mechanical energy of the system is increased over time.
- The incorporation of an evolutionary algorithm (EA)-based optimisation scheme that uses the Lyapunov-based method to optimise the single set of controller gains to be applied throughout the entire refuelling duration.
- The use of a DNN to approximate the automated aerial refuelling (AAR) dynamics over the duration of the refuelling. This model approximation includes the effects of the varying mass, centre-of-gravity (CG) and inertia, and includes the effects of the tanker-generated vortex wake.
- The synthesis of the developed Lyapunov-based control optimisation with the identified DNN model to form an indirect adaptive controller using feedback linearisation.
- The elimination of the need for gain scheduling as the proposed controller schemes are able to use a single set of control gains throughout all phases of aerial refuelling over the duration of fuel transfer and subsequent station-keeping.

Published Work

1. Panday, A. and Pedro, J.O., 2013, An Overview of Aerial Refueling Control Systems Applied to UAVs. In AFRICON, September 2013 (pp. 1-5). IEEE.
2. Panday, A. and Pedro, J.O., 2017, Optimal Control of Nonminimum Phase Receiver Aircraft During Aerial Refuelling, Aeronautical Society of South Africa Annual Conference, October 2017, Pretoria, (pp 1 - 13)
3. Panday, A. and Pedro, J.O., 2018, Particle Swarm-Optimised PID Control of a Receiver Aircraft During Aerial Refuelling, 2018 IEEE Congress on Evolutionary Computation (CEC), Rio de Janiero, 2018, (pp 1-8)

Journal Papers in Submission Process

- Panday, A. and Pedro, J.O., 2022, "Evolutionary Algorithm-Based Feedback Linearisation Control for Aerial Refuelling", *Nonlinear Dynamics*
- Panday, A. and Pedro, J.O., 2022, "Control of a Receiver Aircraft during Aerial Refuelling using Dynamic Neural Network-Based Feedback Linearization", *Journal of Guidance, Control, and Dynamics*

Contents

Declaration i

Acknowledgements iii

Abstract iv

Scope and Contribution vi

Published Work vii

Contents viii

List of Figures xv

List of Tables xxiii

Symbols xxiv

List of Acronyms xxiv

1 Introduction 1

1.1 Background 1

1.2 Research Motivation 3

1.3 Literature Review 4
1.3.1 Introduction 4
1.3.2 Early theoretical foundations and controller design approaches 5
1.3.3 Latest research in automated aerial refuelling control - 2012 to 2022 . 10
1.3.3.1 Probe-drogue refuelling (PDR) method 11
1.3.3.2 Boom-receptacle refuelling (BRR)method 13
1.4 Identified Gaps in Aerial Refuelling Control Research 16
1.5 Research Objectives 18
1.6 Research Methodology 19
1.7 Envisaged Contributions to Knowledge 21
1.8 Thesis Outline 22

2 Aerial Refuelling System Mathematical Modelling 23

2.1 Defining the Aerial Refuelling Problem 24
2.2 Dynamics of a Variable-Mass System 25
2.2.1 Linear momentum - general case 26
2.2.2 Linear momentum - aerial refuelling problem 30
2.2.3 Angular momentum - aerial refuelling case 31
2.3 Dynamics and Kinematics of Variable-Mass System subject to Wind-Field . . 33
2.4 Motion of a Tanker Aircraft in a Wind-Field 36
2.5 Forces and Moments 37
2.6 Actuator Dynamics 38
2.7 Rotation Matrices 39

2.8 Fuel Transfer Model 41
2.9 Atmospheric and Wind Model Elements 42
2.9.1 Atmosphere model 43
2.9.2 Vortex model 43
2.9.3 Turbulence model 46
2.10 Automated Aerial Refuelling System Trim Conditions 48
2.11 Chapter Summary 48

3 Benchmark Controller Design **50**

3.1 Introduction 50
3.2 Receiver Controller 51
3.2.1 Receiver aircraft performance specifications 51
3.2.2 Receiver aircraft controller structure 52
3.3 Tanker Aircraft Controller Design 54
3.3.1 Tanker aircraft controller performance specifications 54
3.3.2 Tanker aircraft controller structure 55
3.4 Manual Tuning of Receiver Controller Parameters 55
3.4.1 Cost function for manually-tuned gains 56
3.4.2 Selection of t_f 57
3.5 Effect of Fuel Transfer in Automated Aerial Refuelling Manoeuvre 57
3.6 Dynamic Simulation of Tanker-Receiver During Automated Aerial Refuelling 58
3.7 Robustness Analysis of the Manually-Tuned Controller Gains Case 64
3.7.1 Mass or refuelling disturbances 65

3.7.2 Turbulence . . . 65
3.7.3 Dynamic simulation of automated aerial refuelling including disturbances 67
3.8 Chapter Summary . . . 71

4 Stability Analysis 77

4.1 Lyapunov Stability Analysis . . . 77
4.1.1 Background and concepts . . . 77
4.1.2 Lyapunov's direct method extended to AAR . . . 78
4.1.3 Stability analysis of system with manually-tuned controller gains . . . 84
4.1.3.1 Qualitative analysis . . . 87
4.2 Static Margin and CG Travel . . . 88
4.3 Chapter Summary . . . 90

5 Hybrid Lyapunov-Based Swarm and Evolutionary Optimisation of PID Control for Automated Aerial Refuelling 91

5.1 Introduction . . . 91
5.2 Tuning of Controller Parameters using Global Optimisation Techniques . . . 92
5.3 Particle Swarm Optimisation . . . 93
5.4 Genetic Algorithm (GA) . . . 95
5.5 Optimisation Parameters and Initialisation . . . 97
5.6 Computed Controller Gains and Initial Results . . . 98
5.7 Extension of Stability Analysis . . . 108
5.8 Application of Extended Stability Analysis to Automated Aerial Refuelling . 110
5.8.1 Computed controller gains . . . 110

5.8.2 Numerical analysis of optimal system energy 110

5.9 Dynamic Simulation of Extended Aerial Refuelling 115

5.10 Chapter Summary 115

6 Nonlinear Control in Aerial Refuelling 126

6.1 Introduction 126

6.2 Input-Output Feedback Linearisation - Theoretical Overview 126

6.2.1 System description in canonical form 130

6.2.2 Zero dynamics and stability 133

6.2.3 Extension to square MIMO system 134

6.3 Application to Automated Aerial Refuelling 137

6.4 Inner-Loop Feedback Linearisation 138

6.5 Outer Loop Command Inversion and Desired Dynamics 139

6.6 Complete FBL+PID Controller 142

6.7 Dynamic Simulation of Automated Aerial Refuelling 144

6.7.1 Tuning and optimisation of the controller gains 144

6.7.2 Final optimised control gains 147

6.7.3 Simulation results 151

6.8 Chapter Summary 160

7 Application of Dynamic Neural Networks in Automated Aerial Refuelling System Modelling 161

7.1 Introduction 161

7.2 Ordinary Differential Equation Representation of DNNs - Theoretical Overview 162

7.3 Dynamic Neural Networks Training and Validation 165
7.3.1 Input-output data profile 165
7.3.2 Trained and validated models 166
7.4 Chapter Summary 174

8 Dynamic Neural Network-Based Feedback Linearisation Controller 175

8.1 Introduction 175
8.2 Dynamic Neural Network-Based Feedback Linearisation 175
8.3 Controller Structure 178
8.4 Dynamic Simulation of Automated Aerial Refuelling 179
8.4.1 Controller gains selection and optimisation 179
8.4.2 Simulation results 180
8.5 Comparison of PID and FBL Controllers During Aerial Refuelling 186
8.6 Chapter Summary 196

9 Conclusions and Recommendations for Future Work 197

9.1 Conclusions 197
9.2 Recommendations for Future Work 202

References 203

A Appendix A - Parameter Specification and Model Validation 214

A.1 System Parameters 214
A.2 Vortex Model Validation 215
A.3 Inner Loop in Nonlinear Affine Form 217

A.4 Outer Loop in Nonlinear Affine Form 220

List of Figures

1.1 Factors to be considered in automated aerial refuelling (Panday and Pedro (2013)) . . . 2

1.2 Conceptual framework for literature review on automated aerial refuelling . . 5

1.3 Research phase 1 . . . 20

1.4 Research phase 2 . . . 20

1.5 Research phase 3 . . . 21

2.1 High-level depiction of key mathematical model elements . . . 23

2.2 Variable mass system (Cveticanin (2016)) . . . 26

2.3 Definition of refuelling position vectors - overlay with Cveticanin (2016) . . . 30

2.4 Receiver aircraft reference frames . . . 39

2.5 Fuel tank layout and position vectors . . . 41

2.6 Refuelling engagement definitions and geometry . . . 44

3.1 Controller design block diagram . . . 52

3.2 Receiver aircraft change in mass during refuelling. . . . 58

3.3 Receiver aircraft body rates relative to tanker. . . . 59

3.4 Receiver aircraft airspeed, angle of attack and sideslip angle. . . . 60

3.5 Receiver aircraft orientation relative to tanker. 61

3.6 Receiver aircraft relative separation from tanker. 61

3.7 Receiver aircraft control surface deflections. 62

3.8 Tanker aircraft state variables. 63

3.9 Tanker aircraft x- y- and z-positions along flight path. 63

3.10 Tanker aircraft control surfaces' deflections. 64

3.11 Receiver aircraft fuel tank masses - baseline and disturbance case. 66

3.12 Receiver aircraft change in mass during refuelling - baseline and disturbance case. 66

3.13 Disturbance profile for tanker aircraft. 67

3.14 Receiver aircraft body rates relative to tanker - baseline and disturbances. . . 68

3.15 Receiver aircraft airspeed, angle of attack and sideslip angle - baseline and disturbances. 69

3.16 Receiver aircraft orientation relative to tanker - baseline and disturbances. . . 70

3.17 Receiver aircraft relative separation from tanker - baseline and disturbances. 71

3.18 Receiver aircraft control surfaces' deflections - baseline and disturbances. . . 72

3.19 CG travel during refuelling - baseline and disturbances. 72

3.20 Receiver aircraft fuel tank centroid position during refuelling - baseline and disturbances. 73

3.21 CG travel vs. mass throughout refuelling - baseline (left) and disturbances (right). 73

3.22 Tanker aircraft state variables - baseline and disturbances. 74

3.23 Tanker aircraft x- y- and z-positions along flight path - baseline and disturbances. 75

3.24 Tanker aircraft control surfaces' deflections - baseline and disturbances. . . . 75

4.1 Growth of spherical region with radius R_1 to region of radius of R_2 under addition of mechanical energy. 80

4.2 Two-dimensional depiction of spherical region from initial R_0 to R_{max}. 80

4.3 Concentric depiction of spherical regions in the state space. 83

4.4 Receiver aircraft mass versus time - depiction of initial and final spherical regions according to mass profile. 85

4.5 Receiver aircraft state variables versus time - Simulation extended to 600s. . 86

4.6 Receiver aircraft control surfaces' deflections versus time - Simulation extended to 600s. 87

4.7 CG position versus time - extended simulation. 89

4.8 CG position versus mass - extended simulation. 89

5.1 Controller block diagram incorporating Lyapunov-based optimisation algorithm 92

5.2 Particle swarm optimisation solution structure at every iteration. 94

5.3 Genetic algorithm iterative methodology. 95

5.4 Two-dimensional mapping of genetic algorithm solution structure. 96

5.5 Evolution of particle swarm optimisation and genetic algorithms' cost functions, Ke_θ, $Ke_{\theta I}$ and Ke_q gains. 100

5.6 Evolution of Ka_ϕ, Ka_p, Kr_ψ and Kr_r gains in particle swarm optimisation and genetic algorithms. 100

5.7 Evolution of Kr_p, Ke_z, Ke_{zI} and $Ke_{\dot{z}}$ gains in particle swarm optimisation and genetic algorithms. 101

5.8 Evolution of Kt_V, Kt_{VI} and $Kt_{\dot{v}}$ and Kt_x gains in particle swarm optimisation and genetic algorithms. 101

5.9 Evolution of Kt_{xI}, $Kt_{\dot{x}}$, $Ka_{\dot{y}}$ and $Kr_{\dot{y}}$ gains in particle swarm optimisation and genetic algorithms. 102

5.10 Evolution of Ka_y, Kr_y, Ka_{yI} and Kr_{yI} gains in particle swarm optimisation and genetic algorithms. 102

5.11 J and $\dot{J}$ versus time - baseline - manually-tuned, PSO-tuned, and GA-tuned controller gains. 104

5.12 Receiver state variables versus time - baseline - manually-tuned, PSO-tuned, and GA-tuned controller gains. 105

5.13 Relative separation and airspeed versus time - baseline - manually-tuned, PSO-tuned, and GA-tuned controller gains. 106

5.14 Control surfaces deflections versus time - baseline - manually-tuned, PSO-tuned, and GA-tuned controller gains. 107

5.15 Nominal motion problem (Slotine and Weiping (1991)). 109

5.16 Evolution of J and K_a gains in particle swarm optimisation and genetic algorithms. 112

5.17 Evolution of K_e gains in particle swarm optimisation and genetic algorithms. 112

5.18 Evolution of K_r gains in particle swarm optimisation and genetic algorithms. 113

5.19 Evolution of K_t gains in particle swarm optimisation and genetic algorithms. 113

5.20 J and $\dot{J}$ versus time - baseline + disturbances - manual-, PSO-, and GA-tuned controller gains. 116

5.21 Airspeeds and aerodynamic angles - baseline + disturbances - manual-, PSO-, and GA-tuned controller gains. 117

5.22 Receiver aircraft body rates relative to tanker versus time - baseline + disturbances - manual-, PSO-, and GA-tuned controller gains. 118

5.23 Receiver aircraft relative Euler angles versus time - baseline + disturbances - manual-, PSO-, and GA-tuned controller gains. 119

5.24 Receiver aircraft x-, y- and z-separations versus time - baseline + disturbances - manual-, PSO-, and GA-tuned controller gains. 120

5.25 Receiver aircraft controller surfaces deflections versus time - baseline + disturbances - manual-, PSO-, and GA-tuned controller gains. 121

5.26 Receiver aircraft mass variation with time – baseline and mass disturbance. . 121

5.27 Receiver aircraft CG variation with time – baseline and mass disturbance. . . 122

5.28 Receiver aircraft CG travel versus receiver aircraft mass – baseline and mass disturbance 122

5.29 Fuel tank centroid variation with time – baseline and mass disturbance. . . . 123

5.30 Fuel in each tank – baseline and mass disturbance. 123

5.31 Tanker aircraft state variables time history. 124

5.32 Tanker aircraft x-, y-, and z-positions along flight path. 124

5.33 Tanker aircraft control surfaces' deflections time history. 125

6.1 Generalised controller block diagram 137

6.2 Feedback linearisation control block - manual tuning of controller gains . . . 143

6.3 Feedback linearisation control block - hybrid Lyapunov-based evolutionary algorithm-optimised controller gains. 144

6.4 Minimum energy threshold - GA optimisation. 145

6.5 Receiver state variables with non-viable gains - deviation apparent. 146

6.6 Receiver control variables with non-viable gains - deviation apparent. 147

6.7 Minimum energy threshold and non-viable region of controller gains. 148

6.8 Minimum energy threshold - GA optimisation 45 runs. 149

6.9 Cost and feedback linearisation controller gains. 150

6.10 Feedback linearisation controller: K_e and K_a controller gains. 150

6.11 Feedback linearisation controller: K_t and K_r controller gains. 151

6.12 Lyapunov cost function and its derivative versus time - baseline + disturbances, manually-tuned and GA-optimised controller gains. 152

6.13 Receiver rotational rates versus time - baseline + disturbances, manually-tuned and GA-optimised controller gains. 153

6.14 Receiver speeds and aerodynamic angles versus time - baseline + disturbances, manually-tuned and GA-optimised controller gains. 154

6.15 Receiver Euler angles versus time - baseline + disturbances, manually-tuned and GA-optimised controller gains. 155

6.16 Receiver x-, y- and z-separation versus time - baseline + disturbances, manually-tuned and GA-optimised controller gains. 156

6.17 Receiver control surfaces' deflections versus time - baseline + disturbances, manually-tuned and GA-optimised controller gains. 157

6.18 Tanker aircraft state variables. 158

6.19 Tanker aircraft x- y- and z-positions along flight path. 158

6.20 Tanker aircraft control surfaces' deflections. 159

7.1 Neural unit (Garces et al., (2003)). 163

7.2 Inside view of neural unit (Garces et al., (2003)). 163

7.3 System identification receiver input data. 167

7.4 System identification - receiver output data. 167

7.5 PDA training and validation trajectories. 168

7.6 PDA MSE. 169

7.7 QDE training and validation trajectories. 170

7.8 QDE MSE. 170

7.9 RDR training and validation trajectories. 171

7.10 RDR MSE. 172

7.11 VDT training and validation trajectories. 173

7.12 VDT MSE. 173

8.1 Controller block diagram - DNN-based FBL controller 178

8.2 Controller block diagram - DNN-based FBL controller with Lyapunov-based GA-optimisation 179

8.3 Evolution of cost function J and K_x and k_1 controller gains. 181

8.4 Evolution of K_e and K_a controller gains. 181

8.5 Evolution of K_t and K_r controller gains. 182

8.6 J and $\dot{J}$ versus time for manually-tuned and GA-tuned controller gains - baseline + disturbances 183

8.7 Receiver rotational rates for manually-tuned and GA-tuned controller gains - baseline + disturbances. 184

8.8 Receiver speeds and aerodynamic angles for manually-tuned and GA-tuned controller gains - baseline + disturbances. 185

8.9 Receiver Euler angles for manually-tuned and GA-tuned controller gains - baseline + disturbances. 186

8.10 Receiver x- y- and z-separation for manually-tuned and GA-tuned controller gains - baseline + disturbances. 187

8.11 Receiver control surfaces deflection for manually-tuned and GA-tuned controller gains - baseline + disturbances. 188

8.12 Tanker aircraft state variables - baseline + disturbances. 188

8.13 Tanker aircraft x- y- and z-positions along flight path - baseline + disturbances. 189

8.14 Tanker aircraft control surfaces' deflections - baseline + disturbances. 189

8.15 ϕ_{TR} vs time from PID, FBL and DNN controllers - baseline + disturbances. . 190

8.16 ψ_{TR} vs time from PID, FBL and DNN controllers - baseline + disturbances. . 190

8.17 p_{TR} vs time from PID, FBL and DNN controllers - baseline + disturbances. . 191

8.18 r_{TR} vs time from PID, FBL and DNN controllers - baseline + disturbances. . 191

8.19 β_R vs time from PID, FBL and DNN controllers - baseline + disturbances. . 192

8.20 y_{TR} vs time from PID, FBL and DNN controllers - baseline + disturbances. . 192

8.21 θ_{TR} vs time from PID, FBL and DNN-based controllers - baseline + disturbances. 193

8.22 V_R vs time from PID, FBL and DNN-based controllers - baseline + disturbances. 194

8.23 z_{TR} vs time from PID and DNN-based controllers - baseline + disturbances. . 194

8.24 δ_{a_R} vs time from PID, FBL and DNN-based controllers - baseline + disturbances. 195

8.25 δ_{r_R} vs time from PID, FBL and DNN-based controllers - baseline + disturbances. 195

A.1 Distribution of vortex induced velocity W_x along wing 216

A.2 Distribution of vortex induced velocity W_x along z-axis 216

A.3 Distribution of vortex induced velocity W_y along x axis 216

A.4 Distribution of vortex induced velocity W_y along z axis 217

A.5 Distribution of vortex induced velocity W_z along x axis 217

A.6 Distribution of vortex induced velocity W_z along wing 217

List of Tables

3.1 Aerial refuelling parameters 51

3.2 Automated aerial refuelling simulation phases 51

3.3 Tanker aircraft nominal/trimmed parameters 55

3.4 Receiver aircraft controller gains and cost function 57

3.5 Automated aerial refuelling simulation phases - disturbance in refuelling . . . 65

4.1 Automated aerial refuelling extended simulation and stability analysis using energy function 88

5.1 Comparison of iteration size and computational time - Particle Swarm Optimisation (PSO) algorithm 97

5.2 Parameters used in swarm and evolutionary algorithms 98

5.3 Controller gains and bounds - PID controller 99

5.4 Controller gains and bounds 111

5.5 Cost function comparisons (including α and β) 115

6.1 Receiver aircraft controller gains and bounds 145

6.2 Receiver aircraft controller gains and bounds within energy limits 149

7.1 Trained DNNs information 168

7.2 Mean-squared error at optimal DNN state 168

8.1 Receiver aircraft DNN-FBL-based controller gains and bounds 180

Symbols

Aerial refuelling

α_R, α_T	receiver/tanker angle of attack	[rad]
AR	wing aspect ratio	[-]
β_R, β_T	receiver/tanker sideslip angle	[rad]
C_D, C_S, C_L	drag, side-force and lift coefficients	[-]
$C_{\mathcal{L}}$, $C_{\mathcal{M}}$, $C_{\mathcal{N}}$	rolling, pitching, and yawing moment coefficients	[-]
D	drag force	[N]
δ_{a_R}, δ_{a_T}	receiver/tanker aileron deflection	[rad]
δ_{e_R}, δ_{e_T}	receiver/tanker elevator deflection	[rad]
δ_{r_R}, δ_{r_T}	receiver/tanker rudder deflection	[rad]
δ_{t_R}, δ_{t_T}	receiver/tanker throttle deflection	[rad]
δT	thrust inclination angle	[rad]
D_{F_R}	fuselage diameter	[m]
e	Oswald efficiency factor	[-]
ϵ	vortex decay	[-]
$\mathbf{F}$, $\mathbf{F_r}$	force, reactive force	[N]
F_x, F_y, F_z	x-, y-, z- components of force	[N]
g	gravitational acceleration	$[m.s^{-2}]$
Γ_k	vortex strength	[m^2/s]
$h_i(t)$	fuel tank centre-of-gravity height	[m]
I_{3x3}	identity matrix	
I_M	inertia matrix prior to refuelling	[kg.m^2]
I_t	variation in inertia matrix	[kg.m^2]
I_x, I_y, I_z	moments of inertia about z- y- and z- axes	[kg.m^2]
I_{xy}, I_{xz}, I_{yz}	products of inertia	[kg.m^2]
$\mathbf{J^{F_r}}$	impulse due to resultant force	[kg.m/s]
$\mathbf{K}$	linear momentum	[kg.m/s]
$\mathbf{L}$	angular momentum	[kg.m^2/s]

L	lift force	[N]
$\mathcal{L}$	resultant rolling moment	[N.m]
l_{f_R}	fuselage length	[m]
$\underline{l}_{i_{F_{R_k}}}$	radius vector	[m]
L_u, L_v, L_w	turbulence scale lengths	[m]
m, M	mass	[kg]
$\mathcal{M}$	resultant pitching moment	[N]
M_{B_R}	receiver pitching moment in body-fixed frame	[N]
$\dot{m}$	rate of fuel transfer	[kg/s]
$\mathcal{N}$	resultant yawing moment	[Nm]
Ω	spatial frequency	[rad/m]
ω		
Φ	reactive force	[N]
$\underline{\hat{\Phi}}$	unit vector orthogonal to the radius vector	[-]
Φ_{u_g}, Φ_{v_g}, Φ_{w_g}	Dryden spectra for translational turbulence	[-]
Φ_{p_g}, Φ_{q_g}, Φ_{r_g}	Dryden spectra for rotational turbulence	[-]
ϕ_{TR}, ϕ_T	receiver relative roll angle, tanker roll angle	[rad]
ψ_{TR}, ψ_T	receiver relative yaw angle, tanker yaw angle	[rad]
p_{TR}, p_T	receiver relative roll rate, tanker roll rate	[rad/s]
q_{TR}, q_T	receiver relative pitch rate, tanker pitch rate	[rad/s]
$\mathbf{r}$, ρ	position vector	[m]
$\dot{\mathbf{r}}$	derivative of position vector	[m/s]
$\dot{r}_{BT}$	tanker velocity in tanker body-fixed frame	[-]
$\mathbf{R_{B_R B_T}}$	transformation matrix - tanker body-fixed frame to receiver body-fixed frame	[-]
$\mathbf{R_{B_R W_R}}$	transformation matrix - receiver wind frame to receiver body-fixed frame	[-]
$\mathbf{R_{B_T T_T}}$	transformation matrix - tanker wind frame to tanker body-fixed frame	[-]
r_{TR}, r_T	receiver relative yaw rate, tanker yaw rate	[rad/s]
S	skew symmetric matrix	[-]
SF	side force	[N]
σ_u, σ_v, σ_w	turbulence intensities	[m/s]
t	time	[s]
T	thrust force	[N]
τ	vortex age	[s]

τ	torque	[N.m]
τ_δ	actuator time constant	[s]
θ_{TR}, θ_T	receiver relative pitch angle, tanker pitch angle	[rad]
u, $\mathbf{u}$	scalar or general reference to control, control vector	[-]
$\mathbf{u}$, $\mathbf{U}$	velocity (general), translational velocity of receiver aircraft	[m/s]
$\dot{\mathbf{U}}$	rate of change of velocity	[m/s^{-2}]
$\mathbf{v}$, $\mathbf{v}_{S1}$, $\mathbf{v}_{S2}$	velocity (general), velocity of mass components in variable mass system	[m/s]
$\mathbf{V}_{fuel}$	fuel velocity	[m/s]
V_k	velocity of UAV_k	[m/s]
V_R, V_{R_B}	receiver airspeed, receiver airspeed in the receiver body-fixed frame	[m/s]
V_T	tanker airspeed	[m/s]
$\mathbf{V}_w$	receiver velocity in receiver body-fixed frame	[m/s]
V_{W_T}	tanker velocity in wind frame	[m/s]
v_x, v_y, v_z	x- y- and z-component of velocity	[m/s]
$\mathbf{W}$, W_{B_R}	wind velocity, in receiver aircraft body-fixed frame	[m/s]
W_{B_x}, W_{B_y}, W_{B_z},	x-, y-, z-component of wind velocity in body-fixed frame	[m/s]
$\dot{\mathbf{W}}$	rate of change of wind velocity	[m/s]
W_{I_T}	wind velocity experienced by the tanker aircraft	[m/s]
$\dot{W}_{I_T}$	is rate of change of wind velocity experienced by the tanker aircraft	[m/s]
w_x, w_y,w_z	x- y- and z-component of wind velocity	[m/s]
$\mathbf{x}$, x	state vector, scalar representation	[-]
x_{TR}, x_T	receiver x-separation, tanker x-coordinate	[m]
$\mathbf{y}$, y	output vector, scalar representation	[-]
y_{TR}, y_T	receiver y-separation, tanker y coordinate	[m]
z_{TR}, z_T	receiver z-separation, tanker z coordinate	[m]

Swarm and evolutionary algorithm optimisation

α, β	optimisation energy limit factors	[-]
J	fitness function	[-]
$\mathbf{G}_{best}$	global best solution	[-]

n	number of controller gains	[-]
N	population size for each controller gain	[-]
N_{Gen}, N_{Iter}	number of generations/iterations	[-]
$\mathbf{N_{new}}$	number of offspring chromosomes to be created	
OS	offspring population	[-]
$\mathbf{P}_{best}$	local best solution	[-]
$\mathbf{PS_1}$, $\mathbf{PS_2}$	parent candidate chromosomes	[-]
S	initial population of chromosomes	[-]
$\mathbf{v_i}$	particle velocity	[-]
$\mathbf{V}$	swarm population velocity	[-]
w_1, w_2, w_3	velocity/social/global weighting factors	[-]
$\mathbf{y}$	offspring vector	[-]
$\mathbf{x}$	particle vector	[-]
$\mathbf{x_i}$	set of gains in swarm	[-]

Feedback linearisation

e	error	[-]
$\mathbf{A}$	system matrix	[-]
$\mathbf{B}$	system matrix	[-]
$C(x)$	characteristic matrix	[-]
η	unobservable dynamics	[-]
$\mathbf{K}$	gain matrix	[-]
λ	FBL control design parameter	[-]
$\mathfrak{L}_{\rho_i}$	linear operator	[-]
$\mathbf{Q}$	optimisation weighting matrix	[-]
r	relative degree	[-]
$\mathbf{R}$	optimisation weighting matrix	[-]
$T(x)$	transformation matrix	[-]
v	pseudo-input	[-]
ξ	observable dynamics	[-]
z	transformed coordinates	[-]

Dynamic neural networks

β	adjustable weight, positive time constant	[-]
γ	adjustable weight	[-]
$\hat{\lambda}$	DNN-FBL control design parameter	[-]

ω	adjustable weight	[-]
σ	DNN activation function	[-]
$\mathbf{W}$	DNN adjustable weight matrix	[-]
v	pseudo-input	[-]
x_n	DNN state	[-]
y_n	DNN output	[-]

List of Acronyms

AAR	automated aerial refuelling
ADRC	active disturbance rejection controller
AFF	autonomous formation flight
BRR	boom-receptacle refuelling
CFD	computational fluid dynamics
CG	centre-of-gravity
DNN	dynamic neural network
DOF	degrees-of-freedom
EA	evolutionary algorithm
GA	genetic algorithm
GPS	global positioning system
HWP	hose whipping phenomenon
LTI	linear time-invariant
LQR	linear quadratic regulator
MAC	mean aerodynamic chord
MIMO	multi-input multi-output
MSE	mean-squared error
NDI	nonlinear dynamic inversion
PDR	probe-drogue refuelling
PID	proportional-integral-derivative
PSO	particle swarm optimisation
QFT	qualitative feedback theory
RBF	radial basis function
RCF	radial constrained force
RR	refuelling receptacle
SAS	stability augmentation system
UAV	unmanned aerial vehicles
UCAS	unmanned combat aerial system
UCAV	unmanned combat aerial vehicle

1 Introduction

1.1 Background

Unmanned Aerial Vehicles (UAVs) are considered key military and political assets in the modern theatre of conflict. From early uses of unmanned platforms over the past five decades to modern versions of these systems, a clear evolution in the design philosophy, complexity and roles of these aircraft is evident. While military operations have served as a platform to showcase the potential of such a flight capability, the commercial use of UAVs is currently on the rise (Gupta et al., (2021), Abeyratne and Khan (2014)).

Both military and commercial use of UAVs will drive the technologies that are needed in these air vehicles (Gupta et al., (2021)). Military systems in current deployment and those of the future will feature strong integration between manned and unmanned platforms (Clouet (2012)). An Unmanned Combat Aerial Vehicle (UCAV) or Unmanned Combat Aerial System (UCAS) will be the next significant development in mirroring the capabilities of manned platforms (Clouet (2012), Abeyratne and Khan (2014)). Studies have shown that regardless of mixed public perception on unmanned aircraft, they are sought after as a key technology with expanding roles (Wilson (2013), Abeyratne and Khan (2014)).

One of the major practical limitations of UAVs currently, is the lack of an in-flight-refuelling capability, as is present in manned aircraft. Studies have consistently highlighted the importance of aerial refuelling capabilities in conflict zones (Roblin (2022), Walton and Clark (2021), Cohen et al., (2014)), especially where Europe has participated in air-strike operations. The deficit in these capabilities within the European Union as compared to the United States has also been highlighted (Cohen et al., (2014), Quintana et al. (2014), Clouet (2012)). Very notably, the aerial refuelling capability has been cited as a force-multiplier and an enabler (Roblin (2022), Quintana et al., (2014)), therefore it is amongst the most significant capabilities for UAVs to have.

Some of the advantages that automated aerial refuelling (AAR) would give a UAV include:

- extended endurances - flying for longer missions (weeks, months, possibly years),
- higher payload-carrying capabilities without compromising on range due to extra weight,
- staying on station for longer periods of time,
- the ability to supplement air power needs, regardless of the distance from the battle i.e., a less complex deployment challenge,
- lower forward basing requirements, and
- smaller logistical trail associated with missions.

These advantages enhance the UAV mission effectiveness, and allow for new operational applications to be explored.

Two methods of aerial refuelling are in use (McAndrew and Witcher (2013)): boom-receptacle refuelling (BRR) and probe-drogue refuelling (PDR). In both cases, fuel will only flow from the tanker to the receiver once appropriate attachment or docking is achieved through the respective hardware. In BRR, the receiver port attaches to the tanker via a rigid telescoping boom fitted to the rear of the tanker. The probe-drogue method has the tanker equipped with a flexible drogue attached to a hose which must dock to the receiver aircraft probe, usually located on one side of the aircraft.

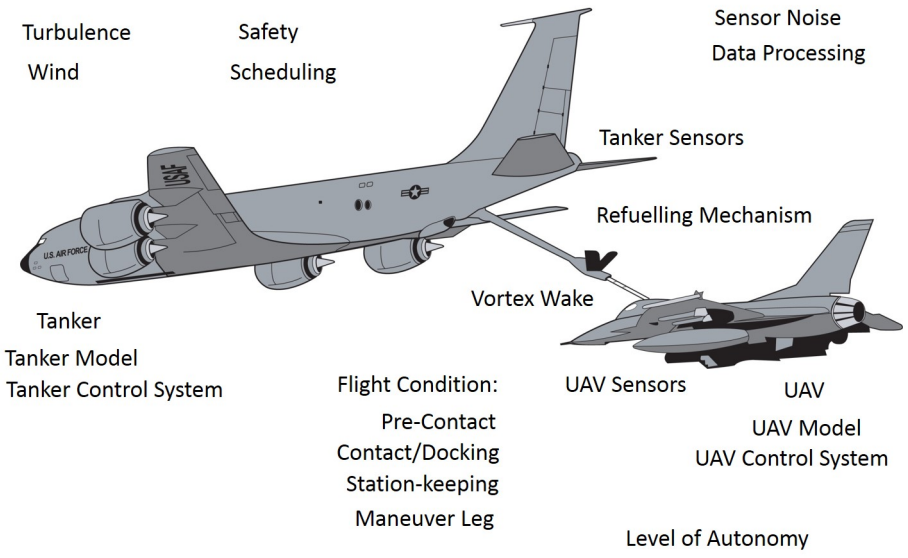


Figure 1.1: Factors to be considered in automated aerial refuelling (Panday and Pedro (2013))

The receiver aircraft must maintain an accurate position relative to the tanker aircraft in an aerial refuelling manoeuvre. However, as depicted in Figure 1.1, there are a variety of factors

to be accounted for so that position control can be achieved during the AAR process. Aircraft modelling, mass and inertia variation, vortex wake effects, non-stationary atmosphere, the effect of refuelling mechanism are amongst the numerous factors which add complexity to the aircraft motion during refuelling, leading to the engagement dynamics being highly nonlinear and strongly cross-coupled.

Considering the high level of complexity associated with aerial refuelling, advanced and reliable control systems are needed. Autonomous aerial refuelling can be considered a challenging task reliant on strong control system performance during the refuelling manoeuvre (DeVries and Paley (2013)). Additionally, aerial refuelling controllers require both stability and performance robustness since uncertainties are inherent in the process (Elliot and Dogan (2010)).

1.2 Research Motivation

The aerial refuelling problem can be defined as the control of the motion of a variable mass system subject to a wind-field, where the desired motion is best formulated or described in a non-inertial reference frame. As this problem is inherently nonlinear, the performance of conventional linear control systems for AAR may not be adequate. Given the number of time-variant complexities, selection of the correct gains required by the controller will impact the system response and stability. Also, the gains are dependent on the operating conditions of the aircraft, should these change, new gains are required. Re-tuning of controller gains, known as gain-scheduling, is not practical and is time consuming (Soares et al., (2006)).

There have been deliberate efforts underway to explore nonlinear design and analysis methods in the development of control laws for new aerospace vehicles (Chai et al., (2021), Michailidis et al., (2020)). Various nonlinear control strategies are available, such as feedback linearisation, sliding mode control, backstepping, singular perturbation method and passivity-based control (Behera and Kar (2010)). Reducing the time spent in the control law design cycle while enhancing the performance, reliability and safety of new controllers would be advantageous considering the present explosion in interest in unmanned aircraft and looking to the future. The increase in complexity within a new aircraft design, including propulsion systems, vehicle management systems and novel sensing and actuating subsystems has led to engineers seeking methods outside of the domain of traditional classical control based on linear time-invariant (LTI) models.

Traditionally, aircraft control laws have developed mainly using linear models of the aircraft dynamics coupled with linear control techniques. It is important to understand success

factors and limitations in the design of traditional controllers using linear models and linear techniques vs. nonlinear controllers. Once a control designer has a representative LTI transfer function $G(s)$, then, he or she has on hand a universally applicable (for the most part) toolbox that can be applied for controller design and analysis. LTI systems and their control design are premised somewhat on a generic model in the form of $G(s)$. This is no longer the case when nonlinear systems are to be analysed and, control techniques applied to LTI systems cannot be directly applied to nonlinear systems, implying that for nonlinear systems, the controller design is system specific, i.e., a generalised control law cannot exist as each nonlinear system is different. Applied without the appropriate analysis, conventional methods may lead to controller designs that are not robust in the presence of unstructured dynamics, parametric uncertainties and unknown dynamics. Control systems that have satisfactory performance under uncertainties are required. (Behera and Kar (2010)).

There has been a growth in the design of optimisation theory-based and artificial intelligence-based controllers for aerospace vehicles to meet the demand for better system performance as systems have become more complex (Chai et al., (2021)). Neural networks offer the ability to approximate complex nonlinear relationships that characterise dynamical systems. Whereas traditional static neural network architectures such as the radial basis function (RBF) have been very powerful tools (Li et al., (2001)), there is a growing interest in the use of dynamic neural networks (DNNs), formulated along the very lines of the nonlinear dynamical systems that they are trying to characterise. Dynamic networks, as opposed to static ones, can adapt their structures or parameters to the input during inference, and therefore enjoy favourable properties that are absent in static models giving the following advantages: increased efficiency; greater representation power; adaptiveness; enhanced scope for compatibility; generality and interpretability (Han et al., (2021)). The combination of a DNN-based dynamical model coupled to a nonlinear design technique becomes an attractive option for control design for systems and processes as complex as AAR.

1.3 Literature Review

1.3.1 Introduction

Compiling a literature review in the field of AAR will naturally be a multi-dimensional endeavour considering the many aspects across scientific disciplines that contribute to its realisation. A conceptual framework for a literature review in the field of AAR control has been formulated and presented in Figure 1.2. Various issues that are pertinent to the study have been visually arranged to give a roadmap for the review and synthesis of relevant literature.

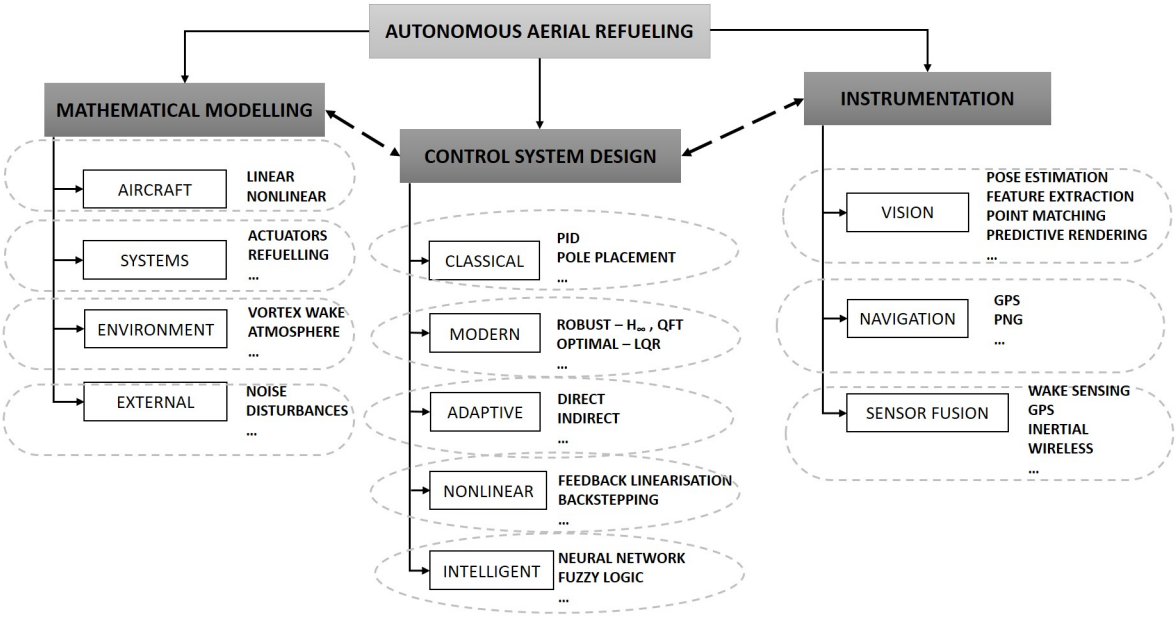


Figure 1.2: Conceptual framework for literature review on automated aerial refuelling

As the success of autonomous refuelling lies in controller design, it will be the central focus of the literature review, as depicted in Figure 1.2. However, as seen in the conceptual framework, control system design, mathematical modelling and instrumentation considerations are interdependent. By selecting control system design as the literature focus area, information regarding mathematical modelling and instrumentation requirements will be revealed as a natural consequence of perusing the literature. The literature will presented chronologically.

1.3.2 Early theoretical foundations and controller design approaches

Interest in aerial refuelling followed as a natural progression from research in autonomous close formation flight. Close autonomous formation flight (AFF) offered the benefit of sustained drag reduction leading to improved efficiency in cooperative aircraft operations. Additional applications arising out of demonstrating AFF technology included AAR, low-visibility formation separation assurance, and UCAV pack and swarm operations (Hanson et al., (2002)). Relative-position station-keeping was demonstrated using global positioning system (GPS)-based technologies in the autonomous formation flight (AFF) program and slight modifications to this existing technology base would give AAR research an advanced starting point (Hansen et al., (2004)).

Since manned aerial refuelling was an operationalised manoeuvre, research in this area was already in existence. The research group of A.W. Bloy at the University of Manchester had made a significant contribution to the field of aerial refuelling research. During the 1980's

(e.g., Bloy et al., (1986)) into the late 1990's and early 2000's (Bloy and Khan (2001), Bloy and Khan (2002)), Bloy's theoretical and experimental research output provided key insights into the aerodynamic effects arising from the tanker-generated wake vortices on the receiver aircraft.

For close formation flight, the vortex wake effects due to the tanker aircraft were incorporated in a novel manner directly in the receiver aircraft dynamic equations of motion (Venkataramanan et al., (2003)). Using well-known aerodynamic vortex models, velocities induced on a receiver by the tanker aircraft vortex wake were able to be written as a function of relative separation between the two aircraft. By using an averaging technique, non-uniformities in the vortex-induced wind field were approximated into uniform wind components. In Saban et al., (2009), finding a compromise between computational accuracy of wake vortex effects and rapidity of execution time and resources led to the development of a wake vortex model to be used in a real-time synthetic simulation environment. Combining vortex lattice methods with the method developed in Venkataramanan et al., (2003) for uniform approximation of non-uniform vortex-induced wind and wind gradients, the method was directly used in a Simulink simulation environment.

Receiver aircraft models also received attention in the early research literature in AAR. The effect of mass variation on the dynamics of the receiver aircraft during aerial refuelling was studied by Mao and Eke (2008). In Waishek et al., (2009), the nonlinear receiver aircraft dynamic equations were written relative to the tanker and included the aerodynamic effect of proximity of the tanker and receiver. The "bow wave" effect, that is, the effect of the receiver aircraft on the tanker aircraft when the receiver aircraft is comparable in size, or larger than the tanker aircraft was also studied (Dogan et al., (2013)).

The proportional-integral-derivative (PID) control technique was used and tested in the formulation of control laws by the United States Air Force Institute of Technology for boom type fully autonomous aerial refuelling manoeuvres in level and turning flight (Ross et al., (2006)) using a variable stability Learjet LJ-25 as receiver and United States Air Force C-12 as tanker. This study offered a lot of practical insight into controller design for AAR using PID, as computer simulations were not done in isolation, but was accompanied by actual flight testing. The system mathematical model was nonlinear, with six degrees-of-freedom (DOF) and inclusive of the effects of turbulence. Controller gains were found by linearising the aircraft model for station-keeping requirements. These gains were then applied to the complete nonlinear aircraft model. Initially, proportional-integral control was considered, but due to insufficient damping, the derivative term was added giving PID control. Sensitivity and robustness properties of the controller were tested through the inclusion of turbulence, noise and maximum controller limits. A reduced set of controller gains (compared to simulation) were implemented in flight test due to problems related to sensor noise. Despite

this drawback, the linear PID controller performed well in the straight manoeuvre, however, suffered lateral overshoot in turning manoeuvres.

Focusing on the UAV manoeuvring to reach contact position (Dogan et al., (2005a)) and the racetrack manoeuvre (Dogan et al., (2007)), multi-input-multi-output (MIMO) linear quadratic regulator (LQR)-based state feedback and integral controllers were developed for BRR. In both studies (Dogan et al., (2005a), Dogan et al., (2007)) the main requirement for the controller was that of tracking the reference trajectory with zero steady-state error in x, y and z co-ordinates of the tanker frame while in the presence of the vortex and by variations in the receiver inertia. A nonlinear receiver aircraft model was developed relative to the tanker and included only the aerodynamic effect of proximity of the tanker. This nonlinear model was linearised around a nominal flight condition (excluding the wind term effects) for the control design; however the linear robust controllers were applied to the full nonlinear model in simulations. Gain scheduling based on speed and turn rate was implemented (Dogan et al., (2007)).

The L_1 adaptive control methodology was applied to the aerial refuelling problem. This controller was used for the longitudinal control of an F-16 aircraft in PDR refuelling (Wang et al., (2006)) to achieve docking with the drogue in a finite time period. In Wang et al., (2008), L_1 was used for control of the BANTAM UAV in PDR refuelling, but expanding on Wang et al., (2006) by including lateral dynamics. In Wise et al., (2008), this method was improved as the defined L_1 stability requirement eliminated the need for selecting and tuning neural network basis functions required by the adaptive control. In these studies, simulations of AAR docking manoeuvre in the presence of wake effects and/or loss in control effectiveness have verified the theory of the control design methodology.

In an early attempt at adaptive control formulation for the aerial refuelling problem, differential game framework was explored (Stepanyan et al., (2003)). A linear optimal control solution defined a guidance law, which the trailing aircraft tracked adaptively. This method was selected due to its advantages in adaptive tracking when applied to highly uncertain environments. A simplified longitudinal model of the F/A-16 aircraft was selected for the problem. The controller task was to fly the receiver aircraft into close proximity of the moving drogue and maintain its position there, without any specific knowledge of the drogue dynamics. The control law was augmented with an adaptive signal to account for uncertainties.

Exploring the application of robust control techniques, Pachter et al., (1997) and Chen et al., (2007) used qualitative feedback theory (QFT) and μ-synthesis techniques respectively in the design of controllers for aerial refuelling. For the QFT controller, the structured uncertainty in the AAR model was the changing aircraft dynamics as refuelling proceeds for BRR. To this end, sixteen plant models were developed in order to represent the plant uncertainty.

The mathematical model considered effects induced by refuelling and that of wind. The outer-loop feedback control system developed controlled altitude, speed and heading. Disturbance rejection was based on wind gusts and fuel flow rate. The μ-synthesis controller (Chen et al., (2007)) was developed for PDR, and considered structured disturbances and atmospheric disturbances. The structured disturbance was the change in weight. In addition, the change in CG position and change in aircraft moments of inertia were initially considered, but then neglected due to the magnitude change relative to that of the aircraft weight. The atmospheric disturbances comprised turbulence gust and wake effects. An equivalent disturbance model for the receiver aircraft was developed simultaneously incorporating all the disturbances modelled. The aim of the control design was to control the receiver attitude, as well as to have the pitch, roll and yaw angles respond linearly with respective control inputs. Simulations showed that these, as well as the robust performance and stability requirements that were stipulated were met. Similarly, in the QFT controller (Pachter et al., (1997)), linear simulations were performed in the presence of all external disturbances. Results showed very little deviation from the defined setpoint. Good disturbance rejection properties were observed.

The early body of research outputs also focused on modelling and control of the refuelling probe-drogue system and the docking phase. The National Aeronautics and Space Administration Dryden AAR project sought to deliver a flight-validated dynamic hose and drogue system model in order to develop an AAR system (Hansen et al., (2004)). Aerodynamic characteristics of a drogue assembly were investigated through wind-tunnel experiments and computational fluid dynamics (CFD)-simulation. An empirical model was developed to determine the drag characteristics of the paradrogue assembly (Ro et al., (2007)). A refuelling drogue modified to include canopy control effectors was studied to improve drogue-docking performance (Williamson et al., (2010)). LQR was used to control a drogue to maintain a fixed relative distance behind a tanker aircraft. The drogue model was modified to include canopies as control effectors in order to address docking challenges such as damping receiver-induced oscillations on the system (Williamson et al., (2010)). Control simulation results showed that a zero-mean error was achievable to 5cm tolerance in light turbulence and with receiver forebody effects. The study also gave insights (actuator force and rate limits) for actuator design to support active feedback control. The development of actively stabilised drogue refuelling systems was considered in Ro et al., (2010). Pre- and post-contact phases have been considered in conceptual control strategies. Detailed modelling of the hose-drogue system was considered, with the hose model comprising 20 links and 82 states representing the tanker horizontal and vertical motion. A linear model was derived at a specified flight condition. A PID controller was designed and used in conjunction with the complete nonlinear model, including atmospheric turbulence. Design requirements specified that the drogue

position be confined within a 10cm radius. A theoretically realistic actuation force was computed for the docking case studied. An actuator design concept to fulfil the active drogue control was not within the scope of the study. Dynamic testing of an actively controlled drogue refuelling system was conducted at the Western Michigan University's wind tunnel (Kuk et al., (2011)).

The boom-receptacle modelling was explored in the early stages of research into AAR, however, not to the same extent as the PDR research detailed earlier. Smith and Kunz (2007) developed equations of motion for the refuelling boom, modelling its motion and dynamic interactions with the tanker. The boom-tanker coupled model was compared to two existing boom-only models used in aerial refuelling improvement studies, and in boom operator training. The coupled model could be improved by including information about the boom itself, such as its exact mass distribution. Integration of the model into an AAR simulation environment and coupling with a tanker model were mentioned as the next steps to extend this work. In McFarlane et al., (2007), the refuelling boom model in Smith and Kunz (2007) was incorporated into a collaborative control scheme for BRR refuelling, focusing on the receiver aircraft longitudinal motion. A cooperative controller was created that produced a target location which both the receiver and refuelling boom could track. Two controllers were designed for the receiver aircraft - the first using the elevator to hold its vertical position below the tanker and the second using the throttle to hold its horizontal position behind the tanker. PID control was used in both cases. Eigenstructure assignment was used to place the longitudinal aircraft and controller modes to ensure close tracking of the hold point. Non-cancellation decoupling in BRR control was addressed in Qu et al., (2009) in order to address the presence of right-hand poles and in Yaohong et al., (2013), the alleviation of boom loads sensed from the nozzle sensors was addressed using LQR while employing the boom model decoupling approach on the two DOF boom model.

Nonlinear control law architectures and its initial developmental steps were broadly investigated in Elliot and Dogan (2010), in which the design of an input–output feedback linearisation (FBL) controller was investigated. The study focused on the developmental steps prior to employment of a MIMO input-output FBL nonlinear controller for AAR. It was found that the use of relative position as primary output appears to render a non-minimum phase system, which cannot be stabilised in a conventional FBL problem. Instead of computing Lie derivatives, linear equivalent matrices were investigated at given conditions which helped in understanding the nature of the influence of the control variables selected. This study gave insights into the structure of the inner- and outer-loops that would be required in order to develop an input-output FBL controller for AAR to primarily maintain a steady relative separation between the tanker and receiver aircraft. An early attempt in examining nonlinear control saw nonlinear dynamic inversion (NDI) combined with neural networks (Panday

and Pedro (2007), Pedro et al., (2013)). A nonlinear F-16 model including the effect of a changing centre of gravity position was used in representing a UCAV during a straight leg segment of aerial refuelling. Radial basis function (RBF) neural networks were developed and trained to approximate the inverse plant dynamics. This study has highlighted the potential of intelligent control and nonlinear modelling with promising results.

The relationship between instrumentation (i.e., sensor) requirements and controller design has been considered in combined control-instrumentation-based studies. These are termed "vision-based methods", and naturally follows on from the requirement that the receiver aircraft must maintain an accurate position relative to the tanker aircraft. Sensors, imaging, positioning, and navigation are some considerations to achieve the goal of accurate receiver-tanker positioning. These techniques can be combined with any control method to give a vision-based control system. More than just positioning, these techniques are best suited to the control system design for the actual probe-to-drogue or boom-to-receptacle docking manoeuvre. Without a pilot or boom operator in the loop to control the docking of the refuelling system components, highly accurate estimations of drogue or receptacle positions are needed. In vision based techniques, pose estimation, i.e., the determination of the aircraft's position and orientation specifically for aerial refuelling has been a major area of research. Point matching and feature extraction are also techniques that have been used in vision systems. Once the pose of the aircraft has been determined, this information can be used in a control law for aerial refuelling. Since the research presented in this report is primarily focused on controller design, a review of advances in vision techniques will not be presented. However, Li et al., (2012) provides a survey of the vision based techniques which could be applied to AAR for UAVs. The survey paper included vision-based navigation, visual servo-control, multi-sensor fusion methods and simulation approaches of AAR in this area. Panday and Pedro (2013) and Thomas et al., (2014) also provide an overview of sensor- and instrumentation-based strategies in AAR. More recently in Belmonte et al., (2019), the broader research community's extensive interest in the development of vision-based solutions for autonomous UAVs was presented, and the contribution of AAR vision-based systems towards this growing body of scientific knowledge featured strongly in the analysis.

1.3.3 Latest research in automated aerial refuelling control - 2012 to 2022

The latest research in AAR control is characterised by an evolution in the complexity of the focus areas of research groups. In addition, specific subsystems are analysed in more detail than was attended to at the start of research into this area. Probe-drogue docking remains a multi-faceted challenge of significant complexity evidenced by the volume of active research in this area, however, more research directed towards BRR is now taking place. While linear

control techniques were still explored in some works, recently, nonlinear control has been considered more frequently than the earlier time-frame when research in AAR began. The latest trends are segmented according to the aerial refuelling method: probe-drogue refuelling (PDR) and boom-receptacle refuelling (BRR).

1.3.3.1 Probe-drogue refuelling (PDR) method

In manned refuelling procedures, experienced pilots can accomplish the refuelling mission by carefully anticipating the movement of the drogue. However, it is still difficult for unmanned aerial refuelling (Dai et al., (2016)). Accordingly, research in PDR-based AAR has placed emphasis on addressing challenges that are specifically applicable to this method of refuelling.

Lou and Zhang (2013) designed an active disturbance rejection controller (ADRC) to reduce the effects of atmospheric turbulence. Altitude and lateral distance controller comprised inner loop PID control. The outer loop had PID as a baseline in one case, and then the proposed ADRC was used in the outer loop for comparison. A tracking differentiator, extended state observer and nonlinear state error feedback were integrated into the ADRC algorithm and parameters were tuned (similar in philosophy to PID). For level refuelling manoeuvres in the presence of turbulence, results showed that the tracking performance of the baseline PID and proposed ADRC controller was same, however disturbance rejection properties were better for the ADRC overall.

The PDR docking procedure was studied by Wu et al., (2013). In this study, the docking procedure required that a reference trajectory for docking with the drogue be generated and tracked. The reference trajectory was designed in two phases – lining up the height and lateral distances as defined, then secondly the probe must follow the drogue height and lateral coordinates. An LQR controller was proposed. Wake effects and the natural oscillation of probe-drogue refuelling system were not considered. The MIMO LQR controller followed the observer well. Fast and smooth docking was achieved.

A semi-active magnetorheological refuelling probe system was proposed and assessed in Choi and Wereley (2013). The suppression of undesirable loads experienced within the hose system during PDR refuelling was sought to be addressed by a smart refuelling probe system (probe, a coil spring, and magnetorheological damper). The developed model of the smart refuelling probe was used with the hose-drogue dynamics with different maximum closure velocities and tanker flight speeds. The proposed system showed significant reductions in probe-and-drogue motions, and was able to prevent the onset of large undesirable hose–drogue motions resulting from tension loads during engagement of the probe.

An integral sliding mode backstepping controller was designed for the hose-drogue aerial refuelling system to address the hose whipping phenomenon (HWP) (Haitao et al., (2014)). HWP refers to the motion of a disabled hose reel between a tanker and receiver aircraft during a PDR aerial refuelling manoeuvre. For coupling to occur again, HWP must be addressed through suitable control design. The control strategy put forward by Haitao et al., (2014) is based on the stabilising the hose tension by reeling the hose in or out based on the relative position between the tanker and receiver. This corresponds directly with angular control of the actuating rotor controlling the extended hose length. The problem was formulated as position tracking and to ensure global stability, backstepping control was selected by the research group.

Drogue system stability at low speed flight was investigated by McAndrew et al., (2015) for unmanned aircraft that are smaller than conventional aircraft. Speed, drogue length and drogue mass were investigated using wind tunnel and CFD data in a full factorial array analysis. The influence and interaction of each parameter was investigated so as to give designers and users statistical insight into the system when considering operational use in poor weather conditions.

A method to model the bow wave effect in PDR was developed by Dai et al., (2016). Inviscid flow around the receiver was modelled, errors caused by absence of viscosity was eliminated and aerodynamic coefficients were used to calculate the induced force on the drogue. This force was then used in a drogue dynamic model to give the motion of the drogue under the bow wave effect. Results were consistent with CFD and flight test data. The bow-wave effect on probe-drogue docking was also investigated by Wei et al., (2016). The study was able to simplify the complex high-order drogue link-connected model through parameter identification giving a second-order linear drogue model at the reference equilibrium state. The external force acting on the drogue due to the bow wave effect was modelled to be nonlinear in nature with its form obtained using CFD and its defining parameters obtained by nonlinear regression. The developed drogue dynamic model under bow wave effect was then compared to experimental results from drogue docking flight tests, and the model showed similarity to the experimental results. The developed model can be used to design a docking controller to overcome the bow wave effect.

Combining laboratory-based testing and computer simulations, Bolien et al., (2017) developed a hybrid testing approach that provided an intermediate de-risking step between component testing and full system flight testing for PDR refuelling. The study provided on-ground validation and preflight verification of probe–drogue contact–impact scenarios in AAR manoeuvrers using off-the-shelf multi-axis industrial robots as part of a hybrid test to interface the refuelling hardware with numerical models of the flight environment and was the first

robotic pseudodynamic testing hybrid simulation of an AAR manoeuvrer using scaled refuelling hardware. Future work will comprise tests with full-scale AAR hardware.

Backstepping high-order sliding-mode-based control was proposed for the docking control problem in AAR (Su et al., (2018)). The receiver docking flight controller was designed through five control loops. Multiple flow disturbances were considered in the receiver aircraft nonlinear model. The unmeasurable lumped disturbances were estimated via a specially designed high-order sliding-mode observer with faster convergence characteristic and higher estimation accuracy. The controller achieved its tracking performance specification at the cost of greater actuator surface deflections.

Applications of neural networks to PDR control have been limited to the vision- or guidance-based approaches. In Ma et al., (2018), a neural network model was used to predict the future position of the drogue as the target point of receiver aircraft. A predictive guidance scheme based on the neural model was proposed to improve the passive tracking of receiver aircraft for drogue during the docking phase of AAR. Aircraft and drogue detection using convolutional neural networks have been addressed in Mash (2017) and Choi et al., (2021) and pose estimation using deep learning has been addressed in Lee (2020).

1.3.3.2 Boom-receptacle refuelling (BRR)method

A pole placement controller designed to regulate the position of a receiver aircraft has been proposed by Kriel et al., (2013). A large aircraft was chosen as the receiver, with a significant distance between the refuelling receptacle and aircraft centre of gravity being a focal point of the study. The aircraft dynamics were adapted to take the position of the refuelling receptacle (RR) as reference point. This formulation introduced two complex zeros in the left half plane. Closed-loop poles were placed based on bandwidth and damping considerations. The proposed RR model was compared to the traditional centre of gravity model at various refuelling positions and system bandwidths. The research revealed, that for large refuelling aircraft, the receptacle dynamics must be considered in the controller design. Placing poles close to the RR zeros induced oscillations at the centre of gravity, however, in light turbulence, regulation of the receptacle position was demonstrated.

A stability augmentation system (SAS) was proposed by Yang et al., (2014), focusing on boom docking and enhancing the safety of the BRR procedure. It was found that the boom attitude response to a step deflection of the elevator or rudder are of low damping ratio and need a long time to reach the commanded steady state. Thus SAS is required for enhanced stability and flying qualities. The study noted that while there may be similarities between the aircraft and refuelling boom (comprising of wing and control surfaces), the characteristics

of motion are different. The refuelling boom essentially has two degrees-of-freedom. MIL-STD-1797 cannot be used and there is a need to formulate basic flying quality requirements and evaluation method for flying boom. The model developed focused on boom attitude motion. The following flying qualities criteria were identified: stability; manoeuvrability; time response; and frequency response. The idealised boom pitching and rolling models were second-order order systems, but in reality the order is higher, considering actuator dynamics and SAS. The final requirements were formulated on the aircraft longitudinal short-period oscillation because of similar characteristics to that of the refuelling boom behaviour.

The BRR docking procedure was considered in detail by Yuan et al., (2014). A multi-control approach was developed in order to take pre-docking and docking control into account. Prior to docking, the boom itself needs position and attitude control within its flying envelope. An LQR controller has been proposed to this end. However, when docking, the external disturbance acts on the boom itself. The change in receiver position, boom load and turbulent airflow must be compensated for by this control scheme – the anti-jamming performance of the boom must be enhanced. H-infinity control based on linear matrix inequality was proposed for the actual docking case. It is yet to be investigated how to optimally switch between the two proposed controllers. A hardware-in-the-loop simulation test platform was set up to perform representative simulations. Results showed that the steady-state error with the H-infinity controller was less than the LQR controller. In the presence of turbulence, the H-infinity controller performed better than the LQR.The anti-jamming capability was improved by use of the H-infinity controller. The switching to the H-infinity docking controller will be studied in future work by the research group.

Liu et al., (2014) used simple linear control design coupled with simulation software design in order to provide a visualisation platform for aerial refuelling simulations. A modular approach in design was adopted with the controller, UAV mathematical model, three-dimensional visual model, simulation result model, and flight parameter visualisation module making up the modules. A standard linear aircraft model (based on conventional simplifying assumptions) was used to define the longitudinal and lateral dynamics. Altitude, velocity and yaw control was considered. The linear model and control were implemented in Matlab first then directly used in the Microsoft Visual Studio 2010 simulation software, where sky and cloud environment were constructed in the visual module. Further work that will be considered by the researchers included the incorporation of wind vortex and uncertainty effects.

Collaborative control techniques are those which coordinate the simultaneous control of two objects, and in the case of the AAR, these would be the flying boom and the receiver aircraft (Thomas et al., (2015)). A simulation environment was developed to evaluate the collaborative control system. The flight control law developed for the receiver was aimed at minimising the difference in position between itself and a set of waypoints along the refuelling approach.

Waypoints were activated successively as preceding waypoints were reached within specified tolerances. A guidance and navigation filter comprised the outer-loop strategy which generated state command parameters. The inner-loop control was a PID controller. A linearised receiver model was used with LQR control to generate the initial controller gains. The automatic boom controller developed by Thomas et al., (2015) is an extension of a previously designed variable structure controller that was incorporated into the developed simulation environment. Target point generation incorporated the use of a weighting factor, which determined the level of collaboration between the boom and the receiver. The docking point also incorporated a weighting factor allowing docking to vary between convergence at datum point or via the shortest displacement point between the boom and receiver. Results from the developed simulation environment showed that the fully cyclic control proposed in the study (compared to the previously designed controller) was able to contain the docking to occur inside the defined envelope, enhancing operational effectiveness and efficiency.

A hardware-in-the-loop simulation test platform was developed by Yan et al., (2016) for the flying boom connection to a refuelling receptacle. A boom attitude tracking controller was designed and an automatic alignment algorithm was developed using vision and laser sensors, providing the attitude controller with the required spatial inputs. Simulation and experimental data showed that the technique was able to track the receptacle position.

When the receiver aircraft makes contact with the flying boom, a radial constrained force (RCF) develops. This force, which cannot be eliminated by the boom operator, has the potential to bend the boom, causing damage and putting the manoeuvre in jeopardy. A flying boom unloading controller was developed by Cao et al., (2017) to eliminate the RCF. Turbulence, bow-wave effect and the tanker's vortex wake were used to disturb the receiver aircraft position relative to the tanker thereby generating RCFs accordingly. Simulations showed that the designed controller was effective in unloading the developed force to levels below those prescribed in research.

A number of BRR-focused studies have investigated sliding-mode control as part of the overall control schemes proposed. Fractional-order sliding-mode control was used to restrict the force caused by the steering angle of spherical joint in BRR (Qu et al., (2015)). The refuelling boom model, steering angle force and command generator were developed and the proposed control law was constructed to address the requirements of automatic load alleviation on the refuelling boom. The effectiveness of the proposed controller was demonstrated by simulation. Yu et al., (2017) developed an adaptive backstepping controller to estimate the unknown upperbound of the vortex wake disturbances and combined this with sliding-mode control to attenuate the disturbances. Dynamic surface control was used for both attitude and velocity subsytems. The controller was limited to the longitudinal model of the receiver aircraft. Lyapunov stability showed the boundedness of the closed-loop system. Focusing on the

attitude control of the flying boom, a sliding mode disturbance observer-based backstepping controller was developed by Wang et al., (2017) to address the effects of disturbances on the flying boom, as well as boom flying qualities. An and Yuan, (2018) used ADRC with sliding-mode control while proposing a novel way of treating internal uncertainties and external aerodynamic disturbances as total disturbances with an extended state observer for state estimation. The equations of motion were formulated with respect to inertial axes.

Fault-tolerant control in AAR was considered in Yu et al., (2018) for the longitudinal dynamics of a receiver aircraft. Actuator faults in the elevator channel were modelled and along with the effects of the vortex wake; these were estimated as lumped uncertainties using disturbance observers. Backstepping control was used as the control scheme for the receiver aircraft.

Neural networks have been applied in the pose estimation problem for BRR in Lee et al., (2020). The performance of two stereo vision systems was quantified in ground tests specially designed to mimic AAR. Convolutional neural networks were proposed to generate three-dimensional point clouds of the target object.

1.4 Identified Gaps in Aerial Refuelling Control Research

From the literature review, it is evident that there is a deep body of knowledge in aerial refuelling, however, AAR of unmanned vehicles is not yet a mature technology. Control systems that have been proposed for aerial refuelling include PID, robust, optimal, and navigation-based systems, and these have been extensively explored either via simulation alone or coupled with laboratory or flight tests. Some techniques were extended further and merged with sensor-based (vision-based) systems. Classical and modern linear control techniques have been applied to the AAR problem by Ross et al., (2006), Ro et al., (2010), Kriel et al., (2013), Liu et al., (2014), Yang et al., (2014), and Yuan et al., (2014), amongst others mentioned in the literature review. Many studies have considered linear aircraft models as the basis for controller design. Controller gains were obtained by tuning linear models and in some of these studies, the linear-derived control gains were applied to the nonlinear system model. When systems are highly nonlinear, as is the case with AAR, there will be a loss of process information when the system is linearised at an equilibrium point, say for AAR, at the start of the refuelling process.

It may be beneficial to consider variations in weight and centre of gravity position, as well as atmospheric (aerodynamic) disturbances as part of the fundamental mathematical modelling. These have been identified as key factors in an aerial refuelling process. It is agreed that these

parameters in themselves may have uncertainties, however removing them completely from the fundamental model leads to an imprecise model. Also, aerodynamic wake effects are a part of the refuelling process, not necessarily a disturbance to aerial refuelling itself.

The major factors that affect the receiver aircraft dynamics are those related to time-varying mass/inertia properties over the duration of the refuelling, and that of the tanker aircraft trailing vortices. In the case of aerial refuelling, these effects can potentially destabilise a receiver aircraft (Dogan et al., (2005a)). These considerations have been included in the studies conducted by the University of Texas at Arlington research group, however, despite developing complex models, the controller strategies used linearised models and linear control. For instance, in Dogan et al., (2007) and Dogan et al., (2005a), although gain scheduling has been applied, this may prove to be ineffective if the aircraft is no longer close to the nominal conditions around which the gains were selected. This can lead to system instability and an altered system response from that expected.

Sliding-mode control has been applied in more recent research outputs. A major drawback of sliding-mode control is that it is prone to high-frequency oscillations known as chattering. Manifestation of this phenomenon in the control surfaces deflections for AAR will not be desirable due to the stringent performance and safety requirements for AAR missions. In Wang et al., (2017), sliding-mode control was applied to the two DOF boom model and in Yu et al., (2017) it was applied only to the longitudinal dynamics of a receiver aircraft in AAR, however, when applied to the more complex probe-drogue docking manoeuvre in Su et al., (2018), the manifestation of this behaviour in the control channel was evident. While sliding-mode control offers a framework to address external disturbances and parametric uncertainty, the potential of feedback linearisation has not been explored. Feedback linearisation has been used successfully to address helicopter and high performance aircraft control. Non-autonomous systems with uniform stability properties have some desirable ability to withstand disturbances (Slotine and Weiping (1991)), and this offers a pathway to controller design by extending Lyapunov stability analysis to this class of systems.

A summary of the key gaps/shortcomings that have been observed:

- Simple mathematical models have been developed for a complex nonlinear problem. There is a lack of complete nonlinear modelling for the receiver aircraft which includes all the necessary components being inherent to the aerial refuelling process - CG position, aerodynamics, vortex wake and varying mass and inertia properties - some of these are addressed in analyses related to disturbances and are framed as factors that are external to the aerial refuelling process.

- Conventional nonlinear control techniques have not been comprehensively considered - sliding-mode control has been applied, whereas, while a preliminary analysis of feedback linearisation was considered showing the possibilities for inner-loop control, further research in this area was not pursued.
- Evolutionary and swarm algorithms have not been applied to AAR controllers to optimise controller gains.
- Limited exploitation of neural networks has been observed in control law development. More recently, neural networks have been applied in vision-systems to detect the tanker aircraft or drogue position, but neural networks have had limited application in controller design. Where neural networks have been applied in control law development, their use has been limited to static neural networks.

In nonlinear control theory, FBL is distinctly different from Jacobian linearisation, which is a linear approximation that is only locally valid. In FBL on the other hand, the nonlinear system under study is transformed into a linear one by using state feedback and a nonlinear coordinate transformation based on a geometric analysis of the system. The elimination of nonlinearities thus allows for conventional linear control techniques to be adopted in order to design control laws. The application of differential geometry has been demonstrated as a successful means of analysing and designing nonlinear control systems, and this theory is grounded in rigorous mathematical foundations (Garces et al., (2003)). Many nonlinear control techniques require a dynamic model of the system, which is usually derived from physical principles. In many instances, access to physical models can prove to be challenging due to a number of factors, e.g., cost, complexity amongst others. However, by using measured input-output system data, the required model can be identified. Neural networks are well suited to this task due to their generalised approximation capability.

While nonlinear control methods have been applied in AAR research, indirect adaptive control using dynamic neural networks has not been explored in the literature. Moreover, the use of a Lyapunov-based approach to designing such control laws, coupled with controller gain optimisation through evolutionary algorithms is a gap in the literature that this study will seek to address.

1.5 Research Objectives

The main objective of the study is to investigate the suitability of using intelligent control techniques for a receiver-tanker system during aerial refuelling.

The research question is: "Can a stable control law be constructed by synthesising techniques in intelligent control for a receiver-tanker refuelling problem?"

The following sub-objectives for the research have been defined:

- To develop the system mathematical model taking all dynamic effects into account,
- To numerically simulate the behaviour of the system based on the developed model,
- To develop a baseline PID controller,
- To develop a framework to address system stability for the developed system using Lyapunov theory,
- To combine an evolutionary algorithm (EA) with PID thereby developing a PID-EA controller,
- To apply feedback linearisation control to the AAR system,
- To optimise the FBL controller gains using using the Lyapunov framework developed previously combined with an evolutionary algorithm,
- To identify a system model using dynamic neural networks,
- To use the dynamic neural network model in an indirect adaptive feedback linearisation controller using the Lyapunov framework developed previously to optimise the controller gains using an evolutionary algorithm,
- To test the robustness and performance of the developed controllers by applying system disturbances.

1.6 Research Methodology

Numerical simulation will be used to address the research objectives set out for this study. MATLAB is well known for its use in engineering and control applications as a programming and computing platform. The MATLAB programming environment will serve as the tool to simulate the developed mathematical system models, as well as the developed control laws. Data from the simulated AAR manoeuvre and controller optimisation will be processed and depicted in time-domain graphs of state variables, as well as in tabular format in the case of controller gains.

The research objectives can be met by arranging the investigation in three distinct phases. In the first phase (Figure 1.3), the system model for AAR is developed, which will be used in the baseline controller design. A single set of control gains for the entire refuelling duration will be found and these will be optimised with evolutionary algorithm techniques using a Lyapunov-based methodology to address stability.

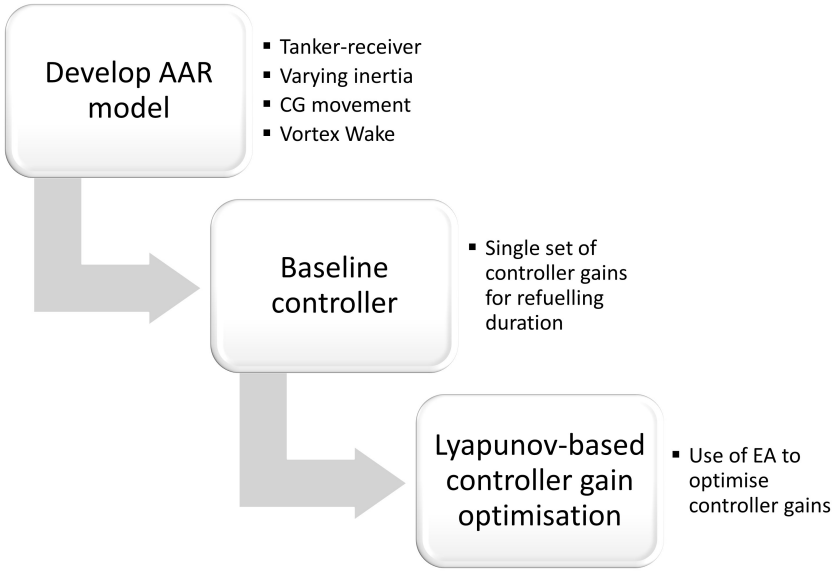


Figure 1.3: Research phase 1

In Figure 1.4 (phase 2), the developed AAR model and Lyapunov-based methodology will be used to develop a feedback linearisation controller in the inner loop, coupled with PID control for the outer-loop. Stability and performance under the influence of disturbances will be examined.

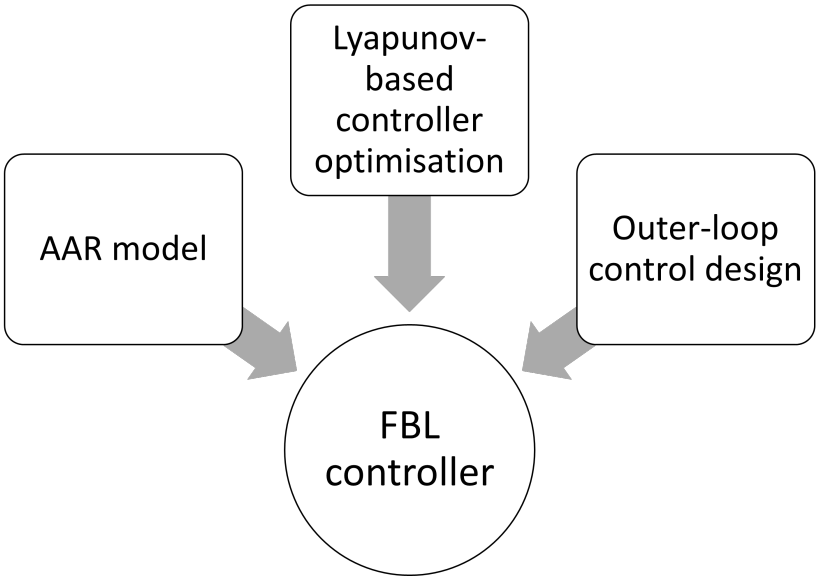


Figure 1.4: Research phase 2

Finally, in phase 3, a DNN model of the system will be developed using a set of generated input-output data. This DNN combined with the elements depicted in Figure 1.5 will be the basis of the design of the DNN-based controller.

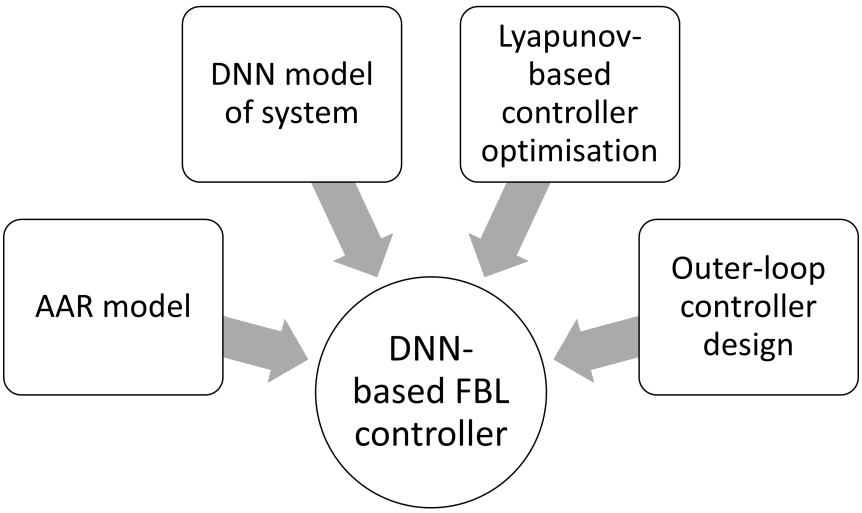


Figure 1.5: Research phase 3

1.7 Envisaged Contributions to Knowledge

There are various envisaged contributions to knowledge arising from this study. These are:

- The first principles development of a variable-mass system dynamic model subject to a wind-field to serve as the integrated nonlinear system model to be controlled and identified using the DNN.
- The extension of Lyapunov stability theory to the aerial refuelling problem, where the mechanical energy of the system is increased over time.
- The incorporation of an EA-based optimisation scheme that uses the Lyapunov-based method to optimise the single set of controller gains to be applied throughout the entire refuelling duration.
- The use of a DNN to approximate the AAR dynamics over the duration of the refuelling. This model approximation includes the effects of the varying mass, CG and inertia, and includes the effects of the tanker-generated vortex wake.
- The synthesis of the developed Lyapunov-based control optimisation with the identified DNN model to form an indirect adaptive controller using feedback linearisation.

- The elimination of the need for gain scheduling as the proposed controller schemes are able to use a single set of control gains throughout all phases of aerial refuelling over the duration of fuel transfer and subsequent station-keeping.

1.8 Thesis Outline

The mathematical modelling of the aerial refuelling system is presented in Chapter 2. The refuelling flight condition and refuelling phases for this research is defined in Chapter 3, where the benchmark controller is designed. System stability using Lyapunov theory is explored in Chapter 4. This is applied to the controller gain optimisation using evolutionary algorithms in Chapter 5. Chapter 6 provides a comprehensive overview of FBL and its application to the AAR problem, after which the FBL-based controller is developed and optimised. The theory underpinning DNNs is presented in Chapter 7. The system identification of the AAR model is detailed in Chapter 7. The DNN-FBL controller is developed and presented in Chapter 8. Finally conclusions and recommendations for future work are presented. The appendix shows system numerical parameters implemented in simulation and elements of the FBL modelling.

2 Aerial Refuelling System Mathematical Modelling

In this chapter, the mathematical model of the aerial refuelling engagement will be presented. In aerial refuelling, the tanker aircraft moves in a prescribed manner (e.g., racetrack pattern) and the receiver aircraft maintains a desirable position and orientation relative to the tanker. The importance of this relationship is reflected in control strategies for aerial refuelling, where the receiver motion is controlled relative to the tanker's. Whilst the receiver motion relative to the tanker is at the heart of the AAR control problem, a deliberate and systematic build up of all contributing factors must be considered, as is the focus of this chapter. Figure 2.1 depicts this systematic build up, where the effects of fuel transfer and wind-field are considered to be an essential part of the nonlinear refuelling mathematical model.

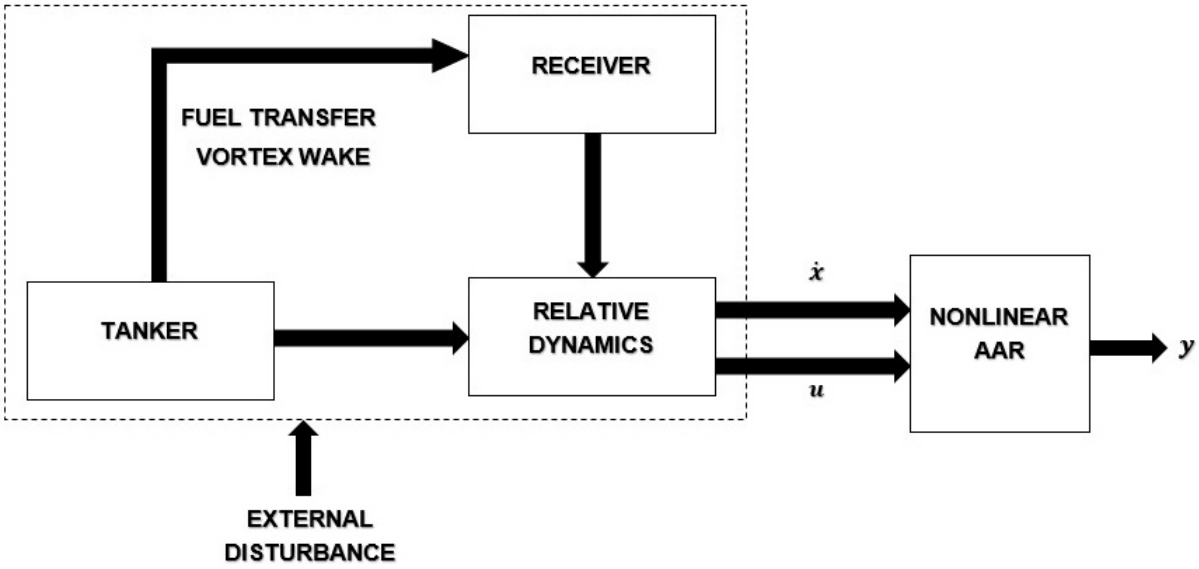


Figure 2.1: High-level depiction of key mathematical model elements

In Section 2.1, the aerial refuelling problem is introduced with definitions of state and control variables. In Section 2.2 the dynamics of a generalised variable mass system is derived and both linear and angular momentum is then considered for the aerial refuelling system. The

dynamics and kinematics for a variable-mass system subject to a wind-field (i.e., a receiver aircraft in an aerial refuelling manoeuvre) is presented in Section 2.3. This is followed by the description of the motion of a tanker aircraft in a wind-field in Section 2.5. The remainder of the Chapter describes the forces, moments, actuator dynamics and reference frames that are associated with the refuelling equations of motion, finally concluding with the fuel transfer model and the atmospheric and wind model elements.

2.1 Defining the Aerial Refuelling Problem

For the purposes of the controller design, the AAR model will be formulated as an affine nonlinear dynamical system (Eqs. 2.1 and 2.2):

$$\dot{\mathbf{x}} = f(\mathbf{x}) + g(\mathbf{x})\mathbf{u} \tag{2.1}$$

$$\mathbf{y} = h(\mathbf{x}) \tag{2.2}$$

$$\mathbf{x} \in \mathbf{R}^n,\ \mathbf{u} \in \mathbf{R}^m,\ \mathbf{y} \in \mathbf{R}^m,\ \mathbf{f}(\mathbf{x}) \in \mathbf{R}^n,\ \mathbf{g}(\mathbf{x}) \in \mathbf{R}^{n\times m},\ \mathbf{h}(\mathbf{x}) \in \mathbf{R}^{m\times n}$$

where $\mathbf{x}$, $\mathbf{u}$ and $\mathbf{y}$ are the state, control and output vectors respectively. $\mathbf{f}(\mathbf{x})$ and $\mathbf{g}(\mathbf{x})$ are functions which characterise the nonlinear affine system, with $\mathbf{h}(\mathbf{x})$ being the function which relates output vector to the state vector. Indices n and m correspond to the dimensions of the state, control and output vectors.

The tanker aircraft state dependencies are written including the effect of a generalised wind-field in Eq. 2.3. Twelve state (Eq. 2.4) and four control variables (Eq. 2.5) describe the tanker motion in six DOF, all referenced with subscript $_T$.

$$\dot{\mathbf{x}}_T = f(\mathbf{x}_T, \mathbf{u}_T, \mathbf{W}_T),\ \mathbf{x}_T \in \Re^{12} \tag{2.3}$$

$$\mathbf{x}_T = [V_T,\, \beta_T,\, \alpha_T,\, p_T,\, q_T,\, r_T,\, \phi_T,\, \theta_T,\, \psi_T,\, x_T,\, y_T,\, z_T]^T \tag{2.4}$$

$$\mathbf{u}_T = [\delta_{a_T},\, \delta_{e_T},\, \delta_{r_T},\, \delta_{T_T}]^T \tag{2.5}$$

Eq. 2.4 is separated into combinations or groupings of variables that will be convenient in the expression of dynamic and kinematic relations later on (Eqs. 2.6 to 2.9):

$$\mathcal{X}_T = [V_T, \beta_T, \alpha_T]^T \tag{2.6}$$

$$\omega_{B_T} = [p_T,\, q_T,\, r_T]^T \tag{2.7}$$

$$Eul_T = [\phi_T,\, \theta_T,\, \psi_T]^T \tag{2.8}$$

$$r_{B_T} = [x_T,\, y_T,\, z_T]^T \tag{2.9}$$

The receiver aircraft state dependencies are expressed in compact form in Eq. 2.10. This is inclusive of the tanker motion, wind-field and mass transfer. The receiver state vector and control input referenced with subscript $_R$ (Eqs. 2.11 and 2.12):

$$\dot{\mathbf{x}}_R = f\left(\mathbf{x}_R,\, \mathbf{x}_T,\, \mathbf{u}_R,\, \mathbf{W}_R,\, \dot{m}\right) \tag{2.10}$$

$$\mathbf{x}_R = [V_R,\, \beta_R,\, \alpha_R,\, p_{TR},\, q_{TR},\, r_{TR},\, \phi_{TR},\, \theta_{TR},\, \psi_{TR},\, x_{TR},\, y_{TR},\, z_{TR}]^T \tag{2.11}$$

$$\mathbf{u}_R = [\delta_{a_R},\, \delta_{e_R},\, \delta_{r_R},\, \delta_{T_R}]^T \tag{2.12}$$

Since the receiver motion will be controlled with respect to the tanker, some of the twelve states given in Eq. 2.11 are defined relative to tanker aircraft, indicated by the subscript $_{TR}$. Combinations or groupings similar to the tanker are presented for the receiver aircraft in Eqs. 2.13 to 2.16:

$$\mathcal{X}_\mathcal{R} = [V_R, \beta_R, \alpha_R]^T \tag{2.13}$$

$$\omega_{B_R B_T} = [p_{TR}, q_{TR}, r_{TR}]^T \tag{2.14}$$

$$Eul_{TR} = [\phi_{TR},\, \theta_{TR},\, \psi_{TR}]^T \tag{2.15}$$

$$\xi = [x_{TR},\, y_{TR},\, z_{TR}]^T \tag{2.16}$$

2.2 Dynamics of a Variable-Mass System

Plastino and Muzzio (1992) have given an overview on the validity of the direct application of Newton's Second Law for variable mass systems. The law cannot be used in its traditional sense when dealing with variable mass systems. When mass varies due to accretion or ablation, relationship Eq. 2.17 will apply. (Note, vector quantities are expressed in bold font in Section 2.2).

$$\frac{d\mathbf{v}}{dt} m(t) = \mathbf{F} + \mathbf{u}\frac{dm}{dt} \tag{2.17}$$

However, this generalised relationship is expressed only considering the linear momentum. In this section, the linear and angular momentum of systems subject to mass variation will be derived so that the dynamics of the AAR system can be expressed for the controller design.

The derivation is adapted from Cveticanin (2016) and Giancoli (2009), with variables defined to be consistent with Cveticanin (2016). The derived vector relationships (inclusive of wind terms) will be compared to those in Waishek (2007) in order to validate the equations developed in this chapter, as well as to ascertain correctness in methodology.

A major assumption in the work of Cveticanin is that the initial body, added body of mass and final body form a unique system. This assumption is the basic criterion for deriving the dynamics of the final body after mass variation.

2.2.1 Linear momentum - general case

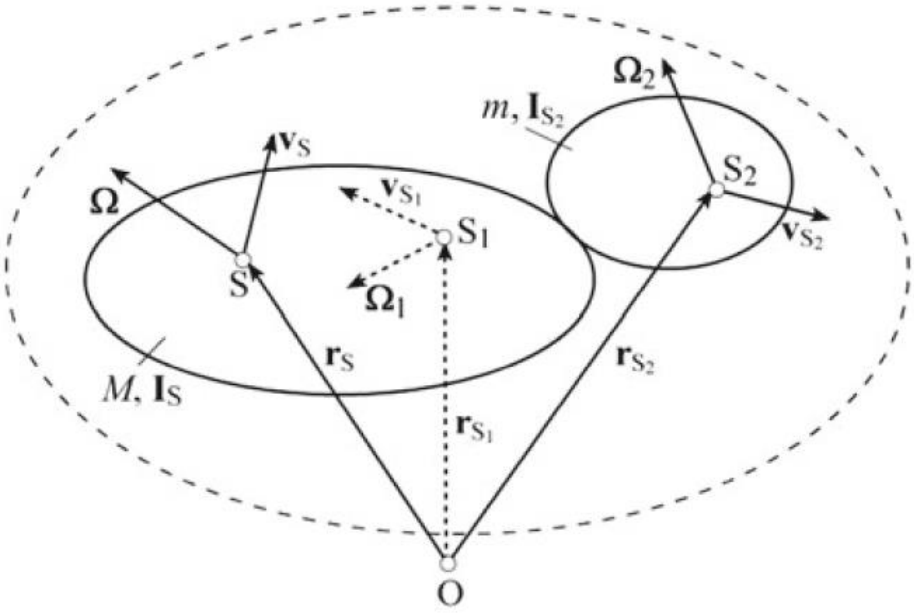


Figure 2.2: Variable mass system (Cveticanin (2016))

The linear momentum of the initial body in Figure 2.2 with mass M located at centre of mass S and velocity $\mathbf{v}_S$ is:

$$\mathbf{K} = M\mathbf{v}_S \tag{2.18}$$

Cveticanin (2016) gives linear momentum of the added mass m with the velocity $\mathbf{v}_{S2}$:

$$\mathbf{K}_2 = m\mathbf{v}_{S2} \tag{2.19}$$

When a body with mass m is added to the body with initial mass M, the linear momentum of the final body is

$$\mathbf{K}_1 = (M+m)\,\mathbf{v}_{S1} \tag{2.20}$$

While mass is being added, it is assumed that the initial, added and final bodies are in a unique system (see Figure 2.2), then the linear momentum $\mathbf{K}_b$ before addition contains two terms corresponding to the initial body and to the added body, i.e., it is:

$$\mathbf{K}_b = \mathbf{K} + \mathbf{K}_2 = M\mathbf{v}_S + m\mathbf{v}_{S2} \tag{2.21}$$

Linear momentum after body addition $\mathbf{K}_a$ is equal to the linear momentum $\mathbf{K}_1$ of the final body

$$\mathbf{K}_a = \mathbf{K}_1 = (M+m)\,\mathbf{v}_{S1} \tag{2.22}$$

Variation of the linear momentum during mass addition is

$$\Delta\mathbf{K} = \mathbf{K}_a - \mathbf{K}_b = M\,(\mathbf{v}_{S1} - \mathbf{v}_S) + m\,(\mathbf{v}_{S1} - \mathbf{v}_{S2}) \tag{2.23}$$

If $\mathbf{F}_r$ is the resultant force acting on a body, then the variation of the linear momentum in a time interval $\triangle t$ is equal to the impulse $\mathbf{J}^{Fr}$ of the resultant force $\mathbf{F}_r$

$$\Delta\mathbf{K} = \mathbf{F}_r \triangle t \equiv \mathbf{J}^{Fr} \tag{2.24}$$

Thus, Eq. 2.23 becomes

$$\Delta\mathbf{K} \equiv M \triangle \mathbf{v} + m\,(\mathbf{v}_{S2} - \mathbf{v}_{S1}) = \mathbf{F}_r \triangle t \tag{2.25}$$

where velocity variation is

$$\triangle \mathbf{v} = \mathbf{v}_{S1} - \mathbf{v}_S \tag{2.26}$$

Introducing $\mathbf{u}$ and $\mathbf{v}$

$$\mathbf{v}_{S2} = \mathbf{u}, \mathbf{v}_{S1} = \mathbf{v} \tag{2.27}$$

Eq. 2.23 further reduces to:

$$M \triangle \mathbf{v} = \mathbf{F}_r \triangle t - \Delta M (\mathbf{u} - \mathbf{v}) \tag{2.28}$$

Now dividing the obtained expression with the infinitesimal time $\triangle t$:

$$M \frac{\triangle \mathbf{v}}{\triangle t} = \mathbf{F}_r - \frac{\triangle M}{\triangle t} (\mathbf{u} - \mathbf{v}) \tag{2.29}$$

For the limit condition, when the infinitesimal time tends to zero, the following is obtained:

$$M \frac{d\mathbf{v}}{dt} = \mathbf{F}_r + \left(- \left| \frac{dM}{dt} \right| \right) (\mathbf{u} - \mathbf{v}) \tag{2.30}$$

i.e.,

$$M \frac{d\mathbf{v}}{dt} = \mathbf{F}_r + \frac{dM}{dt} (\mathbf{u} - \mathbf{v}) \tag{2.31}$$

The differential equation of motion now transforms into

$$M \frac{d\mathbf{v}}{dt} = \mathbf{F}_r + \frac{dM}{dt} (\mathbf{u} - \mathbf{v}) \tag{2.32}$$

The term $\frac{dM}{dt} (\mathbf{u} - \mathbf{v})$ represents the reactive force

$$\mathbf{\Phi} = \frac{dM}{dt} (\mathbf{u} - \mathbf{v}) \tag{2.33}$$

The reactive force is the result of the continual mass variation with time, and is the product of mass variation and the relative velocity of variable mass body. For bodies with constant mass, the reactive force does not exist.

Rewriting:

$$M \frac{d\mathbf{v}}{dt} = \mathbf{F}_r + \Phi \tag{2.34}$$

This can be expressed in its scalar components, for a fixed-coordinate system $Oxyz$, components v_x,v_y,v_z of the velocity $\mathbf{v}$, components u_x,u_y,u_z of the velocity $\mathbf{u}$ and F_x, F_y, F_z, components of the resultant $\mathbf{F}_r$.

$$M \frac{dv_x}{dt} = F_x + \Phi_x, M \frac{dv_y}{dt} = F_y + \Phi_y, M \frac{dv_z}{dt} = F_z + \Phi_z \tag{2.35}$$

The reactive force projections are also given as (Cveticanin (2016)):

$$\Phi_x = \frac{dM}{dt}(u_x - v_x), \Phi_y = \frac{dM}{dt}(u_y - v_y), \Phi_z = \frac{dM}{dt}(u_z - v_z) \tag{2.36}$$

In Cveticanin's discussion of the differential equations of motion, it has been stated that the translational motion of variable mass body is equal to that of the particle with variable mass and is described as:

$$M\frac{d\mathbf{v}}{dt} = \mathbf{F}_r + \Phi \tag{2.37}$$

The above relation is very often rewritten as:

$$\frac{d}{dt}(M\mathbf{v}) = \mathbf{F}_r + \Phi^* \tag{2.38}$$

where

$$\Phi^* = \mathbf{u}\frac{dM}{dt} \tag{2.39}$$

Additionally, Cveticanin further discusses that if a mechanical system containing N particles whose masses $M_i, (i = 1, 2, ..., N)$ are time dependent and their position according to the fixed point O are r_i, then the equation of motion of such a particle is:

$$M_i\frac{d\mathbf{v_i}}{dt} = \mathbf{F}_{ri} + \Phi_i \tag{2.40}$$

i.e.,

$$\frac{d}{dt}(M_i\mathbf{v}_i) = \mathbf{F}_{ri} + \Phi_i^* \tag{2.41}$$

where $\mathbf{F}_{ri}$ includes all external and internal forces and constraints which acts on the particle i. Φ_i is the reactive force and

$$\Phi_i^* = \mathbf{u}_i\frac{dM_i}{dt} \tag{2.42}$$

is the influence force which depends on absolute velocity of the particle additions $\mathbf{u}_i$. Thus, the equation of motion for the system is:

$$\sum_{i=1}^{N}\left(M_i\frac{d\mathbf{v_i}}{dt} - \mathbf{F}_{ri} - \Phi_i\right) = 0 \tag{2.43}$$

or:

$$\sum_{i=1}^{N}\left(\frac{d}{dt}(M_i\mathbf{v}_i)-\mathbf{F}_{ri}-\Phi_i^*\right)=0 \tag{2.44}$$

2.2.2 Linear momentum - aerial refuelling problem

Now that the generalised expression has been derived according to the methodology in Cveticanin (2016), the specific aerial refuelling parameters can be incorporated. In Figure 2.3, the system model from Cveticanin is presented with the refuelling position vectors to be used in moving from the generalised case to the AAR case. Fuel of mass m enters the receiver at the refuelling port with velocity $\mathbf{V}_{fuel}$ and subsequently fills up a number of fuel tanks. A fuel tank represented by Cveticanin's $S2$ will fill up according to the variation in position vector $\mathbf{r}_{s_2}$. However, this can be generalised for any number of fuel tanks (n_{ft}) located at positions r_{m_j} with respect to origin O. The pre-refuelling CG coincided with S, which remains the CG of the un-refuelled aircraft. However, when fuel is being transferred the combined aircraft-fuel tank system now has its CG located at $S1$, in line with Cveticanin, and $\mathbf{r}_{s_1}$ is renamed $\mathbf{r}_{B_R}$.

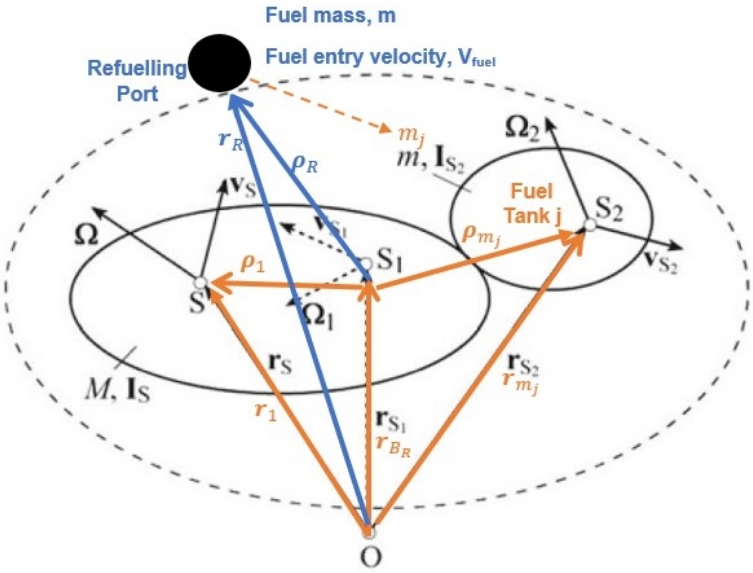


Figure 2.3: Definition of refuelling position vectors - overlay with Cveticanin (2016)

From Figure 2.3, the position vectors are related to each other as follows:

$$\mathbf{r}_1=\mathbf{r}_{B_R}+\boldsymbol{\rho}_1 \tag{2.45}$$

$$\mathbf{r}_{m_j}=\mathbf{r}_{B_R}+\boldsymbol{\rho}_{m_j} \tag{2.46}$$

$$\mathbf{r}_R=\mathbf{r}_{B_R}+\boldsymbol{\rho}_R \tag{2.47}$$

Expressing the linear momentum in terms of the rate of change of position vectors, Eq. 2.44 can be rewritten as:

$$\sum_{i=1}^{N}\left(\frac{d}{dt}(M_i\dot{\mathbf{r}}_i)-\mathbf{F}_{ri}-\Phi_i^*\right)=0 \tag{2.48}$$

If the system above comprises of one receiver aircraft with a single refuelling port and j representing the number of fuel tanks, and combining all of the forces into a generalised term:

$$\sum_{i=1}^{N}\mathbf{F}_{ri}=\sum\mathbf{F} \tag{2.49}$$

then the following can be written:

$$\frac{d}{dt}(M_1\dot{\mathbf{r}}_1)+\sum_{j=1}^{n_{ft}}\frac{d}{dt}(m_j\dot{\mathbf{r}}_{mj})-\sum\mathbf{F}-\Phi_1^*=0 \tag{2.50}$$

The reactive force in Eq. 2.42 due to fuel entering the receiver aircraft at the refuelling port is:

$$\Phi_1^*=\dot{m}\mathbf{V}_{fuel} \tag{2.51}$$

Applying the derivative and noting that the receiver aircraft mass M_1 in system S (Figure 2.3) remains the same, the following is obtained:

$$M_1\ddot{\mathbf{r}}_1+\sum\dot{m}_j\dot{\mathbf{r}}_{mi}+\sum m_j\ddot{\mathbf{r}}_{mj}-\sum\mathbf{F}-\dot{m}\mathbf{V}_{fuel}=0 \tag{2.52}$$

Substituting the vector relations described in Eq. 2.45 - Eq. 2.47, and applying disaggregation of V_{fuel} into its relevant components with respect to the tanker (i.e., $\mathbf{V}_{fuel}=\dot{\mathbf{r}}_{B_T}+\mathbf{V}_{\dot{m}}$) together with the the effect of the wind on the translational motion $\ddot{\mathbf{r}}_{B_R}=\dot{\mathbf{U}}+\dot{\mathbf{W}}$,

$$\dot{\mathbf{U}}=\frac{1}{M+m}\left[\sum\mathbf{F}-\dot{m}\left(\mathbf{U}+\mathbf{W}-\dot{\mathbf{r}}_{B_T}-\mathbf{V}_{\dot{m}}\right)-\sum\left(\dot{m}_j\dot{\rho}_{mj}+m_j\ddot{\rho}_{mj}\right)\right]-\dot{\mathbf{W}} \tag{2.53}$$

2.2.3 Angular momentum - aerial refuelling case

Considering that the forces have been defined above for the aerial refuelling case, it becomes easier to formulate the angular momentum relationships. The linear momentum was written

considering fixed point O in Figure 2.2, which corresponded to the origin of the inertial reference frame. Using Giancoli (2009) together with Cveticanin's discussion for a system of masses whose equation of motion is given in Eq. 2.41, the total angular momentum $\mathbf{L}$ of a system is equivalent to the vector sum of the angular momentum of all the particles in the system:

$$\mathbf{L} = \sum_{i=1}^{N} \mathbf{L}_i \tag{2.54}$$

The resultant torque τ_{net} acting on the system is the sum of the net torques acting on all the particles.

$$\boldsymbol{\tau}_{net} = \sum_{i=1}^{N} \boldsymbol{\tau}_i \tag{2.55}$$

Also, the time rate of change of the angular momentum of a system of particles is equal to the resultant external torque on the system:

$$\frac{d\mathbf{L}}{dt} = \sum \boldsymbol{\tau}_{ext} \tag{2.56}$$

Torque is generically defined as the vector cross product of the position and force vectors:

$$\boldsymbol{\tau} = \mathbf{r} \times \mathbf{F} \tag{2.57}$$

It was earlier discussed that the force is also the same as the rate of change of linear momentum. The angular momentum relationships described above can therefore be directly applied to Eq. 2.48. From Giancoli (2009), $\mathbf{L}$ and $\boldsymbol{\tau}$ are to be calculated about the same origin O.

The rotational equation of motion using generalised position vectors applied to Eq. 2.48, replacing $\boldsymbol{\tau}$ with $\mathbf{M}$ is thus:

$$\sum_{i=1}^{N} \left(\mathbf{r}_i \times \frac{d}{dt}(M_i \mathbf{v} i) - \mathbf{r}_{F_{ri}} \times \mathbf{F}_{ri} - \mathbf{r}_{\Phi_i} \times \Phi_i^* \right) = \sum \boldsymbol{\tau}_{ext} = \sum \mathbf{M} \tag{2.58}$$

The derivation methodology used for the linear momentum case first outlined the generalised relations before incorporating the specific parameters for the refuelling. Here it is not necessary to further proceed with the generalised equation derived above. Instead, Eq. 2.52 can be directly used, also noting that the external forces are given by:

$$\sum \mathbf{F} = M_1 \ddot{\mathbf{r}}_1 + \sum \dot{m}_j \dot{\mathbf{r}}_{mi} + \sum m_j \ddot{\mathbf{r}}_{mj} - \dot{m} \mathbf{V}_{fuel} \tag{2.59}$$

$$\mathbf{r}_1 \times M_1 \ddot{\mathbf{r}}_1 + \mathbf{r}_{mj} \times \sum m_j \dot{\mathbf{r}}_{mj} + \mathbf{r}_{mj} \times \sum \dot{m}_j \ddot{\mathbf{r}}_{mj} - \mathbf{r}_{B_R} \times \sum \mathbf{F} - \mathbf{r}_R \times \dot{m} \mathbf{V}_{fuel} = \sum \mathbf{M} \tag{2.60}$$

Substituting the above resultant force as well as position vectors in Eq. 2.45 - Eq. 2.47, the external moment is given by:

$$\begin{aligned} \rho_1 \quad \times \quad & M_1 \left(\ddot{\mathbf{r}}_{B_R} + \ddot{\rho}_1 \right) + \sum \rho_{mj} \times \left(\dot{m}_j \left(\dot{\mathbf{r}}_{B_R} + \dot{\rho}_{mj} \right) + m_j \left(\ddot{\mathbf{r}}_{B_R} + \ddot{\rho}_{mj} \right) \right) \\ - \quad & \rho_R \times \dot{m} \mathbf{V}_{fuel} = \sum M \end{aligned} \tag{2.61}$$

As in the case of the linear momentum, on applying the fuel velocity components and wind effects, the sum of moments becomes:

$$\begin{aligned} \rho_1 \quad \times \quad & M_1 \left(\dot{\mathbf{U}} + \dot{\mathbf{W}} + \ddot{\rho}_1 \right) + \sum \rho_{mj} \times \dot{m}_j \left(\mathbf{U} + \mathbf{W} + \dot{\rho}_{mj} \right) \\ + \quad & \sum \rho_{mj} \times m_j \left(\dot{\mathbf{U}} + \dot{\mathbf{W}} + \ddot{\rho}_{mj} \right) - \rho_R \times \dot{m} \left(\dot{\mathbf{r}}_{B_T} + \mathbf{V}_{\dot{m}} \right) = \sum M \end{aligned} \tag{2.62}$$

2.3 Dynamics and Kinematics of Variable-Mass System subject to Wind-Field

Translational and rotational state variables were grouped in Eq. 2.13 and Eq. 2.14. Referring to the same groupings of state variables, and using k as the total number of fuel tanks, the translational dynamics, $\dot{\mathcal{X}}_{\mathcal{R}}$ and the rotational dynamics $\dot{\omega}_{B_R B_T}$ can be expressed using the state-space representations (Waishek (2007)):

$$\dot{\mathcal{X}}_{\mathcal{R}} = \mathbf{f_1} \dot{\omega}_{B_R B_T} + c_1 \tag{2.63}$$

$$\dot{\omega}_{B_R B_T} = \mathbf{f_2} \dot{\mathcal{X}}_{\mathbf{R}} + c_2 \tag{2.64}$$

with:

$$\mathbf{f_1} = -\frac{1}{M+m}\mathcal{E}_{\mathbf{R}}^{-\mathbf{1}}\left[\sum_{j=1}^{k} m_j S\left(\rho_{m_j}\right)\right] \tag{2.65}$$

$$\begin{aligned}
c_1 &= \mathcal{E}_{\mathbf{R}}^{-\mathbf{1}}\left[\mathbf{S}\left(\omega_{B_R B_T}\right) + \mathbf{S}\left(\mathbf{R}_{\mathbf{B_R B_T}}\omega_{\mathbf{B_T}}\right)\right]\left(\mathbf{R}_{\mathbf{B}_{\mathbf{B_R}}\mathbf{W_R}}U + W\right) - \mathcal{E}_{\mathbf{R}}^{-\mathbf{1}}\dot{W} \\
&+ \frac{1}{(M+m)}\mathcal{E}_{\mathbf{R}}^{-\mathbf{1}}\left[\mathbf{R}_{\mathbf{B_R B_T I}}\left(F + \dot{m}\dot{r}_{B_T}\right) - \dot{m}\left(\mathbf{R}_{\mathbf{B_R W_R}}U + W - \mathbf{R}_{\mathbf{B_R B_T}}V_{\dot{m}}\right)\right] \\
&- \frac{1}{(M+m)}\mathcal{E}_{\mathbf{R}}^{-\mathbf{1}}\sum_{j=1}^{k}\Bigg(\dot{m}_j\left\{\dot{\rho}_{m_j} - \left[\mathbf{S}\left(\omega_{\mathbf{B_R B_T}}\right) + \mathbf{S}\left(\mathbf{R}_{\mathbf{B_R}}\omega_{\mathbf{B_T}}\right)\right]\rho_{m_j}\right\} \\
&+ m_j\{\ddot{\rho}_{m_j} + \mathbf{S}\left(\omega_{\mathbf{B_R B_T}}\right)\left[\mathbf{S}\left(\omega_{\mathbf{B_R B_T}}\right)\rho_{m_j} - 2\dot{\rho}_{m_j}\right] \\
&+ 2\mathbf{S}\left(\mathbf{R}_{\mathbf{B_R B_T}}\omega_{\mathbf{B_T}}\right)\left[\mathbf{S}\left(\omega_{\mathbf{B_R B_T}}\right)\rho_{m_j} - \dot{\rho}_{m_j}\right] \\
&+ \left[\mathbf{S}^2\left(\mathbf{R}_{\mathbf{B_R B_T}}\omega_{\mathbf{B_T}}\right) - \mathbf{S}\left(\mathbf{R}_{\mathbf{B_R B_T}}\dot{\omega}_{\mathbf{B_T}}\right)\right]\rho_{m_j}\}\Bigg)
\end{aligned} \tag{2.66}$$

$$\mathbf{f_2} = \underline{\underline{\mathbf{I}}}_{\mathbf{t}}^{-1}\left[\sum_{j=1}^{k}\mathbf{S}\left(\rho_{\mathbf{m_j}}\right)m_j\right]\mathcal{E}_{\mathbf{R}} \tag{2.67}$$

For ease of presentation, let:

$$\sum_{j=1}^{k}\mathbf{S}\left(\rho_{\mathbf{m_j}}\right) = \mathbf{\Sigma}^{\star} \text{ and } \sum_{j=1}^{k}\mathbf{S}\left(\rho_{\mathbf{m_j}}\right)\dot{m}_j = \mathbf{\Sigma}_{mj}^{\star} \tag{2.68}$$

$$\begin{aligned}
c_2 &= \underline{\underline{\mathbf{I}}}_{\mathbf{t}}^{-1}M_{B_R}\underline{\underline{\mathbf{I}}}_{\mathbf{t}}^{-1}\mathbf{S}\left(\omega_{\mathbf{B_R B_T}} + \mathbf{R}_{\mathbf{B_R B_T}}\omega_{\mathbf{B_T}}\right)\underline{\underline{\mathbf{I}}}_{\mathbf{M}}\left(\omega_{B_R B_T} + \mathbf{R}_{\mathbf{B_R B_T}}\omega_{B_T}\right) \\
&+ \underline{\underline{\mathbf{I}}}_{\mathbf{t}}^{-1}\mathbf{\Sigma}^{\star}\left[m_j\left(\omega_{B_R B_T}^T + \omega_{B_T}^T\mathbf{R}_{\mathbf{B_R B_T}}^{\mathbf{T}}\right)\rho_{m_j}\left(\omega_{\mathbf{B_R B_T}} + \mathbf{R}_{\mathbf{B_R B_T}}\omega_{\mathbf{B_T}}\right) + m_j\ddot{\rho}_{m_j} + \dot{m}_j\dot{\rho}_{m_j}\right] \\
&+ \underline{\underline{\mathbf{I}}}_{\mathbf{t}}^{-1}\left[\mathbf{\Sigma}_{mj}^{\star}\right]\left\{-\left[\mathbf{S}\left(\omega_{\mathbf{B_R B_T}}\right) + \mathbf{S}\left(\mathbf{R}_{\mathbf{B_R B_T}}\omega_{\mathbf{B_T}}\right)\right]\left(\mathbf{R}_{\mathbf{B_R W_R}}U + W\right) + \dot{W}\right\} \\
&+ \underline{\underline{\mathbf{I}}}_{\mathbf{t}}^{-1}\left[\sum_{j=1}^{k}\mathbf{S}\left(\rho_{\mathbf{m_j}}\right)\dot{m}_j\right]\left(\mathbf{R}_{\mathbf{B_R W_R}}U + W\right) \\
&- 2\underline{\underline{\mathbf{I}}}_{\mathbf{t}}^{-1}\sum_{j=1}^{k}m_j\left[\left(\rho_{m_j}^T\dot{\rho}_{m_j}\right)\mathbf{I_{3\times 3}} - \dot{\rho}_{m_j}\rho_{m_j}^T\right]\left(\omega_{B_R B_T + \mathbf{R_{B_R B_T}}}\omega_{B_T}\right) \\
&- \underline{\underline{\mathbf{I}}}_{\mathbf{t}}^{-1}\sum_{j=1}^{k}\dot{m}_j\left[\left(\rho_{m_j}^T\dot{\rho}_{m_j}\right)\mathbf{I_{3\times 3}} - \dot{\rho}_{m_j}\rho_{m_j}^T\right]\left(\omega_{B_R B_T + \mathbf{R_{B_R B_T}}}\omega_{B_T}\right) \\
&- \mathbf{S}\left(\omega_{B_R B_T}\right)\mathbf{R}_{\mathbf{B_R B_T}}\omega_{B_T} - \mathbf{R}_{\mathbf{B_R B_T}}\dot{\omega}_{B_T} \\
&- \underline{\underline{\mathbf{I}}}_{\mathbf{t}}^{-1}\dot{m}\mathbf{S}\left(\rho_R\right)\left(\mathbf{R}_{\mathbf{B_R B_T}}\mathbf{R}_{\mathbf{B_T I}}\dot{r}_{B_T} + \mathbf{R}_{\mathbf{B_R B_T}}V_{\dot{m}}\right)
\end{aligned} \tag{2.69}$$

All $\mathbf{R}_{\bigtriangledown}$ and $\mathcal{E}$ matrices are defined in the sections to follow. $\mathbf{S}(\bigtriangledown)$ refers to the application of the skew-symmetric operator to the parameter $\bigtriangledown$ specified within the brackets.

A further simplification in the representation above can be made by defining V_W, which is the receiver velocity vector expressed in the receiver body-fixed frame directly. Expressing this directly offers the benefit of being able to construct the control problem with quantities in the appropriate frame of reference, whilst having flexibility in depiction of dynamic simulation results.

$$V_W = \mathbf{R_{B_R W_R}} U + W \tag{2.70}$$

Also, $\underline{\underline{\mathbf{I}}}_{\mathbf{M}}$ is the inertia of the receiver matrix excluding the fuel transfer.

$$\underline{\underline{\mathbf{I}}}_{\mathbf{M}} = \begin{bmatrix} I_x & -I_{xy} & -I_{xz} \\ -I_{yx} & I_y & -I_{yz} \\ -I_{zx} & -I_{zy} & I_z \end{bmatrix}_{\mathbf{R}} \tag{2.71}$$

The variation in the inertia matrix is given by:

$$\underline{\underline{\mathbf{I}}}_{\mathbf{t}} \equiv \left\{ \underline{\underline{\mathbf{I}}}_{\mathbf{M}} + \sum m_j \left[\left(\rho_{mj}^T \rho_{mj} \right) \mathbf{I_{3\times 3}} - \rho_{mj} \rho_{mj}^T \right] \right\} \tag{2.72}$$

The state variables describing the receiver aircraft translational and rotational kinematics relative to the tanker aircraft was earlier grouped in Eq. 2.16 and Eq. 2.15 respectively.

The receiver translational kinematics is given below, incorporating V_W:

$$\dot{\xi} = \mathbf{R^T_{B_R B_T}} V_W - \mathbf{R_{B_T I}} \dot{r}_{B_T} + \mathbf{S}(\omega_{\mathbf{B_T}}) \xi \tag{2.73}$$

In scalar form, the receiver aircraft rotational kinematics are expressed in Eqs. 2.74 through to 2.76:

$$\dot{\psi}_{TR} = (q_{TR} \sin\phi_{TR} + r_{TR} \cos\phi_{TR}) \sec\theta_{TR} \tag{2.74}$$

$$\dot{\theta}_{TR} = q_{TR} \cos\phi_{TR} - r_{TR} \sin\phi_{TR} \tag{2.75}$$

$$\dot{\phi}_{TR} = p_{TR} + (q_{TR} \sin\phi_{TR} + r_{TR} \cos\phi_{TR}) \tan\theta_{TR} \tag{2.76}$$

The receiver aircraft rotational kinematics now includes:

$$\dot{\omega}_{B_R} = \dot{\omega}_{B_R B_T} + S(\omega_{B_R B_T}) R_{B_R B_T} \dot{\omega_{B_T}} \tag{2.77}$$

2.4 Motion of a Tanker Aircraft in a Wind-Field

The tanker equations of motion presented in this section includes the effect of wind so that the effects of a disturbance on the refuelling can be tested. The equations have been taken from (Dogan et al., (2008)) and (Lee et al., (2011)).

The tanker translational kinematics is written in Eq. 2.4 in vector form with respect to the inertial frame:

$$\dot{\mathbf{r}}_{B_T} = \mathbf{R}^{\mathbf{T}}_{\mathbf{B_T I}} \mathbf{R}_{\mathbf{B_T W_T}} V_{w_T} + W_{I_T} \tag{2.78}$$

and, V_{W_T} is the tanker velocity in the tanker wind frame (Eq. 2.79).

$$\mathbf{V}_{W_T} = [V_T,\, 0,\, 0]^T \tag{2.79}$$

Included is the wind velocity components acting on the tanker aircraft (Eq. 2.80) in the inertial reference frame.

$$W_{I_T} = [W_{T_x}, W_{T_y}, W_{T_z}]^T \tag{2.80}$$

with each element being the inertial x- y- and z- components.

The tanker rotational kinematics is expressed in matrix form in Eq. 2.81:

$$\mathbf{R}_{\mathbf{B_T I}} \dot{\mathbf{R}}_{\mathbf{B_T I}} = -\mathbf{S}(\omega_{\mathbf{B_T}}) \tag{2.81}$$

In scalar form, these are expressed as:

$$\dot{\psi}_T = (q_T \sin\phi_T + r_T \cos\phi_T) \sec\theta_T \tag{2.82}$$

$$\dot{\theta}_T = q_T \cos\phi_T - r_T \sin\phi_T \tag{2.83}$$

$$\dot{\phi}_T = p_T + (q_T \sin\phi_T + r_T \cos\phi_T) \tan\theta_T \tag{2.84}$$

The tanker translational dynamics is expressed with respect to the tanker body-fixed frame:

$$\begin{aligned}\dot{\mathcal{X}}_{\mathbf{T}} &= \mathcal{E}_{\mathbf{T}}^{-\mathbf{1}}[\mathbf{S}(\omega_{\mathbf{B_T}})](R_{B_TW_T}V_{W_T}) - \mathcal{E}_{\mathbf{T}}^{-\mathbf{1}}\mathbf{R}_{\mathbf{B_TI}}\dot{W}_{I_T} \\ &+ \frac{1}{(m)}\mathcal{E}_{\mathbf{T}}^{-\mathbf{1}}(R_{B_TI}M_T + R_{B_TW_T}A_T + P_T) \end{aligned} \tag{2.85}$$

and

tanker rotational dynamics:

$$\dot{\omega}_{B_T} = \underline{\underline{\mathbf{I}}}_{\mathbf{t}}^{-\mathbf{1}}[M_{B_T} + \mathbf{S}\omega_{B_T}\underline{\underline{I}}_t\omega_{B_T}] \tag{2.86}$$

$$M_{B_T} = [\mathcal{L}_\mathcal{T}, \mathcal{M}_\mathcal{T}, \mathcal{N}_\mathcal{T}]^T \tag{2.87}$$

$$\underline{\underline{I}}_t = \begin{bmatrix} I_x & -I_{xy} & -I_{xz} \\ -I_{yx} & I_y & -I_{yz} \\ -I_{zx} & -I_{zy} & I_z \end{bmatrix} \tag{2.88}$$

2.5 Forces and Moments

The applied force and moment vectors have three sources: (i) aerodynamics, (ii) propulsion and (iii) gravity.

Aerodynamic forces are dependent on velocity relative to surrounding air mass, which differs from the groundspeed when there is a wind-field (Etkin and Reid (1996)). This is accounted for, both in the case of the tanker and the receiver aircraft.

Tanker and receiver mass, aerodynamic and propulsive forces and moments are expressed in the same format. The $\bigtriangledown$ symbol refers to either tanker $_T$ or receiver $_R$, as applicable.

The gravitational force acting on the tanker/receiver is given with respect to the inertial reference frame as:

$$M_\bigtriangledown = [0,\, 0,\, m_\bigtriangledown g]^T \tag{2.89}$$

The aerodynamic forces acting on the tanker/receiver is given with respect to each aircraft's wind frame:

$$A_\bigtriangledown = [-D_\bigtriangledown, -S_\bigtriangledown, -L_\bigtriangledown]^T \tag{2.90}$$

The propulsive force acting on the each aircraft in the their own body-fixed frame is given by Eq. 2.91, where $\delta_{T_{inc}}$ is the thrust inclination angle in pitch.

$$P_{\triangledown} = [T_{\triangledown} \cos \delta_{T_{inc}}, 0, -T_{\triangledown} \sin \delta_{T_{inc}}]^T \tag{2.91}$$

Thrust of tanker/receiver aircraft engine is given as:

$$T_{\triangledown} = T_{max_{\triangledown}} \delta_{t_{\triangledown}} \tag{2.92}$$

Lift, side and drag forces, and rolling pitching and yawing moments are given:

$$L_{\triangledown} = \frac{1}{2} \rho_{\triangledown} V_{\triangledown}^2 S_{\triangledown} C_{L_{\triangledown}} \tag{2.93}$$

$$SF_{\triangledown} = \frac{1}{2} \rho_{\triangledown} V_{\triangledown}^2 S_{\triangledown} C_{S_{\triangledown}} \tag{2.94}$$

$$D_{\triangledown} = \frac{1}{2} \rho_{\triangledown} V_{\triangledown}^2 S_{\triangledown} C_{D_{\triangledown}} \tag{2.95}$$

$$\mathcal{L}_{\triangledown} = \frac{1}{2} \rho_{\triangledown} V_{\triangledown}^2 S_{\triangledown} b_{\triangledown} C_{\mathcal{L}_{\triangledown}} \tag{2.96}$$

$$\mathcal{M}_{\triangledown} = \frac{1}{2} \rho_{\triangledown} V_{\triangledown}^2 S_{\triangledown} \bar{c}_{\triangledown} C_{M_{\triangledown}} + \Delta z_{\triangledown} T_{\triangledown} \tag{2.97}$$

$$\mathcal{N}_{\triangledown} = \frac{1}{2} \rho_{\triangledown} V_{\triangledown}^2 S_{\triangledown} b_{\triangledown} C_{N_{\triangledown}} \tag{2.98}$$

The corresponding coefficients (implied subscript $\triangledown$ is omitted) are defined:

$$C_D = C_{D_0} + \frac{C_L^2}{\pi \mathrm{AR\ e}} \tag{2.99}$$

$$C_S = C_{S_0} + C_{S\delta_a} \delta_a + C_{S\beta} \beta + C_{S\delta_r} \delta_r \tag{2.100}$$

$$C_L = C_{L0} + C_{L\alpha} \alpha + C_{L_\alpha^2} (\alpha - \alpha_{ref})^2 + C_{L_q} \frac{\bar{c}}{2V} q + C_{L\delta_e} \delta_e \tag{2.101}$$

$$C_{\mathcal{L}} = C_{\mathcal{L}0} + C_{\mathcal{L}\delta_a} \delta_a + C_{\mathcal{L}\delta_r} \delta_r + C_{\mathcal{L}_p} \frac{b}{2V} p + C_{\mathcal{L}_r} \frac{b}{2V} r + C_{\mathcal{L}\beta} \beta \tag{2.102}$$

$$C_{\mathcal{M}} = C_{\mathcal{M}0} + C_{\mathcal{M}\alpha} \alpha + C_{\mathcal{M}_q} \frac{\bar{c}}{2V} q + C_{\mathcal{M}\delta_e} \delta_e \tag{2.103}$$

$$C_{\mathcal{N}} = C_{\mathcal{N}0} + C_{\mathcal{N}\delta_a} \delta_a + C_{\mathcal{N}\delta_r} \delta_r + C_{\mathcal{N}_p} \frac{b}{2V} p + C_{\mathcal{N}_r} \frac{b}{2V} r + C_{\mathcal{N}\beta} \beta \tag{2.104}$$

2.6 Actuator Dynamics

Actuator dynamics for each control surface was included and was modelled as a first-order system with time constant $\tau_{\delta_{\triangledown}}$. The subscript $\triangledown$ refers to the tanker or receiver aircraft and

is of the same form for each control surface.

$$\dot{\delta}_{\triangledown} = \frac{1}{\tau_{\delta_{\triangledown}}}(\delta_{\triangledown_0} - \delta_{\triangledown}) \tag{2.105}$$

2.7 Rotation Matrices

The presentation of the equations of motion in matrix form in the preceding sections were heavily reliant on rotational matrices to transform quantities conveniently expressed in their natural frame of physical operation to other frames required for the specific form of the equations of motion. This is applicable to both the tanker and receiver aircraft. The frames and rotation matrices are depicted in Figure 2.4.

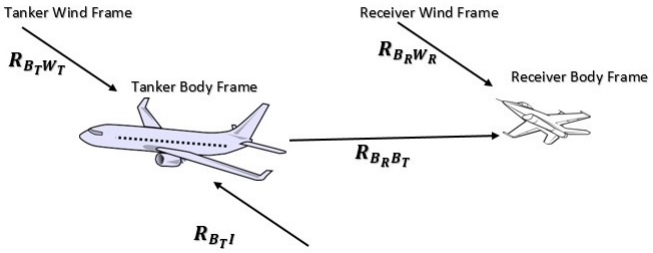


Figure 2.4: Receiver aircraft reference frames

For the tanker, the body axis is used as the main frame of reference. However, when convenient, the inertial and wind axes will be used to write values and then transformed to the body axes, as shown for a generic quantity $\mathbf{x}$ in Eqs. 2.106 and 2.107.

$$\mathbf{x}_{B_T} = R_{B_T I}\mathbf{x}_I \tag{2.106}$$

$$\mathbf{x}_{B_T} = R_{B_T W_T}\mathbf{x}_{W_T} \tag{2.107}$$

The rotation matrix from the tanker inertial to tanker body-fixed axes is shown in Eq. 2.108.

$$\mathbf{R_{B_T I}} = \begin{bmatrix} R_{11} & R_{12} & R_{13} \\ R_{21} & R_{22} & R_{23} \\ R_{31} & R_{32} & R_{33} \end{bmatrix} \tag{2.108}$$

However, the rotational matrix $\mathbf{R_{B_R B_T}}$, that transforms quantities from the tanker's body-fixed frame to the receiver's body-fixed frame in Eq 2.109 has similar form to $\mathbf{R_{B_T I}}$ as given in Eq. 2.110.

$$\mathbf{x}_R = R_{B_R B_T}\mathbf{x}_T \tag{2.109}$$

$$\mathbf{R_{B_R B_T}} = \begin{bmatrix} R_{11} & R_{12} & R_{13} \\ R_{21} & R_{22} & R_{23} \\ R_{31} & R_{32} & R_{33} \end{bmatrix} \tag{2.110}$$

The components of matrices in Eqs 2.108 and 2.110 are given in Eq 2.111. The $\bigcirc$ symbol will refer to either tanker Euler angles ϕ_T, θ_T, ψ_T, which describe the tanker aircraft orientation relative to the inertial reference frame, or the Euler angles relative to the tanker aircraft ϕ_{TR}, θ_{TR}, ψ_{TR}, as applicable.

$$\begin{aligned}
R_{11} &= \sin\theta_{\bigcirc}\cos\psi_{\bigcirc} \\
R_{12} &= \cos\theta_{\bigcirc}\sin\psi_{\bigcirc} \\
R_{13} &= -\sin\theta_{\bigcirc} \\
R_{21} &= \sin\phi_{\bigcirc}\sin\theta_{\bigcirc}\cos\psi_{\bigcirc} - \cos\theta_{\bigcirc}\sin\psi_{\bigcirc} \\
R_{22} &= \sin\phi_{\bigcirc}\sin\theta_{\bigcirc}\sin\psi_{\bigcirc} + \cos\phi_{\bigcirc}\cos\psi_{\bigcirc} \\
R_{23} &= \sin\phi_{\bigcirc}\cos\theta_{\bigcirc} \\
R_{31} &= \cos\phi_{\bigcirc}\sin\theta_{\bigcirc}\cos\psi_{\bigcirc} + \sin\phi_{\bigcirc}\sin\psi_{\bigcirc} \\
R_{32} &= \cos\phi_{\bigcirc}\sin\theta_{\bigcirc}\sin\psi_{\bigcirc} - \sin\phi_{\bigcirc}cos\psi_{\bigcirc} \\
R_{33} &= \cos\phi_{\bigcirc}\cos\theta_{\bigcirc}
\end{aligned} \tag{2.111}$$

The rotation matrix from the wind reference frame to body-fixed reference frame is shown in Eq. 2.112. The angles $\alpha_{\bigtriangledown}$ and $\beta_{\bigtriangledown}$ are the angle of attack and sideslip angle respectively. The $\bigtriangledown$ symbol will refer to either tanker $_T$ or receiver $_R$, as applicable.

$$\mathbf{R_{B_{\bigtriangledown} W_{\bigtriangledown}}} = \begin{bmatrix} \cos\beta_{\bigtriangledown}\cos\alpha_{\bigtriangledown} & -\sin\beta_{\bigtriangledown}\cos\alpha_{\bigtriangledown} & -\sin\alpha_{\bigtriangledown} \\ \sin\beta_{\bigtriangledown} & \cos\beta_{\bigtriangledown} & 0 \\ \cos\beta_{\bigtriangledown}\sin\alpha_{\bigtriangledown} & -\sin\beta_{\bigtriangledown}\sin\alpha_{\bigtriangledown} & \cos\alpha_{\bigtriangledown} \end{bmatrix} \tag{2.112}$$

The matrix $\mathcal{E}_{\bigtriangledown}$ and its inverse used in the expression of the translational dynamics with triad $\mathcal{X}_{\bigtriangledown} = [V_{\bigtriangledown}, \beta_{\bigtriangledown}, \alpha_{\bigtriangledown}]^T$ are given in Eqs. 2.113 and 2.114 respectively. The $\bigtriangledown$ symbol will refer to either tanker $_T$ or receiver $_R$, as applicable.

$$\mathcal{E}_{\triangledown} = \begin{bmatrix} \cos\beta_{\triangledown}\cos\alpha_{\triangledown} & -V_{\triangledown}\sin\beta_{\triangledown}\cos\alpha_{\triangledown} & -V_{\triangledown}\cos\beta_{\triangledown}\cos\alpha_{\triangledown} \\ \sin\beta_{\triangledown} & V_{\triangledown}\cos\beta_{\triangledown} & 0 \\ \cos\beta_{\triangledown}\sin\alpha_{\triangledown} & -V_{\triangledown}\sin\beta_{\triangledown}\sin\alpha_{\triangledown} & V_{\triangledown}\cos\beta_{\triangledown}\cos\alpha_{\triangledown} \end{bmatrix} \tag{2.113}$$

$$\mathcal{E}_{\triangledown}^{-1} = \begin{bmatrix} \cos\alpha_{\triangledown}\ \cos\beta_{\triangledown} & \sin\beta_{\triangledown} & \cos\beta_{\triangledown}\ \sin\alpha_{\triangledown} \\ -\frac{1}{V_{\triangledown}}\cos\alpha_{\triangledown}\ \sin\beta_{\triangledown} & \frac{1}{V_{\triangledown}}\cos\beta_{\triangledown} & -\frac{1}{V_{\triangledown}}\sin\alpha_{\triangledown}\ \sin\beta_{\triangledown} \\ -\frac{1}{V_{\triangledown}}\sec\beta_{\triangledown}\ \sin\alpha_{\triangledown} & 0 & \frac{1}{V_{\triangledown}}\cos\alpha_{\triangledown}\ \sec\beta_{\triangledown} \end{bmatrix} \tag{2.114}$$

2.8 Fuel Transfer Model

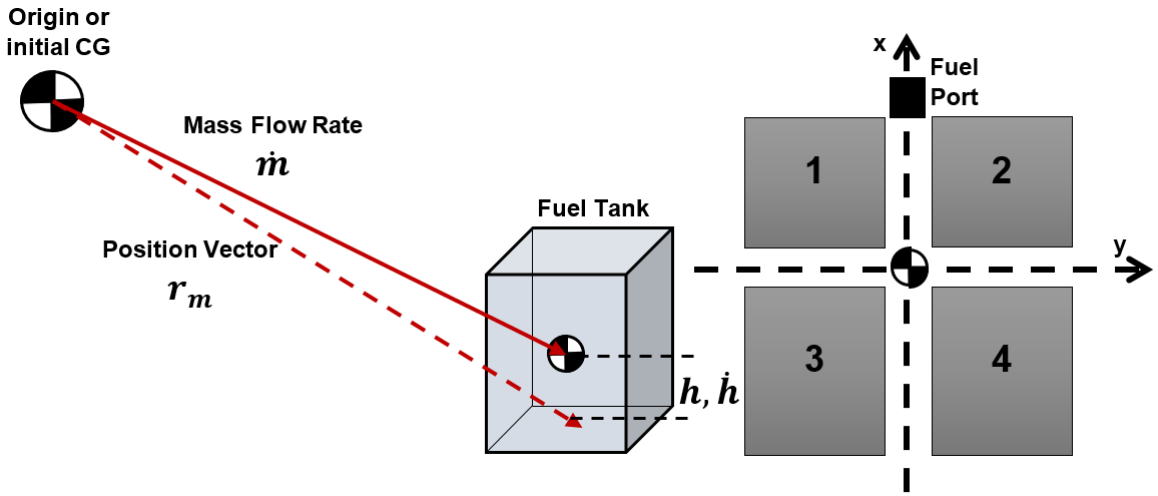


Figure 2.5: Fuel tank layout and position vectors

Figure 2.5 depicts the rectangular shape and position of a single fuel tank relative to a reference origin, which could also be the initial CG of the receiver aircraft. The position vector in the receiver aircraft's body-fixed frame can be written as:

$$\mathbf{r}_m = [x_m(t),\, y_m(t),\, z_m(t)]^T \tag{2.115}$$

The total mass in the fuel tank after time t has elapsed since the start of refuelling is:

$$m_T(t) = \int_0^t \dot{m}(\tau)d\tau \tag{2.116}$$

With the rectangular shape of the fuel tank, a further assumption would be that it fills up uniformly as mass enters with a steady flow rate $\dot{m}$. As seen in Figure 2.5, the CG of fuel in the tank thus only experiences a variation in height.

For this study, the receiver aircraft is modelled with 4 fuel tanks. Fore tanks 1 and 2 uniformly fill up first, each tank with mass flow rate $0.5\dot{m}$ and then aft tanks 3 and 4 are filled in a similar manner.

$$\dot{m}_1 = \dot{m}_2 = 0.5\dot{m} \tag{2.117}$$

$$\dot{m}_3 = \dot{m}_4 = 0.5\dot{m} \tag{2.118}$$

Using subscript i to refer to any of the 4 fuel tanks:

$$\mathbf{r}_{m_i} = [x_{m_i}(t),\, y_{m_i}(t),\, z_{m_i}(t)]^T \tag{2.119}$$

Applying the assumptions mentioned above and defining

a_i as the length of fuel tank i

b_i as the breadth of fuel tank i

ρ_{fuel} as the density of the fuel

$[x_{m_i}(0),\, y_{m_i}(0),\, z_{m_i}(0)]^T$ as the CG of the ith fuel tank prior to refuelling commencing

then, the change in the height of the CG in the ith tank is given by:

$$h_i(t) = \frac{m_i(t)}{\rho_{fuel} a_i b_i} \tag{2.120}$$

Finally, the position vector of the ith fuel tank CG in the receiver body-fixed frame is given by:

$$\mathbf{r}_{m_i} = \begin{bmatrix} x_i(0) \\ y_i(0) \\ z_i(0) - \frac{h_i(t)}{2} \end{bmatrix} \tag{2.121}$$

2.9 Atmospheric and Wind Model Elements

Key to building a six-DOF model is the incorporation of the environment within which it will fly and perform the AAR manoeuvre. The effect of winds and gusts on an aircraft in a six-DOF motion is to produce a change in the incidence angles, thus altering the aerodynamic

forces and moments (Zipfel (2000)). As incidence angles are calculated from the aircraft velocity vector with respect to the surrounding air - these must be considered in the AAR analysis.

2.9.1 Atmosphere model

The U.S. Standard Atmosphere model detailed in Chapter 2 of Stengel (2004) was used in this study.

2.9.2 Vortex model

The receiver aircraft will fly directly in the vortex wake generated by the tanker aircraft. Modelled as a wind-field acting on the receiver aircraft, it has dependence on position $\mathbf{x}$ (Stengel (2004)) as shown in Eq. 2.122.

$$\mathbf{W}(\mathbf{x},t) = \begin{bmatrix} w_x(\mathbf{x},t) \\ w_y(\mathbf{x},t) \\ w_z(\mathbf{x},t) \end{bmatrix} \tag{2.122}$$

The spatial wind shear (Eq 2.123) is represented by the Jacobian matrix of $\mathbf{w}$ with respect to position $\mathbf{x}$ (Stengel (2004)):

$$\mathbf{w_x} \triangleq \mathbf{W} \triangleq \begin{bmatrix} \frac{\partial w_x(\mathbf{x},t)}{\partial x} & \frac{\partial w_x(\mathbf{x},t)}{\partial y} & \frac{\partial w_x(\mathbf{x},t)}{\partial z} \\ \frac{\partial w_y(\mathbf{x},t)}{\partial x} & \frac{\partial w_y(\mathbf{x},t)}{\partial y} & \frac{\partial w_y(\mathbf{x},t)}{\partial z} \\ \frac{\partial w_z(\mathbf{x},t)}{\partial x} & \frac{\partial w_z(\mathbf{x},t)}{\partial y} & \frac{\partial w_z(\mathbf{x},t)}{\partial z} \end{bmatrix} \tag{2.123}$$

The literature review gave an overview of models that have been developed to account for the vortex wake effect in dynamic simulations of AAR. The Lamb-Oseen vortex model with exponential decay was examined by Stengel (2004), whereas Venkataramanan et al., (2003) developed a model based on a modified horseshoe vortex inclusive of exponential decay.

The choice of either vortex model yeilds a similar cylindrical flow when comparing Eq (2.1-16) in Stengel (2004) to Eq (26) in Venkataramanan et al., (2003). The non-uniform nature of the wind distribution over the aircraft has been identified as a challenge in the dynamic response model that is to be built (Stengel (2004)).

In this study the methodology developed by Venkataramanan et al., (2003) will be used as it includes a technique that will average out the non-uniform wind field over the aircraft and will estimate an effective translational and rotational wind velocity at the CG of the receiver aircraft in the receiver aircraft's body-fixed frame. The derivation will not be repeated here, but the more significant equations used are presented.

The modified horseshoe vortex has the form:

$$W = \frac{\Gamma}{2\pi r_R}[1 - e^{-\frac{r^2}{4\epsilon\tau}}] \tag{2.124}$$

The tanker will produce two straight, semi-infinite trailing vortex filaments (F_{RT} from the right wing and F_{LT} from the left wing) that stay parallel to its velocity vector, with the transversal separation equal to the effective wing span. The engagement geometry is described below.

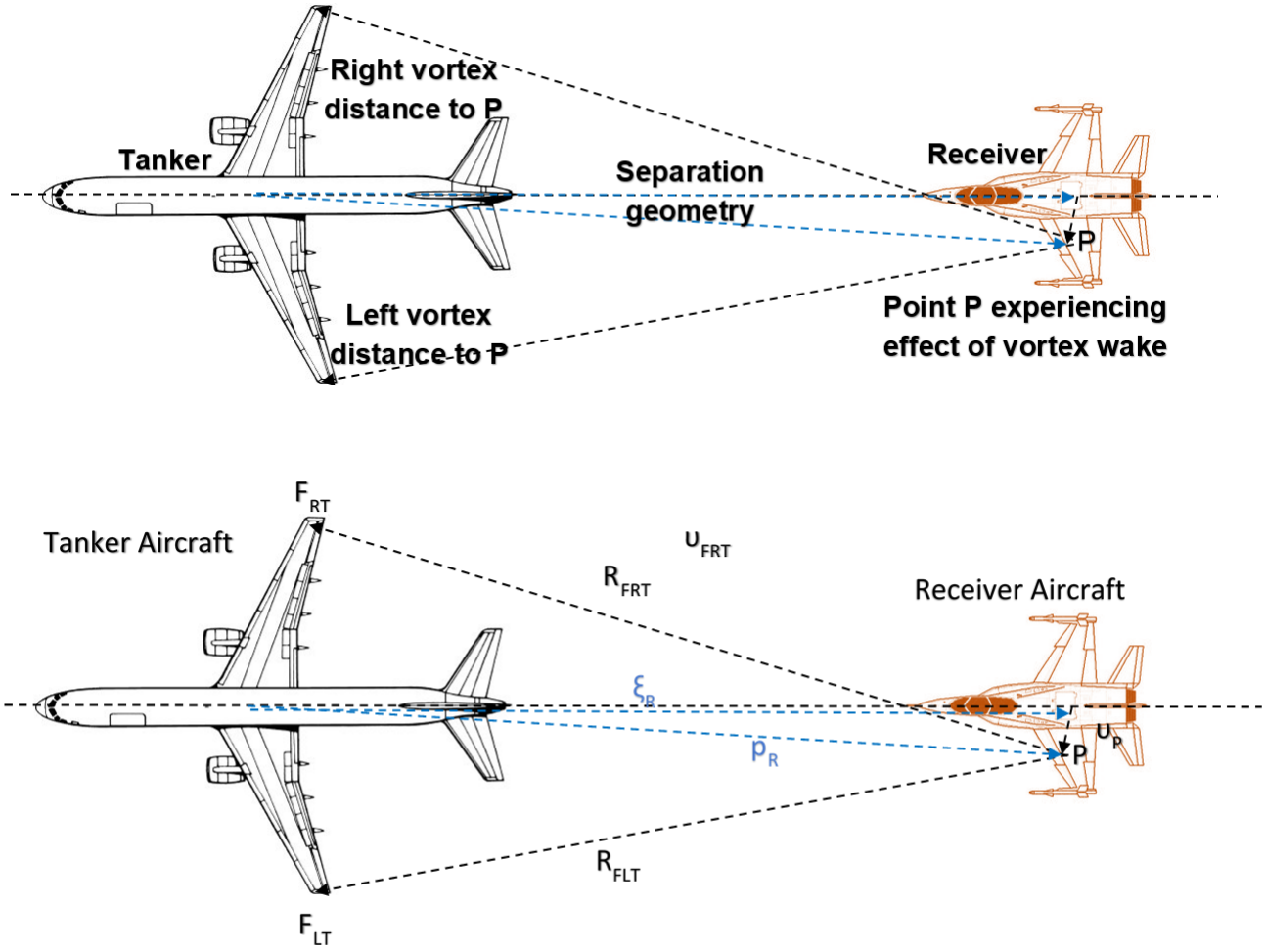


Figure 2.6: Refuelling engagement definitions and geometry

The induced upwash and sidewash experienced by the receiver UAV due to the trailing vortices from the tanker are calculated as explained below.

The induced-velocity vector acting at an arbitrary point P on receiver due to the right trailing vortex filament (F_{RT}) produced by the tanker

$$\underline{W}_{F_{R_T}} = \underline{\hat{\Phi}} \frac{\Gamma_T}{2\pi \left| \underline{l}_{F_{R_T}} \right| yz} \left[1 - e^{-\left(\frac{\left| \underline{l}_{F_{R_T}} \right| yz}{4\epsilon\tau} \right)} \right] \tag{2.125}$$

$$\Gamma_T = \frac{1}{2} C_{L_T} V_T \bar{c}_T \tag{2.126}$$

$\underline{l}_{F_{R_T}}$ is defined in detail in Venkataramanan et al. (2003)

Following the method, when resolved along the wind axes, a net sidewash and upwash are produced, which can be written directly in the body-fixed frame of the receiver aircraft.

$$\underline{W}_B = \mathbf{R_{B_R B_T}}(\mathbf{R_{B_T W_T}}) \begin{bmatrix} 0 \\ W_{SW_{net}} \\ -W_{UW_{net}} \end{bmatrix} = \begin{bmatrix} W_{B_x} \\ W_{B_y} \\ W_{B_z} \end{bmatrix} \tag{2.127}$$

The averaging technique is used to move from a non-uniform distribution to a uniform one. Point P is traversed in three directions: along the body longitudinal axis, from wingtip to wingtip and along the diameter of the fuselage. The x-direction methodology is given below.

$$W_{B_{x_1 y}} = \frac{1}{b_R/2} \int_{a=-b_R/2}^{0} W_{B_x} da \tag{2.128}$$

$$W_{B_{x_2 y}} = \frac{1}{b_R/2} \int_{a=0}^{b_R/2} W_{B_x} da \tag{2.129}$$

$$W_{B_{x_1 z}} = \frac{1}{D_{F_R}/2} \int_{z=-D_{F_R}/2}^{0} W_{B_x} dz \tag{2.130}$$

$$W_{B_{x_2 z}} = \frac{1}{D_{F_R}/2} \int_{z=0}^{D_{F_R}/2} W_{B_x} dz \tag{2.131}$$

$$W_{B_x} = \frac{\left[W_{B_{x_1 y}} + W_{B_{x_2 y}} + W_{B_{x_1 z}} + W_{B_{x_2 z}} \right]}{4} \tag{2.132}$$

$$\frac{\partial W_{B_x}}{\partial y} = \frac{1}{b_R/2} \left[W_{B_{x_2 y}} - W_{B_{x_1 y}} \right] \tag{2.133}$$

$$\frac{\partial W_{B_x}}{\partial z} = \frac{1}{D_{F_R}/2}\left[W_{B_{x_1 z}} - W_{B_{x_2 z}}\right] \tag{2.134}$$

Also, the body angular velocities p; q; r are derived from the effective wind gradients (obtained as described in section 3), using the following relation:

$$\begin{bmatrix} p \\ q \\ r \end{bmatrix} = -\begin{bmatrix} \frac{\partial W_{B_z}}{\partial y} - \frac{\partial W_{B_y}}{\partial z} \\ \frac{\partial W_{B_x}}{\partial z} - \frac{\partial W_{B_z}}{\partial x} \\ \frac{\partial W_{B_y}}{\partial x} - \frac{\partial W_{B_x}}{\partial y} \end{bmatrix} \tag{2.135}$$

2.9.3 Turbulence model

Atmospheric turbulence, which is air movement on a small scale, is expressed using statistical descriptors like standard deviation and power spectral density to classify the severity and spectral characteristics of turbulence (Zipfel, 2000). In Dogan et al., (2008), the MIL-F-8785C specifications for Dryden turbulence (Moorhouse and Woodcock (1982)) are already expressed with power spectral density functions since this is modelled as a stochastic process. The power spectral density functions are expressed in terms of Ω, the spatial frequency in radians per meter, σ_u, σ_v, σ_w, the turbulence intensities in meters per second, and L_u, L_v, L_w, the scale lengths in meters. MIL-F-8785C also provides the spectra for the angular velocity disturbance components in the body frame due to turbulence (Dogan et al., (2008)).

The Dryden spectra for the translational turbulence velocity components in the body-fixed frame of an aircraft is:

$$\Phi_{u_g}(\Omega) = \sigma_u^2 \frac{2L_u}{\pi} \frac{1}{1 + (L_u\Omega)^2} \tag{2.136}$$

$$\Phi_{v_g}(\Omega) = \sigma_v^2 \frac{2L_v}{\pi} \frac{1 + 12(L_v\Omega)^2}{(1 + 4(L_v\Omega)^2)^2} \tag{2.137}$$

$$\Phi_{w_g}(\Omega) = \sigma_w^2 \frac{2L_w}{\pi} \frac{1 + 12(L_w\Omega)^2}{(1 + 4(L_w\Omega)^2)^2} \tag{2.138}$$

The Dryden spectra for the rotational turbulence velocity components in the body frame of an aircraft is:

$$\Phi_{p_g}(\omega) = \frac{\sigma_w^2}{2VL_w} \frac{0.8\left(\frac{2\pi L_w}{4b}\right)^{\frac{1}{3}}}{1+\left(\frac{4b\omega}{\pi V}\right)^2} \tag{2.139}$$

$$\Phi_{q_g}(\omega) = \frac{\pm\left(\frac{\omega}{V}\right)^2}{1+\left(\frac{4b\omega}{\pi V}\right)^2}\Phi_{w_g}(\omega) \tag{2.140}$$

$$\Phi_{r_g}(\omega) = \frac{\mp\left(\frac{\omega}{V}\right)^2}{1+\left(\frac{3b\omega}{\pi V}\right)^2}\Phi_{v_g}(\omega) \tag{2.141}$$

The power spectral density functions can be expressed in terms of angular frequency, using the following relationships:

$$\Omega = \frac{\omega}{V} \tag{2.142}$$

$$\Phi_i(\Omega) = V\Phi_i\left(\frac{\omega}{V}\right) \tag{2.143}$$

In state-space form, the x-component of the translational turbulence velocity is given by (Dogan et al., (2008)):

$$\dot{u}_g = -\frac{V}{L_u}u_g + \sigma_u\sqrt{\frac{2V}{\pi L_u}}\eta \tag{2.144}$$

The y- and z-components of the translational turbulence velocity is given in Eq. 2.145.

$$\begin{bmatrix} \dot{x}_1 \\ \dot{x}_2 \end{bmatrix} = \begin{bmatrix} 0 & 1 \\ -\frac{V^2}{L^2} & \frac{-2V}{L} \end{bmatrix}\begin{bmatrix} x_1 \\ x_2 \end{bmatrix} + \begin{bmatrix} 0 \\ \frac{V^2}{L^2} \end{bmatrix}\eta \tag{2.145}$$

$$\{v_g, w_g\} = \sigma\sqrt{\frac{L}{\pi V}}(x_1 + \sqrt{3}\frac{L}{V}x_2) \tag{2.146}$$

where $\sigma = \sigma_v$ and $L = L_v$ for v_g and $\sigma = \sigma_w$ and $L = L_w$ for w_g.

The angular velocity turbulence x-axis component in state-space form is:

$$\dot{p}_g = \frac{\pi V}{4b}\left[-p_g + \frac{\sigma_w}{L_w^{1/3}}\sqrt{\frac{0.8}{V}}\left(\frac{\pi}{4b}\right)^{\frac{1}{6}}\eta\right] \tag{2.147}$$

The y- and z-axes angular velocity components of the turbulence is given in state-space form:

$$\begin{bmatrix} \dot{x}_1 \\ \dot{x}_2 \\ \dot{x}_3 \end{bmatrix} = \begin{bmatrix} 0 & 1 & 0 \\ 0 & 0 & 1 \\ -\frac{\pi V^3}{L^2 ab} & -\frac{\pi V^2}{L^2 ab}\left(\frac{ab}{\pi}+2L\right) & -\frac{\pi V}{Lab}\left(\frac{2ab}{\pi}+L\right) \end{bmatrix} \begin{bmatrix} x_1 \\ x_2 \\ x_3 \end{bmatrix} + \begin{bmatrix} 0 \\ 0 \\ \frac{\pi V^3}{L^2 ab} \end{bmatrix} \eta \quad (2.148)$$

$$\{q_g, r_g\} = \sigma\sqrt{\frac{L}{\pi V^3}}(x_2 + \sqrt{3}\frac{L}{V}x_3) \quad (2.149)$$

Similarly, $\sigma = \sigma_w$, $L = L_w$ and $a = 4$ for q_g and $\sigma = \sigma_v$, $L = L_v$ and $a = 3$ for r_g.

2.10 Automated Aerial Refuelling System Trim Conditions

The trim problem is to find the control settings that yield a steady-flight condition. The object is to set the vector Eq. 2.150 to zero:

$$\dot{\mathbf{x}}_d = f_d\left(\mathbf{x}_d, \mathbf{u}, \mathbf{w}\right) = 0 \quad (2.150)$$

by the proper choice of control $\mathbf{u}$ subject to the constant values of $\dot{\mathbf{x}}_d$ and disturbance $\mathbf{w}$, where

$$\mathbf{x}_d = [V, \alpha, \beta, p, q, r, z]^T \quad (2.151)$$

The remaining components,

$$\mathbf{x}_k = [x, y, \phi, \theta, \psi]^T \quad (2.152)$$

may be treated as fixed or free parameters

Subscripts have been omitted, as this methodology can be applied to both the tanker and receiver aircraft as presented above.

Minimising a performance index J

$$J = \{\dot{\mathbf{x}}_d\}^T Q \{\dot{\mathbf{x}}_d\} \quad (2.153)$$

will lead to the optimal solution to the trim problem.

2.11 Chapter Summary

In this chapter, the aerial refuelling system model was constructed by developing equations of motion for both the tanker and receiver aircraft. The tanker aircraft equations of motion

included the effect of a wind field, allowing the effects of disturbance by turbulence to be examined. The receiver aircraft equations were developed using the theoretical framework for a variable mass system. The linear momentum for a variable mass system was derived following the methodology as outlined in Cveticanin (2016). Then, the parameters specific to aerial refuelling were introduced and following Cveticanin's discussion regarding a system of particles, the translational dynamics was derived. Using Giancoli (2009), the angular momentum for the variable system was written, which then allowed the refuelling-specific parameters to be easily incorporated. The effects of wind were introduced into the dynamic equations through its effect on the rate of change of position vectors. The vector equations were transformed into its matrix-equivalent form required for state-space control implementation. The translational and rotational kinematics of the receiver relative to the tanker aircraft were also presented. Then, the forces and moments acting on both aircraft were identified and mathematically expressed in the form required for use in the equations of motion. The matrices used in the equations of motion were discussed and presented. The fuel transfer model was defined and the position vector of a generalised fuel tank was written. The chosen atmosphere model was referenced, and the vortex wake and turbulence models were elaborated upon. Finally, the methodology used to determine the AAR system trim conditions was summarised.

3 Benchmark Controller Design

3.1 Introduction

Before a complex control structure (such as that ultimately envisaged in this research) can be developed, it is important for there to be a baseline against which its performance can be compared. With this in mind, a benchmark control case will be developed for the receiver aircraft during refuelling. A PID controller will be developed to control the receiver aircraft motion relative to the tanker. The developed PID controller will be directly applied to the nonlinear receiver aircraft model inclusive of the effects of fuel transfer, varying mass and inertia properties while subject to flight in the tanker aircraft's vortex wake.

The PID controller was selected as it is the most common control method used in engineering systems. It is versatile in that it can be applied in various ways - standalone, or as part of a hierarchical, distributed control system, or even built into embedded components.

Another reason that PID control is the architecture of choice in a wide variety of industrial applications is due to its efficiency and simplicity. PID/classical linear control techniques have been applied to the AAR problem by Ross et al., (2006), Ro et al., (2010), Liu et al., (2014), Yang et al., (2014), and Kriel et al., (2013). These studies have all considered linearised aircraft models as the basis for controller design. Controller gains were obtained by tuning linear models and in some of these studies, the linearly-derived control gains were applied to the nonlinear system model. When systems are highly nonlinear, as is the case with AAR, there will be a loss of process information when the system is linearised at an equilibrium point, say for AAR, at the start of the refuelling process.

In section 3.2 the receiver aircraft controller is presented, followed by the tanker controller in section 3.3. Manual tuning of controller gains is detailed in section 3.4. The effect of fuel transfer is explored in section 3.5 and the dynamic simulation of aerial refuelling is presented in section 3.6. Controller robustness is considered in section 3.7 with two disturbance cases defined to test the controller performance under the selected control gains.

3.2 Receiver Controller

The receiver aircraft geometric, aerodynamic and flight parameters were extracted from Dorsett and Mehl (1996) and Waishek et al., (2009). The conditions at which AAR was considered is given in Table 3.1.

Table 3.1: Aerial refuelling parameters

Parameter	**Value**
Initial receiver mass	11,281 kg
Tanker and receiver speed	190 m/s
Tanker altitude	7,010 m
Receiver x-separation from tanker	-25.33 m
Receiver y-separation from tanker	0 m
Receiver z-separation from tanker	6.46 m
Fuel flow rate	34.6 kg/s
Tanks 1 and 2 combined mass	2,148 kg
Tanks 3 and 4 combined mass	3,898 kg

Table 3.2 describes the three phases of the AAR manoeuvre developed in this study. The receiver aircraft flies for a short period on station, behind the tanker in its refuelling position. Thereafter, fuel transfer is initiated and the first two of four tanks are fuelled to capacity. Finally, the second two of the four fuel tanks are fuelled to capacity.

Table 3.2: Automated aerial refuelling simulation phases

Phase	**Description**	**Time (s)**
I	Receiver stays on station, no fuel, in vortex wake	0 - 25
II	Tanks 1 and 2 fuelled, in vortex wake	25 - 85
III	Tanks 3 and 4 fuelled, in vortex wake	85 - 195

3.2.1 Receiver aircraft performance specifications

The primary requirement of the control design is to maintain a fixed relative separation from the tanker, with zero steady-state error in x_{TR}, y_{TR}, and z_{TR}, while subject to a vortex wind field and varying mass and inertia characteristics in a straight leg refuelling manoeuvre. The transient behaviour expected at the times when fuelling commences and completes (Table 3.2) should be minimal and not destabilise the aircraft. The relative orientation of the receiver aircraft defined by its roll, pitch and yaw angles should be close enough to their nominal values throughout the manoeuvre. Prior to refuelling, the pitch angle should remain steady.

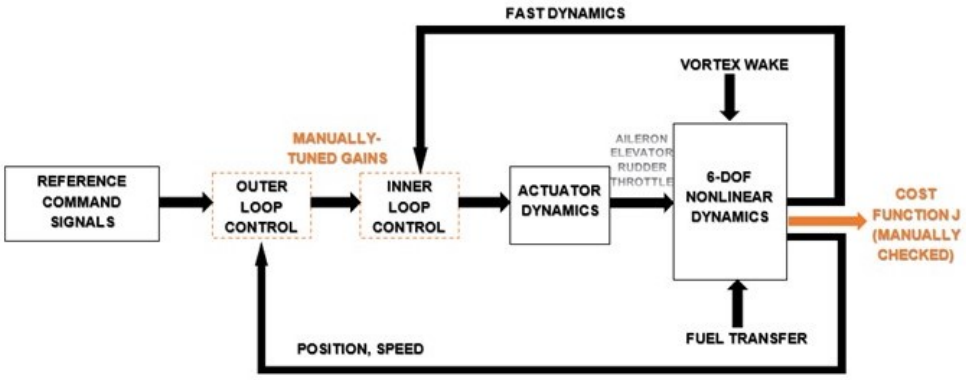


Figure 3.1: Controller design block diagram

The receiver aircraft speed, V_R, should be the same as the tanker aircraft throughout the manoeuvre, also with zero steady-state error. The control inputs generated by the controller should not cause significant saturation on the magnitudes and rates of the actuators. Lastly, it was desired that a single set of control gains be used for the entire simulation and that gain scheduling should not be incorporated in the control design. These gains should be applied directly to the nonlinear receiver model and no system linearisation should be employed.

3.2.2 Receiver aircraft controller structure

In order to meet zero-steady state requirements, integrator states based on error, $\dot{e} = y_c - y$, were added to the original state-space model for all the outer loop states. The controller block diagram is depicted in Fig. 3.1. Inner-loop control addresses the fast dynamics p_{TR}, q_{TR}, and r_{TR}, while the outer loop primarily addressed the speed and position tracking requirements. Four control laws were developed.

The augmented system dynamics is then described as:

$$\begin{bmatrix} \dot{x}_e \\ \dot{e} \end{bmatrix} = \mathbb{F}(x, e) + g(x)\, u \tag{3.1}$$

$\mathbb{F}(x)$ is a function of $f(x)$ and $h(x)$. With this notation, the generalised PID control law can be written as:

$$u = K_P \dot{e} + K_D \ddot{e} + K_I \int_0^t \dot{e} d\tau \tag{3.2}$$

The elevator channel control law was developed to be representative of an altitude hold autopilot described in Stevens et al., (2016). The commanded pitch angle in Eq. 3.3 is given by Eq. 3.4,

$$\begin{aligned}\tau_e\dot{\delta}_e + \delta_e =& \delta_{e_0} + Ke_\theta\left(\theta_c - \theta_{TR}\right) + Ke_q\left(q_c - q_{TR}\right) \\ &+ Ke_{\theta I}\int_0^t \left(\theta_c - \theta_{TR}\right) dt\end{aligned} \tag{3.3}$$

$$\begin{aligned}\tau_e\theta_c =& Ke_z\left(z_c - z_{TR}\right) + Ke_{\dot{z}}\left(\dot{z}_c - \dot{z}_{TR}\right) \\ &+ Ke_{zI}\int_0^t \left(z_c - z_{TR}\right) dt\end{aligned} \tag{3.4}$$

Speed and x-separation control was achieved by the throttle channel. The control law developed in this study is given by:

$$\begin{aligned}\tau_t\dot{\delta}_t + \delta_t =& \delta_{t_0} + Kt_V\left(V_c - V_R\right) + Kt_{\dot{V}}\left(\dot{V}_c - \dot{V}_R\right) \\ &+ Kt_{VI}\int_0^t \left(V_c - V_R\right) dt + Kt_x\left(x_c - x_{TR}\right) \\ &+ Kt_{\dot{x}}\left(\dot{x}_c - \dot{x}_{TR}\right) + Kt_{xI}\int_0^t \left(x_c - x_{TR}\right) dt\end{aligned} \tag{3.5}$$

Lateral-directional control laws were written based on the straight flight path under consideration in the study. Separate wing-level or turn-coordination control laws were not specifically developed, as the main performance objective was to achieve zero steady-state error in y_{TR}. However, roll angle control can be adequately achieved through the action of Ka_ϕ, Ka_p, Ka_ψ, and Kar in Eq. 3.6, and yaw angle control through Kr_ψ, Kr_r, Kr_ϕ, and Krp in Eq. 3.7. The control laws incorporate the coupling effects between the roll and yaw dynamics by including these in both the aileron and rudder channels (e.g., Ka_ψ and Kr_ϕ).

$$\begin{aligned}\tau_a\dot{\delta}_a + \delta_a =& \delta_{a_0} + Ka_\phi\left(\phi_c - \phi_{TR}\right) + Ka_p\left(p_c - p_{TR}\right) \\ &+ Ka_\psi\left(\psi_c - \psi_{TR}\right) + Ka_r\left(r_c - r_{TR}\right) \\ &+ Ka_y\left(y_c - y_{TR}\right) + Ka_y\left(\dot{y}_c - \dot{y}_{TR}\right) \\ &+ Ka_{yI}\int_0^t \left(y_c - y_{TR}\right) dt\end{aligned} \tag{3.6}$$

$$\begin{aligned}\tau_r\dot{\delta}_r + \delta_r =& \delta_{r_0} + Kr_\psi\left(\psi_c - \psi_{TR}\right) + Kr_r\left(r_c - r_{TR}\right) \\ &+ Kr_\phi\left(\phi_c - \phi_{TR}\right) + Kr_p\left(p_c - p_{TR}\right) \\ &+ Kr_y\left(y_c - y_{TR}\right) + Kr_{\dot{y}}\left(\dot{y}_c - \dot{y}_{TR}\right) \\ &+ Kr_{yI}\int_0^t \left(y_c - y_{TR}\right) dt\end{aligned} \tag{3.7}$$

3.3 Tanker Aircraft Controller Design

The tanker aircraft control design was modelled on Thomas et al., (2015). A linear tanker aircraft model was used in conjunction with the turbulence model which served the role of disturbing the tanker aircraft motion. The nonlinear model developed earlier in Chapter 2 was linearised in accordance with Chapter 4 of Stengel (2004) adapting the Matlab code developed by Stengel for the flight condition under study. The matrices **A** and **B** contain the aerodynamic and stability properties of the aircraft through the relations given in Chapter 2 of this thesis. The state-space representation becomes (including disturbance w):

$$\dot{x} = \mathbf{A}x + \mathbf{B}u + w \tag{3.8}$$

with

$$\Delta x = \begin{bmatrix} \triangle V & \triangle\alpha & \triangle\beta & \triangle p & \triangle q & \triangle r & \triangle\phi & \triangle\theta & \triangle\psi & \triangle x & \triangle y & \triangle z \end{bmatrix}^T \tag{3.9}$$

$$\Delta u = \begin{bmatrix} \triangle\delta_{aT} & \triangle\delta_{eT} & \triangle\delta_{rT} & \triangle\delta_{tT} \end{bmatrix}^T \tag{3.10}$$

$$\tag{3.11}$$

The parameters in Table 3.3 are to be regulated to their nominal values.

3.3.1 Tanker aircraft controller performance specifications

The primary requirement of the tanker control design is the regulation of the tanker aircraft flight path in the presence of turbulence. The position of the receiver aircraft is to be maintained at a fixed orientation and separation from the tanker, making the tanker flight path regulation crucial. Also, the tanker translational and rotational dynamics affect the motion of the receiver as seen in the state-space representation in Chapter 2. Stable tanker dynamics are required for the receiver aircraft to safely and successfully refuel.

Table 3.3: Tanker aircraft nominal/trimmed parameters

Parameter	**Value**
Speed V_T	190 m/s
Altitude h_T	7,010 m
Angle of attack α_T	-1.1171 deg
Pitch orientation θ_T	-1.1171 deg
Elevator deflection δ_{eT}	2.5569 deg
Throttle deflection δ_{tT}	0.4434
All other state and control variables	0

3.3.2 Tanker aircraft controller structure

In line with Thomas et al., (2015), a full-state feedback controller was designed using the state-feedback linear quadratic regulator LQR giving control with the form

$$\mathbf{u} = -\mathbf{K}\mathbf{x} \tag{3.12}$$

The control gain matrix $\mathbf{K}$ is to be determined by minimising the quadratic performance index:

$$J = \frac{1}{2}\int_0^\infty \left[(\mathbf{x})^T \boldsymbol{Q}(\mathbf{x}) + \mathbf{u}^T \boldsymbol{R}\mathbf{u}\right] dt \tag{3.13}$$

Actuator dynamics were incorporated for each control surface according to the following relationship, τ_u is the time constant for each control surface, u_{inst} is the instantaneous surface deflection and u is the deflection commanded from the control law above.

$$\dot{u} = \frac{1}{\tau_u}(u_{inst} - u) \tag{3.14}$$

The control derivatives $\dot{\delta}_a$, $\dot{\delta}_e$, $\dot{\delta}_r$ and $\dot{\delta}_T$ are subject to the following constraints:

$$|\delta_a| \leq \delta_{a_{max}} \quad |\delta_e| \leq \delta_{e_{max}} \quad |\delta_r| \leq \delta_{r_{max}} \quad 0 \leq \delta_T \leq 1 \tag{3.15}$$

3.4 Manual Tuning of Receiver Controller Parameters

Ziegler-Nichols tuning criteria for PID controllers stipulates that the proportional gain must be tuned first to minimise rise time, then the derivative gain is tuned to address overshoot

and lastly the integral gain is adjusted to eliminate steady-state error. Controller gains were manually tuned for the benchmark controller design. Manual tuning was performed in order to gain an understanding of the system response, and also to develop a bounded search space for the evolutionary and swarm algorithms that will be applied later on.

Whilst trying to adhere to the Ziegler-Nichols methodology, the aerial refuelling system was tuned systematically according to its inner and outer-loop segmentation. The following tuning sequence was adopted for the aerial refuelling system:

- Inner loop PD gains (e.g., Ke_θ, Ke_q)
- Inner loop I gains (e.g., $Ke_{\theta I}$)
- Outer loop PD gains (e.g., Ke_z, $Ke_{\dot{z}}$)
- Outer loop I gains (e.g., Ke_{zI})

The next sequential step was initiated once the cost function J and the system response was manually checked and found to be acceptable.

From this process, it was found that Ke_θ was the most sensitive parameter to tune in the inner loop. Manual tuning also revealed that the gains $Ka_{\phi I}$, Ka_r, Ka_ψ, $Kr_{\psi I}$, and Kr_p needed to be zero. The least sensitive variables to tune were the outer loop thrust gains. Table 5.3 lists the final values of the manually-tuned gains as well as the lower and upper bounds that would be required to define a search space.

3.4.1 Cost function for manually-tuned gains

The controller gains used in the respective control laws can be determined by minimising the quadratic cost function

$$J = \int_0^{t_f} \left[(\mathbf{x} - \mathbf{x}_c)^T \boldsymbol{Q} (\mathbf{x} - \mathbf{x}_c) + \mathbf{u}^T \boldsymbol{R} \mathbf{u} \right] dt \tag{3.16}$$

where $\mathbf{x}$ refers to the state variable vector defined in Eq. 2.11, and $\mathbf{x}_c$ to its commanded or nominal value. The diagonal matrix $\boldsymbol{Q}$ penalises the error between the commanded/nominal and measured state variables, while the diagonal matrix $\boldsymbol{R}$ penalises the control variables. After numerous attempts at finding the appropriate values for these matrices, unweighted identity matrices were found to have given the best indication of system cost for the manoeuvre. Since the gains are manually tuned in this chapter, the cost function was manually inspected as gains were tuned according to the methodology described earlier.

3.4.2 Selection of t_f

Through manual tuning, it was found that the selection of the final time t_f played a major factor in determining the appropriate controller gains and search space. In line with the conventional PID tuning approach, initial efforts focused on the traditional performance specifications e.g., over/undershoot, settling time, etc. With this methodology in mind, t_f was selected so that a steady response could be achieved in the first 5 - 10 seconds of the simulation.

However, fuel transfer only begins at 25 s and the second set of tanks starts to refuel at 85s. The optimum gains with $t_f = 5s$ did not work well when applied to the full simulation ending at 195s. This is due to sensitivity on Ke_θ, which was positive when J was formulated with $t_f = 5s$. When t_f was extended into the refuelling time frame beyond 25s, it emerged that Ke_θ needed to be negative.

Tanks 3 and 4 only started refuelling at 85s into the simulation. This too posed a challenge in realising an initial set of controller gains and the search-space bounds. Eventually, it was found that when J was formulated with $t_f = 195s$, the best possible outcome was attained.

Table 3.4: Receiver aircraft controller gains and cost function

Gain	**Value**	**Gain**	**Value**	**Gain**	**Value**
Ke_θ	-3.4	Ke_z	-400	$Kt_{\dot{x}}$	12
$Ke_{\theta I}$	1.26	Ke_{zI}	-540	$Ka_{\dot{y}}$	-10
Ke_q	7.5	$Ke_{\dot{z}}$	5	$Kr_{\dot{y}}$	1
Ka_ϕ	120	Kt_V	-12	Ka_y	-10
Ka_p	10	Kt_{VI}	0	Kr_y	1
Kr_ψ	400	$Kt_{\dot{V}}$	0	Ka_{yI}	-10
Kr_r	-50	Kt_x	75	Kr_{yI}	1
Kr_ϕ	-250	Kt_{xI}	18		

3.5 Effect of Fuel Transfer in Automated Aerial Refuelling Manoeuvre

From the literature review, it is expected that the receiver aircraft dynamics will be affected by the refuelling itself. Mao (2008), Waishek et al., (2009) and Haitao et al., (2016) show

that the longitudinal parameters are affected when symmetric refuelling is performed. The pitch rate must increase when fuel is added, since the linear and angular momentum are impacted by the addition of fuel through the term $\dot{m}V_{\dot{m}}$. As such, the angle of attack and relative pitch orientation will accordingly increase to accommodate the addition of fuel into the receiver aircraft fuel tanks. The variation of pitch rate with time will also be impacted by the change of fuel from the fore tanks into the aft tanks. The dynamic simulation in section 3.6 will include the effect of no fuel transfer to see how the addition of fuel into the receiver aircraft affects the system behaviour.

3.6 Dynamic Simulation of Tanker-Receiver During Automated Aerial Refuelling

In Figure 3.2, it can be seen that the receiver aircraft mass remains constant at its baseline value of $11,281$ kg until $t = 25s$ when the fuel transfer from the tanker begins. Fuel is transferred at a constant flow rate till tanks 1 and 2 are filled, and fuel is then transferred to tanks 3 and 4 at $t = 85s$ till $t = 195s$

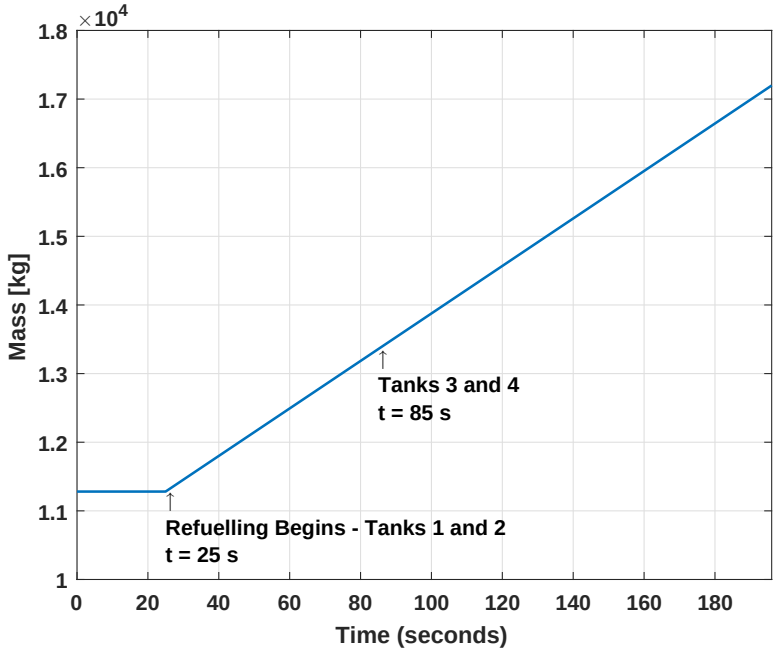


Figure 3.2: Receiver aircraft change in mass during refuelling.

In order for the receiver aircraft to hold a fixed position relative to the tanker while mass and inertia properties are changing during the manoeuvre, the body rates will not remain zero as in the case where there would be no refuelling. Figure 3.3 shows that pitch rate q_{TR} increases twice: the first at the time fuel is introduced into the forward tanks, and then again when

fuel is transferred to the aft tanks. The control law inner-loop is modelled on the inner-loop of an altitude hold autopilot and the manually-tuned control gains are able to maintain the increase in pitch rate appropriately at constant value [s] according to the refuelling phases when mass is introduced.

Since the refuelling pattern is symmetric, the lateral-directional dynamics would not be affected in the same manner as the longitudinal. Also, the roll and yaw control channel structure was constructed differently to that of the pitch channel. Proportional control was applied to roll rate p_{TR} and yaw rate r_{TR}. An outcome of the control design was to maintain fixed y-separation from the tanker, thus inevitably, control of the lateral-directional body rates had impact on y_{TR} over time as revealed in the manual tuning process. When applying the manually-tuned gains, a very slight drift in roll and yaw rates at the end of the manoeuvre is present (in the range of 1e−6 deg/s). However, its effect is minimal, as will be seen when lateral-directional disturbances are applied later on. When only the vortex wake is in effect between $0 - 25s$, the body rates are fixed at nominal values (in this case, 0 rad/s).

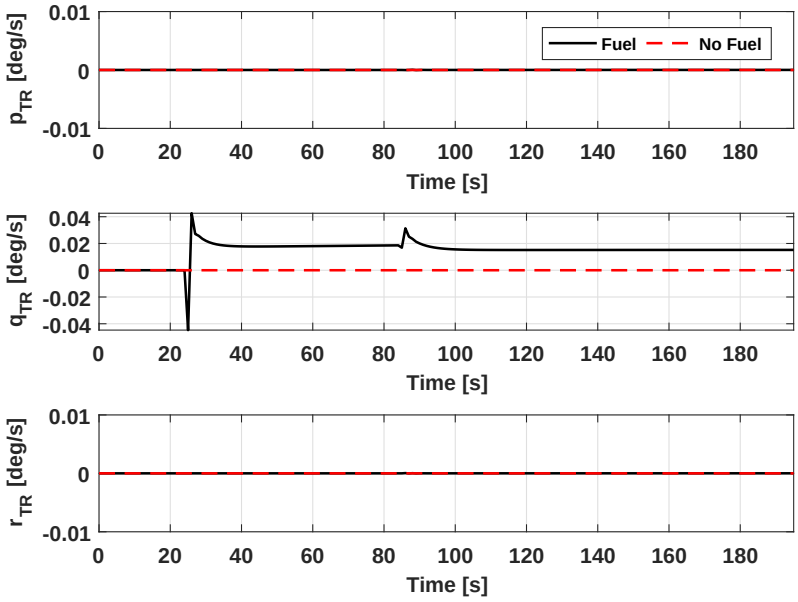


Figure 3.3: Receiver aircraft body rates relative to tanker.

As the pitch rate is affected by the refuelling, these effects will be translated to other longitudinal state variables. The receiver aircraft angle of attack increases in response to fuel being added to the tanks (see comparison to no-fuel case in Figure 3.4). The receiver aircraft airspeeds are maintained at constant values, with the total airspeed in the wind-frame V_R being 190.055 m/s. PID control was applied to the speed channel in the outer-loop. Again, when only the vortex wake is in effect between $0 - 25s$, the state variables are also fixed at nominal values as seen with the body rates. A very slight drift in sideslip angle β_R is evident

at the end of the refuelling manoeuvre - due to the effects discussed above - with value order of magnitude 1e−4.

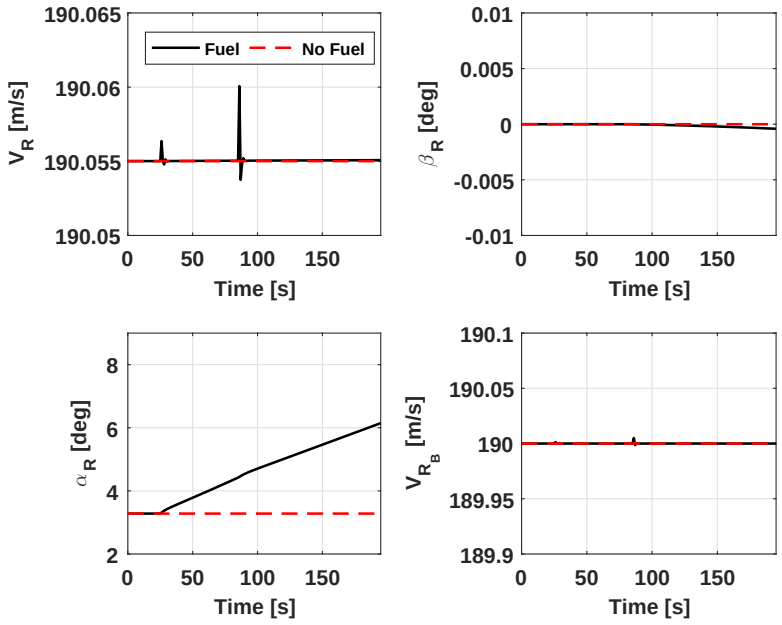


Figure 3.4: Receiver aircraft airspeed, angle of attack and sideslip angle.

Figure 3.5 compares the receiver aircraft Euler angles relative to the tanker. For the no-refuelling case, these angles remain at their nominal values, however, as fuel is introduced, the pitch orientation θ_{TR} increases with time, similar to the trend observed for α_R above. Roll and yaw angles maintain their nominal values in the initial stages and also see a similar trend to that of β_R, with the same order of magnitude 1e−4.

The time history of the receiver separation from the tanker, x_{TR}, y_{TR}, and z_{TR}, is presented in Figure 3.6. Position was controlled with PID gains in the outer-loop of the refuelling controller. The separation is maintained, with x_{TR} being slightly sensitive to the fuel entering the aft tanks (a slight notch is observed at $t = 85s$ then returning to nominal value of 25.33). The height z_{TR} was affected by the fuel entering the forward tanks at $t = 25s$ - a deviation of 0.0001 m was experienced by the receiver, which slowly rectified towards the end of the refuelling. These deviations and subsequent recoveries are acceptable within the refuelling limits.

If no fuel were added to the receiver aircraft flying in the vortex wake of the tanker, all control surface deflections would remain constant at their nominal values, as seen in Figure 3.7. In line with the expectations of a symmetric refuelling scheme, only the receiver elevator and throttle would experience deviations from their nominal values to maintain the receiver aircraft in its required position throughout the period of fuel transfer. When fuel is transferred

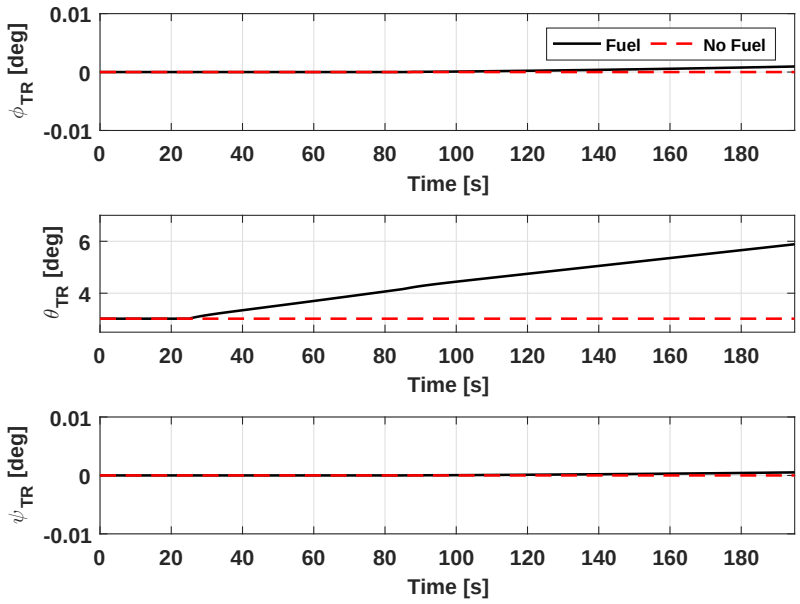


Figure 3.5: Receiver aircraft orientation relative to tanker.

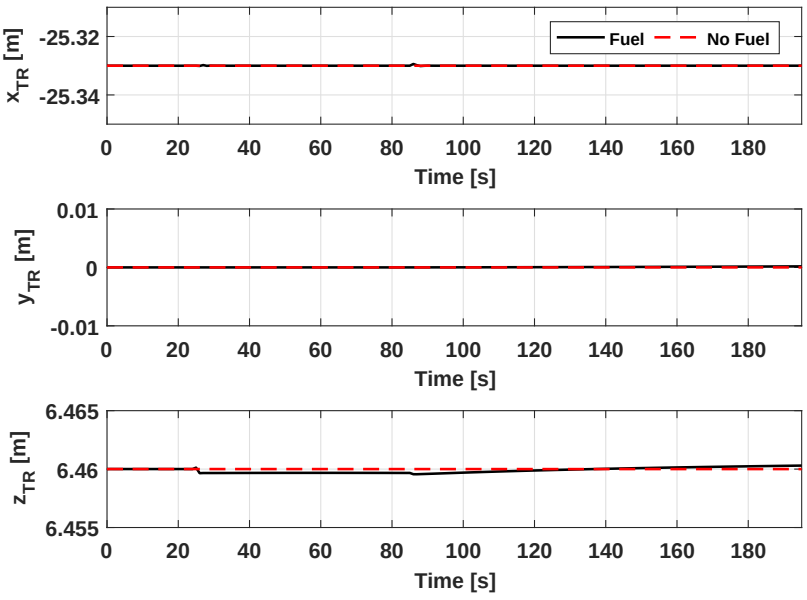


Figure 3.6: Receiver aircraft relative separation from tanker.

to the forward tanks at $t = 25s$, δ_{e_R} adjusts constantly to a more negative deflection. Then at the time of the aft tanks refuelling ($t = 85s$), the elevator reverses its negative deflection trajectory in line with the need to meet system performance specifications. The throttle deflection δ_{t_R} continuously increases as fuel is increased. The trend is similar to that of θ_{TR} and α_R earlier. These control surfaces remain within their physical limits throughout the manoeuvre. The aileron and rudder also experience the slow drift described earlier. Deflections δ_{a_R} and δ_{r_R} are at $0.01deg$ at $t = 195s$. In all instances, the receiver aircraft maintains its nominal state when only the vortex wake is in effect between $0 - 25s$.

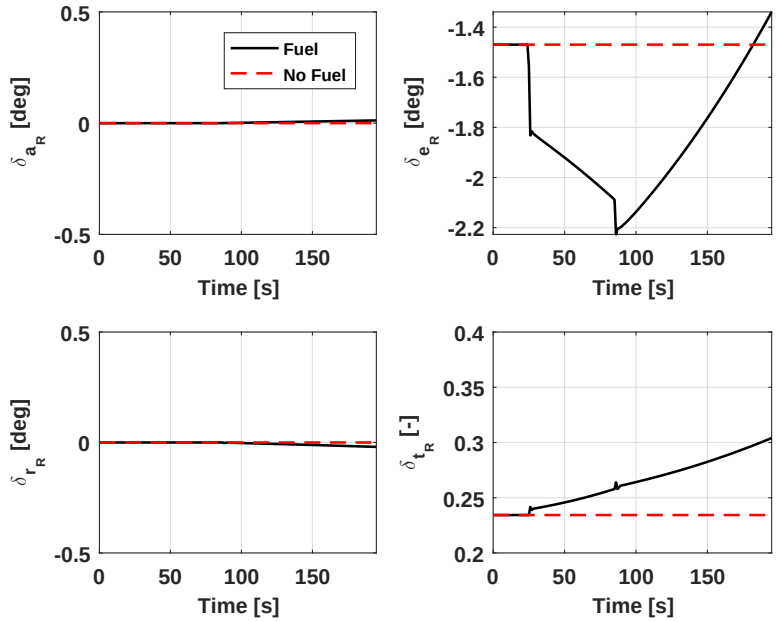


Figure 3.7: Receiver aircraft control surface deflections.

The tanker aircraft dynamic simulation is the same regardless of whether the receiver receives fuel or not, and only one set of results are presented. The tanker aircraft state variables V_T, β_T, α_T, p_T, q_T, r_T, ϕ_T, θ_T and ψ_T time histories are shown in Figure 3.8. All state variables are maintained at nominal value.

Figure 3.9 shows the tanker position over time, and Figure 3.10 shows the tanker control surfaces' deflections over time. The tanker maintains a steady height while moving forward, and all control surfaces' deflections are fixed at the nominal values.

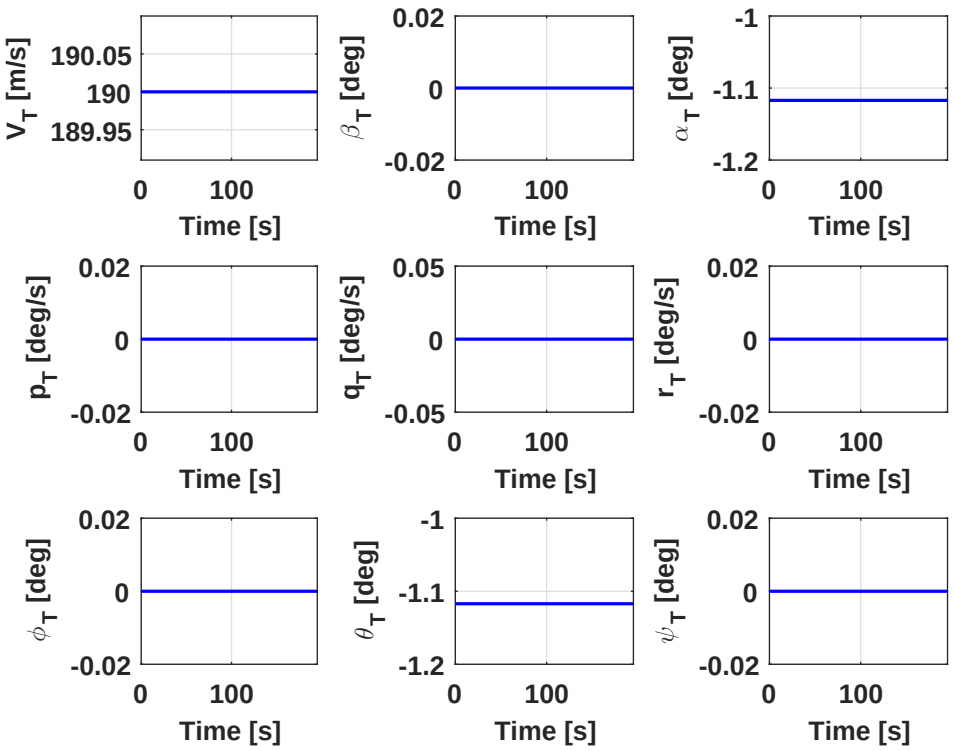


Figure 3.8: Tanker aircraft state variables.

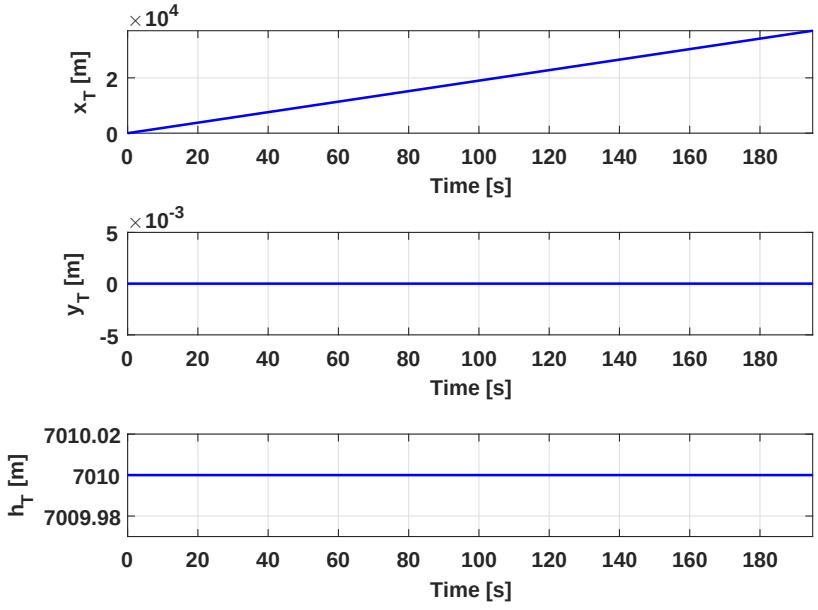


Figure 3.9: Tanker aircraft x- y- and z-positions along flight path.

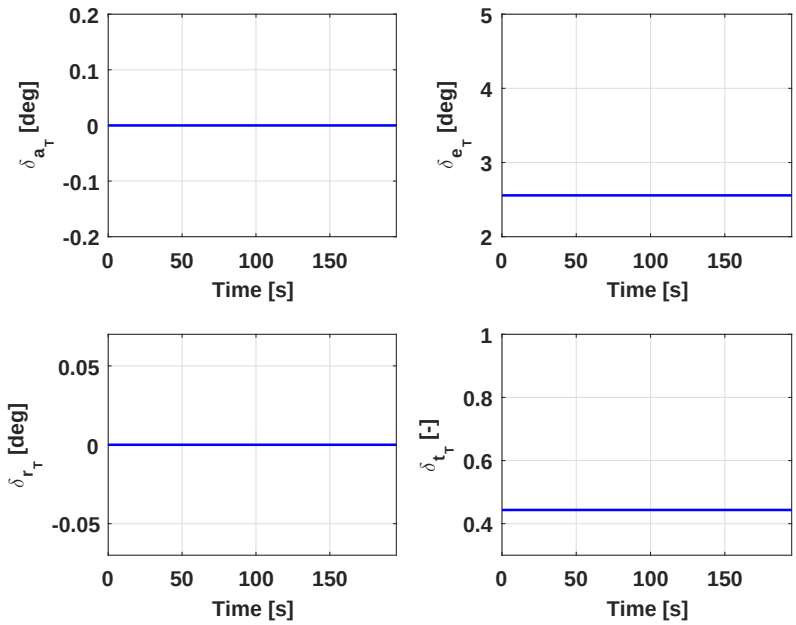


Figure 3.10: Tanker aircraft control surfaces' deflections.

3.7 Robustness Analysis of the Manually-Tuned Controller Gains Case

Whilst the refuelling dynamics is itself altered over the three defined phases of the manoeuvre, these effects have been modelled as inherent to the system. Thus, one of the most significant control specifications was to manually tune a set of control gains that would be applicable to all phases of the manoeuvre. This did offer some sort of variability that the controller would have to overcome while refuelling under standard conditions.

In the previous section, the same set of manually-tuned control gains were applied to the system where $\dot{m} = 0$, i.e., the receiver was flying in the vortex wake of the tanker with no fuel transfer. The gains, when applied to the no-fuel system, were able to maintain the receiver aircraft position fixed relative to the tanker with all states held at their nominal values. The gains did not need to be changed or manipulated in any way. An amount of robustness of the control gains can be inferred from this.

The presence of a slow drift in lateral-directional body rates relative to the tanker was seen in the previous section. The robustness of the manually-tuned controller gains must be ascertained in any case, and more so with the body rates order of magnitude of 1e−6 deg/s

being present. It is pertinent thus that disturbances must be defined to test the system performance with the same set of manually-tuned control gains.

3.7.1 Mass or refuelling disturbances

The effect of fuel transfer was seen in the previous section. However, the fuel transfer was symmetric, leading to significant effects present in the longitudinal channel.

Table 3.5 describes the disturbed refuelling profile applied to the receiver aircraft flying in the tanker vortex wake. The longitudinal effects would be examined by applying a 75% flow rate to forward tanks 1 and 2. An asymmetric condition was then introduced between $t = 85s$ and $t = 195s$, with tank 3 being filled to half its capacity and no fuel was transferred to tank 4 at all.

Table 3.5: Automated aerial refuelling simulation phases - disturbance in refuelling

Phase	**Description**	**Time (s)**
I	Receiver stays on station, no fuel	0 - 25
II	Tanks 1 and 2 filled to 75% capacity	25 - 85
III	Tank 3 filled to 50% capacity	85 - 195
	Tank 4 NOT filled i.e., 0% capacity	

Figure 3.11 compares the fuel tank mass increases with time for the baseline symmetric refuelling case and the newly defined mass disturbance case.

Tanks 1 and 2 fill up with a gradient adjusted by the scaling of the flow rate to 75%. Tank 3 similarly fills up with a gradient adjusted by the scaling of the flow rate to 50%. Finally, tank 4 mass remains at 0 kg.

The total aircraft mass increase with time for both the baseline and disturbance case is presented in Figure 3.12. The effect of the scaling and zero fuel transfer can be seen to be distinctly different to that of the baseline case.

3.7.2 Turbulence

The tanker aircraft state variables appear explicitly in some of the state equations of the receiver aircraft written relative to the tanker. Disturbing the tanker aircraft will allow the disturbance effects to be propagated onto the receiver aircraft directly. A turbulence profile for the tanker flying at $V_T = 190$ m/s at $h = 7010$ m was generated and is shown in Figure 3.13. This will introduce longitudinal and lateral-directional disturbances to be countered by

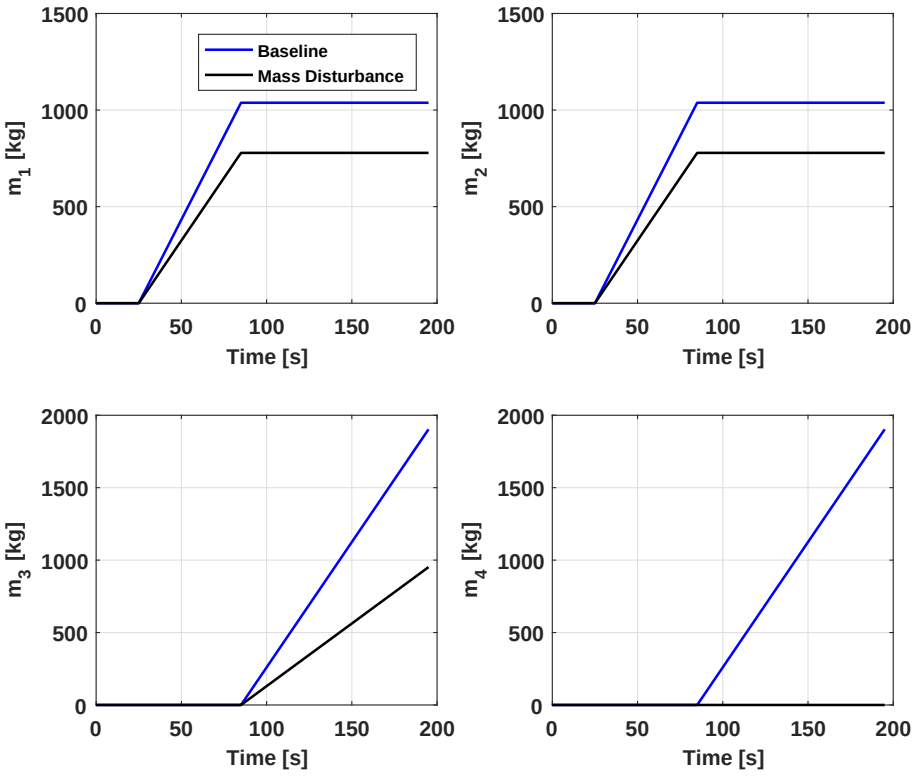


Figure 3.11: Receiver aircraft fuel tank masses - baseline and disturbance case.

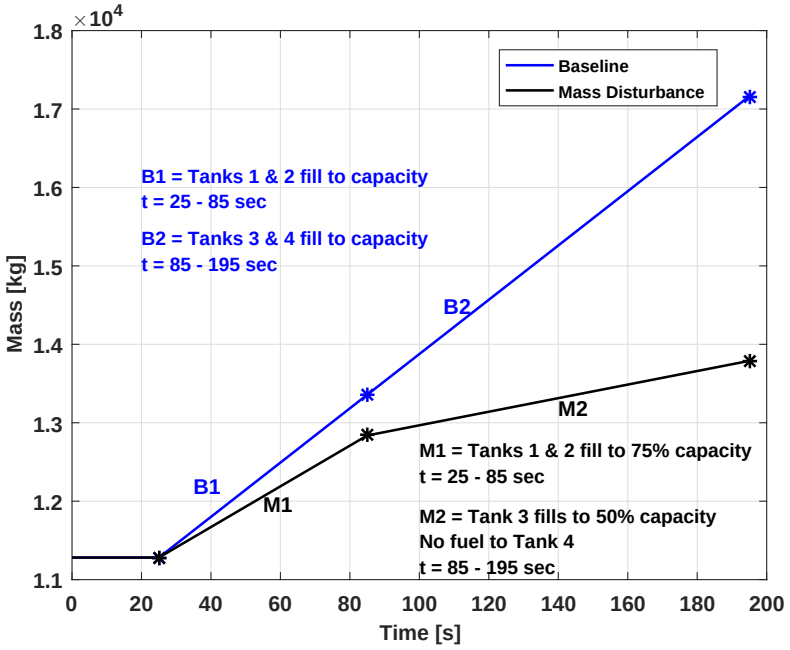


Figure 3.12: Receiver aircraft change in mass during refuelling - baseline and disturbance case.

the control system across all three refuelling phases. For this disturbance case, the refuelling happens as intended (original definition in Table 3.5), however, turbulence is switched on between $t = 100s$ and $t = 130s$.

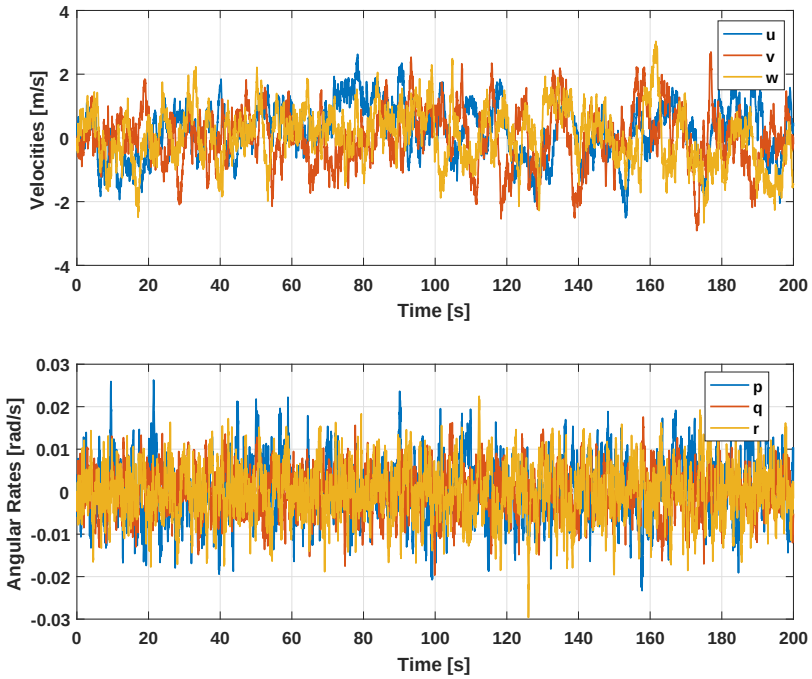


Figure 3.13: Disturbance profile for tanker aircraft.

3.7.3 Dynamic simulation of automated aerial refuelling including disturbances

Figures 3.14 - 3.16 overlay the undisturbed motion (i.e., baseline) of the receiver and tanker state and control variables with the same variables for both disturbance cases. Starting with the pitch rate in Figure 3.14, in Phase II, when the forward tanks are being filled to 75% capacity, the pitch rate required to keep the receiver aircraft steady relative to the tanker is now less than the baseline case (100% fuelling). The same is observed for Phase III where only tank 3 is filled to 50% capacity. The same control gains tuned for the baseline case was still able to maintain pitch dynamics required for steady aerial refuelling. The effect of turbulence on the tanker aircraft is seen in the pitch dynamics as well. The pitch rate is disturbed when turbulence was introduced between $t = 100s$ and $t = 130s$, and settles back to the baseline value at approximately $t = 140s$.

The asymmetric refuelling starting at $t = 85s$ induced a short-lived spike in the roll rate p_{TR} and yaw rate r_{TR}. The adequacy of the manually-tuned gains is apparent now, since, when

applied to the system with asymmetric refuelling, divergent behaviour is not induced, and the trend is maintained - a very slight drift in roll and yaw rates at the end of the manoeuvre is present (this time in the range of 1e−5 deg/s).

When turbulence was introduced, the system experienced transient behaviour and was able to return to baseline behaviour at approximately $t = 160s$. The roll and yaw rates settle to baseline behaviour slower than the pitch rate.

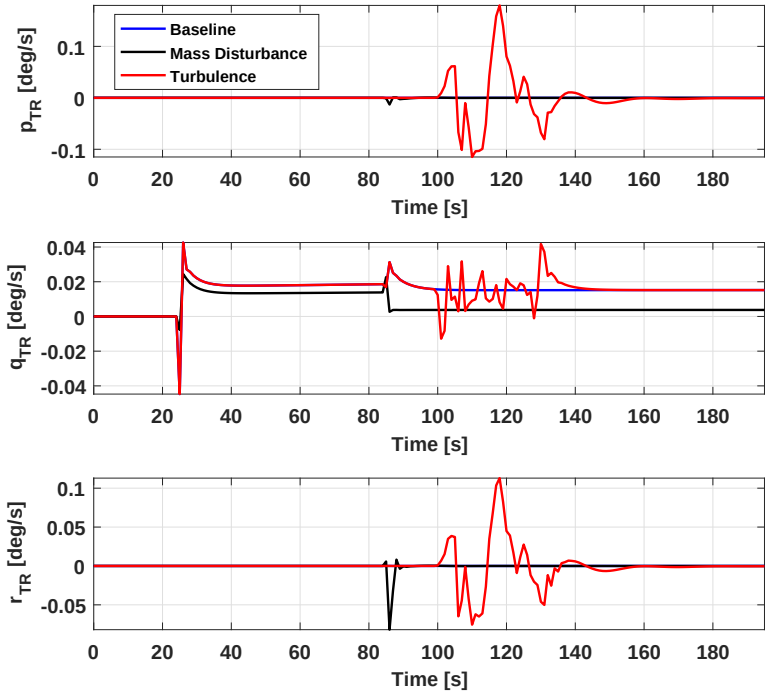


Figure 3.14: Receiver aircraft body rates relative to tanker - baseline and disturbances.

The time history of the airspeeds, angle of attack and sidelip angle is presented in Figure 3.15. The effect of the disturbed fuel transfer profile is most prominent in α_R and β_R in Phase II, when fuel is symmetrically supplied at 75% of the baseline case; as expected, α_R increases at a slower rate compared to the baseline case. In Phase III, with only one tank being supplied fuel, the slope of α_R becomes shallower and as expected, its final orientation is less than the baseline case.

Sideslip angle β_R is only affected at the start of Phase III, when fuel is asymmetrically introduced (into tank 3 only). It reaches a value of 0.01 deg at the end of refuelling. This value is within the allowable state limits for the aircraft.

When turbulence was introduced, the angle of attack α_R response was slightly affected (small magnitude transient on the same gradient) compared to the baseline case, however, β_R experienced a prominent transient upset, which only settled to baseline value at the end of the refuelling manoeuvre. The controller is able to return the sideslip to its baseline behaviour, albeit very slowly - this slow return does not introduce divergent behaviour in the lateral-directional channels.

The airspeeds were less sensitive to the changes in mass distribution and were more affected by the turbulence experienced by the tanker. The controller was able to return the airspeeds to baseline values at approximately $t = 140s$.

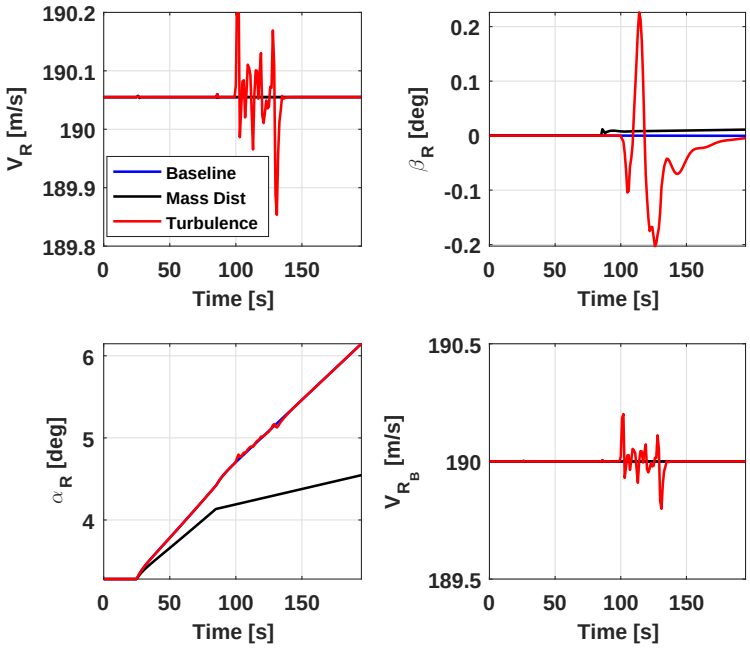


Figure 3.15: Receiver aircraft airspeed, angle of attack and sideslip angle - baseline and disturbances.

Euler angle θ_{TR} in Figure 3.16 under disturbed conditions behaved in a similar manner to α_R discussed above. Angles ϕ_{TR} and ψ_{TR} are affected by the asymmetric refuelling and slowly increase to $\phi_{TR} = -0.0262$ deg ; $\psi_{TR} = -0.0133$ deg at $t = 195s$. When turbulence is applied, ϕ_{TR} and ψ_{TR} are disturbed to within a magnitude of 0.5 deg, and slowly settle towards the baseline case at $t = 195s$.

The time history of the receiver separation from the tanker, x_{TR}, y_{TR}, and z_{TR}, is presented in Figure 3.17 for the disturbance cases. The effects of asymmetric fuel transfer were minimal, as can be seen in the y_{TR} profile, where a negligible deviation of -0.005m was built-up at the end of refuelling. Turbulence effects were most prominent in the x_{TR} and y_{TR} states. In line with the trends identified earlier, the longitudinal x_{TR} settles at $t = 140s$ with the lateral

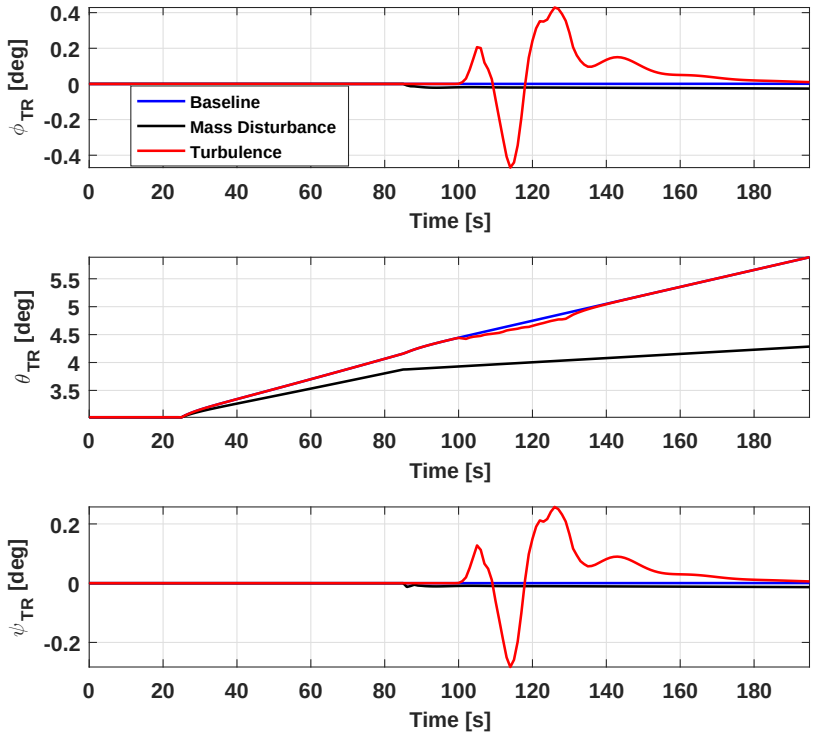


Figure 3.16: Receiver aircraft orientation relative to tanker - baseline and disturbances.

y_{TR} slowly reaching baseline value at $t = 195s$. Disturbed height z_{TR} followed its baseline behaviour in trend for both cases. All deviations and subsequent recoveries are acceptable within the refuelling limits.

The effects of the mass disturbance can be seen in all four control surface deflections in Figure 3.18. With less fuel being added in both Phases II and III, the elevator δ_{e_R} and throttle δ_{t_R} follow trends uncovered earlier in the longitudinal channel. In Phase II, with 75% of fuel transfer compared to the baseline case, the elevator and throttle deflections increase with a shallower slope

If no fuel were added to the receiver aircraft flying in the vortex wake of the tanker, all control surface deflections would remain constant at their nominal values, as seen in Figure 3.18. In line with the expectations of a symmetric refuelling scheme, only the receiver elevator and throttle would experience deviations from their nominal values to maintain the receiver aircraft in its required position throughout the period of fuel transfer. When fuel is transferred to the forward tanks at $t = 25s$, δ_{e_R} adjusts to a more negative deflection. Then at the time of the aft tanks refuelling ($t = 85s$), the elevator reverses its negative deflection trajectory in line with the need to meet system performance specifications. The throttle deflection δ_{t_R} continuously increases as fuel is increased. The trend is similar to that of θ_{TR} and α_R earlier.

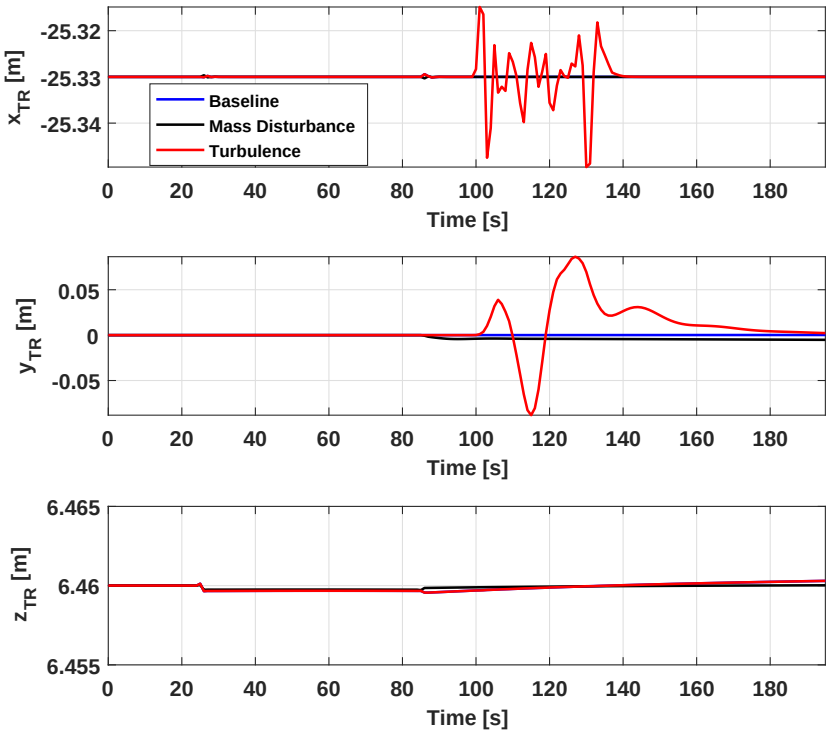


Figure 3.17: Receiver aircraft relative separation from tanker - baseline and disturbances.

These control surfaces remain within their physical limits throughout the manoeuvre. The aileron and rudder also experience the slow drift described earlier. Deflections δ_{a_R} and δ_{r_R} are at 0.01 deg at $t = 195s$. In all instances, the receiver aircraft maintains its nominal state when only the vortex wake is in effect between $0 - 25s$.

3.8 Chapter Summary

A baseline PID controller for the receiver aircraft was developed and applied to the nonlinear aerial refuelling model developed in Chapter 2. Performance specifications for the receiver and tanker aircraft were given in line with norms for the aerial refuelling manoeuvre. Tanker and receiver specifications were given. Single set of controller gains for all three phases/segments. The tanker was controlled by LQR. A manual-tuning procedure was applied to the inner and outer-loops of the proposed control scheme. A quadratic cost function J was constructed for manual checking of the tuning outcomes. The receiver aircraft control laws were constructed so that δ_e was responsible for the vertical separation control (i.e., height-hold), while speed and x-separation were controlled with δ_t. The lateral-directional control used a combination of aileron and rudder in the outer loop for the y-channel control. The tuning showed gain Ke_θ

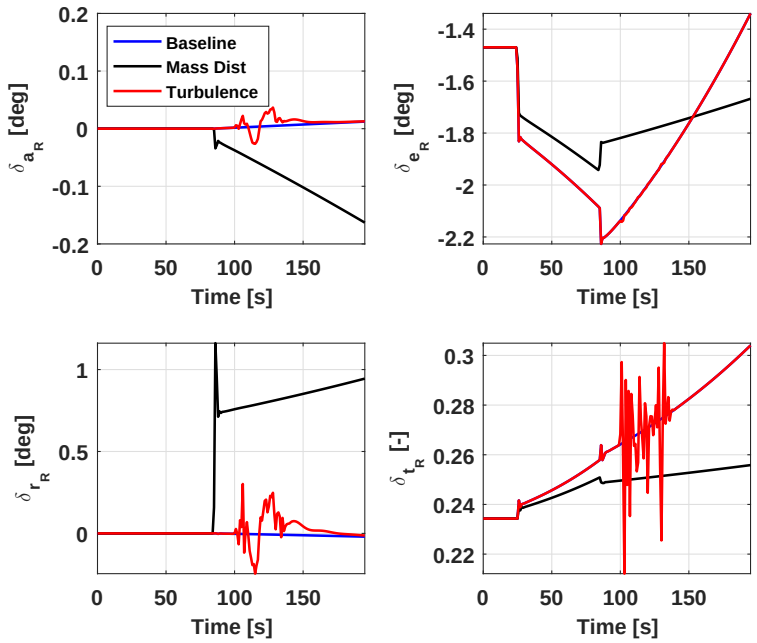


Figure 3.18: Receiver aircraft control surfaces' deflections - baseline and disturbances.

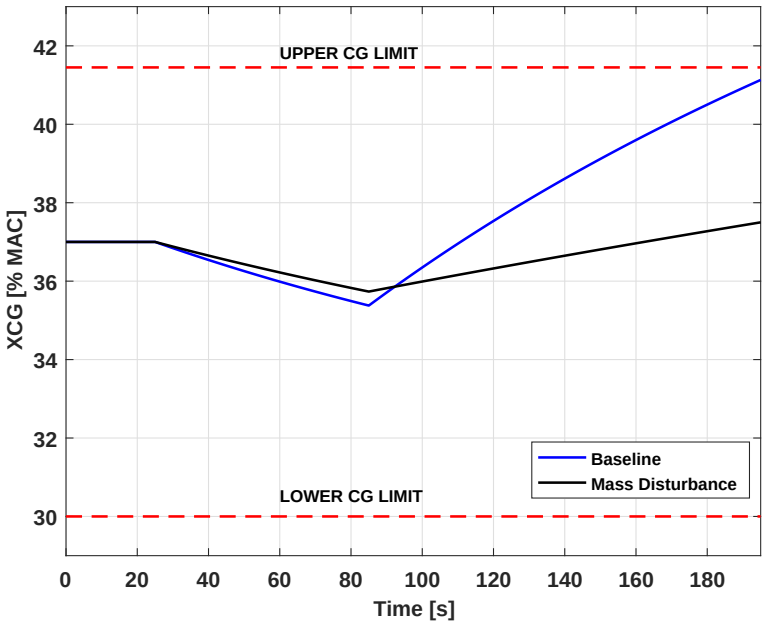


Figure 3.19: CG travel during refuelling - baseline and disturbances.

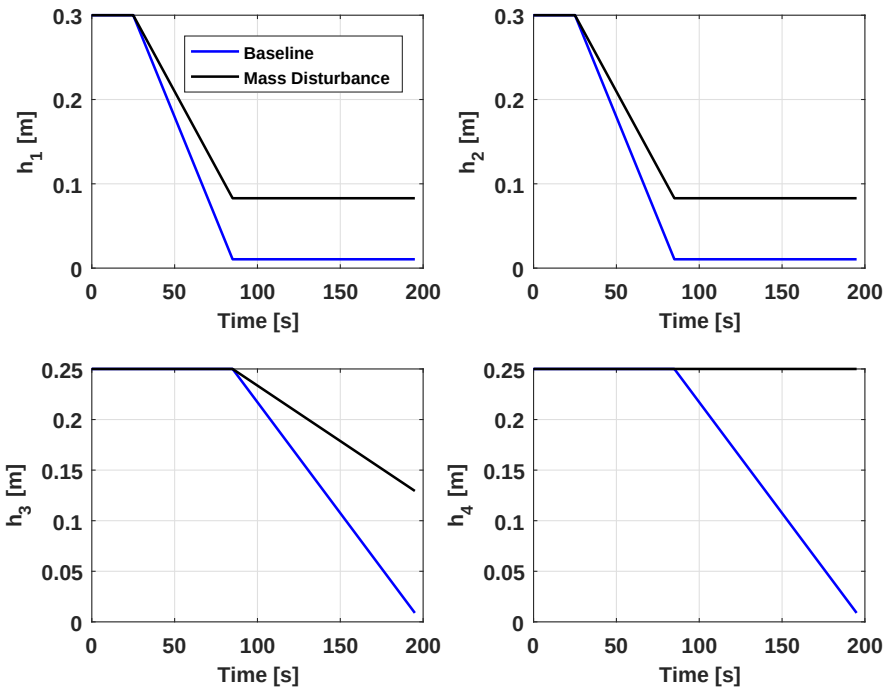


Figure 3.20: Receiver aircraft fuel tank centroid position during refuelling - baseline and disturbances.

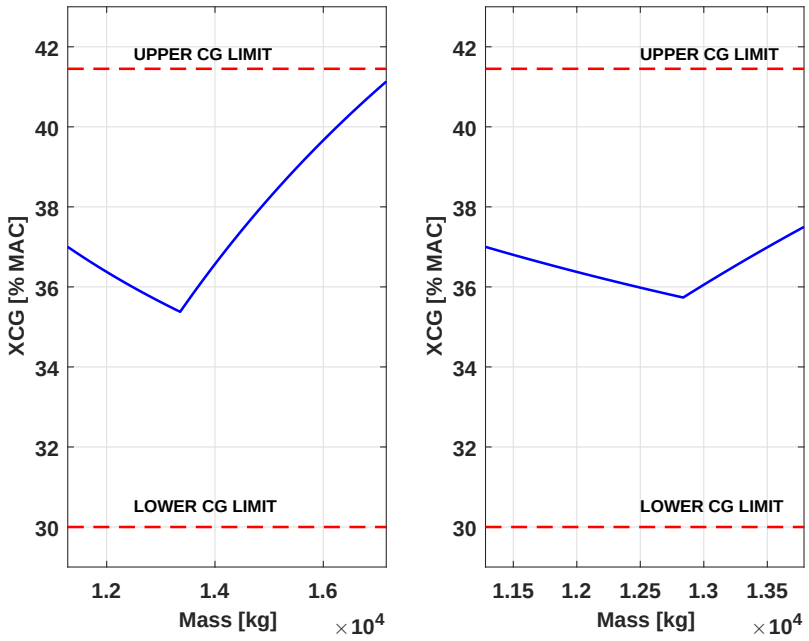


Figure 3.21: CG travel vs. mass throughout refuelling - baseline (left) and disturbances (right).

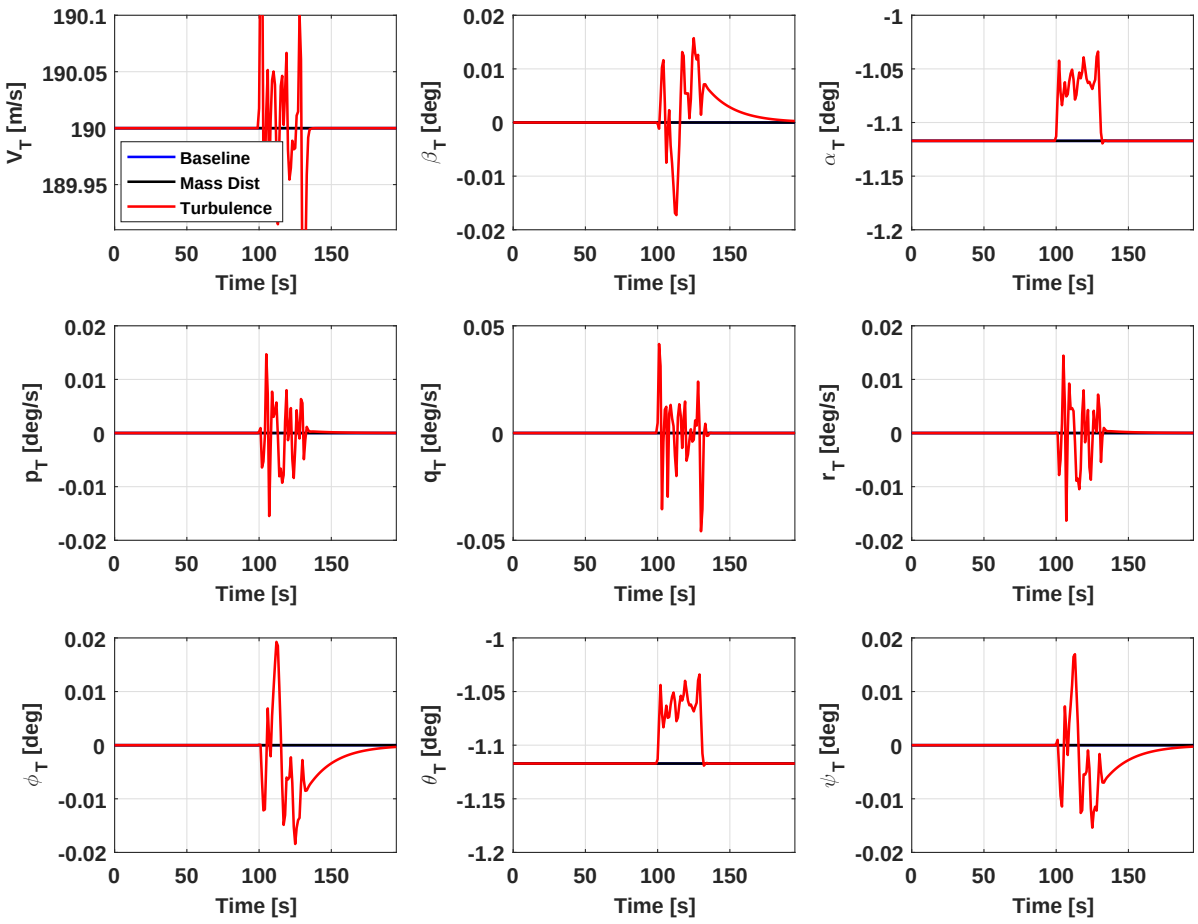


Figure 3.22: Tanker aircraft state variables - baseline and disturbances.

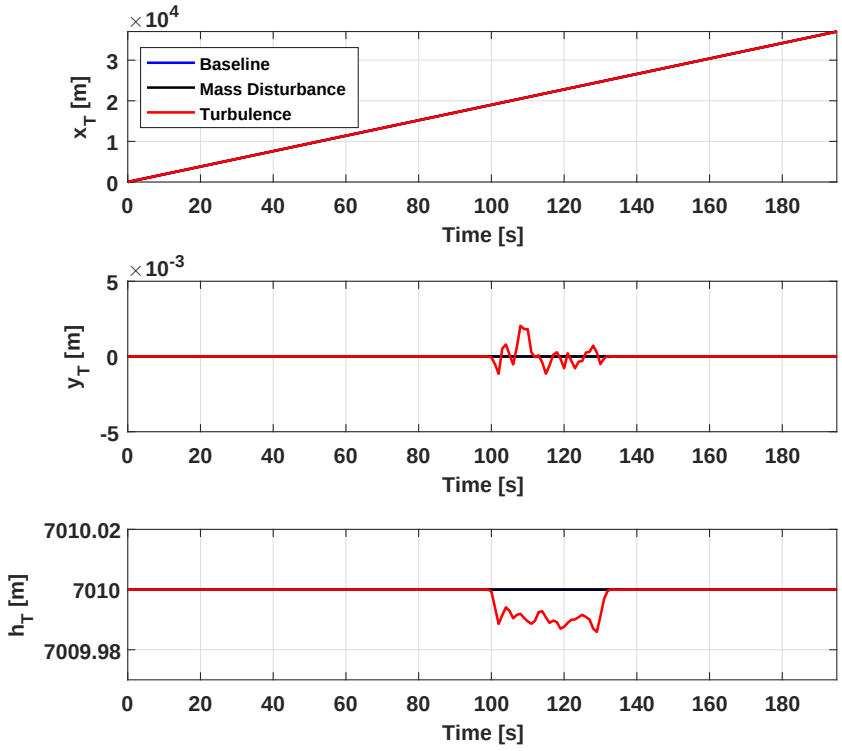


Figure 3.23: Tanker aircraft x- y- and z-positions along flight path - baseline and disturbances.

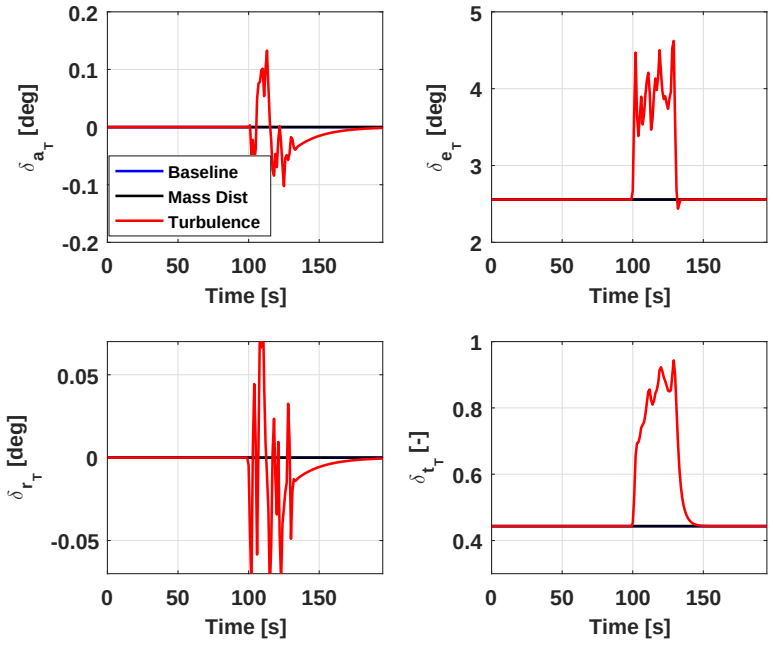


Figure 3.24: Tanker aircraft control surfaces' deflections - baseline and disturbances.

was the most sensitive parameter to tune in the inner loop. The least sensitive variables to tune were the outer-loop thrust gains. The case for no refuelling was presented. Robustness of control law was tested with disturbances in mass flow rate and turbulence. The controller was able to maintain the aircraft as required in specifications. The CG travel was within limits. Stability analysis of the controlled system will be carried out in Chapter 4. A major aim of the control design was to select a single set of controller gains for all three phases of refuelling. This was achieved. The benchmark PID controller was thus developed to compare performance to the nonlinear and dynamic neural network controllers that will be developed later on.

4 Stability Analysis

Stability of the complex system must be ascertained. However, since tools do not readily exist for systems like the one under study, a new analysis must be considered and developed given the complexities associated with aerial refuelling. Lyapunov stability theory will be extended to develop a theorem for AAR to optimise controller gains selection. However, manual tuning was performed in Chapter 3 and based on the theory to be developed in this chapter, it is necessary to come up with a methodology to analyse the system stability under the control law developed in Chapter 3. This chapter thus has two purposes: to develop a Lyapunov-based stability theorem for AAR and to perform a stability analysis for the system subject to the control law and manually-tuned gains developed in Chapter 3.

4.1 Lyapunov Stability Analysis

4.1.1 Background and concepts

Amongst the various properties of control systems, stability has significant importance, as this affects its ultimate usefulness. Lyapunov's Direct Method (developed as early as 1892) has become the most important tool for nonlinear system analysis and design. This method allows insight into the stability of a nonlinear system by constructing a scalar "energy-like function" for the system and examining its time variation (Slotine and Weiping (1991), Terrell (2009)). Ultimately, for the AAR system, a Lyapunov function can be constructed that will give insight into the system behaviour.

In general, a nonlinear system is represented by differential equations of the form:

$$\dot{\mathbf{x}} = \mathbf{f}(\mathbf{x}, \mathbf{u}, t) \tag{4.1}$$

$$\mathbf{u} = \mathbf{g}(\mathbf{x}, t) \tag{4.2}$$

$$\dot{\mathbf{x}} = \mathbf{f}(\mathbf{x}, \mathbf{u}, t)[\mathbf{x}, \mathbf{g}(\mathbf{x}, t), t] \tag{4.3}$$

Definition 4.1 (Haddad and Chellaboina (2008)) A state $\mathbf{x}^*$ is an equilibrium state of the system if once $\mathbf{x}(t)$ is equal to $\mathbf{x}^*$, it remains equal to $\mathbf{x}^*$ for all future time.
Thus, the constant vector $\mathbf{x}^*$ satisfies

$$\mathbf{0} = \mathbf{f}(\mathbf{x}^*) \tag{4.4}$$

The solution of this equation gives the equilibrium state/point. Further to this, stability of motion may be of importance for the system analysis. In that case, there is interest in understanding whether a system remains close to its original motion trajectory if slightly perturbed away from it. In Slotine and Weiping (1991), this type of problem is shown to be able to be transformed into an equivalent stability problem around an equilibrium point.

Let B_R denote a spherical region/ball defined by $\|\mathbf{x}(0)\| < R$ in the state-space, and S_R the sphere itself defined by $\|\mathbf{x}(0)\| = R$.

Definition 4.2 (Haddad and Chellaboina (2008)) The equilibrium state is said to be stable if, for any $R > 0$, there exists $r > 0$ such that if $\|\mathbf{x}(0)\| < r$, then $\|\mathbf{x}(t)\| < R$ for all $t \geq 0$. Otherwise the equilibrium point is unstable.

This implies that for a ball of arbitrarily-defined radius $\mathbf{B}_R$ a value $r(R)$ can be found such that the starting state of the ball at time t_0 guarantees that the state will stay within the ball thereafter.

Definitions of asymptotic and exponential stability, and positive definitive and Lyapunov functions can be found in standard texts on nonlinear systems and control and will not be repeated here.

4.1.2 Lyapunov's direct method extended to AAR

In Slotine and Weiping (1991), the basic philosophy of Lyapunov's direct method has been stated to be the mathematical extension of a fundamental physical observation: if the total energy of a mechanical system is continuously dissipated, then the nonlinear system must eventually settle down to an equilibrium point. Therefore, the stability of a system can be analysed through the variation of a scalar function. A comparison of the definitions of stability and mechanical energy gave the following observations:

- zero energy corresponds to the equilibrium point
- asymptotic stability implies the convergence of mechanical energy to zero

- instability is related to the growth of mechanical energy

However, in AAR, the system is one where the mechanical energy is increased by design. In this study the increase in mechanical energy has had the advantage of being modelled as part of the system dynamics and not as a disturbance. This then allows for the extrapolation of Lyapunov's direct method so that the nominal motion or equilibrium point problem can be formulated appropriately for a system subject to increases in mechanical energy.

In aerial refuelling, the mass cannot increase from its initial value at t_0 to infinity at some time $t \gg t_0$ as there are physical limits imposed on the aircraft. The fuel tank location and sizes put a physical bound on the maximum energy that the system is able to receive. The implication is that the ball expands to a finite radius R, based on the energy addition. It is important to know the stability of this point else the origin of the final spherical region may exhibit unstable and thus undesirable behaviours. Also, the aircraft static margin and CG limits are to be factored in and also provide a maximum bound to the radius R. When radius R is attained, mechanical energy must be conserved.

The sphere described by Slotine and Weiping is the starting point in the development of a stability analysis for systems such as AAR. Let R_1 be an initial spherical region in the state-space, with $\mathbf{x}_1$ the equilibrium point of the state. Mechanical energy is introduced in such a manner that it increases radius R_1 to R_2 as depicted in Figure 4.1. From the initial understanding of the AAR system obtained in the previous chapter, the mass flow rate (and its variation) would determine the limit imposed on the system states within the sphere of radius R_2.

In two-dimensions, Figure 4.2 shows that the spherical region in the state-space that the system can migrate to, represented by radius R_{max}, will be due to physical system limitations. At this point no further mechanical energy can be introduced into the system and thus becomes the final spherical region in the state-space that can be studied to gain insights into the system stability with additional mechanical energy. The intermediate spherical regions must also exhibit stable properties. Practical usefulness of this will be shown in a later chapter.

The distinction between autonomous and non-autonomous systems must be considered before proceeding to the next steps of the stability analysis. Drawing on the definition in Marquez (2003), for a general nonlinear system $\dot{\mathbf{x}} = \mathbf{f}(\mathbf{x}, \mathbf{u}, t)$ to be autonomous, $\mathbf{f}$ must not depend explicitly on time, i.e., $\dot{\mathbf{x}} = \mathbf{f}(\mathbf{x})$. While fuel is being transferred to the receiver aircraft, the system is non-autonomous. Although mass is not an aircraft state variable, the effect of $\dot{m}$ on the receiver states has been shown in Chapter 3. However, when refuelling is completed, and the receiver aircraft remains on station behind the tanker aircraft, the system can be

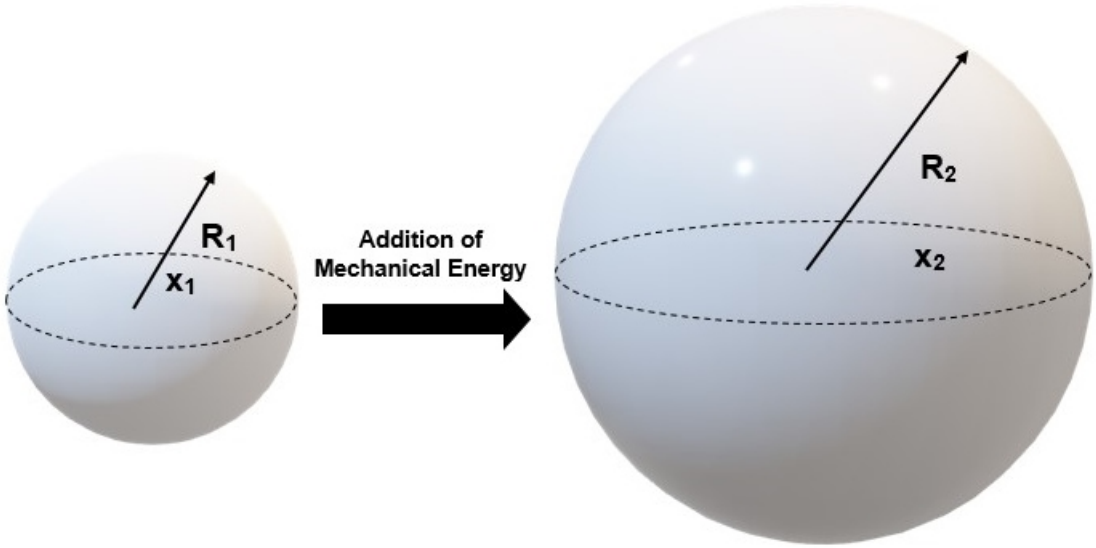


Figure 4.1: Growth of spherical region with radius R_1 to region of radius of R_2 under addition of mechanical energy.

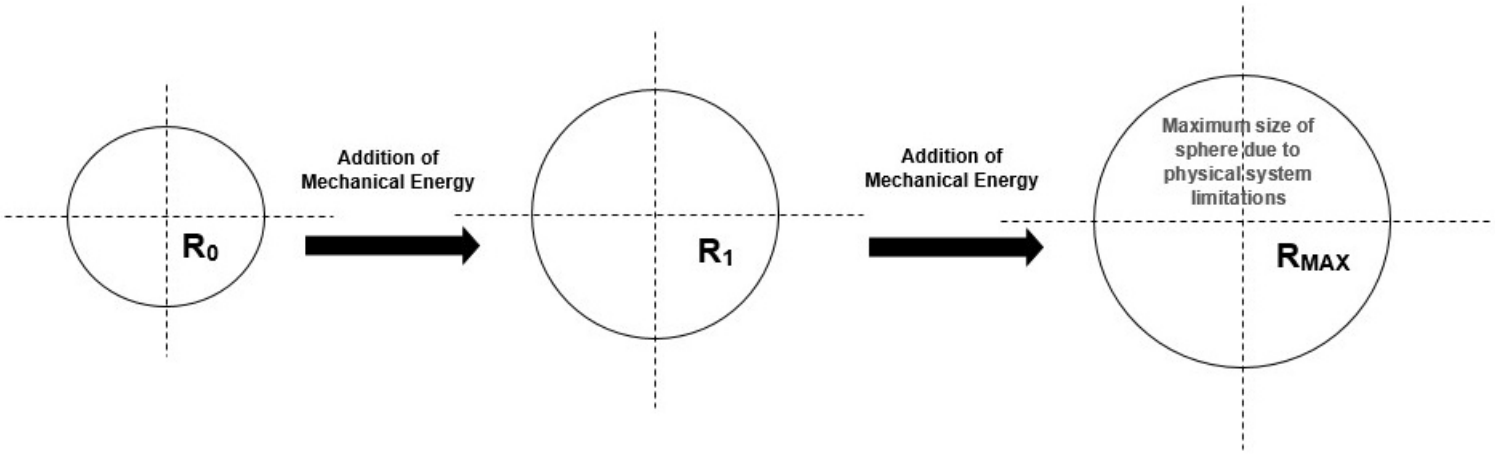


Figure 4.2: Two-dimensional depiction of spherical region from initial R_0 to R_{max}.

considered autonomous as $\dot{m} = 0$. Definition 4.1 and 4.2 above were given for an autonomous system. Definition 4.3, 4.4 and 4.5 are given for non-autonomous systems.

Definition 4.3 (Marquez (2003)) The equilibrium point $\mathbf{0}$ is stable at t_0 if for and $R > 0$ there exists a positive scalr $r(R, t_0)$ such that

$$\| \mathbf{x}(t_o) \| < r \quad \Rightarrow \quad \| \mathbf{x}(t) \| < R \quad \forall t > t_0 \tag{4.5}$$

Otherwise the equilibrium point $\mathbf{0}$ is unstable.

The definition means that the state can be kept in a ball of arbitrarily small radius R by starting the state trajectory in a ball of sufficiently small radius r. This differs from definition 4.2 in that the radius r of the initial ball may depend on the initial time t_0.

Definition 4.4 (Marquez (2003)) The equilibrium point $\mathbf{0}$ is asymptotically stable at time t_0 if:

- it is stable,
- $\exists r(t_0) > 0$ such that $\| \mathbf{x}(t_o) \| < r(t_0) \quad \Rightarrow \quad \| \mathbf{x}(t) \| \to \mathbf{0}$ as $t \to \infty$.

Definition 4.5 (Slotine and Weiping (1991)) The equilibrium point $\mathbf{0}$ is locally uniformly stable if the scalar r in definition 4.3 can be chosen independently of t_0, i.e., if $r = r(R)$

The next step is to construct an appropriate positive definite function that meets the definition for a Lyapunov function. It is important that this function also includes a proxy for the system energy, else pertinent system information will be lost. In this instance, mass would be the most intuitive selection. For non-autonomous systems, the Lyapunov function will be a scalar function with explicit time-dependence, i.e., $V = V(\mathbf{x}, t)$. Definitions for positive definite and decrescent functions are given.

Definition 4.6 (Nikravesh (2013)) A scalar time-varying function is locally positive definite if $V(\mathbf{0}, t) = 0$ and there exists a time-invariant positive definite function $V_0(\mathbf{x})$ such that:

$$\forall t \geq t_0, \quad V(\mathbf{x}, t) \geq V_0(x). \tag{4.6}$$

A time-varying function is locally positive definite if it dominates a time-invariant locally positive definite function.

Definition 4.7 (Marquez (2003)) A scalar time-varying function is decrescent if $V(\mathbf{0}, t) = 0$ and there exists a time-invariant positive definite function $V_1(\mathbf{x})$ such that

$$\forall t \geq t_0, \quad V(\mathbf{x}, t) \leq V_1(\mathbf{x}) \tag{4.7}$$

A scalar function $V(\mathbf{x}, t)$is decrescent if it is dominated by a time-invariant positive definite function.

Theorem 4.1: **Lyapunov stability for a non-autonomous AAR system**
If in a spherical region of the state-space initially given by radius R_0, which when subject to addition of mechanical energy continuously increases in radius to R_{final}, there exists a scalar function $V(\mathbf{x}, t)$ with continuous first partial derivatives such that:

- $V(\mathbf{x}, t)$ includes a scalar proxy for system energy,
- $V(\mathbf{x}, t)$ is and remains positive definite as radius R increases from $R_0 \rightarrow R_{final}$,
- $\dot{V}(\mathbf{x}) \leq 0$ is and remains negative semi-definite as radius R increases from $R_0 \rightarrow R_{final}$,

then the equilibrium point $\mathbf{0}$ is stable in the sense of Lyapunov. If furthermore,

- $V(\mathbf{x}, t)$ is decrescent,

then $\mathbf{0}$ is uniformly stable at R_{final}, as well as the instantaneous equilibrium points $\mathbf{0}$ along the trajectory of $R_0 \rightarrow R_{final}$ are also stable.

Proof
Consider the following Lyapunov function:

$$V(\mathbf{x}, t) = mx^2 \tag{4.8}$$

where m corresponds to the additional fuel introduced in each fuel tank during refuelling (i.e., $m = m_1 + m_2 + m_3 + m_4$, $m_i = \int \dot{m}_i dt$) and thus is a scalar proxy for system energy. $V(\mathbf{x}, t)$ dominates a time-invariant locally positive definite function $V_0(\mathbf{x}) = x^2$ Also, the selected Lyapunov function is decrescent as it is dominated by a time-invariant positive definite function $V_1(\mathbf{x}) = Mx^2$, where M is the maximum allowable weight of the aircraft. Also, since refuelling can begin at rate $\dot{m}$ at any time after docking and remaining on station, the scalar r is independent of t_0, the instance that refuelling occurs. Instead, as shown in Figure 4.1, the growth of the ball (i.e., R) is dependent on the addition of mechanical energy, thus $r = r(R)$. As fuel is added between t_{start} and t_{final}, the AAR system will move continuously through a series of equilibrium points as R increases from R_0 to R_{final}.

The system migration from $R_0 \rightarrow R_{final}$ is depicted in Figure 4.3. The concentric circles represent the spherical regions of the state-space with increasing radius. It is seen that $R_{final} > R_0$.

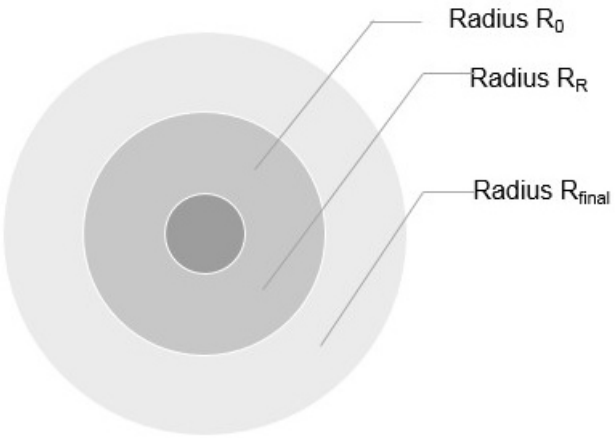


Figure 4.3: Concentric depiction of spherical regions in the state space.

Now that an appropriate Lyapunov function has been selected, and the growth of the spherical region has been depicted for the AAR system, the proof of the proposed theorem corresponds to the proof detailed in Slotine and Weiping (1991) page 107 to 110 and Marquez (2003) page 116 for the generic case. Applying the analysis at each successive instance as R moves from $R_0 \rightarrow R_{final}$, uniform asymptotic stability is proven from $R_0 \rightarrow R_{final}$. $\boxplus$

Taking the derivative:

$$\frac{dV}{dt} = \frac{dV}{dt} + \frac{dV}{dx}\frac{dx}{dt} \tag{4.9}$$

gives:

$$\dot{V} = x^2\dot{m} + 2xm\dot{x} \tag{4.10}$$

As mass flow rate appears in the expression for $\dot{V}$, there is already an intuitive expectation of an upper bound that the system states would converge to once refuelling is completed.

Given a stable equilibrium point at the start, with mechanical energy being added, a control law can be formulated to ensure that the system is lead to a final equilibrium point, where the system is thus settled at this new equilibrium point. An appropriate control can be designed using optimisation techniques to select control gains to meet the requirements for stability, i.e, $\dot{V}(\mathbf{x}) \leq 0$. The incorporation of this minimisation criteria in the selection of controller gains will be addressed in the next chapter.

4.1.3 Stability analysis of system with manually-tuned controller gains

One of the purposes of this chapter was to establish the stability properties of the AAR for the manually-tuned controller gains and thus gain insights into the system behaviour. With this in mind, for the manually-tuned gains, there must be some way of analysing the stability of the AAR system where the controller gains have been manually tuned. The system behaviour has already been shown in the previous chapter and a full data set is thus available for analysis.

Examining the control effort required to maintain the receiver aircraft at a fixed separation from the tanker, an intuitive substitute of the aircraft state would be the control surface deflections $\mathbf{u}$. Whilst m serves to perturb the system from its pre-refuelling state $\mathbf{x}$, control effort is required to meet AAR requirements. The throttle deflection increases, while the elevator travel compensates first for a forward CG movement as the first two tanks fill up, while then moving aft as the second two tanks are filled.

To analyse the stability of the final system state when mass addition was completed, the simulation was extended to 600 seconds where the receiver remained on station in the vortex wake of the tanker. Figure 4.4 shows the time variation of the aircraft mass during aerial refuelling and for the extended phase from 195s to 600s whilst it remains on station in the tanker vortex wake. At the completion of fuel transfer, the aircraft mass remains constant; however, it is also necessary to examine the aircraft states and control deflections to get a complete understanding of the system behaviour.

In Figure 4.5, it can be seen that the aircraft state variables remain fixed at final values required to maintain the receiver aircraft steady and fixed in position relative to the tanker aircraft. The same trend is observed in Figure 4.6 for the control surface deflections. The aileron and rudder deflections have a small short-lived transient response once the fuel transfer is instantaneously brought to zero flow rate. However, relative pitch rate settles back towards zero and the elevator deflection has become less negative than when the simulation ended at 195s. The throttle deflection has also decreased slightly and remains fixed at this new equilibrium value till 600s. The effect of stopping fuel flow did not destabilise the aircraft, and the aircraft is able to maintain its relative position and orientation for a long period of time. It is thus evident that the aircraft state $\mathbf{x}$ and control $\mathbf{u}$ converges to a new equilibrium point after refuelling has ended.

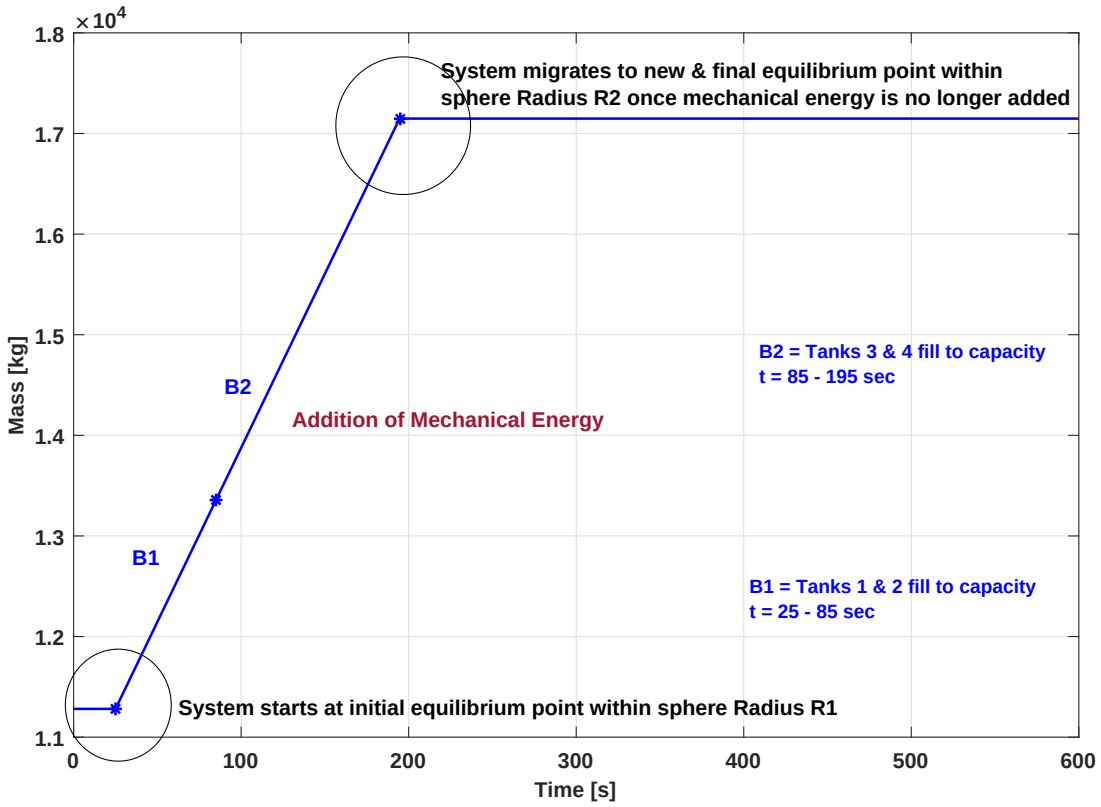


Figure 4.4: Receiver aircraft mass versus time - depiction of initial and final spherical regions according to mass profile.

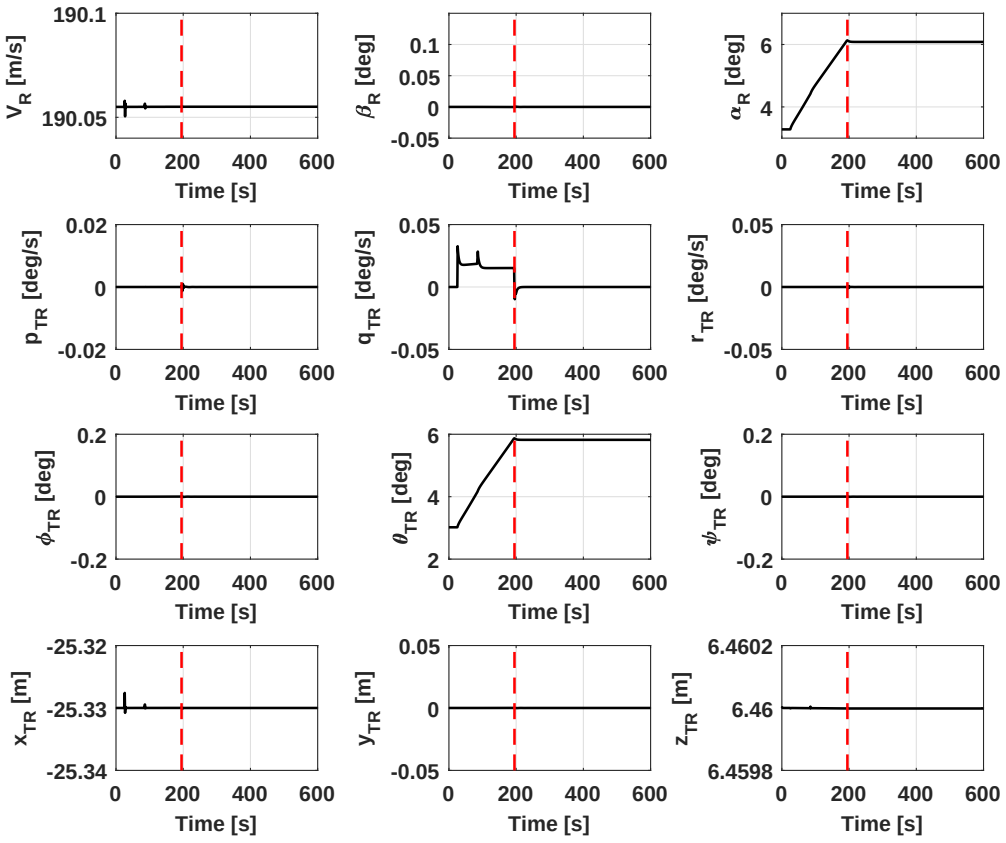


Figure 4.5: Receiver aircraft state variables versus time - Simulation extended to 600s.

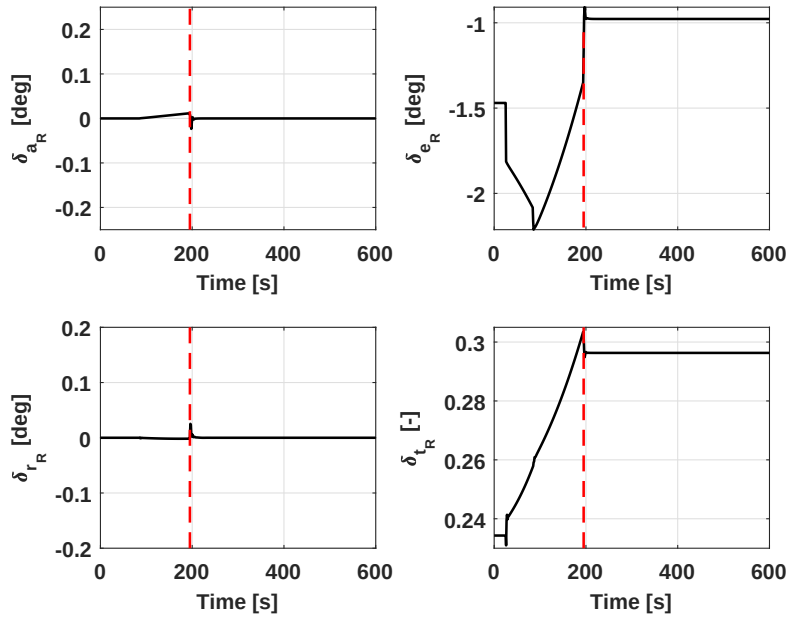


Figure 4.6: Receiver aircraft control surfaces' deflections versus time - Simulation extended to 600s.

4.1.3.1 Qualitative analysis

Using only the data generated thus far, a qualitative examination can be attempted by constructing a Lyapunov-like energy function for the period 0 - 600 sec. Let the Lyapunov-like energy function E be defined as:

$$E_{\triangle u} = \frac{1}{2} m \left| \triangle u \right|^2 = \frac{1}{2} \int_{t1}^{t2} \dot{m} dt \left| \triangle u \right|^2 \tag{4.11}$$

$$\triangle u = u_0 - u \tag{4.12}$$

Then, similar to the Lyapunov analysis, the derivative of the energy function is given by:

$$\frac{dE_{\triangle u}}{dt} = \frac{1}{2} \left| \triangle u \right|^2 \dot{m} + \int_{t1}^{t2} \dot{m} dt \left| \triangle \dot{u} \right| \tag{4.13}$$

Then, examining Figure 4.6 with three phases of refuelling defined in Table 4.1, it can be seen that for 0 - 25s, the system has zero mechanical energy prior to the refuelling, and the energy function derivative is also zero. When fuel is added between 25 and 195s, the system mechanical energy increases, and so too does the derivative. The mechanical energy increases since both mass and control effort away from the initial state is required during the aerial

Table 4.1: Automated aerial refuelling extended simulation and stability analysis using energy function

Time (s)	**Energy Function** E	**Derivative,** $\dot{E}$
0 - 25 s	$E = \frac{1}{2}\text{const}\,\lvert 0\rvert^2 = 0$	$\frac{dE}{dt} = \frac{1}{2}\lvert 0\rvert^2 0 + \text{const}\,\lvert 0\rvert = 0$
25 - 195 s	$E = \frac{1}{2}m\,\lvert\triangle u\rvert^2 = \uparrow$	$\frac{dE}{dt} = \frac{1}{2}\lvert\triangle u\rvert^2 \dot{m} + \dot{m}(t_2 - t_1)\,\lvert\triangle \dot{u}\rvert \neq 0 = \uparrow$
195 - 600 s	$E = \frac{1}{2}\text{const}\,\lvert\text{const}\rvert^2 > 0$	$\frac{dE}{dt} = \frac{1}{2}\lvert\text{const}\rvert^2 0 + const\,\lvert 0\rvert = 0$

refuelling manoeuvre. The derivative of the energy function must increase, since a fuel rate that increases the mass is in play. However, in the last phase (195 - 600s), the mechanical energy, though greater than zero - is now constant with the energy derivative being zero as well. The $|\triangle u|$ is fixed as no further control effort is required and the mass is fixed, giving a non-zero constant system energy. Mechanical energy is conserved since the flow rate has now disappeared and the mass remains fixed.

The developed control law with manually-tuned gains does show that once mechanical energy is added then, under the control law developed, is such that equilibrium point $\mathbf{x}$ steadily moves to another equilibrium point, where mechanical energy is conserved. The control law developed takes the equilibrium point $\mathbf{x}$ and moves it to $\mathbf{x}_1$. This means that there is a boundedness aspect as well.

4.2 Static Margin and CG Travel

The receiver aircraft has allowable CG range between $30\% - 41.45\%$ mean aerodynamic chord (MAC), with nominal CG listed as 38%. However, if the aerial refuelling manoeuvre with the given flow rate is initiated at the nominal value, then the aft limit would be exceeded. Thus, in order to meet the CG limits and static margin requirements, the starting point was at 37% MAC.

Figures 4.7 and 4.8 show the CG position variation with time and mass respectively for the extended 600s simulation. The aircraft remains within allowable limits throughout the manoeuvre.

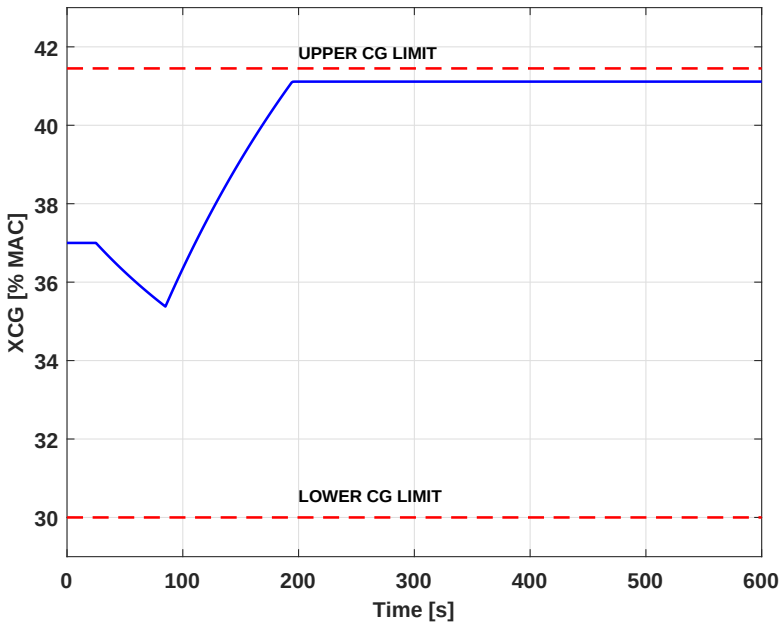


Figure 4.7: CG position versus time - extended simulation.

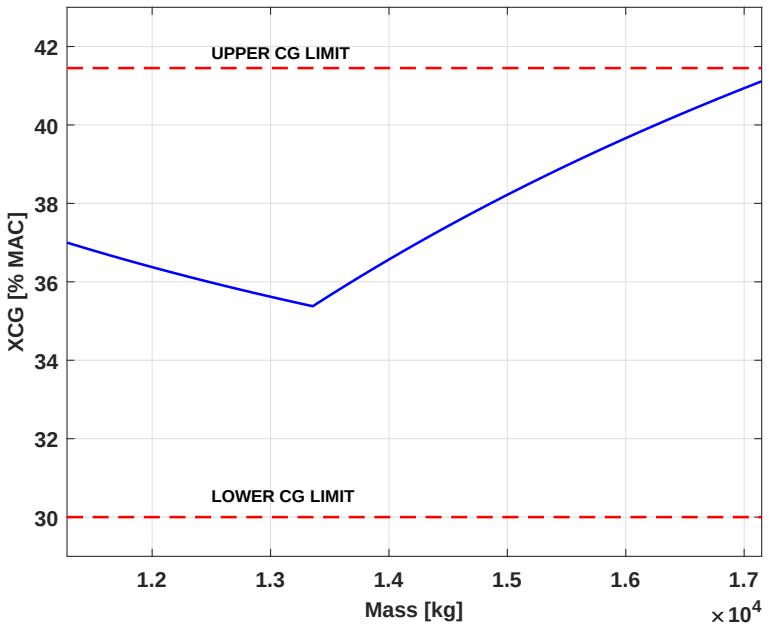


Figure 4.8: CG position versus mass - extended simulation.

4.3 Chapter Summary

Two aims were defined for this chapter: to develop a Lyapunov-based stability theorem for AAR; and to perform a stability analysis for the system controlled by manually-tuned controller gains in Chapter 3. These aims were achieved.

The fundamentals of Lyapunov stability theory was extended to the aerial refuelling system where mechanical energy of the system was increased as fuel was added to the receiver aircraft. A Lyapunov function was constructed that included the mass as a proxy for the system energy. A theorem was developed to show that as mechanical energy is added, the system states, as they move from $\mathbf{x}_0$ to $\mathbf{x}_{final}$ meet the criteria for uniform stability at the origin of each spherical region moving from radius R_0 to R_{final}. The Lyapunov function developed can now be incorporated into an optimisation routine to select the most appropriate or optimal controller gains to achieve system stability. The growth of radius R from R_0 to R_{final} is affected by the selected mass flow rate and imposes an upper limit to $\mathbf{x}_{final}$ attained at the end of fuel transfer.

The system simulation was extended from 195s to 600s to examine whether mechanical energy is conserved once fuel transfer had been completed. The receiver aircraft remained in the tanker vortex wake from 195s to 600s with zero fuel transfer rate imposed.

The results showed, that for the controller gains manually selected in Chapter 3, the receiver aircraft state and control variables did indeed remain fixed once fuel transfer was completed, maintaining its relative position and orientation to the tanker aircraft. State variables such as relative pitch attitude steadily increased as fuel was introduced into the system and remained steady once fuel transfer was completed. A complete set of data was therefore available to examine in a stability analysis.

In order to show that the manually-tuned controller developed in Chapter 3 met the conditions for stability developed in this Chapter, a Lyapunov-like energy function was constructed to analyse the data generated for the manoeuvre from 0s to 600s. Using control effort away from the initial values ($|\triangle \mathbf{u}|$) as a substitute for system state $\mathbf{x}$, a qualitative assessment of the system energy was performed which revealed that addition of mass increased the system energy and that when the fuel transfer is completed, mechanical energy of the system is increased compared to the initial state and is conserved following completion of fuel transfer. The aircraft CG variation remained within upper and lower bounds during the refuelling manoeuvre.

5 Hybrid Lyapunov-Based Swarm and Evolutionary Optimisation of PID Control for Automated Aerial Refuelling

5.1 Introduction

In Chapter 3, PID controller gains were manually tuned to give a single set of controller gains that could be applied across the different phases of the refuelling process. A generalised cost function was developed, $J = \int_0^{t_f} \left[(\mathbf{x} - \mathbf{x}_c)^T \boldsymbol{Q} (\mathbf{x} - \mathbf{x}_c) + \boldsymbol{u}^T \boldsymbol{R} \boldsymbol{u} \right] dt$, against which performance of the manually-tuned gains could be ascertained and a bounded search space could be found. In formulating the gain selection as an optimisation problem, an optimal set of PID control gains can be found within the bounded search space.

Chapter 4 analysed the stability of the manually-tuned gains qualitatively through the construction of a Lyapunov-like energy function, E. Moreover, in Chapter 4, a Lyapunov function V for the AAR system was constructed - whose derivative $\dot{V}$ can be used in a cost function to determine appropriate controller gains to meet stability requirements.

Combining $\dot{V} = 2xm\dot{x} + x^2\dot{m}$ with generalised J above, the new cost function J now becomes:

$$J = \int_0^{t_f} \left[(\mathbf{x} - \mathbf{x}_c)^T \boldsymbol{Q} (\mathbf{x} - \mathbf{x}_c) + \boldsymbol{u}^T \boldsymbol{R} \boldsymbol{u} \right] + \left[2\mathbf{x}^T m\dot{\mathbf{x}} + \mathbf{x}^T \dot{m}\mathbf{x} \right] dt \tag{5.1}$$

Minimising Eq. 5.1 will lead to the selection of optimal controller gains that ensure system stability, with $J \longrightarrow$ constant value K_J as $t \longrightarrow t_f$ and $\dot{J}$ being driven to $K_j \leq 0$ as $t \longrightarrow t_f$.

The controller block diagram in Figure 5.1, similar to that given earlier in Chapter 3 is now updated to reflect use of the optimisation routine to compute the controller gains.

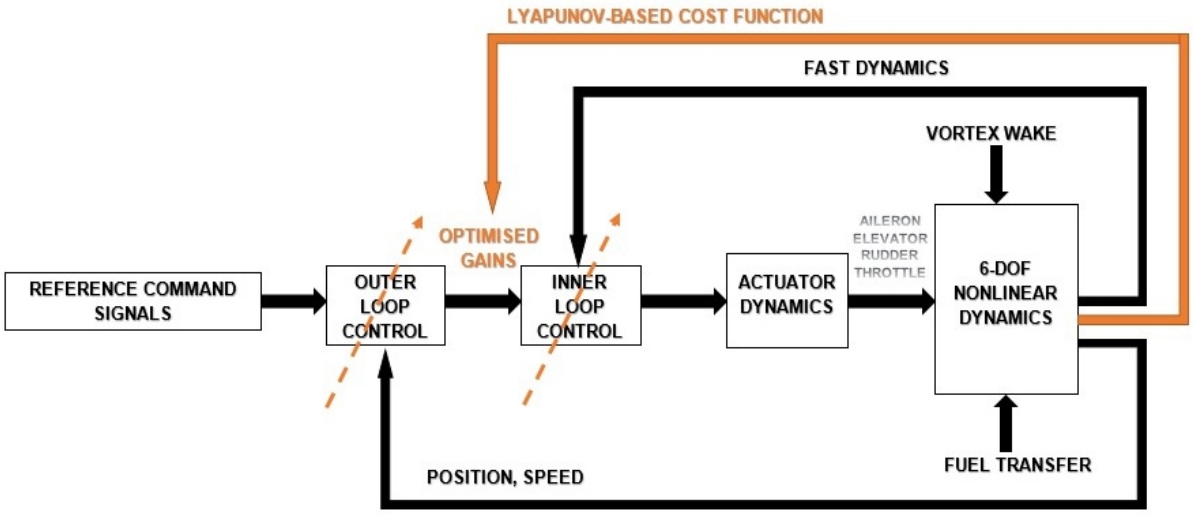


Figure 5.1: Controller block diagram incorporating Lyapunov-based optimisation algorithm

The rationale for adopting global optimisation techniques for tuning controller parameters is outlined in section 5.2. The particle swarm and genetic algorithm methods are detailed in sections 5.3 and 5.4 respectively. The parameters required to be set and initialised are given in section 5.5. The optimised controller gains are presented in section 5.6, along with some results that revealed the presence of an energy threshold that affects system stability. In section 5.7, an extension of the stability analysis is presented, leading to its application in the AAR system under optimisation in section 5.8. The dynamic simulation of aerial refuelling is presented for the baseline and disturbance cases in section 5.9.

5.2 Tuning of Controller Parameters using Global Optimisation Techniques

When systems are characterised by nonlinear and time varying behaviour, biologically-inspired heuristic algorithms can be used to tune PID parameters to meet performance specifications (e.g., good setpoint tracking and disturbance rejection (Jayachitra and Vinodha (2014))). Gradient-free optimisation techniques inspired by naturally occurring phenomena have gained popularity over traditional optimisation algorithms (Venter and Sobieszczanski-Sobieski (2003), Rezaee Jordehi and Jasni (2013)). Some of the categories of these techniques include: stochastic, evolutionary, physical, probabilistic, swarm, immune and neural (Sindhuja et al., (2018)).

Amongst these, PSO, classified under a family of techniques known as swarm intelligence, has proven its simplicity to implement and has been used in PID control design for nonlinear systems (Chang and Shih (2010), Mavrovouniotis et al., (2017)). Advantages offered by

swarm intelligence and PSO in particular, when compared to traditional algorithms (non-heuristic, gradient-based) can be summarised as follows: fewer parameters to be tuned, high accuracy with a comparatively lower computational expense, less sensitive to dimensionality issue, and easier incorporation of constraints and multiple objectives into the algorithm. At the same time, evolutionary algorithms such as the genetic algorithm (GA) offer similar advantages such as: derivative information not required, can handle a large number of variables, complex cost surfaces can be developed for optimisation (Haupt and Haupt (2004)).

The PSO and GA techniques were thus selected in the present study to answer the question: "*Can a single set of PID controller gains be found by using computational intelligence methods applied directly to the nonlinear system, that would meet all stipulated performance specifications and stability requirements during the refuelling manoeuvre?*"

5.3 Particle Swarm Optimisation

PSO is a global optimisation technique that was inspired by the social behaviour of birds and fish. This technique draws on the collective behaviours of such biological agents that interact together within their environment, and from which global behaviour patterns begins to define their interaction. When applied to an n-dimensional optimisation problem, i.e., there are n variables to optimise, the very same local and global behaviour patterns can be described mathematically in a manner that iteratively leads towards a global convergent solution (Mavrovouniotis et al., (2017), Lynn et al., (2018), Dangor et al., (2014)).

A swarm of N particles that are candidate solutions for every n is defined, $S = \{\mathbf{x_0}, \mathbf{x_1}, \mathbf{x_2}, \ldots, \mathbf{x_N}\}$. Each one of these particles has a position (Eq. 5.2) and a velocity (Eq. 5.3):

$$\mathbf{x_i} = [x_{i,1}, x_{i,2}, ..., x_{i,n}] \in \mathbb{R}^n \tag{5.2}$$

$$\mathbf{v_i} = [\mathrm{V}_{i,1}, \mathrm{v}_{i,2}, ..., \mathrm{v}_{i,n}] \in \mathbb{R}^n \tag{5.3}$$

The aim is to find the best position of the particle and the best position of the swarm iteratively over a number of iterations, N_{Iter}. This is done by defining a fitness function (i.e., J) to compare the best positions yielded by the particular set of candidate solutions of n in N. Once this is ascertained, the particle's personal best solution, including position ($\mathbf{P}_{best}$) is stored and the swarm's best solution ($\mathbf{G}_{best}$) is similarly stored. The solution progresses

to convergence after checking that the current solution is fitter than the previous and then adjusting its trajectory accordingly with the velocity and position updating algorithms given as:

$$\begin{aligned}\mathbf{V}(t+1) =& w_1\mathbf{V}(t) + w_2 rand1(1,N)(\mathbf{P}_{best} - \mathbf{x}(t)) \\ &+ w_3 rand2(1,N)(\mathbf{G}_{best} - \mathbf{x}(t))\end{aligned} \tag{5.4}$$

$$\mathbf{x}(t+1) = \mathbf{x}(t) + \mathbf{V}(t+1) \in \mathbb{R}^n \tag{5.5}$$

The updating algorithms are dependent on the previous position ($\mathbf{x}$) and velocity ($\mathbf{V}$) vectors as well as on the local best ($\mathbf{P}_{best}$) and global best ($\mathbf{G}_{best}$) candidates. Here, t refers to the previous iteration and $t+1$ to the next iteration. Weightings can be selected to favour local convergence or global convergence through the terms $(\mathbf{P}_{best} - \mathbf{x}(t))$ and $(\mathbf{G}_{best} - \mathbf{x}(t))$ respectively. The previous iteration velocity is weighted by w_1, limiting or enhancing the effect of the previous velocity on the new computed velocity. w_2 is the social weighting on the effect of the local search towards the particle's new velocity, w_3 is the global weighting and controls how much the global search affects the particle's new velocity, and $rand1(1,N)$ and $rand2(1,N)$ are vectors of random numbers with a size N. These vectors allow for the local and global searches for each particle having different rates. A two-dimensional visualisation of the PSO algorithm solution structure at every generation is shown in Figure 5.2. When N swarm rows of n candidate solutions are found and the fitness J is obtained, the best performing J locally in the n-particle space and globally in the N-swarm space are compared to the previously found best solutions.

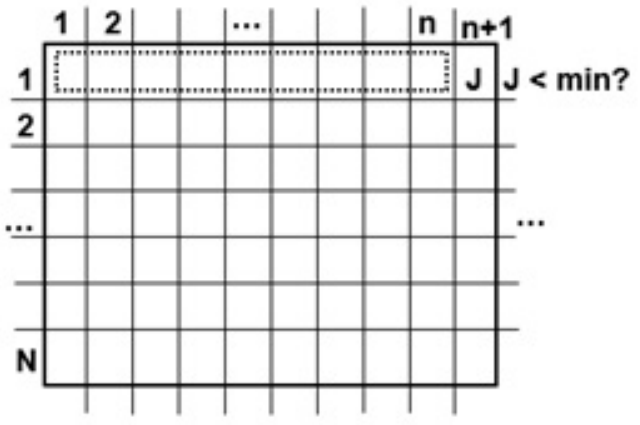


Figure 5.2: Particle swarm optimisation solution structure at every iteration.

5.4 Genetic Algorithm (GA)

The GA is an evolutionary optimisation technique based on the principles of genetics and natural selection. The algorithm allows the evolution of a population of individuals to a state where there is maximum fitness. The evolution process is underpinned by a set of selection rules which ensure the fitness objective is attained (Haupt and Haupt (2004)).

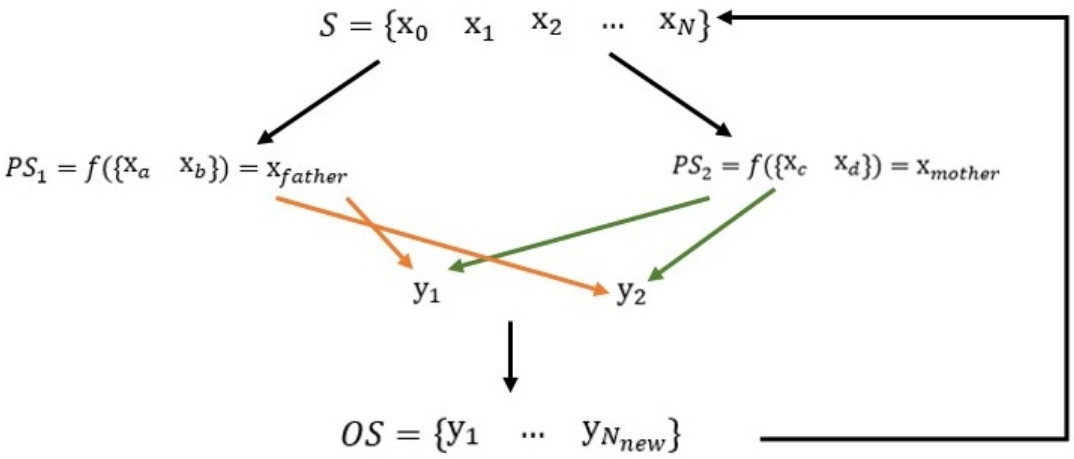


Figure 5.3: Genetic algorithm iterative methodology.

Figure 5.3 describes the GA iterative methodology. An initial population of chromosomes S is generated randomly between the upper and lower bounds, i.e., $S = \{\mathbf{x_0}, \mathbf{x_1}, \mathbf{x_2}, \ldots, \mathbf{x_N}\}$. As each evolutionary generation occurs, the dimension of S will be $N \times n$, with n being the number of variables (i.e., the number of controller gains) to be solved by the GA and N is the population size for each controller gain. Each iteration of the algorithm is termed a generation.

The cost function J for each set of gains $\mathbf{x_i}$ is calculated and the population in S is then rearranged according to lowest fitness. From chromosomes in S, candidate chromosomes called parents ($\mathbf{PS_1}$ and $\mathbf{PS_2}$) are selected and tested against superior fitness in order to obtain a pair to produce offspring $\mathbf{y}$.

The chromosome with best fitness between randomly selected $\mathbf{x_a}$ and $\mathbf{x_b}$ becomes the "father"- $\mathbf{x_{father}}$. Similarly, the "mother"($\mathbf{x_{mother}}$) is the chromosome with best fitness between randomly selected $\mathbf{x_c}$ and $\mathbf{x_d}$.

The total number of offspring chromosomes to be created is specified as $\mathbf{N_{new}}$. Once a viable father and mother are found, the selected pair then produce two offspring using the crossover

technique. Mating continues till $\mathbf{N_{new}}$ offspring are created and the offspring are collectively those defined in $OS = \{\mathbf{y_0}, \mathbf{y_1}, \mathbf{y_2}, \ldots, \mathbf{y_N}\}$. The offspring in OS are evaluated for fitness.

S's next generation is then updated, where the worst fit chromosomes in S are replaced by the offspring in OS. This process continues over the stipulated number of generations (N_{Gen}), which is the termination criterion set for the GA.

At each iteration, j, two new offspring are produced from the j^{th} father and mother pair ($\mathbf{PS_{1j}}$ and $\mathbf{PS_{2j}}$) as follows (Dangor et al., (2014)):

$$\mathbf{y}_{1j} = \mathbf{P}_{1j} rand(1, n) + \mathbf{P}_{2j}(1 - rand(1, n)) \tag{5.6}$$

$$\mathbf{y}_{2j} = \mathbf{P}_{1j}(1 - rand(1, n)) + \mathbf{P}_{2j} rand(1, n) \tag{5.7}$$

$\mathbf{y}_{1j}$ and $\mathbf{y}_{2j}$ are the two new offspring that are produced as a result of mating. Once all iterations have been completed, the set of offspring $OS = \{\mathbf{y_0}, \mathbf{y_1}, \mathbf{y_2}, \ldots, \mathbf{y_N}\}$ is obtained.

Figure 5.4 is a two-dimensional mapping of the process outlined above.

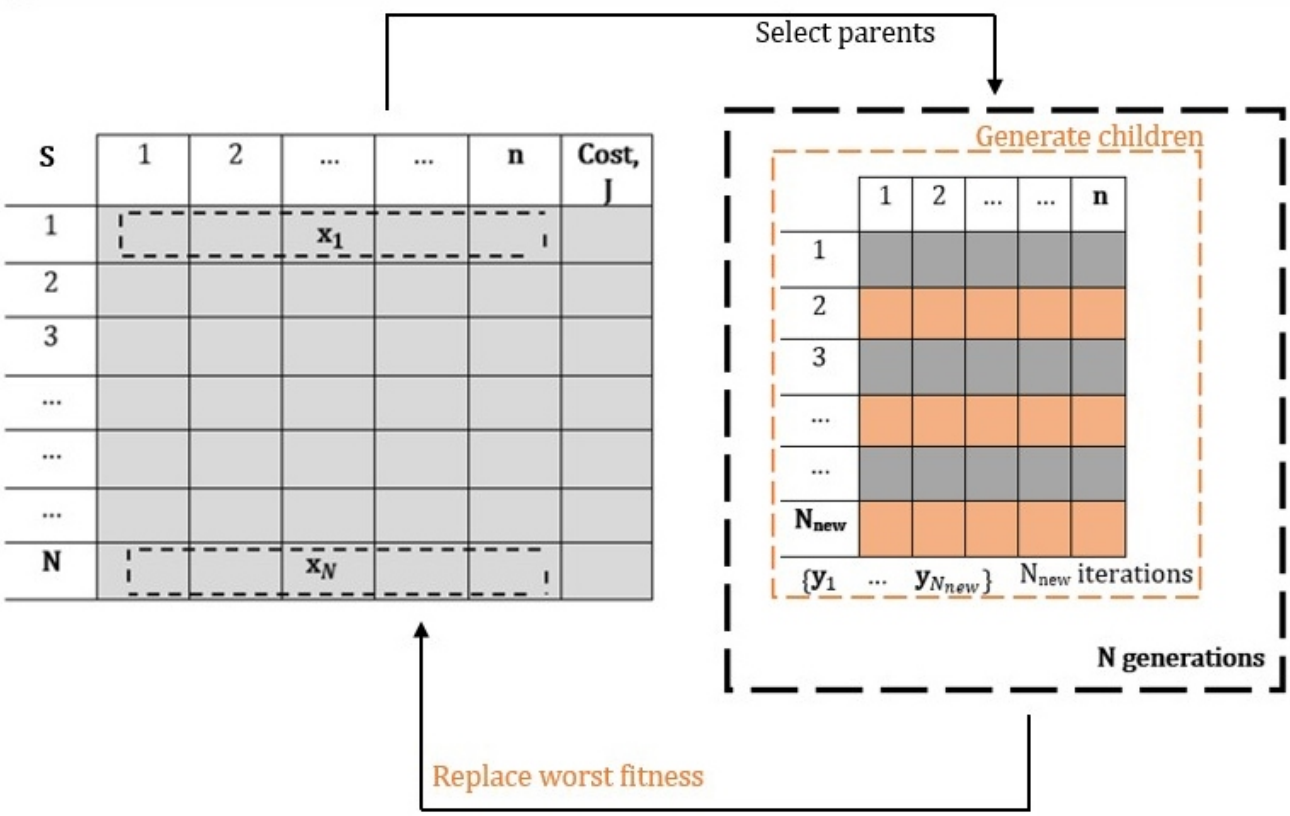


Figure 5.4: Two-dimensional mapping of genetic algorithm solution structure.

5.5 Optimisation Parameters and Initialisation

One of the drawbacks of GA is the increase in computational time due to the large population of solutions generated (Haupt and Haupt (2004)). Some also measure the performance of the GA against the number of fitness function evaluations. Function calls can be classified expensive if certain tasks are required at each generation. Kramer (2017) also highlights a challenge found in the AAR control problem in Chapter 3: the simulation model has to be run to completion to evaluate the GA generated parameters - requiring the fitness function evaluation to take a long time to execute. These drawbacks are equally applicable to the PSO algorithm as well. For the controller gain optimisation, the AAR simulation is extended to 600 s, in line with Theorem 4.1 developed in Chapter 4.

To demonstrate the above challenges through simulation, the PSO algorithm was run with large and small iterations and swarm size to analyse the trend in respect of loss of accuracy and computational time. Table 5.1 summarises the outcome of three runs. The most computationally intense was with 150 iterations and swarm size of 50. The run-time was 15.3 hours. A lean case - 15 iterations with a swarm size of 5 - gave the lowest run-time: 2 minutes, with only a 1.82% deviation from the cost function attained in the most rigorous case. A middle option of 50 iterations with swarm size of 15 gave cost function deviation of 0.35% compared to the first run with 150 iterations.

Table 5.1: Comparison of iteration size and computational time - PSO algorithm

Iterations	**Swarm Size**	**Cost, J**	**Computational Time**	**J Deviation**
150	50	2.61332E+08	15.3 hours	0.000%
50	15	2.60420E+08	39 minutes	-0.349%
15	5	2.56570E+08	2 minutes	-1.822%

The process of manual tuning yielded a bounded search space inside which an optimal set of controller gains could be found. Manual tuning also gave qualitative insights into stability of the system through the sensitivity of particular controller gains being within a certain range of values (e.g., positive or negative). The simulation results in Table 5.1 used the manual-tuned gains as the initial guess and the algorithm search for a solution set within the upper and lower bounds of the search space. It is therefore not surprising that the smaller swarm/iteration runs delivered a potential set of controller gains within 2% deviation from the 150 iteration case.

Stability Theorem 4.1 requires that for an aerial refuelling system starting at a particular equilibrium point prior to fuel transfer, the equilibrium point must steadily move to another equilibrium point, where mechanical energy is conserved. Cost function J is meant to provide

a set of controller gains that allows the system to satisfy Theorem 4.1. If the algorithm were to search from $-\infty$ to $+\infty$, it would be too computationally expensive and would not reflect the established limits of gains in relation to performance and stability. The bounds of the search space allows for reducing the intensity of the search parameters, while still attaining minimal computation expense, improved execution speed and the prevention of early convergence of the algorithm.

Table 5.2: Parameters used in swarm and evolutionary algorithms

Simulation and Optimisation Parameters	**Value**
Number of Controller Gains, n	23
Q, **R** matrices	**I**
PSO Swarm Size, N	50
PSO Parameter w_1	0.5
PSO Parameter w_2	2
PSO Parameter w_3	2
Number of PSO Iterations, N_{Iter}	150
GA Chromosome Population Size, N	50
Number of GA Offpring Chromosomes, N_{new}	20
Number of GA Generations N_{Gen}	150
Extended AAR Simulation Time, t_f	600s

5.6 Computed Controller Gains and Initial Results

Table 5.3 lists the controller gains obtained by the PSO and GA routines with the manually-tuned gains as the initial guess/starting point. Also included is the optimisation cost function. The final cost function for the PSO-tuned gains is less than that of the GA-tuned gains. The evolution of the cost function, J, with generation is shown in Figure 5.5 and the evolution of the controller gains as iterations/generations advance is shown in Figures 5.5 to Figure 5.10. The trend is the same for all the 23 controller gains over 150 generations. The GA converges within 20 generations, whereas the PSO converges at around 45 iterations.

The PSO- and GA-tuned controller gains were applied to the nonlinear system in the baseline case, where no disturbances were considered. In Figure 5.11, the cost function and its derivative are shown over the duration of the refuelling manoeuvre including the extension to 600s while the receiver aircraft remains on station. It can be seen that the cost function of the system under the PSO- and GA-optimised gains is reduced compared to that of the manually-tuned gains. Also, the cost function derivative shows a step increase when refuelling is initiated and a step decrease when refuelling has ended and the receiver remains on station.

Table 5.3: Controller gains and bounds - PID controller

Gain	**Manually-tuned**	**PSO-Optimised**	**GA-Optimised**	**Lower Bound**	**Upper Bound**
Ke_θ	-3.4	-0.964	-4.059	-10	0
$Ke_{\theta I}$	1.26	6.329	4.205	0	10
Ke_q	7.5	2.252	7.493	0	10
Ka_ϕ	120	62.120	122.423	0	200
Ka_p	10	4.970	8.034	0	20
Kr_ψ	400	332.947	253.909	0	400
Kr_r	-50	-26.898	-12.452	-100	0
Kr_ϕ	-250	-239.212	-42.443	-300	0
Ke_z	-400	-283.718	-253.178	-420	-213
Ke_{zI}	-540	-503.627	-471.860	-600	-440
$Ke_{\dot{z}}$	5	1.335	1.413	0	5
Kt_V	-12	-6.169	-7.291	-14	-2
Kt_{VI}	0	-0.805	3.746	-3	5
$Kt_{\dot{V}}$	0	0.304	-0.154	-2	1
Kt_x	75	32.660	56.572	0	100
Kt_{xI}	18	24.950	15.651	0	25
$Kt_{\dot{x}}$	12	15.664	3.229	0	20
$Ka_{\dot{y}}$	-10	-3.614	-6.004	-10	-2
$Kr_{\dot{y}}$	1	6.183	6.908	0	10
Ka_y	-10	5.178	0.123	-10	10
Kr_y	1	3.824	2.426	-10	10
Ka_{yI}	-10	-0.194	-2.525	-10	10
Kr_{yI}	1	4.332	4.966	-10	10
Cost, J	2.160E+08	1.817E+08	1.772E+08		

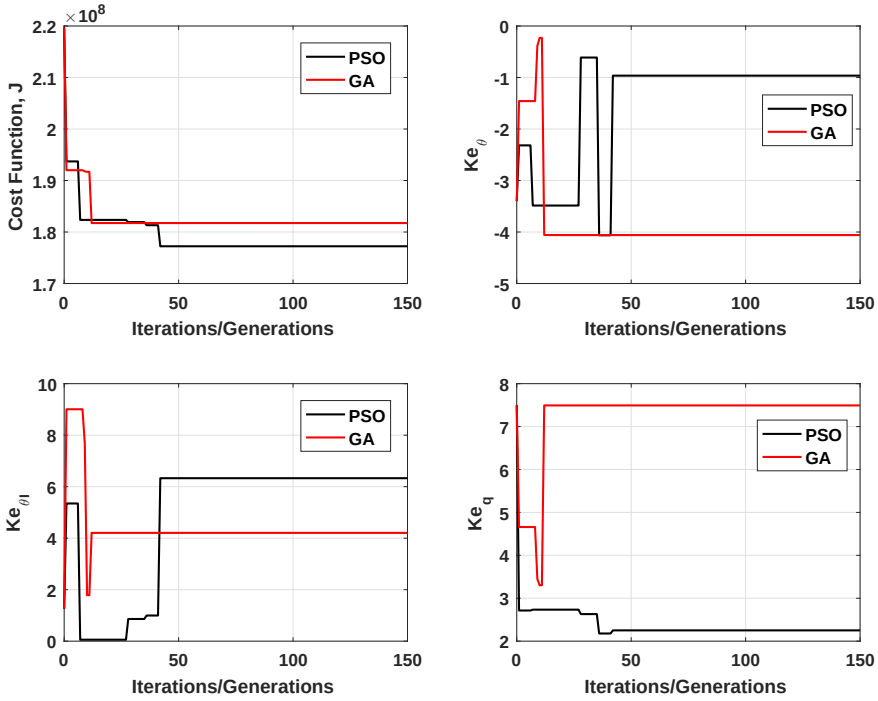


Figure 5.5: Evolution of particle swarm optimisation and genetic algorithms' cost functions, Ke_θ, $Ke_{\theta I}$ and Ke_q gains.

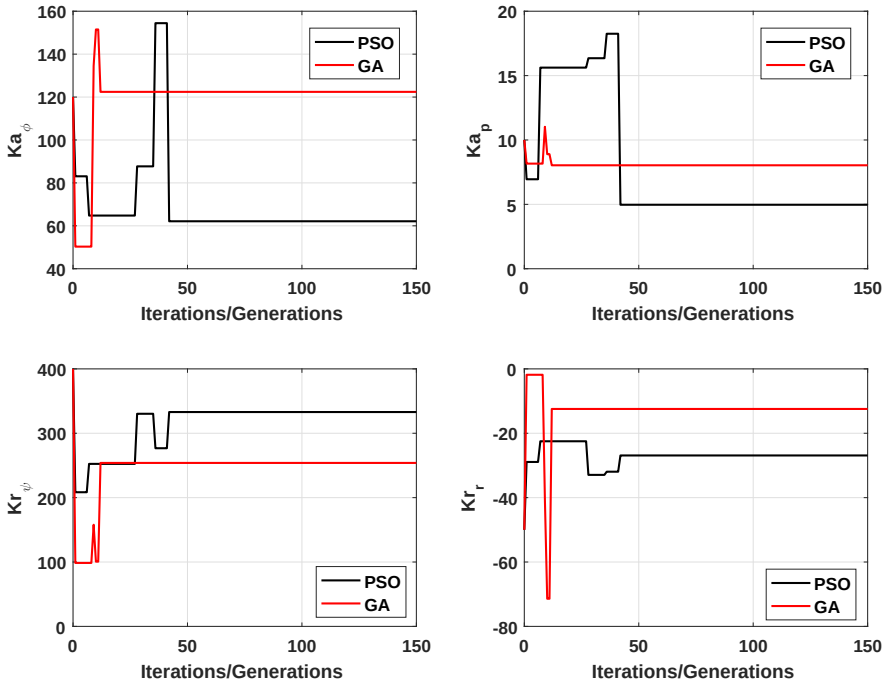


Figure 5.6: Evolution of Ka_ϕ, Ka_p, Kr_ψ and Kr_r gains in particle swarm optimisation and genetic algorithms.

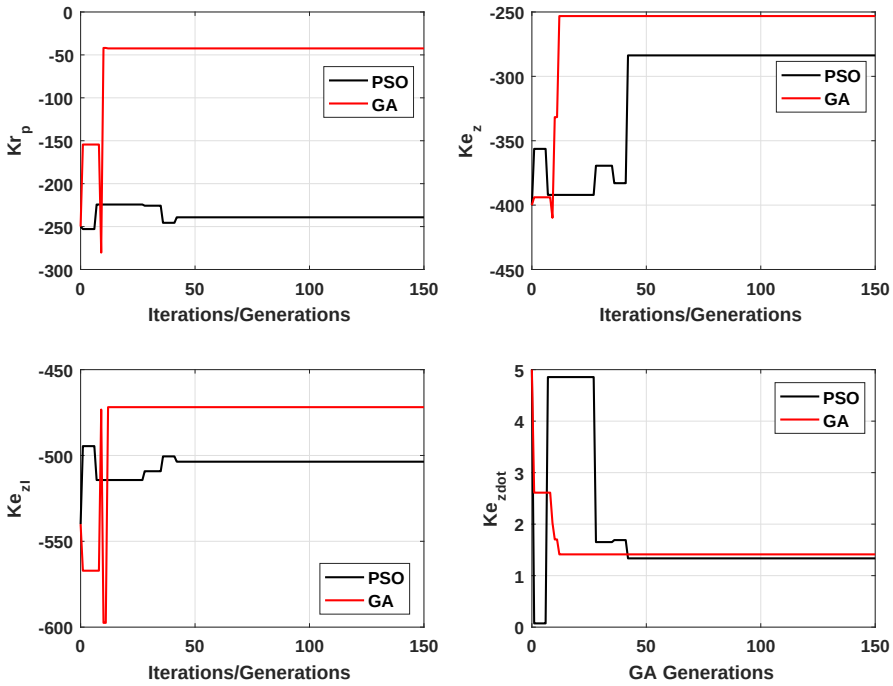


Figure 5.7: Evolution of Kr_p, Ke_z, Ke_{zI} and $Ke_{\dot{z}}$ gains in particle swarm optimisation and genetic algorithms.

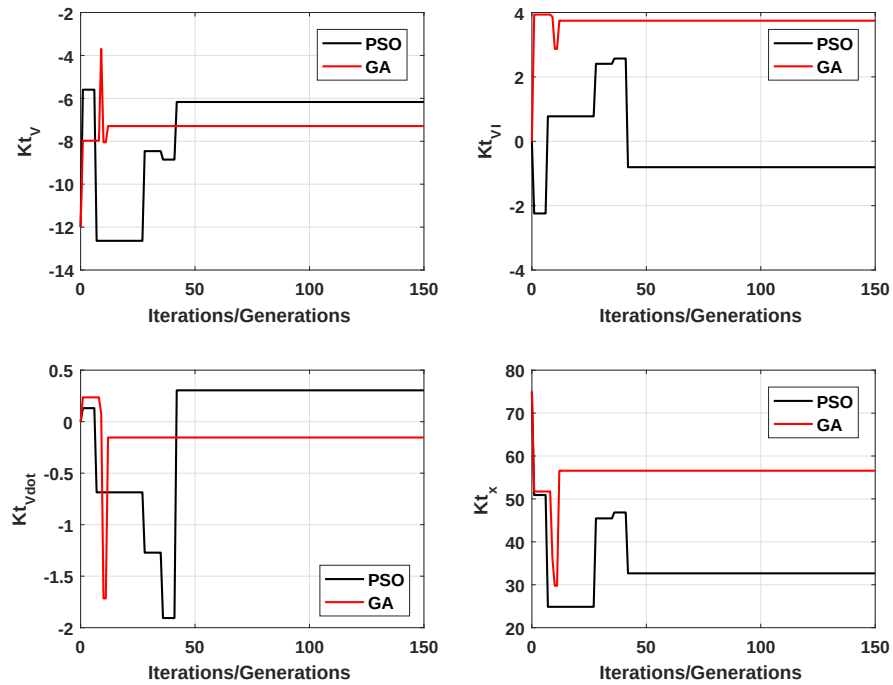


Figure 5.8: Evolution of Kt_V, Kt_{VI} and $Kt_{\dot{v}}$ and Kt_x gains in particle swarm optimisation and genetic algorithms.

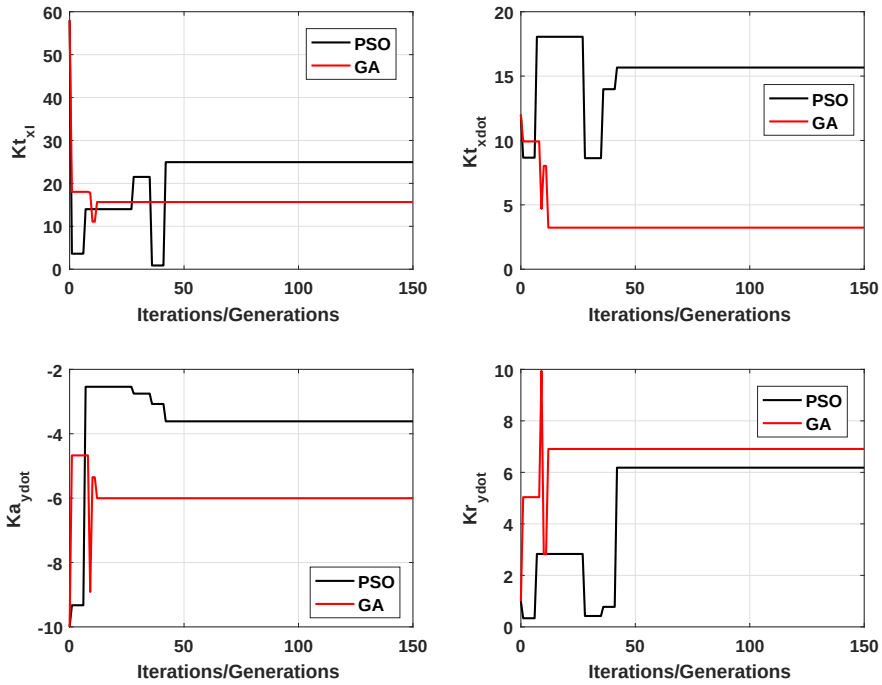


Figure 5.9: Evolution of Kt_{xI}, $Kt_{\dot{x}}$, $Ka_{\dot{y}}$ and $Kr_{\dot{y}}$ gains in particle swarm optimisation and genetic algorithms.

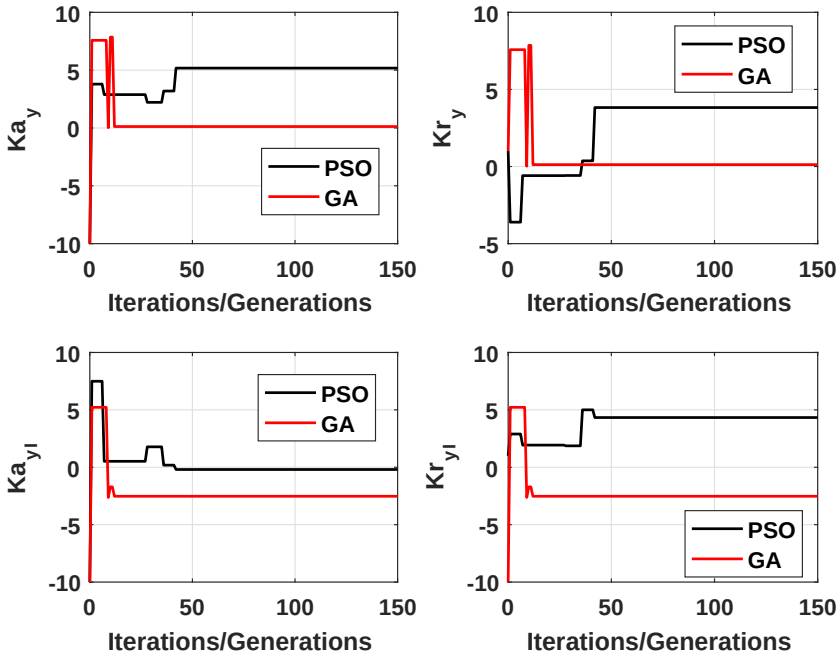


Figure 5.10: Evolution of Ka_y, Kr_y, Ka_{yI} and Kr_{yI} gains in particle swarm optimisation and genetic algorithms.

The cost function derivative is driven to zero in the phases where no fuel is transferred (1s to 25s and 196s to 600s). The state and control variables time histories are shown in Figures 5.12 to 5.14. The system, when run with the PSO-tuned controller gains applied showed that the lateral-directional performance diminished compared to the manually-tuned case. This occurred at the instance that the aft fuel tanks began refuelling. Also, the trend in z-separation, showed that a steady-state error had developed. The deviation in z-separation for the PSO algorithm was -0.00005m, or 50 microns. In order to determine the significance of this numerical value, the degree of accuracy required for the aerial refuelling manoeuvre and the sensor capabilities must be considered. Differential GPS and vision-based sensor systems are able to provide accuracy within centimetres in position estimation and 0.25 deg in angular orientation in order to guarantee successful boom docking (Bowers (2005), Johnson et al. (2017)). The z-separation was therefore well within acceptable limits throughout the manoeuvre, even though the trend seemed to indicate a steady state-error. The GA-tuned controller gains introduced a short transient in the longitudinal state variables such as the airspeeds and x-separation.

The disturbance profiles defined in Table 3.5 and Figure 3.13 were applied to the system using the PSO- and GA-optimised gains. The PSO- and GA-optimised controller gains were not able to provide sufficient control for both the disturbance cases. While it is known that the PID controller has limitations, including issues of robustness, the poor performance here cannot merely be attributed to the use of the PID controller. It is expected that optimised controller gains perform better than manually-tuned gains. Thus a deeper examination is warranted given the complexity of the system under control.

From Figures 5.11 to 5.14, it was seen that the optimisation algorithms had the effect of minimising the system cost through J, state variables (such as angle of attack, pitch orientation) and control variables (elevator and throttle deflections). However, in all instances, the same amount of mass has been introduced into the system. As the stability problem has been addressed by considering the addition of mechanical energy into the system, the effect of the optimisation has been a reduction in the overall system energy, as the state variables are accounted for in both the Lyapunov function and the cost function J.

As robustness is an important consideration in controller design, the results obtained here shows that the optimisation algorithm may minimise the system energy or cost, J, to a such a point, that the system trajectories under disturbances may not be located within the ball of radius R defined earlier. A certain amount of system energy must be maintained under optimisation with cost function J so that stability and performance objectives are maintained. This is formally described in section 5.7.

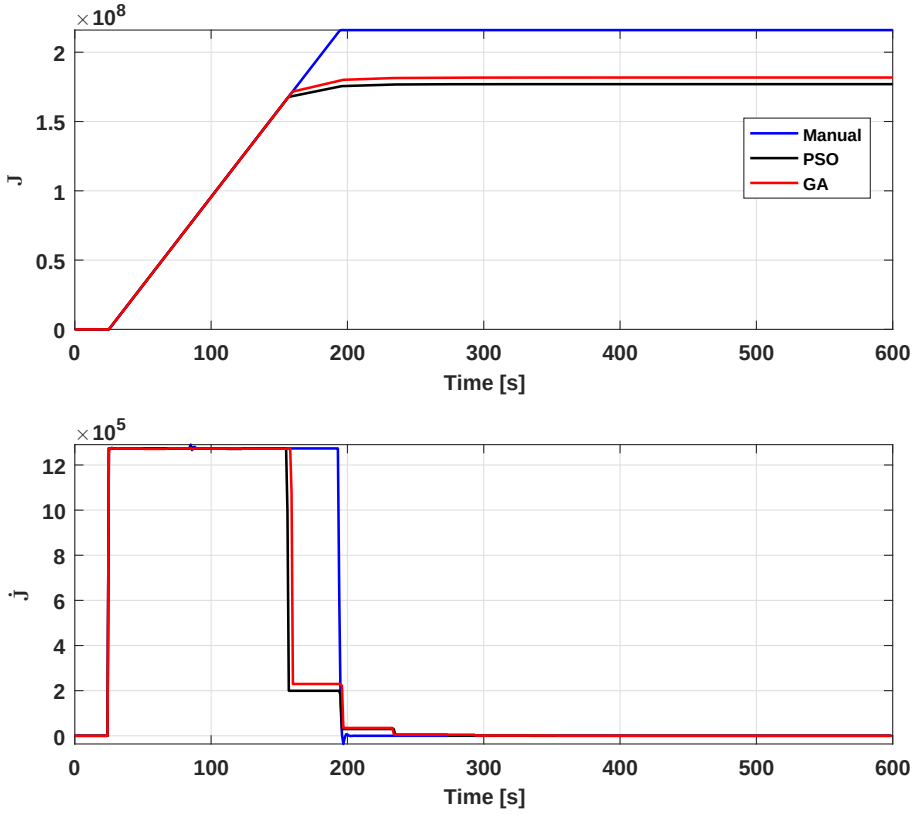


Figure 5.11: J and $\dot{J}$ versus time - baseline - manually-tuned, PSO-tuned, and GA-tuned controller gains.

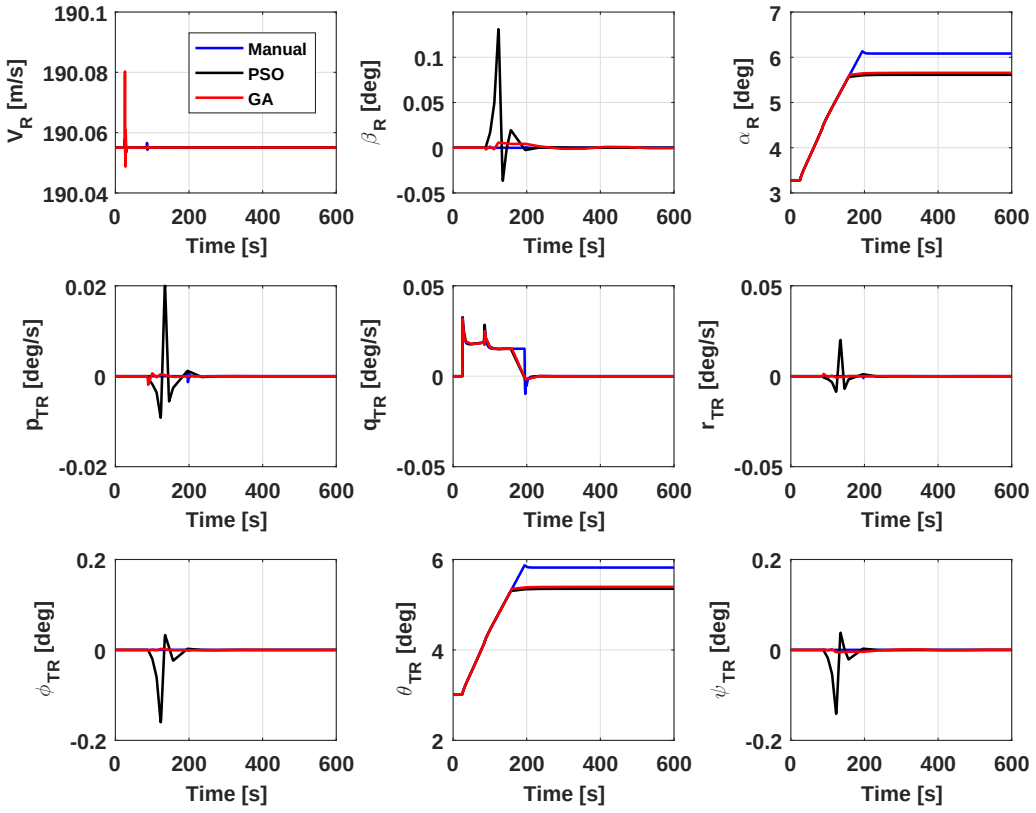


Figure 5.12: Receiver state variables versus time - baseline - manually-tuned, PSO-tuned, and GA-tuned controller gains.

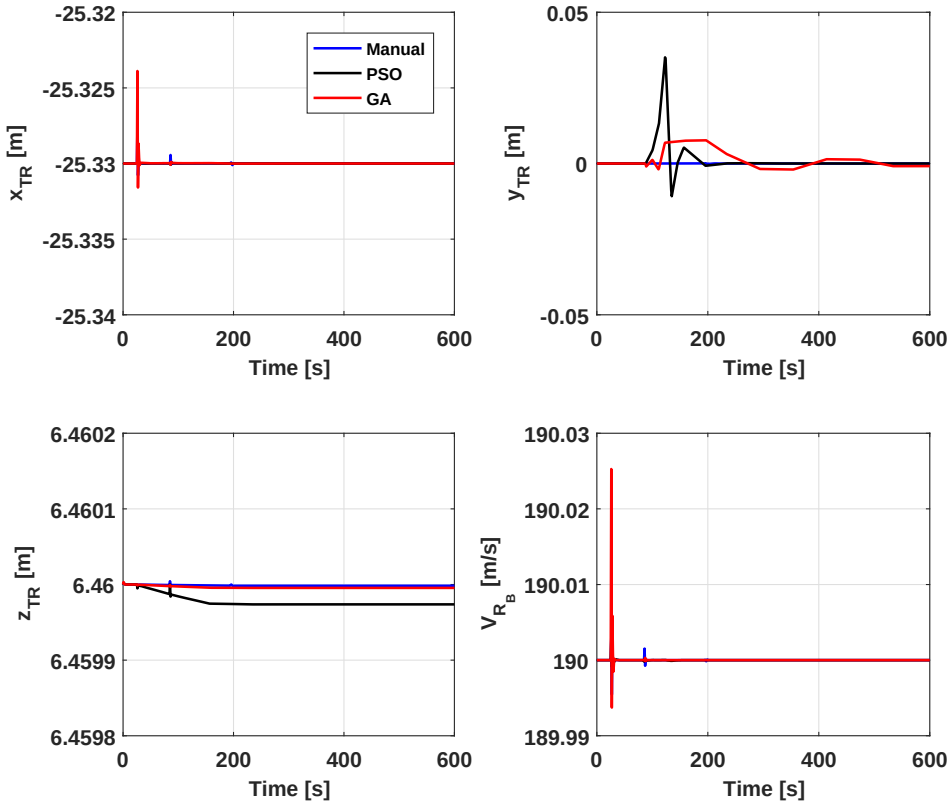


Figure 5.13: Relative separation and airspeed versus time - baseline - manually-tuned, PSO-tuned, and GA-tuned controller gains.

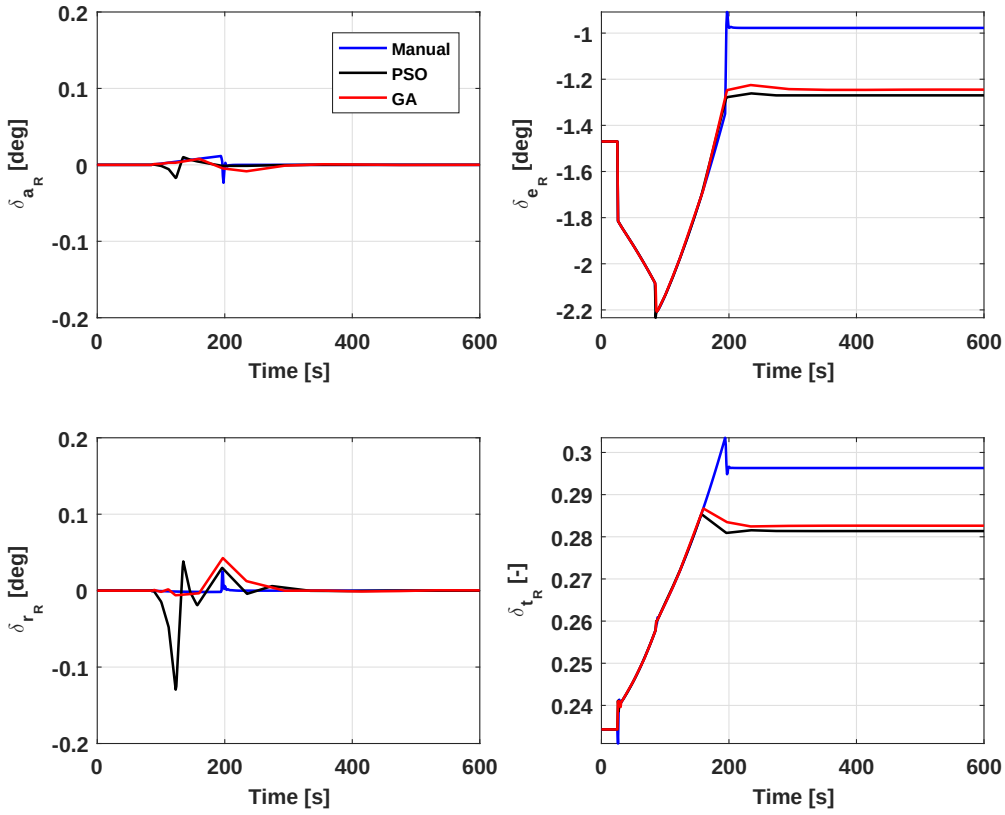


Figure 5.14: Control surfaces deflections versus time - baseline - manually-tuned, PSO-tuned, and GA-tuned controller gains.

5.7 Extension of Stability Analysis

Proposition 5.1 When controller gains are optimised using evolutionary algorithms with cost function $J = \int_0^{t_f} \left[(x - x_c)^T \boldsymbol{Q} (x - x_c) + \boldsymbol{u}^T \boldsymbol{R} \boldsymbol{u} \right] + \left[2x^T m\dot{x} + x^T \dot{m} x \right] dt$, its minimisation will lead to the selection of optimal controller gains that ensure system stability, with $J \longrightarrow$ constant value K_J as $t \longrightarrow t_f$ and $\dot{J}$ being driven to $K_j \leq 0$ as $t \longrightarrow t_f$.

However, the consequence is that the system energy represented through J, will be reduced compared to the case when gains were determined manually. Under an optimisation scheme, a minimum system energy must be available in order for stability to be maintained, and for a degree of robustness to disturbances to remain, i.e., $J_{manual} > J > J_{minimum}$

If $J < J_{minimum}$, then too much of energy would have been shed during the optimisation process, and there would be insufficient energy to maintain stable migration from system radius R_1 to R_2 as described in Chapter 4. Thus, there exists a minimum energy threshold, below which, the system becomes unstable.

Proof

Proof of this proposition is based on formulating the problem as a nominal motion problem subject to perturbation (Slotine and Weiping (1991)) or as the translation of a non-zero trajectory (Marquez (2003)). Instead of considering stability around an equilibrium point, stability is now examined from the perspective of the motion, i.e., whether a system will remain close to its original motion trajectory if slightly perturbed away from it. In the case of the AAR optimisation, the "perturbation" refers to the motion under optimisation of the control. In Figure 5.15, the nominal motion trajectory is labelled $\mathbf{x}(t)$. Thus the "perturbed" motion, i.e., the motion that results from applying the optimised controller gains would correspond to $\mathbf{x}^*(t)$.

Let $E = \mathbf{x} - \mathbf{x}_{min}$ and the corresponding Lyapunov function be represented by V_{min} where $V_{min} = m\mathbf{x}_{min}^2$. Then the Lyapunov function corresponding to the manually-tuned controller gains, V is larger than the EA-optimised Lyapunov function by a factor α. For ease of representation, $\mathbf{x}$ is written as x in the remainder of this proof.

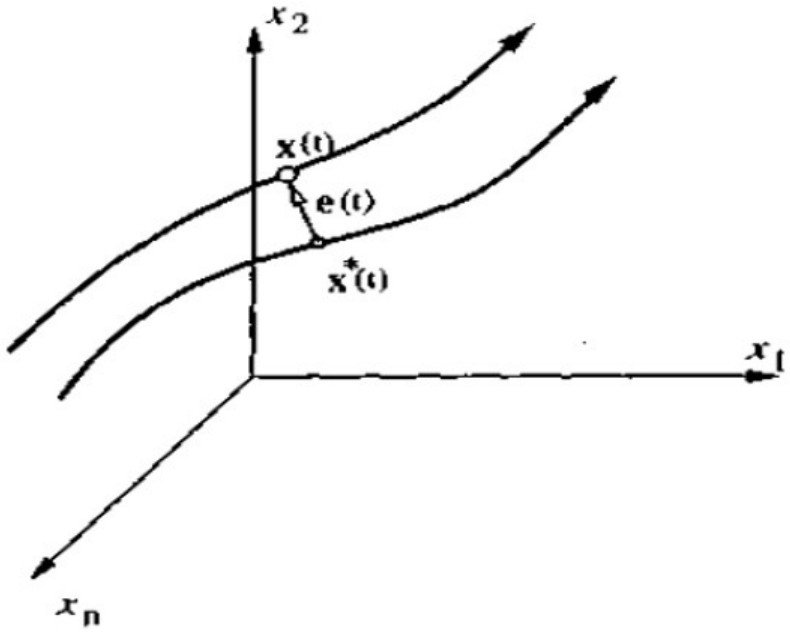


Figure 5.15: Nominal motion problem (Slotine and Weiping (1991)).

$$\alpha V_{min} = V \tag{5.8}$$

$$\alpha \left(m x_{min}^2\right) = m x^2 \tag{5.9}$$

$$\alpha \left(m \left[x - E\right]^2\right) = m x^2 \tag{5.10}$$

$$\alpha \left[x^2 - 2xE + E^2\right] = x^2 \tag{5.11}$$

$$E^2 - 2xE + (\alpha - 1)\, x^2 \tag{5.12}$$

$$E = \frac{2x \pm \sqrt{4x^2\left(1 - (\alpha - 1)\right)}}{2} \tag{5.13}$$

$$E = x\left(1 \pm \frac{\sqrt{2 - \alpha}}{2}\right) \tag{5.14}$$

It can be seen that the parameter α cannot be greater than 2 as the square root would lead to an imaginary solution. Also, the lower limit of α is 1, meaning that the motion trajectory of the manually-tuned controller gains is the same as the motion trajectory that of the optimised controller gains ($V = V_{min}$). Now let $\beta = \frac{1}{\alpha}$. Hence:

$$2 > \alpha > 1 \tag{5.15}$$

$$0.5 < \beta < 1 \tag{5.16}$$

Therefore in general, J may be optimised to upto half of the manually-tuned controller gains system cost, and there exists an optimal value of α and β within their bounds, for the AAR

system for which the stability of the motion can be maintained when subject to optimisation. ⊞

As mentioned in Chapter 4, the physical system itself imposes a maximum bound on the mechanical energy that can be introduced, however, the results in this Chapter have shown that under optimisation, there is also a lower energy bound that must not be exceeded in order for stability to be maintained, and for robustness under disturbances. While the proposition above shows that the system energy is bound by a factor of two (or half), the optimal factor (α / β) for an AAR system would need to be found using numerical parameters specific to the system, although, at this point, one can intuitively say that the minimum energy bound would be related to the addition of mass (i.e., mechanical energy) into the system. The numeric determination of the parameters α and β will also be addressed later on in this Chapter.

5.8 Application of Extended Stability Analysis to Automated Aerial Refuelling

Instead of immediately calculating the optimum values of α and β and thus ascertaining the energy limit for the system, the number of optimisation iterations/generations was first explored. The algorithms were set to run to 150 iterations/generations, which over this duration, the energy limit was crossed. In order to gain some sense of the system performance as this minimum energy threshold is reached, the number of optimisation iterations/generations was sequentially decreased from 150. It was found that when the optimisation algorithms were run for 50 iterations/generations, sufficient stability and robustness in the system was maintained.

5.8.1 Computed controller gains

Table 5.4 contains the optimised controller gains and cost function values for 50 iterations/generations. Figures 5.16 to 5.19 shows the evolution of the controller gains.

5.8.2 Numerical analysis of optimal system energy

In order to verify numerically that the new optimised J for both the PSO and GA algorithms falls within the optimal bounds for the AAR system in this study, the optimal values of α and β were determined. The values of α and β were then applied to the cost function

Table 5.4: Controller gains and bounds

Gain	**Manual-tuned**	**PSO-Optimised**	**GA-Optimised**	**Lower Bound**	**Upper Bound**
Ke_θ	-3.4	-8.9930	-4.9152	-10	0
$Ke_{\theta I}$	1.26	5.3094	5.9186	0	10
Ke_q	7.5	4.9724	7.2389	0	10
Ka_ϕ	120	40.9470	58.5098	0	200
Ka_p	10	9.9302	12.6738	0	20
Kr_ψ	400	290.4255	130.9124	0	400
Kr_r	-50	-47.5941	-45.3447	-100	0
Kr_ϕ	-250	-171.4991	-111.0784	-300	0
Ke_z	-400	-258.7967	-277.0583	-420	-213
Ke_{zI}	-540	-534.2583	-549.2263	-600	-440
$Ke_{\dot{z}}$	5	2.2188	1.7271	0	5
Kt_V	-12	-11.4055	-6.8824	-14	-2
Kt_{VI}	0	-0.2039	2.2592	-3	5
$Kt_{\dot{V}}$	0	0.8871	-1.6489	-2	1
Kt_x	75	49.8902	26.7965	0	100
Kt_{xI}	18	21.3819	17.2071	0	25
$Kt_{\dot{x}}$	12	3.9911	5.6684	0	20
$Ka_{\dot{y}}$	-10	-3.0053	-7.0828	-10	-2
$Kr_{\dot{y}}$	1	2.1416	3.1135	0	10
Ka_y	-10	6.7228	4.8993	-10	10
Kr_y	1	-1.9147	-1.1573	-10	10
Ka_{yI}	-10	4.6870	6.8385	-10	10
Kr_{yI}	1	-2.1024	-3.2072	-10	10
Cost, J	2.160E+08	2.0249e8	1.8924e8		

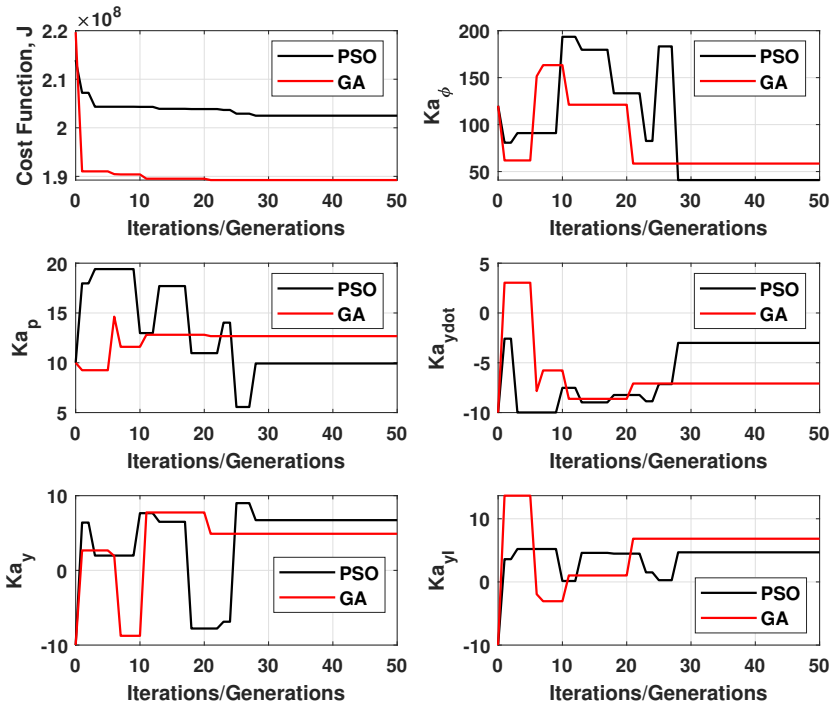


Figure 5.16: Evolution of J and K_a gains in particle swarm optimisation and genetic algorithms.

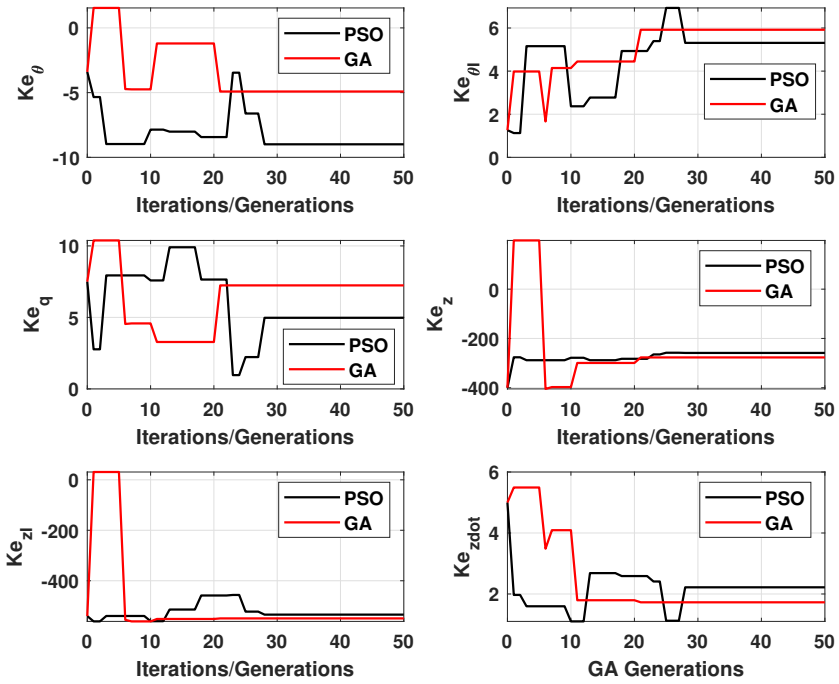


Figure 5.17: Evolution of K_e gains in particle swarm optimisation and genetic algorithms.

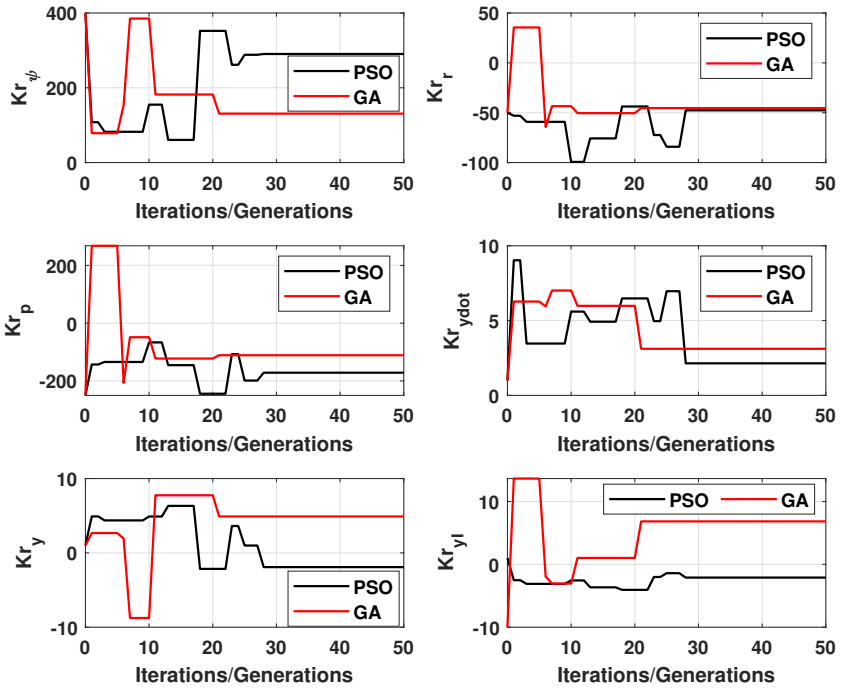


Figure 5.18: Evolution of K_r gains in particle swarm optimisation and genetic algorithms.

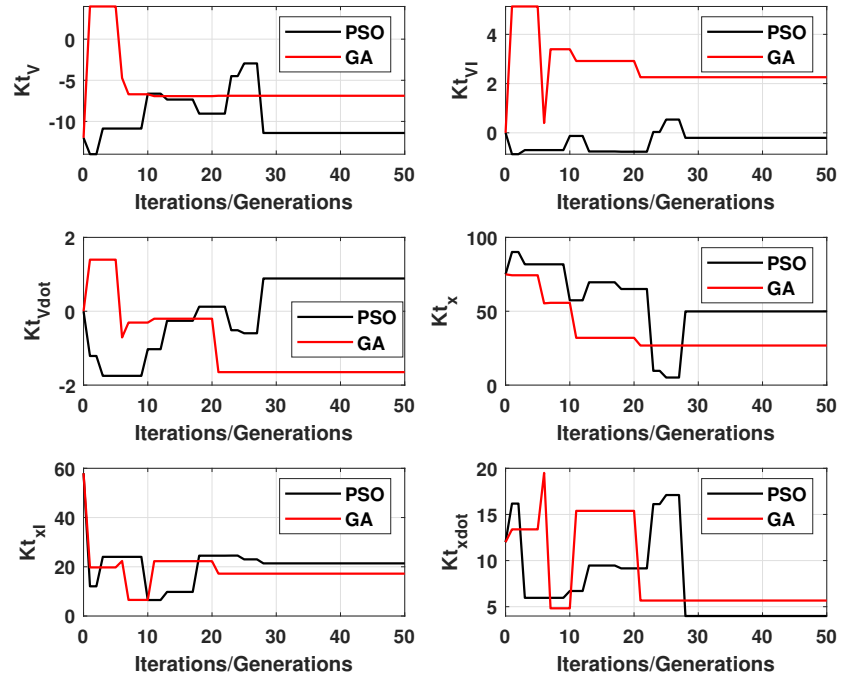


Figure 5.19: Evolution of K_t gains in particle swarm optimisation and genetic algorithms.

value obtained from manual tuning given in Table 5.4. As the Lyapunov function selected included mass as a proxy for system energy, the same principle is adopted here. The motion trajectory $\mathbf{x}_{min}(t)$ whose Lyapunov function is V_{min}, has the same mass m as the nominal or manually-tuned motion trajectory. The total energy introduced into the system is the total amount of fuel added into the fuel tank, $\triangle m$. The motion trajectory must be stable whilst $\triangle m$ is added to the baseline mass of the receiver aircraft. The minimum energy that should be maintained in the AAR system thus is related to the percentage of fuel added into the system, i.e., $\frac{\triangle m}{M}$. Hence, using β:

$$\beta = 0.5 + \frac{\triangle m}{M} \tag{5.17}$$

$$\frac{\triangle m}{M} = \frac{6046}{17327} = 0.3489 \tag{5.18}$$

Therefore, $\beta = 0.8489$ and $\alpha = 1.1780$ and the limits are as follows.

$$1.1780 > \alpha > 1 \tag{5.19}$$

$$0.8489 < \beta < 1 \tag{5.20}$$

This means that the Lyaupunov function of the optimised system should not fall below $0.8489V$, or using α, the Lyapnov function for the nominal/manually-tuned system motion should not be more than 1.1780 times greater than the optimised system motion trajectory. A numerical check can confirm that the proposition is valid for this AAR system with 6046 kg of fuel transferred to the receiver aircraft. Table 5.5 shows that when 150 iterations/generations was applied in the optimisation algorithm, the α and β parameters were out of the bounds established earlier in both the PSO and GA routines. However, when 50 iterations/generations were applied in the optimisation algorithm, then the α and β parameters were within the bounds for the AAR system under study, also for both routines. This result verifies the intuitive notion that the ratio of the added mass to the total mass plays a vital role in establishing the minimum energy that must be maintained in the system subject to minimisation with cost function $J = \int_0^{t_f} \left(\left[(x - x_c)^T \boldsymbol{Q} (x - x_c) + \boldsymbol{u}^T \boldsymbol{R} \boldsymbol{u} \right] + \left[2x^T m\dot{x} + x^T \dot{m} x \right] \right) dt$. By initially adopting an approach where the number of optimisation iterations was sequentially reduced to examine system stability manually, the maximum number of iterations/generations to provide the required stability and robustness was also established. Using this approach also allowed for the numerical verification of the notion presented in the proposition.

Table 5.5: Cost function comparisons (including α and β)

	J_{manual}	J_{PSO}	β PSO	α PSO	J_{GA}	β GA	α GA
original (150)	2.1600	1.8170	0.8412	1.1888	1.7720	0.8204	1.2190
new (50)	2.1600	2.0249	0.9375	1.0667	1.8924	0.8761	1.1414

5.9 Dynamic Simulation of Extended Aerial Refuelling

The controller gains obtained in Table 5.4 were applied to the Matlab model and the dynamic simulation results are presented below, superimposing the time trajectories of the state and control variables of the nominal system with that of the system subject to the defined disturbances. The state and control variables time domain results obtained via the PSO and GA optimisation routines are also shown side-by-side with those obtained from manually-tuned controller gains (Figures 5.20 to 5.25).

Trends discussed in Chapter 3 also manifested in the aircraft behaviour when optimised controller gains were applied and the dynamic simulation was extended to include station-keeping from 196s to 600s. The lateral-directional control variables were the most sensitive to disturbances. Turbulence introduced the transient behaviour to a greater degree than for the asymmetric refuelling scenario. The application of the PSO- and GA-optimised gains led to improved performance, where all receiver state variables were able to return to their nominal values, and effects of transient behaviours manifesting in the refuelling and/or station-keeping phases were minimised, with deviations within the limits acceptable for the refuelling manoeuvre.

The variation of the receiver aircraft mass over the refuelling and station-keeping period is shown in Figure 5.26, inclusive of the variation when the mass disturbance was applied. The variation of the receiver aircraft CG with time and mass is shown in Figures 5.27 and 5.28 for the baseline and mass disturbance cases. Fuel tank centroid and mass variations for the AAR manoeuvre are given in Figures 5.29 and 5.30. The CG limits are not exceeded. The tanker aircraft state variables and control surfaces' deflections (Figures 5.31 to 5.33) are shown for its nominal motion and the turbulence disturbance. The tanker is brought back to its nominal state after being subjected to a turbulence disturbance.

5.10 Chapter Summary

This chapter focused on the optimisation of manually-tuned controller gains using particle swarm optimisation and genetic algorithms. The stability criterion was incorporated into the

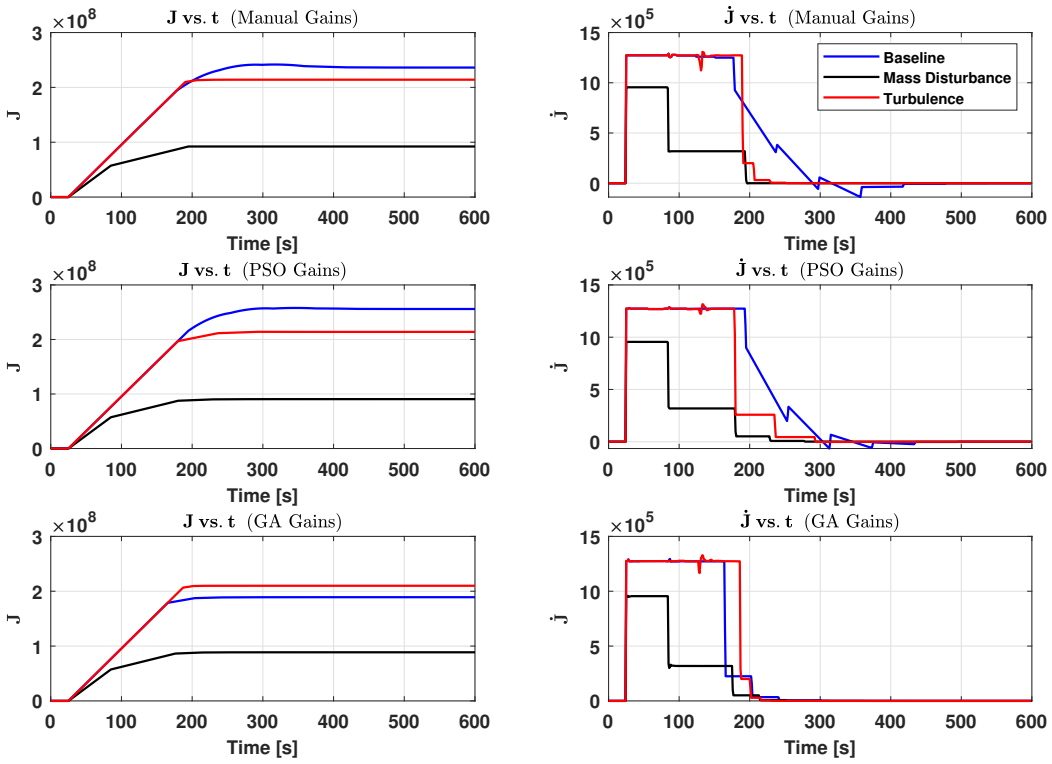


Figure 5.20: J and $\dot{J}$ versus time - baseline + disturbances - manual-, PSO-, and GA-tuned controller gains.

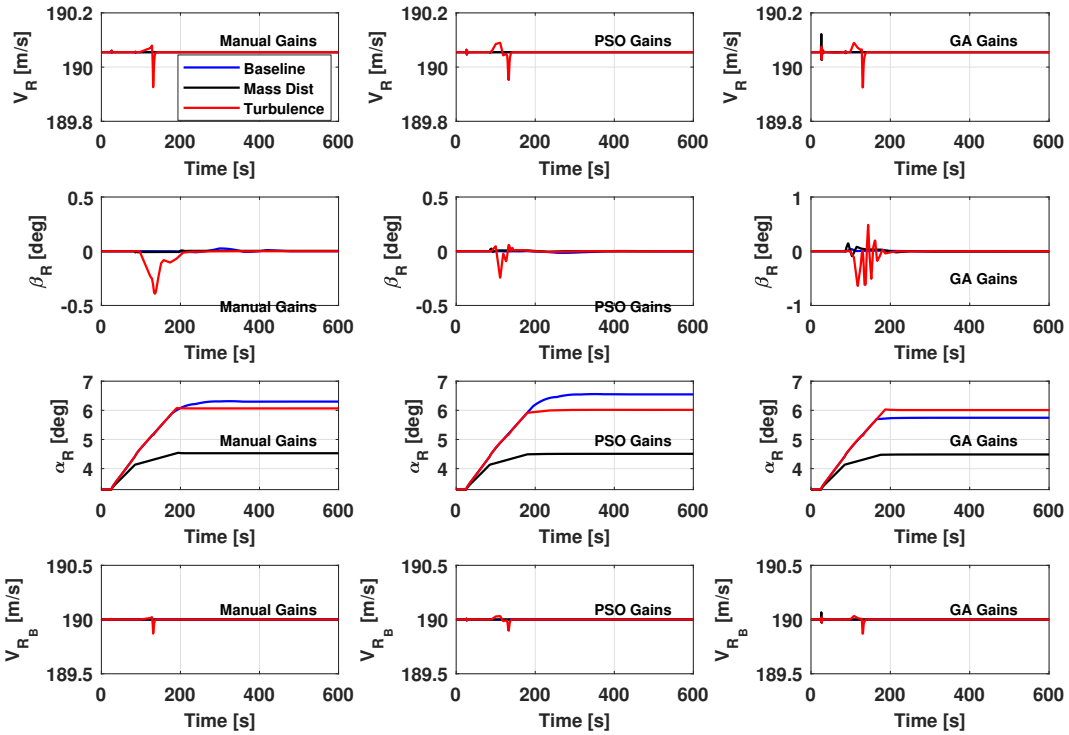


Figure 5.21: Airspeeds and aerodynamic angles - baseline + disturbances - manual-, PSO-, and GA-tuned controller gains.

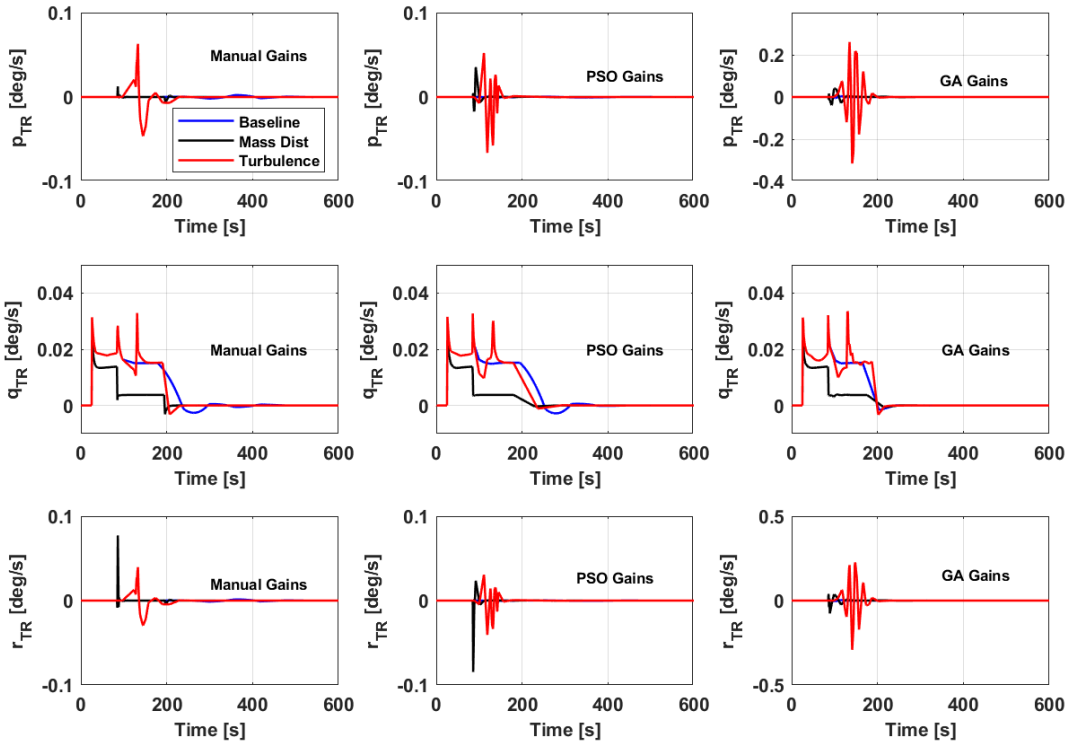


Figure 5.22: Receiver aircraft body rates relative to tanker versus time - baseline + disturbances - manual-, PSO-, and GA-tuned controller gains.

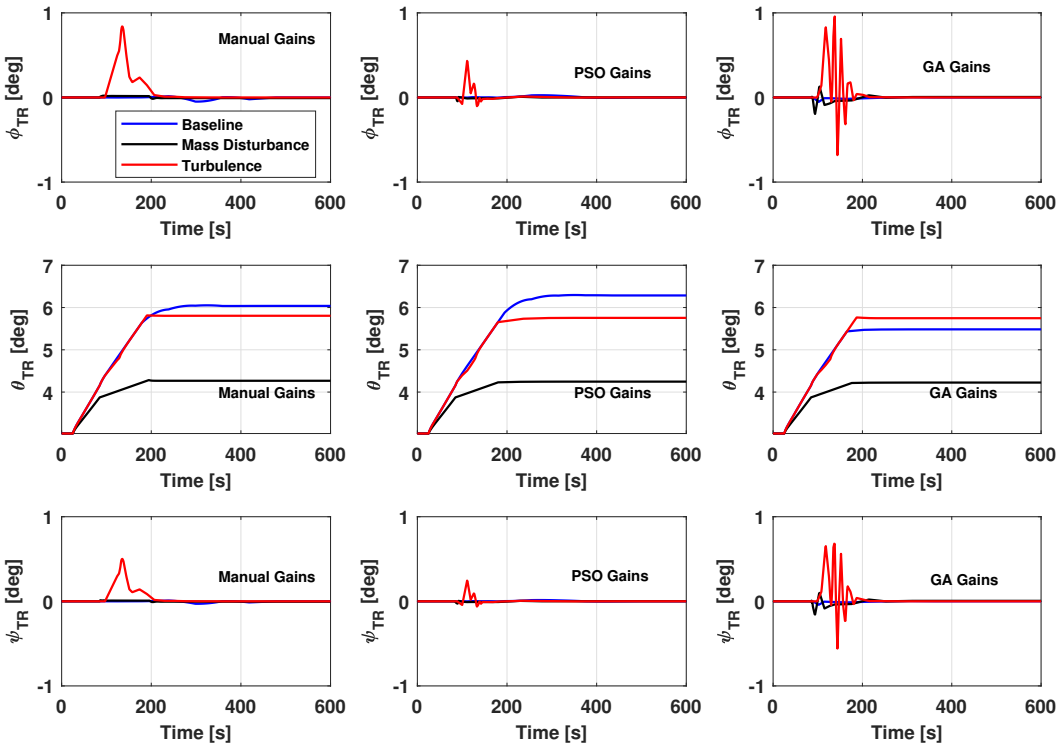


Figure 5.23: Receiver aircraft relative Euler angles versus time - baseline + disturbances - manual-, PSO-, and GA-tuned controller gains.

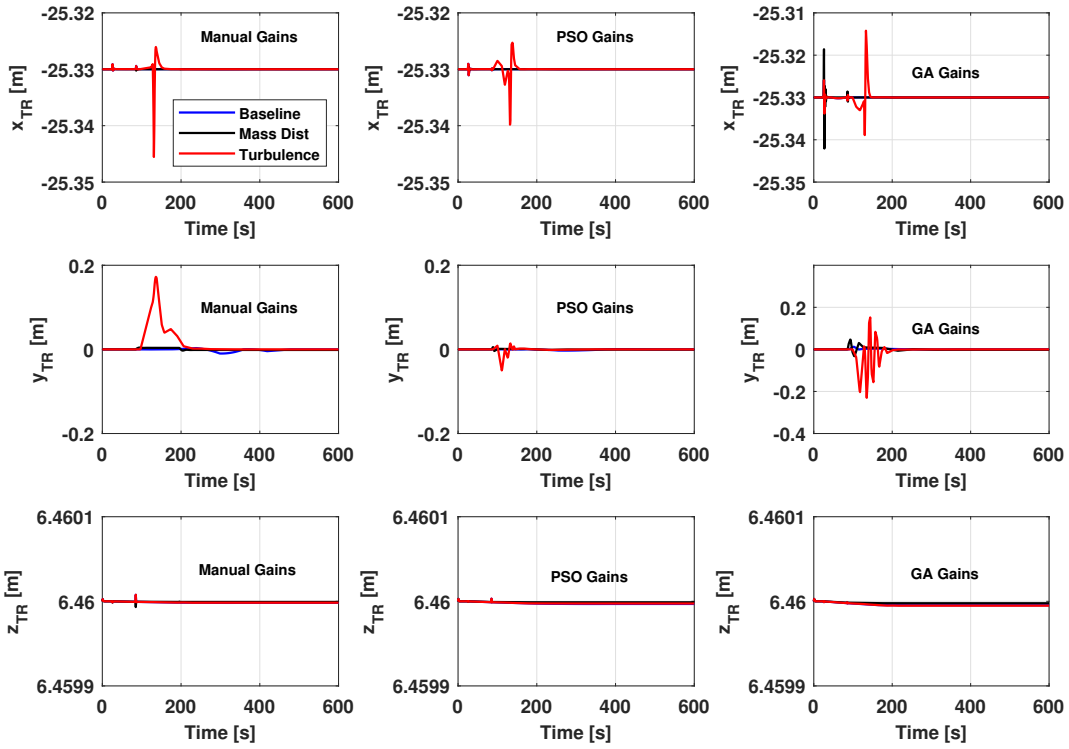


Figure 5.24: Receiver aircraft x-, y- and z-separations versus time - baseline + disturbances - manual-, PSO-, and GA-tuned controller gains.

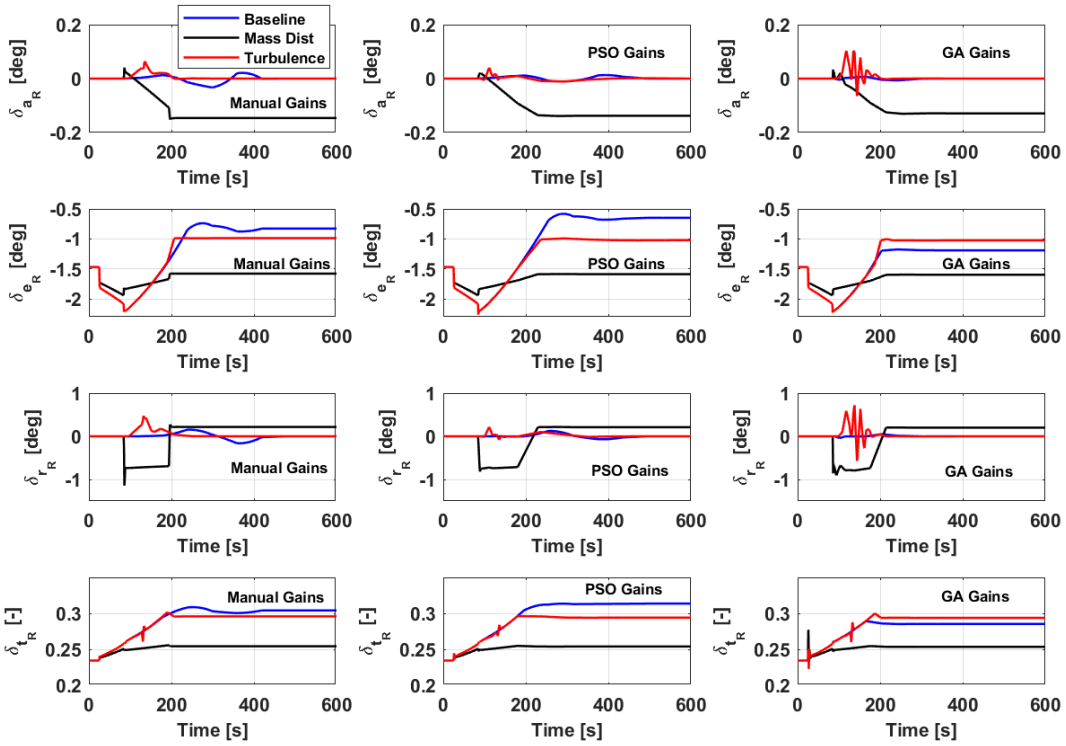


Figure 5.25: Receiver aircraft controller surfaces deflections versus time - baseline + disturbances - manual-, PSO-, and GA-tuned controller gains.

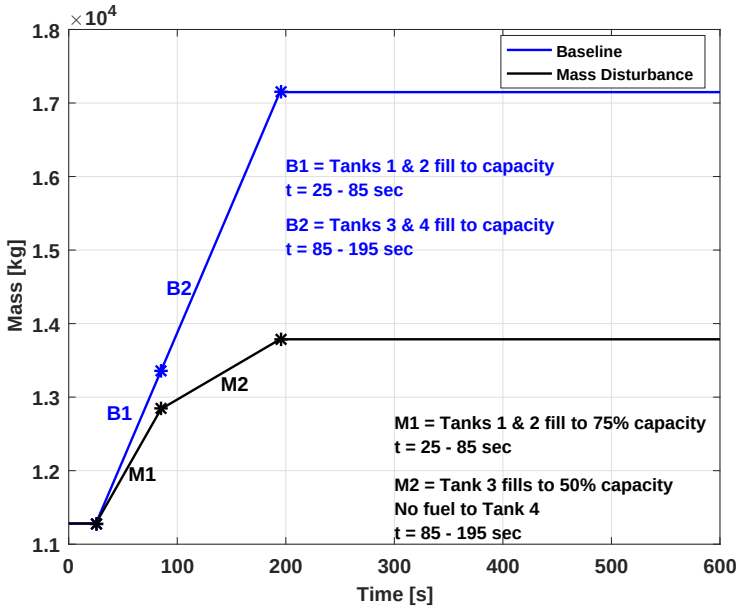


Figure 5.26: Receiver aircraft mass variation with time – baseline and mass disturbance.

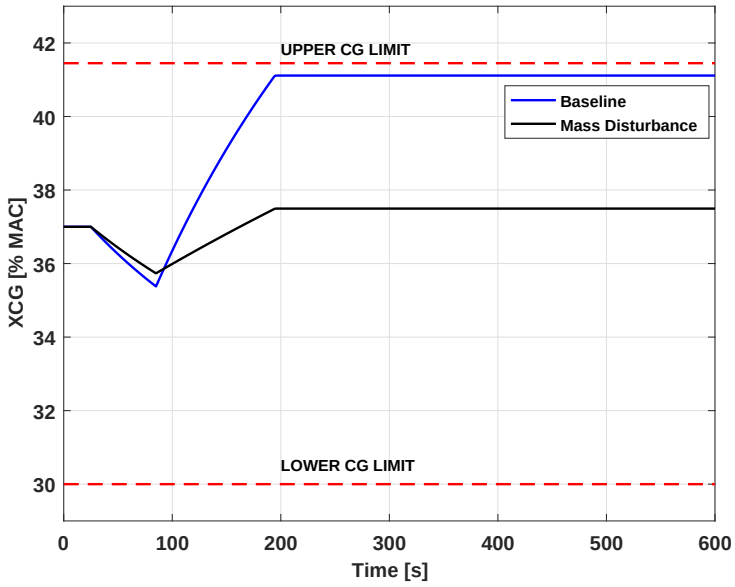


Figure 5.27: Receiver aircraft CG variation with time – baseline and mass disturbance.

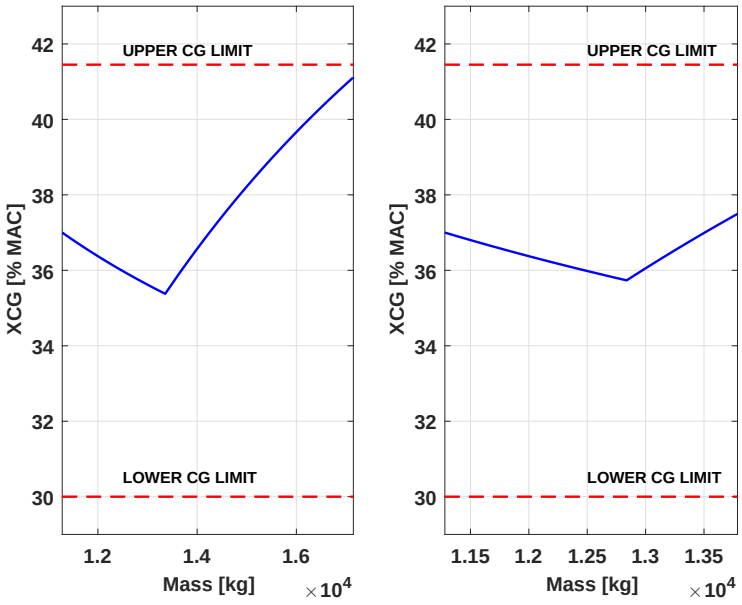


Figure 5.28: Receiver aircraft CG travel versus receiver aircraft mass – baseline and mass disturbance

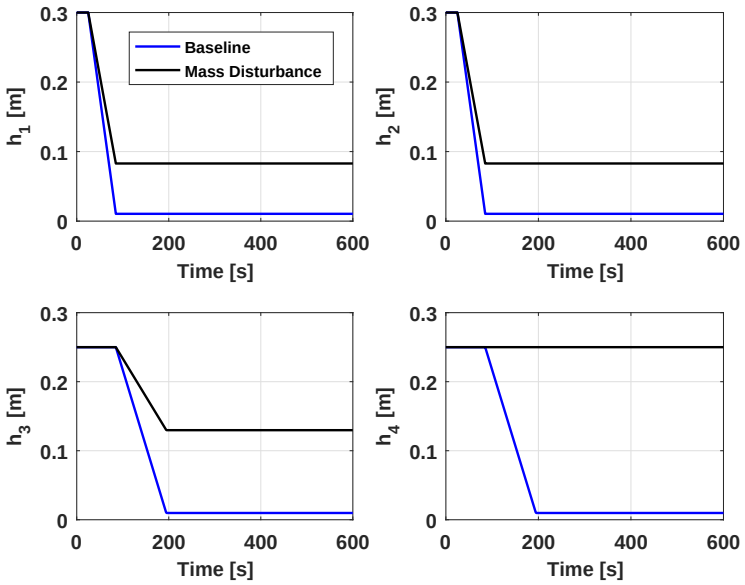


Figure 5.29: Fuel tank centroid variation with time – baseline and mass disturbance.

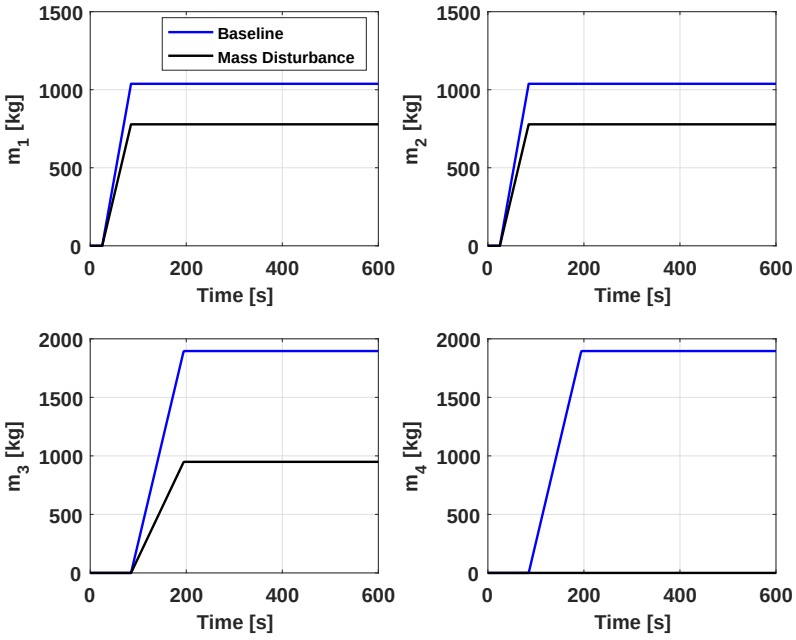


Figure 5.30: Fuel in each tank – baseline and mass disturbance.

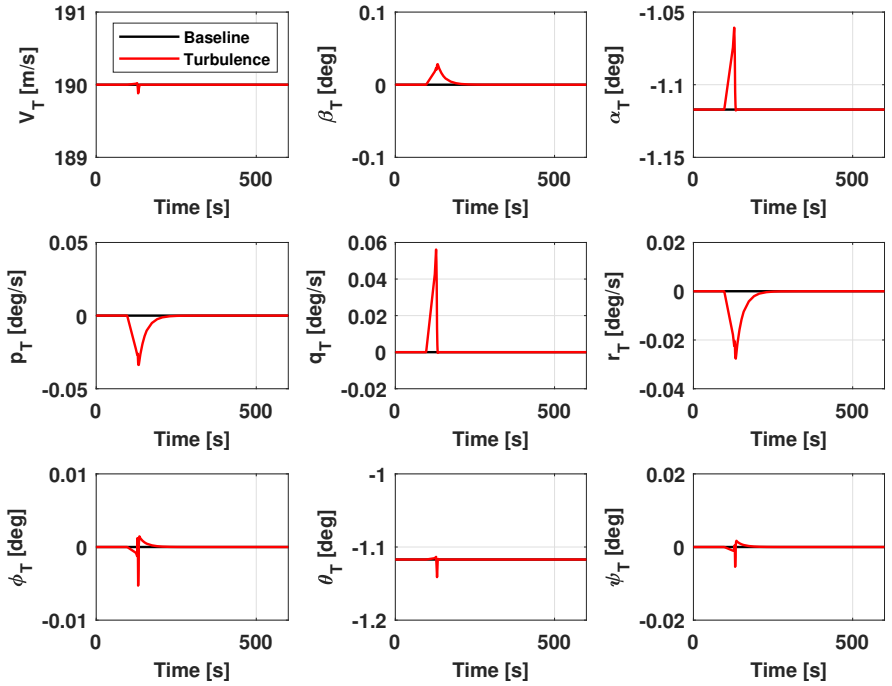


Figure 5.31: Tanker aircraft state variables time history.

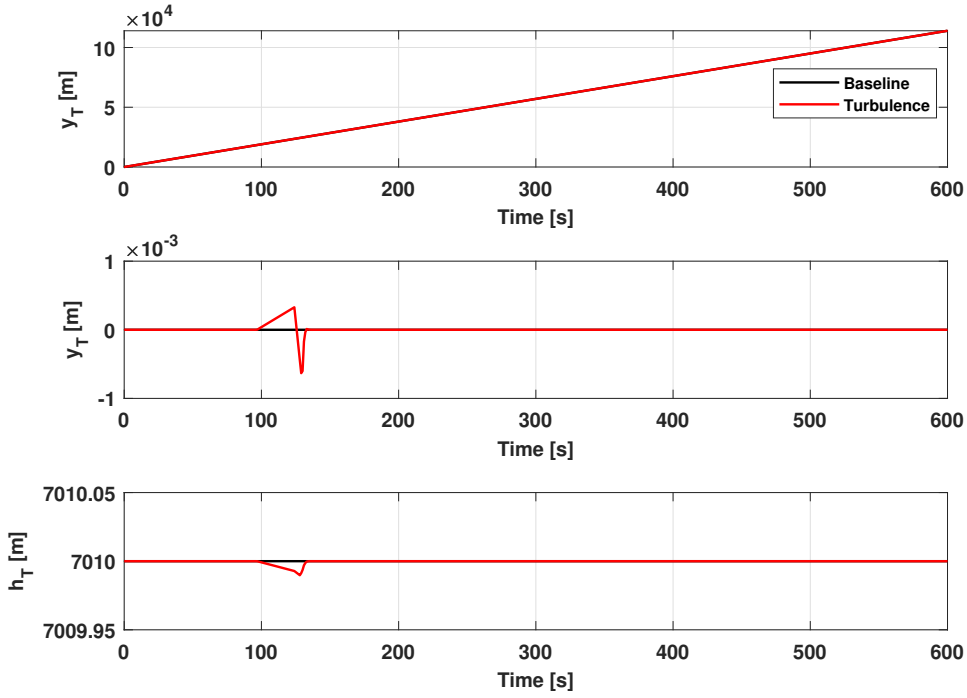


Figure 5.32: Tanker aircraft x-, y-, and z-positions along flight path.

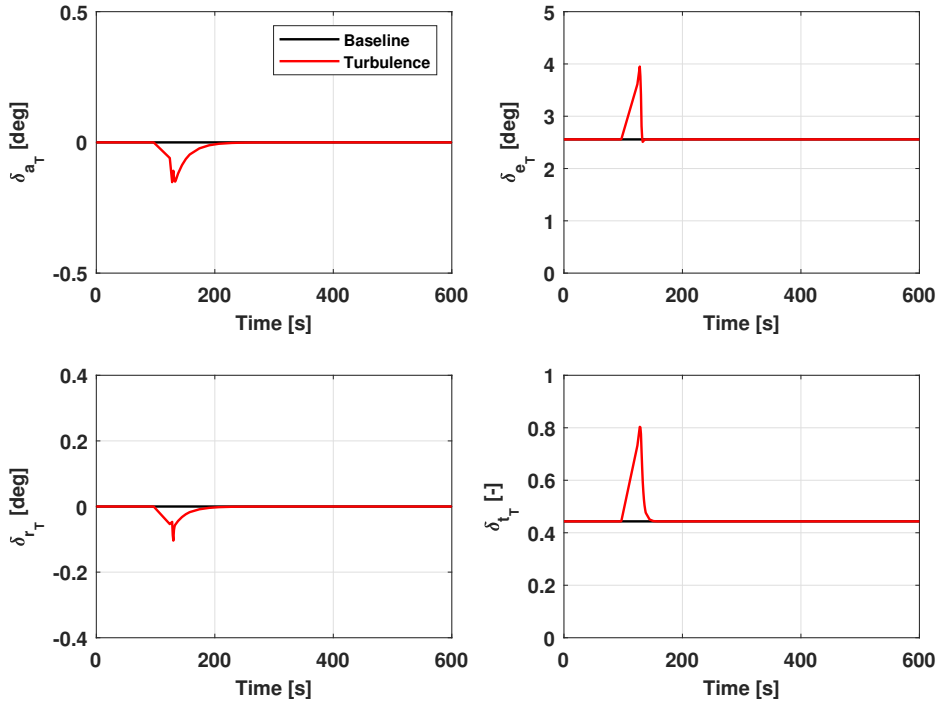


Figure 5.33: Tanker aircraft control surfaces' deflections time history.

cost function, allowing both performance and stability to be addressed while obtaining optimised controller gains. It was found that the minimisation of the cost function led to state and control variables minimisation, thus reducing system energy, while the same amount of mass was introduced as in the case of manual tuning. This impacted the robustness of the benchmark PID controller as the controller gains obtained from 150 iterations/generations could not provide stable control. A proposition was developed, wherein it was shown that if the state corresponding to the manually-tuned equilibrium point is minimised, then the new optimised state corresponds to a perturbed motion away from the nominal (i.e., the original manually-tuned motion trajectory). It was shown that the amount of energy that should remain in the system under a minimisation routine is bounded in order for stability and performance robustness to be maintained. The optimisation algorithms were able to provide controller gains with cost functions within this limit when run to 50 iterations/generations. The PSO-optimised controller gains performed poorly compared to the GA-optimised gains in the baseline case. It was found that the lateral-directional state variables were most susceptible to disturbances. The optimised controller gains did offer improvements in the system behaviour compared to the manually-tuned gains; however, the system performance with the optimised controller gains was, in some instances subject to more transient behaviours, which were dissipated, keeping the aircraft states and control surfaces' deflections within limits.

6 Nonlinear Control in Aerial Refuelling

6.1 Introduction

The aerial refuelling process is characterised by strong nonlinearity in its dynamics. Conventional linearisation (i.e., Jacobian linearisation) about an equilibrium point followed by controller design will not be effective for AAR. Vital defining relationships between key parameters will be lost in the Jacobian linearisation process, not to mention the effects of continuous mass transfer as the receiver is refuelled in the vortex wake of the tanker being simplified or omitted. A linear approximation of the complex refuelling system developed in Chapter 2 will not suffice as a basis for controller design. Stability analysis has shown that these inherent aspects cannot be ignored. Amongst the nonlinear control techniques available for use in AAR, feedback linearisation offers a methodology where, through the use of algebraic transformations, a nonlinear system can be reframed into a linear one. Standard linear controller design techniques can be used to synthesise stabilising feedback controllers for the nonlinear system (Marquez (2003), Haddad and Chellaboina (2008)).

In section 6.2, an overview of input-output feedback linearisation will be given, including its extension to MIMO systems. Its application to the AAR control problem is outlined in section 6.3. The inner- and outer-loop control design will be addressed in sections 6.4 and 6.5 respectively, and the overall controller structure will be presented in section 6.6. The dynamic simulation results will be presented and discussed in section 6.7.

6.2 Input-Output Feedback Linearisation - Theoretical Overview

In input-output feedback linearisation, a nonlinear transformation is applied to a system, in conjunction with a new input variable v (or pseudo-input variable), such that the nonlinear system behaves linearly from the new input v to output y.

Definition 6.1 (Khalil (2015)) A nonlinear system:

$$\dot{\mathbf{x}} = f(\mathbf{x}) + G(\mathbf{x})\mathbf{u} \tag{6.1}$$

where $f : D \to R^n$ and $G : D \to R^{n\times p}$ are sufficiently smooth on a domain $D \subset R^n$, is said to be feedback linearisable if there exists a diffeomorphism $T : D \to R^n$ such that $D_z = T(D)$ contains the origin and change of variables $z = T(x)$ transforms system in Eq. 6.1 into the form

$$\dot{z} = Az + B\gamma(x)[u - \alpha(x)] \tag{6.2}$$

with (A, B) controllable and $\gamma(x)$ nonsingular for all $x \in D$

Consider the single-input-single-output (SISO) nonlinear affine system (Khalil (2015)):

$$\dot{\mathbf{x}} = f(\mathbf{x}) + g(\mathbf{x})\mathbf{u} \tag{6.3}$$

$$\mathbf{y} = h(\mathbf{x}) \tag{6.4}$$

$$\mathbf{x} \in \mathbf{R}^n,\ \mathbf{u} \in \mathbf{R}^m,\ \mathbf{y} \in \mathbf{R}^m,\ \mathbf{f}(\mathbf{x}) \in \mathbf{R}^n,\ \mathbf{g}(\mathbf{x}) \in \mathbf{R}^{n\times m},\ \mathbf{h}(\mathbf{x}) \in \mathbf{R}^{m\times n}$$

where f, g and h are sufficiently smooth in a domain $D \subset R^n$, the mappings $f : D \to R^n$ and $g : D \to R^n$ are called vector fields on D.

Supposing the system is SISO, and replacing $\mathbf{x}$, $\mathbf{y}$ and $\mathbf{u}$ with x, y, and u for ease of presentation, then taking the derivative of y:

$$\begin{aligned} \dot{y} &= \frac{\partial h}{\partial t} = \frac{\partial h}{\partial x}\frac{\partial x}{\partial t} = \frac{\partial y(x)}{\partial x}\dot{x} \\ &= \frac{\partial h}{\partial x}\left[f(x) + g(x)u\right] \\ &= L_f y(x) + L_g y(x)u \end{aligned} \tag{6.5}$$

where $\frac{\partial y}{\partial x} f(x)$ is defined as $L_f y(x)$, which is referred to as the Lie derivative of $y(x)$ along f.

If $L_g h(x) = 0$, then $\dot{y} = L_f h(x)$ is independent of u. Taking the next derivative:

$$\begin{aligned} \ddot{y} &= \frac{\partial^2 h}{\partial^2 t} = \frac{\partial \frac{\partial h}{\partial t}}{\partial x}\frac{\partial x}{\partial t} = \frac{\partial \frac{\partial h}{\partial t}}{\partial x}\dot{x} \\ &= \frac{\partial L_f y(x)}{\partial x}\left[f(x) + g(x)u\right] \\ &= L_f^2 y(x) + L_g y(x) L_f y(x)u \end{aligned} \tag{6.6}$$

If $L_g y(x) L_f y(x) = 0$, then continue to take successive derivatives until u appears. In this way, the derivative will be taken until the control explicitly appears. The superscript refers to the derivative.

$$\begin{aligned} y &= h(x) \\ \dot{y} &= L_f h(x) \\ y^{(2)} = \ddot{y} &= L_f^2 h(x) \\ &\vdots \\ y^{(r-1)} &= L_f^{r-1} h(x) \\ y^{(r)} &= L_f^r h(x) + L_g L_f^{r-1} h(x) u \end{aligned} \tag{6.7}$$

Eq. 6.7, where u explicitly appears, shows that the system defined by Eqs. 6.3 - 6.4 is input-output linearisable, since the state feedback control:

$$u = \frac{1}{L_g L_f^{r-1} h(\mathbf{x})} \left[-L_f^r h(\mathbf{x}) + v \right] \tag{6.8}$$

reduces the input-output map to:

$$y^{(r)} = v \tag{6.9}$$

which is a chain of integrators. The relative degree is denoted by r, and defined as follows:

Definition 6.2 (Marquez (2003)) The nonlinear system defined by eqs. 6.3 - 6.4 has relative degree r, $1 \leq r \leq n$ in a region $D_0 \in D$ if

$$L_g L_f^{i-1} h(x),\ i = 1, 2, \cdots, r-1;\ L_g L_f^{r-1} h(x) \neq 0 \tag{6.10}$$

for all $x \in D_0$

The following proposition is constructed from Khalil (2015) and Terrell (2009).

Proposition 6.1 For the class of nonlinear affine systems in definition 6.1, for the change of variables suggested by $z = T(x)$ which transforms the nonlinear system into a linear one, there must be a state feedback control of the form:

$$u = \alpha(x) + \beta(x) v \tag{6.11}$$

The structural properties of the system must allow the cancellation of nonlinearities. To cancel a nonlinear term $\alpha(x)$ by subtraction, the control u and the nonlinearity $\alpha(x)$ must always appear together as a sum $u + \alpha(x)$. To cancel nonlinear term $\gamma(x)$ by division, the control u and the nonlinearity $\gamma(x)$ must always appear as a product $\gamma(x)u$. If matrix $\gamma(x)$ is nonsingular in the domain of interest, it can be cancelled by $u = \beta(x)v$ where $\beta(x) = \gamma^{-1}(x)$. The ability to use feedback to convert a nonlinear state equation to a controllable linear state equation by cancelling nonlinearities requires the nonlinear state equation to have the structure:

$$\dot{x} = Ax + B\gamma(x)[u - \alpha(x)] \tag{6.12}$$

where A is $n \times n$, B is $n \times p$, the pair (A, B) is controllable, the functions $\alpha : R^n \to R^p$ and $\gamma : R^n \to R^{p \times p}$ are defined in a domain $D \subset R^n$, that contains the origin, and the matrix $\gamma(x)$ is nonsingular for every $x \in D$. If the state equation takes the form of Eq. 6.12 then it can be linearised via the state feedback control $u = \alpha(x) + \beta(x)v$, where $\beta(x) = \gamma^{-1}(x)$, to obtain the linear state equation $\dot{x} = Ax + Bv$.

For stabilisation, v can be designed as $v = -Kx$, such that $A - BK$ is Hurwitz. The overall nonlinear stabilising state feedback control is (Khalil (2015)):

$$u = \alpha(x) - \beta(x)Kx \tag{6.13}$$

From Hedrick and Girard (2015), with $\alpha(x) = L_f^r h(x)$ and $\beta(x) = L_g L_f^{r-1} h(x)$, then

$$y^{(r)} = L_f^r h + L_g L_f^{r-1} h(x)u = \alpha(x) + \beta(x)u \equiv v(x) \tag{6.14}$$

where $\beta(x) \neq 0$.

$v(x)$ is called the synthetic input or synthetic control. This gives an r-integrator linear system of the form:

$$\frac{Y(s)}{V(s)} = \frac{1}{s^r} \tag{6.15}$$

Any linear control method can be used to design the synthetic input v (Hedrick and Girard (2015)).

$$\upsilon = -\sum_{k=0}^{r-1} c_k L_f^k h(x) = -c_0 y - c_1 \dot{y} - c_2 \ddot{y} ... \tag{6.16}$$

The synthetic input v:

$$y^{(r)} = v(x) \tag{6.17}$$

The control law:

$$u = \frac{1}{\beta(x)} \left[\upsilon - \alpha(x) \right] \tag{6.18}$$

or explicitly:

$$u = \frac{1}{L_g L_f^{r-1} h(\mathbf{x})} \left[\upsilon - L_f^r h(\mathbf{x}) \right] \tag{6.19}$$

Applying the designed v, the new transfer function mapping the new external input υ to the system output y is given as:

$$G(s) = \frac{Y(s)}{V(s)} = \frac{1}{s^r + c_{r-1} s^{r-1} + \ldots c_0 s^0} \tag{6.20}$$

The resulting closed-loop polynomial is of the form:

$$p(s) = s^r + c_{r-1} s^{r-1} + \ldots c_0 s^0 \tag{6.21}$$

6.2.1 System description in canonical form

In definition 6.1, the idea of a state transformation was introduced, which allowed the system to be represented in a new set of variables (implying a new set of coordinates), where a linear mapping has been realised. The method described in the preceding section derived a linear mapping between the input and output variables. This is different to the case where a linear mapping is made (via feedback) involving the full state. This intuitively implies that since the state dimension n is greater than the output dimension m, there ought to be further analysis of the system, and possibly additional transformations required.

In fact, it is the relative degree, r (definition 6.2), that is central to the further development of the intuitive implication above. The key outcomes from Proposition 4.1.3 in Isidori (1995) and Theorem 8.1 from Khalil (2015) are presented.

The system described in Eqs. 6.3 - 6.4 has relative degree r at point x^o. Then $r \leq n$. Set:

$$\begin{aligned} \phi_1(x) &= L_f^0 h(x) \\ \phi_2(x) &= L_f^1 h(x) \\ &\cdots \\ \phi_r(x) &= L_f^{(r-1)} h(x) \end{aligned} \tag{6.22}$$

If r is strictly less than n, it is always possible to find $n-r$ more functions $\phi_{r+1}(x), \ldots, \phi_n(x)$ such that the mapping:

$$\Phi(x) = \begin{pmatrix} \phi_{r+1}(x) \\ \ldots \\ \phi_n(x) \end{pmatrix} \tag{6.23}$$

has a Jacobian matrix that is nonsingular at x^o and therefore qualifies as a local coordinates transformation in a neighbourhood of x^o. It is always possible to choose $\phi_{r+1}(x), \ldots, \phi_n(x)$ in such a way that:

$$L_g \phi_i(x) = 0 \text{ for all } r+1 \leq i \leq n \tag{6.24}$$

The above description is presented in new coordinates:

$$z = T(x) = \begin{bmatrix} h(x) \\ \vdots \\ L_f^{r-1} h(x) \\ - - - \\ \phi_{r+1}(x) \\ \vdots \\ \phi_n(x) \end{bmatrix} = \begin{bmatrix} \phi(x) \\ - - - \\ \psi(x) \end{bmatrix} = \begin{bmatrix} \xi \\ - - - \\ \eta \end{bmatrix} \tag{6.25}$$

where ϕ_{r+1} to ϕ_n are chosen such that $T(x)$ is a diffeomorphism on a domain $D_0 \in D$ and:

$$\frac{d\phi_i}{dx} g(x) = 0 \text{ for } 1 \leq i \leq n-r, \ \forall x \in D_0 \tag{6.26}$$

z is fully comprised of:

$$z = \begin{bmatrix} z_1 \\ z_2 \\ \ldots \\ z_r \\ z_{r+1} \\ \ldots \\ z_n \end{bmatrix} = \begin{bmatrix} \xi & \eta \end{bmatrix}^T \tag{6.27}$$

It is important to note that ξ is the observable dynamics of the system which corresponds to r system states as the relative degree is r. Thus η represents the unobservable or internal dynamics of the system which contains $n-r$ states, the difference between the total number of state variables and the relative degree.

The new diffeomorphic coordinates are expressed in normal form or state-space form as:

$$\dot{\eta} = f_0(\xi, \eta) \tag{6.28}$$

$$\dot{\xi} = A\xi + Bv = A\xi + B\gamma(x)[u - \alpha(x)] \tag{6.29}$$

$$y = C\xi \tag{6.30}$$

where $\xi \in R^r$, $\eta \in R^{n-r}$ and (A, B, C) is a canonical form representation of a chain of r integrators, and

$$f_0(\xi, \eta) = \frac{\partial \phi}{\partial x} f(x) \mid_{x=T^{-1}(z)} \tag{6.31}$$

$$\gamma(x) = L_g L_f^{r-1} h(x) \tag{6.32}$$

$$\alpha(x) = -\frac{L_f^r h(x)}{L_g L_f^{r-1} h(x)} \tag{6.33}$$

The matrices are given by:

$$A = \begin{bmatrix} 0 & 1 & 0 & \dots & 0 \\ 0 & 0 & 1 & 0 & \dots \\ \dots & \dots & \dots & \dots & \dots \\ 0 & 0 & \dots & 0 & 1 \\ 0 & 0 & \dots & 0 & 0 \end{bmatrix}, \; B = \begin{bmatrix} 0 \\ 0 \\ \dots \\ 0 \\ 1 \end{bmatrix}, \; C = \begin{bmatrix} 1 & 0 & \dots & 0 \end{bmatrix} \tag{6.34}$$

Applying v as designed in Eq. 6.16,

$$A = \begin{bmatrix} 0 & 1 & 0 & \dots & 0 \\ 0 & 0 & 1 & 0 & \dots \\ \dots & \dots & \dots & \dots & \dots \\ 0 & 0 & \dots & 0 & 1 \\ -c_0 & -c_1 & \dots & -c_{r-2} & -c_{r-1} \end{bmatrix}, \; B = \begin{bmatrix} 0 \\ 0 \\ \dots \\ 0 \\ 1 \end{bmatrix}, \; C = \begin{bmatrix} 1 & 0 & \dots & 0 \end{bmatrix} \tag{6.35}$$

6.2.2 Zero dynamics and stability

The stability of the input-output linearised system (or, the $v - y$ system) has been addressed in Eqs. 6.14 and 6.16. The roots of the closed-loop polynomial in Eq. 6.21 will allow for stability and performance requirements to be met.

However, this analysis extends only to the ξ portion of the system defined within coordinates z. The stability of the internal dynamics, η (described by Eq. 6.29) must also be examined.

For a nonlinear system, the zero-dynamics are analysed. The zero-dynamics are defined to be the internal dynamics of the system when the system output is kept at zero by the input. The zero-dynamics are an intrinsic feature of a nonlinear system, which does not depend on the choice of control law or the desired trajectories (Terrell (2009)).

Setting $\xi = 0$ in Eq. 6.29, the zero dynamics are (Terrell (2009), Marquez (2003)):

$$\dot{\eta} = f_0(0, \eta) \tag{6.36}$$

Examining the stability of zero-dynamics is much easier than examining the stability of internal dynamics, because the zero-dynamics only involves the internal states. The system is said to be minimum phase if Eq. 6.36 has an asymptotically stable equilibrium point in the domain of interest (Haddad and Chellaboina (2008)).

If $T(x)$ is chosen such that the origin $(\eta = 0, \xi = 0)$ is an equilibrium point of Eq. 6.29 to Eq. 6.30, then the system is said to be minimum phase if the origin of the zero dynamics is asymptotically stable. The original coordinates can characterise the zero dynamics:

$$y(t) \equiv 0 \Rightarrow \xi(t) \equiv 0 \Rightarrow u(t) \equiv \alpha(x(t)) \tag{6.37}$$

If the output is identically zero, the solution of the state equation must be confined to the set:

$$Z^* = \{x \in D_0 \mid h(x) = L_f h(x) = \dots L_f^{r-1} h(x) = 0\} \tag{6.38}$$

and the input must be:

$$u = u^*(x) \stackrel{\text{def}}{=} \alpha(x) \mid_{z \in Z^*} \tag{6.39}$$

The restricted motion of the system is described by:

$$\dot{x} = f^*(x) \stackrel{\text{def}}{=} [f(x) + g(x)\alpha(x)] \mid_{z \in Z^*} \tag{6.40}$$

6.2.3 Extension to square MIMO system

Extending this to the square MIMO case, where $m = n$:

$$\dot{\mathbf{x}} = \sum_{i=1}^{n} f_i(\mathbf{x}) + \sum_{j=1}^{n} g_j(\mathbf{x})\mathbf{u} \tag{6.41}$$

$$y_i = h_i(x)\,,\ i = 1 \ldots n \tag{6.42}$$

Consider the nonlinear affine system

$$\dot{\mathbf{x}} = \sum_{i=1}^{n} f_i(\mathbf{x}) + \sum_{j=1}^{n} g_j(\mathbf{x})\mathbf{u} \tag{6.43}$$

$$y_i = h_i(x)\,,\ i = 1 \ldots n \tag{6.44}$$

$$\mathbf{x} \in \mathbf{R}^n,\ \mathbf{u} \in \mathbf{R}^m,\ \mathbf{y} \in \mathbf{R}^m,\ \mathbf{f}(\mathbf{x}) \in \mathbf{R}^n,\ \mathbf{g}(\mathbf{x}) \in \mathbf{R}^{n \times m},\ \mathbf{h}(\mathbf{x}) \in \mathbf{R}^{m \times n}$$

with:

$$f(x) = \begin{bmatrix} f_1(x_1, \ldots, x_n) \\ \vdots \\ f_n(x_1, \ldots, x_n) \end{bmatrix}_{n \times 1} \tag{6.45}$$

$$g(x) = [\ g_1(x_1, \ldots, x_n),\ \ \cdots\ ,\ \ g_n(x_1, \ldots, x_n)\ ]_{n \times m} \tag{6.46}$$

$$h(x) = \begin{bmatrix} h_1(x_1, \ldots, x_n) \\ \vdots \\ h_p(x_1, \ldots, x_n) \end{bmatrix}_{n \times 1} \tag{6.47}$$

$$u = \begin{bmatrix} u_1 & \cdots & u_m \end{bmatrix}^T u \in \mathbf{R}^m \tag{6.48}$$

$$y = \begin{bmatrix} y_1 & \cdots & y_m \end{bmatrix}^T y \in \mathbf{R}^m \tag{6.49}$$

Applying successive derivatives as described earlier, the system is represented as:

$$\frac{d^k y_i}{dt^k} = y_i^{(k)} = \begin{cases} L_f^k h_i(x), & k = 1, \cdots, r_i - 1 \\ L_f^k h_i(x) + \sum\limits_{j=1}^{m} L_{g_j} L_f^{k-1} h_i(x) u_j, & k = r_i \end{cases} \tag{6.50}$$

The vector of relative degrees at point x_0 is $\left\{ \begin{array}{cccc} r_1, & r_2, & \ldots & r_m \end{array} \right\}$ if

$L_{gi}L_f^k h_i(x) = 0, \;\; i = 1, \ldots, m, \;\; k = 0, \ldots, r_{i-2}$ for all x in the neighbourhood of x_0

The characteristic matrix $C(x)$ thus becomes:

$$C(x) = \begin{bmatrix} L_{g_1}L_f^{r_1-1}h_1(x) & L_{g_2}L_f^{r_1-1}h_1(x) & ... & L_{g_m}L_f^{r_1-1}h_1(x) \\ L_{g_1}L_f^{r_2-1}h_2(x) & L_{g_2}L_f^{r_2-1}h_2(x) & ... & L_{g_m}L_f^{r_2-1}h_2(x) \\ ... & ... & ... & ... \\ L_{g_1}L_f^{r_m-1}h_m(x) & L_{g_2}L_f^{r_m-1}h_m(x) & ... & L_{g_m}L_f^{r_m-1}h_m(x) \end{bmatrix} \tag{6.51}$$

and must be nonsingular at x_0. The total relative degree is $r = r_1 + r_2 + ...r_m$

Note, for tracking (where non-zero setpoint regulation is a special case:)

$$\frac{d^k e_i}{dt^k} = e_i^{(k)} = \begin{cases} L_f^k h_i(x) - y_d^{(k)}, & k = 1, \cdots, r_i - 1 \\ L_f^k h_i(x) - y_d^{(k)} + \sum L_{g_j} L_f^{k-1} h_i(x) u_{j,} & k = r_i \end{cases} \tag{6.52}$$

$$e_i = y_i - y_{i_d} \tag{6.53}$$

Then, system in Eq. 6.43 is input-output linearisable if there exists a static state feedback control of the form (Garces et al., (2003)):

$$u = P(x) + Q(x)v(t) \tag{6.54}$$
$$P(x) \in \mathbf{R}^m, \; Q(x) \in \mathbf{R}^{m \times m} \text{ nonsingular}, \; v \in \mathbf{R}^m$$

and linear operators of the form:

$$\mathfrak{L}_{\rho_i} = \sum_{k=1}^{\rho_i} \lambda_{ik} \frac{d^k}{dt^k}, i = 1, \ldots, m \tag{6.55}$$

with constant coefficients

$$\lambda_{ik} = \begin{bmatrix} \lambda_{ik}^1 & \lambda_{ik}^2 & \ldots & \lambda_{ik}^m \end{bmatrix} \tag{6.56}$$

satisfying $\lambda_{i\rho_i} \neq 0$, ρ_i the order of the operator and

$$det\left(\begin{bmatrix} \left(\sum_{k=0}^{\rho_1} \lambda_{1k} s^k\right) & \left(\sum_{k=0}^{\rho_2} \lambda_{2k} s^k\right) & \ldots & \left(\sum_{k=0}^{\rho_m} \lambda_{mk} s^k\right) \end{bmatrix}_{m \times m} \right) \neq 0 \tag{6.57}$$

such that:

$$\sum_{i=1}^{m} \mathfrak{L}_{\rho_i} y_i = v \tag{6.58}$$

Hence, the Laplace domain representation is as follows:

$$y(s) = G(s)v(s) = [B(s)]^{-1} v(s) \tag{6.59}$$

where

$$B(s) = \left(\left[\begin{array}{cccc} \left(\sum_{k=0}^{\rho_1} \lambda_{1k} s^k\right) & \left(\sum_{k=0}^{\rho_2} \lambda_{2k} s^k\right) & \dots & \left(\sum_{k=0}^{\rho_m} \lambda_{mk} s^k\right) \end{array} \right]_{m \times m} \right) \tag{6.60}$$

$y(s)$ and $v(s)$ are the Laplace domain transformations of $y(t)$ and $v(t)$

Using Theorem 3.1.1 of Garces et al., (2003), for arbitrary $\lambda_{ik} \in R^n (k = 0, \dots, r_i;\ i = 1 \dots m)$, a state feedback control of the form in Eq. 6.54 defined by:

$$u(t) = \left(\left[\begin{array}{cccc} \lambda_{1r_1} & \dots & \lambda_{mr_m} \end{array} \right]_{m \times m} C(x) \right)^{-1}_{m \times m} \times \left(v - \sum_{i=1}^{m} \sum_{k=0}^{r_i} \lambda_{ik} L_f^k h_i(x) \right)_{m \times 1} \tag{6.61}$$

applied to the system described by Eq. 6.43 where $C(x)$, the characteristic matrix given by Eq. 6.51, produces a linearised input-output description given by:

$$\sum_{i=1}^{m} \sum_{k=0}^{r_i} \lambda_{ik} \frac{d^k y_i}{dt^k} = v \tag{6.62}$$

when the following conditions hold:

- the vector of relative degrees is well defined
- λ_{ik} satisfies

$$det \left(\left[\begin{array}{cccc} \left(\sum_{k=0}^{r_1} \lambda_{1k} s^k\right) & \left(\sum_{k=0}^{r_2} \lambda_{2k} s^k\right) & \dots & \left(\sum_{k=0}^{r_m} \lambda_{mk} s^k\right) \end{array} \right]_{m \times m} \right) \neq 0 \tag{6.63}$$

$$det([\ \lambda_{1r_1} \quad \lambda_{2r_2} \quad \dots \quad \lambda_{m_{rm}}\ ]) \neq 0 \tag{6.64}$$

In the linearising control law, $u = P(x) + Q(x)v(t)$, thus:

$$P(x) = -([\ \lambda_{1r_1} \quad \lambda_{2r_2} \quad \dots \quad \lambda_{m_{rm}}\ ]_{m \times m} C(x))^{-1}_{m \times m} \left(\sum_{i=1}^{m} \sum_{k=0}^{r_i} \lambda_{ik} L_f^k h_i(x) \right)_{m \times 1} \tag{6.65}$$

$$Q(x) = \left(\left[\begin{array}{cccc} \lambda_{1r_1} & \dots & \lambda_{mr_m} \end{array} \right]_{m \times m} C(x) \right)^{-1}_{m \times m} \tag{6.66}$$

By appropriate selection of λ_{ik}, input-output linearisation and decoupling can be achieved. That is, the system, now feedback linearised, also has the ith output depending on the ith input (Garces et al., (2003)).

Again, the system can be represented in a canonical form and the zero dynamics can be examined for stability, as presented for the SISO case. The stability of the internal dynamics is given by the boundedness of the solution of Eq. 6.43 with no external input ($v = 0$). Proposition 3.1.5 and Proposition 3.1.7 of Garces et al., (2003) address the internal stability of the system (i.e., the boundedness of solution to system Eq. 6.43 under control law 6.54 when the external input $v(t)$ is zero, and when $v(t) \neq 0$ respectively).

6.3 Application to Automated Aerial Refuelling

From the design of the PID controller in Chapter 3, the primary requirement of the control design is to maintain a fixed relative separation and orientation with respect to the tanker, while subject to a vortex wind field and varying mass and inertia characteristics in a straight leg refuelling manoeuvre. A generalised depiction of the controller block diagram is given in Figure 6.1. A more detailed block diagram will be presented once the constituent blocks are developed further.

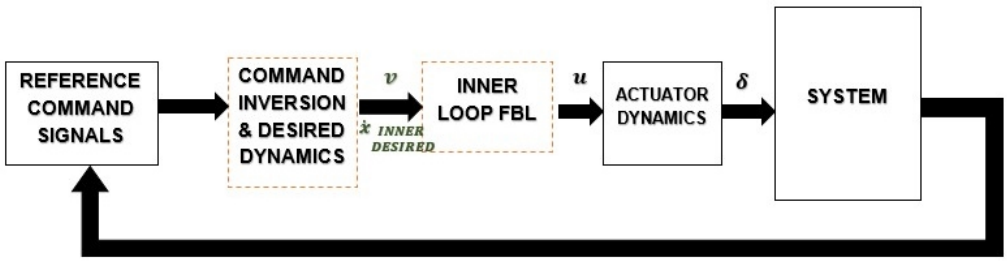


Figure 6.1: Generalised controller block diagram

For AAR, an inner-loop control will be required to stabilise the fast dynamics, while an outer-loop control will be required to maintain the relative orientation. The outer-loop command variables are: x_{TR}, y_{TR} z_{TR}, and ϕ_{TR}. The command inversion and desired dynamics module (see Figure 6.1) relates these to the inner-loop variables: V_R, p_{TR} q_{TR}, and r_{TR}. Based on the desired dynamics, commanded controls are: $\mathbf{u}_R = [\delta_{a_R}, \delta_{e_R}, \delta_{r_R}, \delta_{T_R}]^T$

6.4 Inner-Loop Feedback Linearisation

The inner loop is defined as follows:

$$\dot{\mathbf{x}}_{inner} = f_{inner}(\mathbf{x}) + g_{inner}(\mathbf{x})\,\mathbf{u}_R \tag{6.67}$$

$$\mathbf{y_{inner}} = C\mathbf{x}_{inner} \tag{6.68}$$

$$\mathbf{x}_{inner} = [V_R,\, p_{TR},\, q_{TR},\, r_{TR}]^T \tag{6.69}$$

$$\mathbf{u}_R = [\delta_{a_R},\, \delta_{e_R},\, \delta_{r_R},\, \delta_{T_R}]^T \tag{6.70}$$

Note from Chapter 2 that V_R is grouped in Equation 2.13 and p_{TR} q_{TR}, and r_{TR} are grouped in Equation 2.14. Thus expressing the translational and rotational dynamics in nonlinear affine form:

$$\dot{\mathcal{X}}_{\mathcal{R}} = f_{\mathcal{X}}(\mathbf{x}) + g_{\mathcal{X}}(\mathbf{x})\,\mathbf{u}_R \tag{6.71}$$

$$\dot{\omega}_{B_R B_T} = f_{\omega}(\mathbf{x}) + g_{\omega}(\mathbf{x})\,\mathbf{u}_R \tag{6.72}$$

where $f_{\mathcal{X}}$, $g_{\mathcal{X}}$, f_{ω} and g_{ω} are defined in Appendix A. Eqs. 6.71 and 6.72 are combined to represent Eq. 6.67.

Now applying feedback linearisation:

$$\begin{aligned} \dot{y}_{inner_1} = \dot{V}_R &= \frac{\partial h_1}{\partial t} = \frac{\partial h_1}{\partial x}\frac{\partial x}{\partial t} = \frac{\partial y_1(x)}{\partial x}\dot{x} \\ &= \frac{\partial h_1}{\partial x}\left[f(x) + g(x)u\right] \\ &= L_f y_1(x) + L_g y_1(x) u \end{aligned} \tag{6.73}$$

$$\begin{aligned} \dot{y}_{inner_2} = \dot{p}_{TR} &= \frac{\partial h_2}{\partial t} = \frac{\partial h_2}{\partial x}\frac{\partial x}{\partial t} = \frac{\partial y_2(x)}{\partial x}\dot{x} \\ &= \frac{\partial h_2}{\partial x}\left[f(x) + g(x)u\right] \\ &= L_f y_2(x) + L_g y_2(x) u \end{aligned} \tag{6.74}$$

$$\begin{aligned} \dot{y}_{inner_3} = \dot{q}_{TR} &= \frac{\partial h_3}{\partial t} = \frac{\partial h_3}{\partial x}\frac{\partial x}{\partial t} = \frac{\partial y_3(x)}{\partial x}\dot{x} \\ &= \frac{\partial h_3}{\partial x}\left[f(x) + g(x)u\right] \\ &= L_f y_3(x) + L_g y_3(x) u \end{aligned} \tag{6.75}$$

$$\begin{aligned}\dot{y}_{inner_4} = \dot{r}_{TR} &= \frac{\partial h_4}{\partial t} = \frac{\partial h_4}{\partial x}\frac{\partial x}{\partial t} = \frac{\partial y_4(x)}{\partial x}\dot{x} \\ &= \frac{\partial h_4}{\partial x}\left[f(x) + g(x)u\right] \\ &= L_f y_4(x) + L_g y_4(x) u \end{aligned} \tag{6.76}$$

However, since there is non-zero setpoint regulation in the selected output variables in the inner loop, Eqs. 6.52 and 6.53 were adopted to incorporate the non-zero desired value.

In the case of the selected y_{inner}, the control variables $[\delta_{a_R}, \delta_{e_R}, \delta_{r_R}, \delta_{T_R}]^T$ appear after a single differentiation.

The relative degree is thus: $\left\{ \; r_1 = 1, \quad r_2 = 1, \quad r_3 = 1, \quad r_4 = 1 \; \right\}$

A generalised expression of the result is thus given in matrix form:

$$\begin{bmatrix} \dot{y}_1 \\ \dot{y}_2 \\ \dot{y}_3 \\ \dot{y}_4 \end{bmatrix} = \begin{bmatrix} L_f h_1(x) \\ L_f h_2(x) \\ L_f h_3(x) \\ L_f h_4(x) \end{bmatrix} + \begin{bmatrix} L_{g1} h_1(x) & L_{g2} h_1(x) & L_{g3} h_1(x) & L_{g4} h_1(x) \\ L_{g1} h_2(x) & L_{g2} h_2(x) & L_{g3} h_2(x) & L_{g4} h_2(x) \\ L_{g1} h_3(x) & L_{g2} h_3(x) & L_{g3} h_3(x) & L_{g4} h_3(x) \\ L_{g1} h_4(x) & L_{g2} h_4(x) & L_{g3} h_4(x) & L_{g4} h_4(x) \end{bmatrix} \begin{bmatrix} u_1 \\ u_2 \\ u_3 \\ u_4 \end{bmatrix} \tag{6.77}$$

For the control law $u = P(x) + Q(x)v(t)$, the synthetic control $v(t)$ is designed using λ_{ik}, which when appropriately selected, can decouple the system where the i^{th} output depends on the i^{th} external input.

Using Eq. 6.62 with $m = 4$ and $r_i = 1$ according to the relative degree, $v(t)$ is:

$$v_1 = \lambda_{10}(y_1 - y_{1d}) + \lambda_{11}(\dot{y}_1 - \dot{y}_{1d}) \tag{6.78}$$

$$v_2 = \lambda_{20}(y_2 - y_{2d}) + \lambda_{21}(\dot{y}_2 - \dot{y}_{2d}) \tag{6.79}$$

$$v_3 = \lambda_{30}(y_3 - y_{3d}) + \lambda_{31}(\dot{y}_3 - \dot{y}_{3d}) \tag{6.80}$$

$$v_4 = \lambda_{40}(y_4 - y_{4d}) + \lambda_{41}(\dot{y}_4 - \dot{y}_{4d}) \tag{6.81}$$

6.5 Outer Loop Command Inversion and Desired Dynamics

The principles of feedback linearisation will be applied to the outer-loop command inversion block in order to obtain the desired dynamics.

Defining the outer-loop system in nonlinear affine form:

$$\dot{\mathbf{x}}_{outer} = f_{outer}(\mathbf{x}) + g_{outer}(\mathbf{x})\,\mathbf{u}_{ps} \tag{6.82}$$

$$\mathbf{y}_{outer} = C\mathbf{x}_{outer} \tag{6.83}$$

$$\mathbf{x}_{outer} = [x_{TR},\, \phi_{TR},\, y_{TR},\, z_{TR}]^T \tag{6.84}$$

$$\mathbf{u}_{ps} = [V_R,\, p_{TR},\, q_{TR},\, r_{TR}]^T \tag{6.85}$$

where, in this loop, the pseudo or virtual control is defined u_{ps}. The functions f_{outer} and g_{outer} are defined in Appendix A.

The step preceding the inner-loop feedback linearisation (Figure 6.1) requires that the kinematics be related to the pseudo or virtual control $v(t)$. Earlier, the translational kinematics was written as:

$$\dot{\xi} = \mathbf{R}^{\mathbf{T}}_{\mathbf{B_R B_T}}\mathbf{R}_{\mathbf{B_R W_R}}U + \mathbf{R}^{\mathbf{T}}_{\mathbf{B_R B_T}}W - \mathbf{R}_{\mathbf{B_T I}}\dot{r}_{B_T} + \mathbf{S}(\omega_{\mathbf{B_T}})\xi \tag{6.86}$$

Although V_R appears explicitly through U, p_{TR}, q_{TR}, r_{TR} does not. The translational kinematics is thus rearranged to allow ω_{TR} (i.e., p_{TR}, q_{TR}, r_{TR}) to appear explicitly, by using matrix relationships in the term $\mathbf{S}(\omega_{\mathbf{B_T}})\xi$. The following is thus obtained:

$$\dot{\xi} = \mathbf{R}^{\mathbf{T}}_{\mathbf{B_R B_T}}\mathbf{R}_{\mathbf{B_R W_R}}U + \mathbf{R}^{\mathbf{T}}_{\mathbf{B_R B_T}}W - \mathbf{R}_{\mathbf{B_T I}}\dot{r}_{B_T} - \mathbf{S}(\xi)\mathbf{R}^{\mathbf{T}}_{\mathbf{B_R B_T}}\omega_{BR} + \mathbf{S}(\xi)\mathbf{R}^{\mathbf{T}}_{\mathbf{B_R B_T}}\omega_{TR} \tag{6.87}$$

Including the equation for $\dot{\phi}_{TR}$, all four outer-loop state variables are now written. The outer-loop command variables are now able to be written in terms of the inner-loop command variables.

The principles developed earlier were based on the application of successive differentiation until the control explicitly appeared. This principle is also used in the command inversion block. The technique used for the command inversion and desired dynamics is adapted from Zhang et al. (2020), where a control algebraic equation is solved using a Lyapunov function in order to shape the synthetic input v to get the desired tracking performance in the outer loop. Under the methodology in Zhang et al. (2020), the derivative of the original control $\dot{u}$ is taken as the new control inputs - in line with giving the desired dynamics for the inner-loop feedback linearisation. This arrangement also appears to mimic a backstepping controller and so is a "pseudo-backstepping" scheme in that sense.

Summarising the methodology from Zhang et al. (2020) using Eq. 6.17 as a starting point:

For a feedback-linearisable system where the control explicitly appears after k derivatives (as summarised in Eq. 6.9), here written for a system with four outputs in y, Eq. 6.17:

$$\begin{bmatrix} \frac{d^k y_1}{dt^k} \\ \frac{d^k y_2}{dt^k} \\ \frac{d^k y_3}{dt^k} \\ \frac{d^k y_4}{dt^k} \end{bmatrix} = \begin{bmatrix} v_1(x,u) \\ v_2(x,u) \\ v_3(x,u) \\ v_4(x,u) \end{bmatrix} \tag{6.88}$$

Then, let:

$$v = \begin{bmatrix} v_1 \\ v_2 \\ v_3 \\ v_4 \end{bmatrix} = z \tag{6.89}$$

In line with the relationships developed earlier in the chapter, z is thus a function of the output and successive derivatives.

$$z = \begin{bmatrix} z_1(y_1, \dot{y}_1, \ldots, y_1^{(k-1)}, y_{1d}) \\ z_2(y_2, \dot{y}_2, \ldots, y_2^{(k-1)}, y_{2d}) \\ z_3(y_3, \dot{y}_3, \ldots, y_3^{(k-1)}, y_{3d}) \\ z_4(y_4, \dot{y}_4, \ldots, y_4^{(k-1)}, y_{4d}) \end{bmatrix} \tag{6.90}$$

The algebraic control equations that will synthesise the control law development are given below, along with the Lyapunov function:

$$v(x,u) - z = 0 \tag{6.91}$$

$$V_s = \frac{1}{2} h^T h \tag{6.92}$$

$$h = v - z \tag{6.93}$$

Taking the derivative of the Lyapunov function:

$$\dot{V}_s = h^T \left(\frac{\partial h}{\partial u} \dot{u} + \frac{\partial h}{\partial x} \dot{x} + \frac{\partial h}{\partial z} \dot{z} \right) \tag{6.94}$$

If $\dot{u}$ is defined as:

$$\dot{u} = -K_s \left(\frac{\partial h}{\partial u} \right)^T h - \left(\frac{\partial h}{\partial u} \right)^{-1} \left(\frac{\partial h}{\partial x} \dot{x} + \frac{\partial h}{\partial z} \dot{z} \right) \tag{6.95}$$

Then the derivative of the Lyapunov function is negative-definite:

$$\dot{V}_s = -h^T \frac{\partial v}{\partial u} K_s \left(\frac{\partial v}{\partial u} \right)^T h \leq 0 \tag{6.96}$$

The control law is given by:

$$u = \int_0^t \left[-K_s \left(\frac{\partial v}{\partial u} \right)^T (v - z) - \left(\frac{\partial v}{\partial u} \right)^{-1} \left(\frac{\partial v}{\partial x} \dot{x} - \dot{z} \right) \right] dt, u(t_0) = u_0 \tag{6.97}$$

The state-space form of the error dynamics is:

$$\dot{e} = \mathbf{A}e + \mathbf{B}(v - r) \tag{6.98}$$

Matrices $\mathbf{A}$ and $\mathbf{B}$ are of the form defined earlier in Eq. 6.34

The variable z is now explicitly defined as follows:

$$z = \begin{bmatrix} k_1 & 0 & 0 & 0 \\ 0 & k_1 & 0 & 0 \\ 0 & 0 & k_1 & 0 \\ 0 & 0 & 0 & k_1 \end{bmatrix} \begin{bmatrix} y_{1d} - y_1 \\ y_{2d} - y_2 \\ y_{3d} - y_3 \\ y_{4d} - y_4 \end{bmatrix} + \begin{bmatrix} \dot{y}_{1d} \\ \dot{y}_{2d} \\ \dot{y}_{3d} \\ \dot{y}_{4d} \end{bmatrix} \tag{6.99}$$

Poles of this system can be specified to shape the desired dynamics. Theorem 1 in Zhang et al. (2020) shows that the error converges to zero and the controller in Eq. 6.97 asymptotically tracks the reference signal. The theorem and proof will not be repeated here.

6.6 Complete FBL+PID Controller

The generalised controller block diagram in Figure 6.1 can now be re-depicted to show the complete system and control loops. Also, a PID controller is used to close the outer loop and provide feedback control so that the primary controller design requirements set out in Chapter 3 are met. The complete scheme is now shown in Figure 6.2 for the case where controller gains are manually tuned.

The PID controller comprises four control laws, given as follows:

$$\begin{aligned} \delta e_{PID} =& Ke_z(z_{com} - z_{TR}) + Ke_{zI} \int (z_{com} - z_{TR}) dt \\ &+ Ke_{\dot{z}}(\dot{z}_{com} - \dot{z}_{TR}) \end{aligned} \tag{6.100}$$

$$\delta a_{PID} = Ka_\phi(\phi_{com} - \phi_{TR}) + Ka_{\phi I} \int (\phi_{com} - \phi_{TR}) dt + Ka_\phi(\dot{\phi}_{com} - \dot{\phi}_{TR}) \tag{6.101}$$

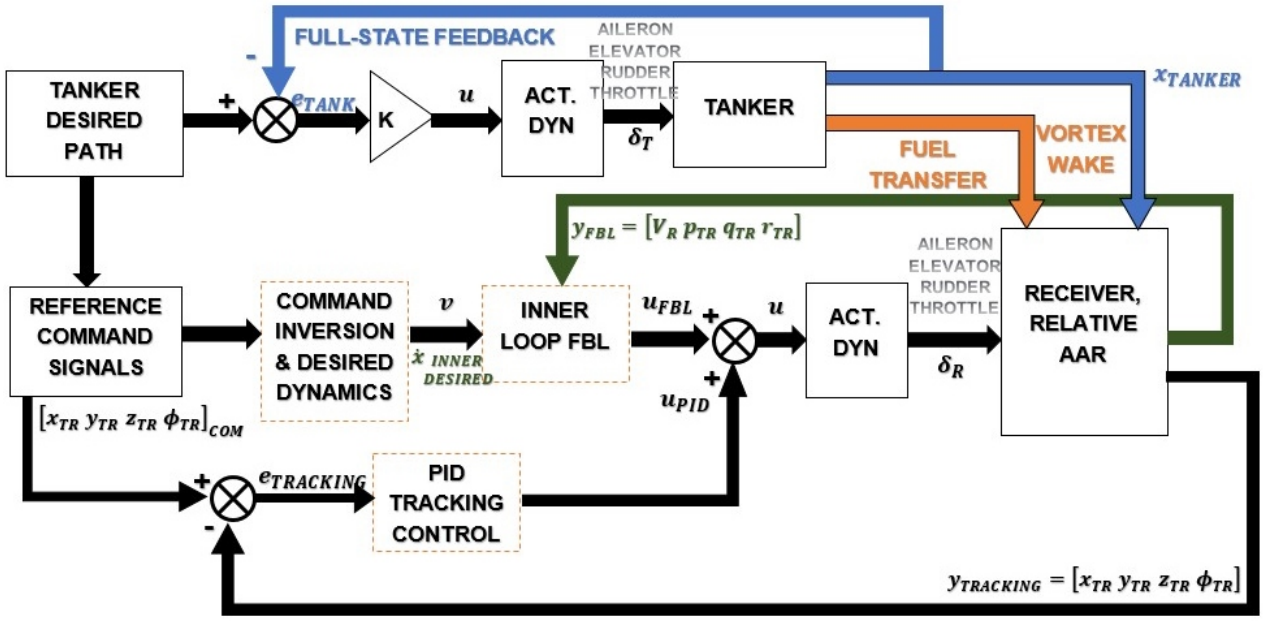


Figure 6.2: Feedback linearisation control block - manual tuning of controller gains

$$\delta r_{PID} = Kr_y(y_{com} - y_{TR}) + Kr_{yI}\int(y_{com} - y_{TR})dt + Kr_{\dot{y}}(\dot{y}_{com} - \dot{y}_{TR}) \tag{6.102}$$

$$\delta t_{PID} = Kt_x(x_{com} - x_{TR}) + Kt_{xI}\int(x_{com} - x_{TR})dt + Kt_{\dot{x}}(\dot{x}_{com} - \dot{x}_{TR}) \tag{6.103}$$

The total control signal is made up of the sum of the feedback-linearised portion and the PID contribution, as follows:

$$\begin{aligned} u_{\delta a} &= \delta a_{FBL} + \delta a_{PID} \\ u_{\delta e} &= \delta e_{FBL} + \delta e_{PID} \\ u_{\delta r} &= \delta r_{FBL} + \delta r_{PID} \\ u_{\delta t} &= \delta t_{FBL} + \delta t_{PID} \end{aligned} \tag{6.104}$$

Applying the actuator dynamics as defined in Chapter 3, the control laws developed here in Chapter 6 are the following:

$$\begin{aligned} \dot{\delta}_a &= \tfrac{1}{\tau_{\delta a}}(-u_{\delta a} + \delta a_0) \\ \dot{\delta}_e &= \tfrac{1}{\tau_{\delta e}}(-u_{\delta e} + \delta e_0) \\ \dot{\delta}_r &= \tfrac{1}{\tau_{\delta r}}(-u_{\delta r} + \delta r_0) \\ \dot{\delta}_t &= \tfrac{1}{\tau_{\delta t}}(-u_{\delta t} + \delta t_0) \end{aligned} \tag{6.105}$$

The genetic algorithm developed in Chapter 5 was used to optimise the controller gains for nonlinear controller designed in this chapter. Controller block diagram in Figure 6.3 shows

the incorporated algorithm and blocks where optimised gains have been applied. Twenty controller gains were optimised, twelve were from the PID feedback control and the additional eight were in the feedback-linearisation loop.

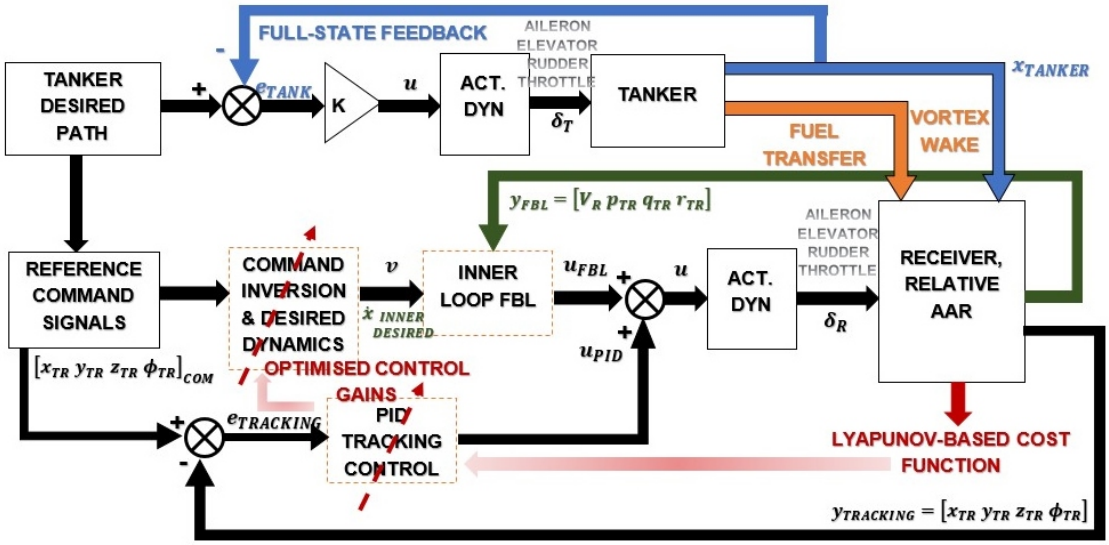


Figure 6.3: Feedback linearisation control block - hybrid Lyapunov-based evolutionary algorithm-optimised controller gains.

6.7 Dynamic Simulation of Automated Aerial Refuelling

6.7.1 Tuning and optimisation of the controller gains

Table 6.1 shows the manually-tuned values of the controller gains, as well as the upper and lower bounds that will be used in the genetic algorithm optimisation.

Although the presence of the minimum energy threshold was established in Chapter 5, the genetic algorithm was set run to 150 generations to observe changes, if any, in behaviour due to the difference in controller structure.

In Figure 6.4, two independent genetic algorithm runs to 150 generations were performed and the cost function evolution with time is shown. Each run began with its own (different) guess values from the defined search space. In both cases, examining the trend of the function J, the algorithm performance is as expected. However, the minimum energy level at $J = 1.752e8$ (shown by the red dashed line) is exceeded in both cases, with run 2 being only marginally exceeded. The effect of this will only become obvious once the dynamic simulation of AAR is performed with the controller gains derived from these runs. The minimum energy level

Table 6.1: Receiver aircraft controller gains and bounds

Gain	**Value**	**LB**	**UB**
Ke_z	-197	-197	-1
Ke_{zI}	-50	-50	-1
$Ke_{\dot{z}}$	-0.2	-1	-0.2
Ka_{ϕ}	-10	-100	-10
$Ka_{\phi I}$	10	10	20
$Kr_{\dot{\phi}}$	50	-50	-1
Kt_x	-40	-109	-40
Kt_{xI}	-99	-305	-34
$Kt_{\dot{x}}$	-600	-1000	-550
Kr_y	44	10	100
Kr_{yI}	100	-400	100
$Kr_{\dot{y}}$	-10	-10	10
K	diag[1 1 1 1]	diag[0.96]; $[4 \times 4]$	diag[1 1 1 1]
k_1	diag[1 1 1 1]	diag[0.96]; $[4 \times 4]$	diag[1 1 1 1]

at $J = 1.752e8$ was ascertained through trial-and-error in order to gain an understanding of the system performance instead of immediately applying parameters α and β.

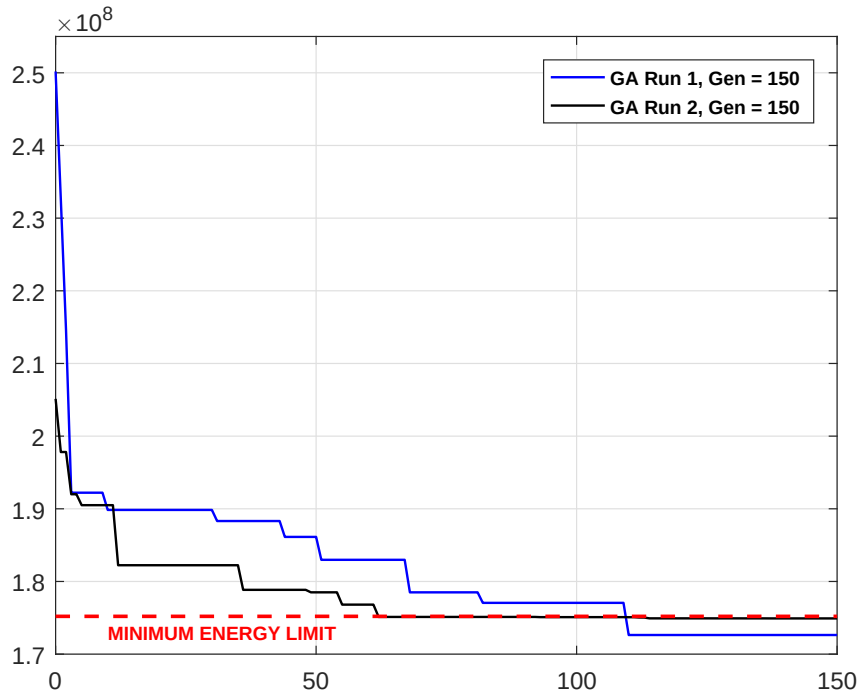


Figure 6.4: Minimum energy threshold - GA optimisation.

When the controller gains obtained from the optimisation set to 150 generations were applied to the refuelling manoeuvre, the divergent (and thus unstable) results can be seen in Figure 6.5 for the receiver state variables and in Figure 6.6 for the receiver control variables. These results are obviously unacceptable and validate the principle of a mininum level of energy to remain in the system. It is interesting to note that in the case of FBL, the poor results with these controller gains manifested in the baseline case, prior to the analysis with disturbances, allowing for a close examination of the threshold relationship to the number of generations.

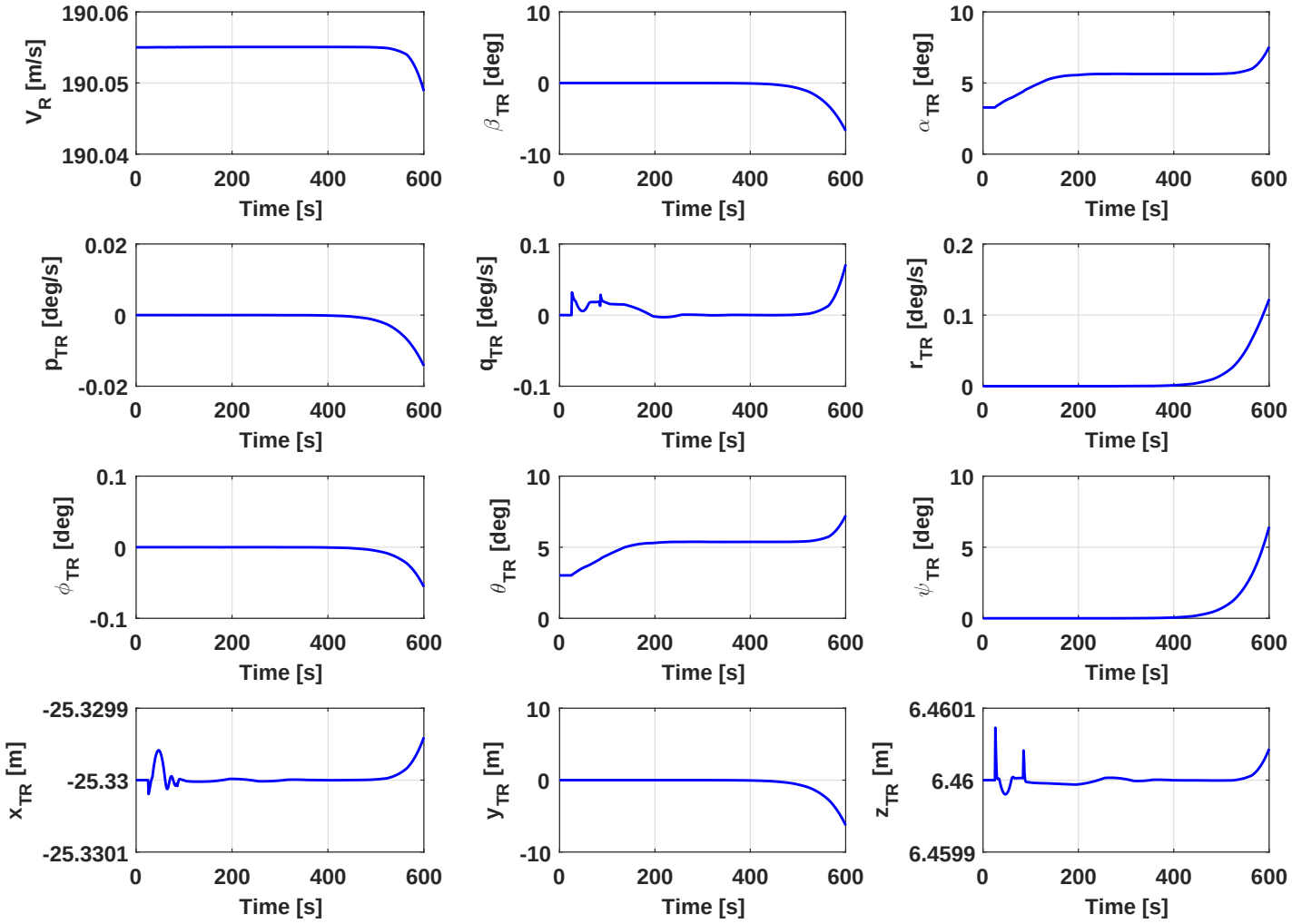


Figure 6.5: Receiver state variables with non-viable gains - deviation apparent.

The region of non-viable gains is shown in Figure 6.7. For the two independent runs of the algorithm, the minimum energy limit was breached at 110 generations for run 1 and at 62 generations for run 2. To show the effect on the controller gains itself, evolution of gain Ke_z is shown. Upon first glance, the trend shows the correct behaviour as expected in such an

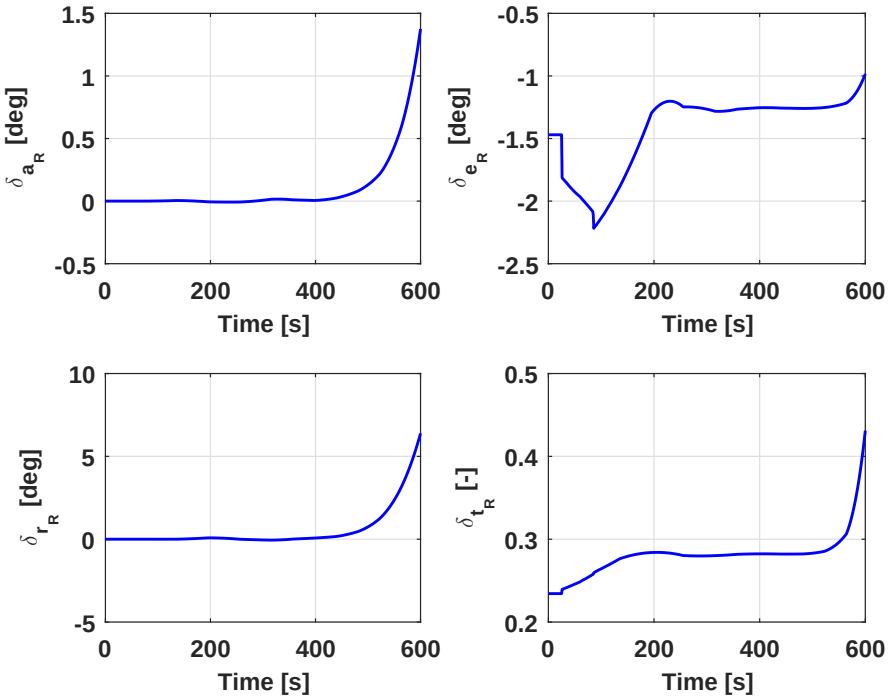


Figure 6.6: Receiver control variables with non-viable gains - deviation apparent.

optimisation routine, however, examination of the state and control behaviour shows that the controller gains selected from the region beyond the minimum energy will not yield a stable system, in line with the findings of the previous chapter.

6.7.2 Final optimised control gains

It was found that the 45 generations should be applied to the system to optimise the controller gains for the FBL system. The final controller gains obtained after optimisation is given in Table 6.2. When applying the parameter β to the manually-tuned J:

$$\begin{aligned} J_{min} = \beta \times J_{manual} \quad &= 0.8498 \times 2.051e8 \\ J_{min} &= 1.7411e8 \end{aligned} \tag{6.106}$$

Thus, the evolution of the cost function J for a new run of the genetic algorithm showed convergence within the minimum energy limit. This is also depicted in Figure 6.8.

The evolution of the controller gains are presented in Figures 6.9 to 6.11.

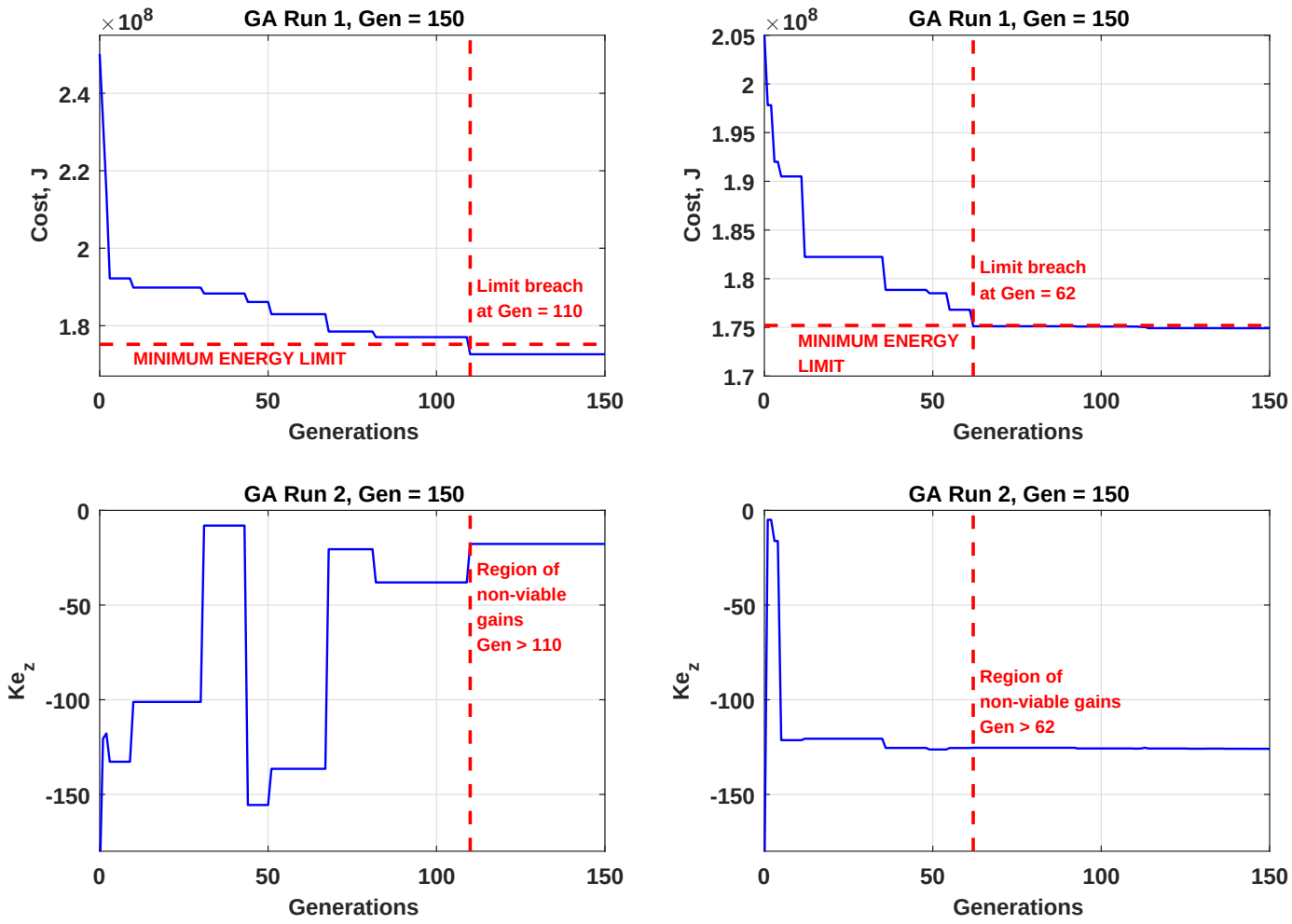


Figure 6.7: Minimum energy threshold and non-viable region of controller gains.

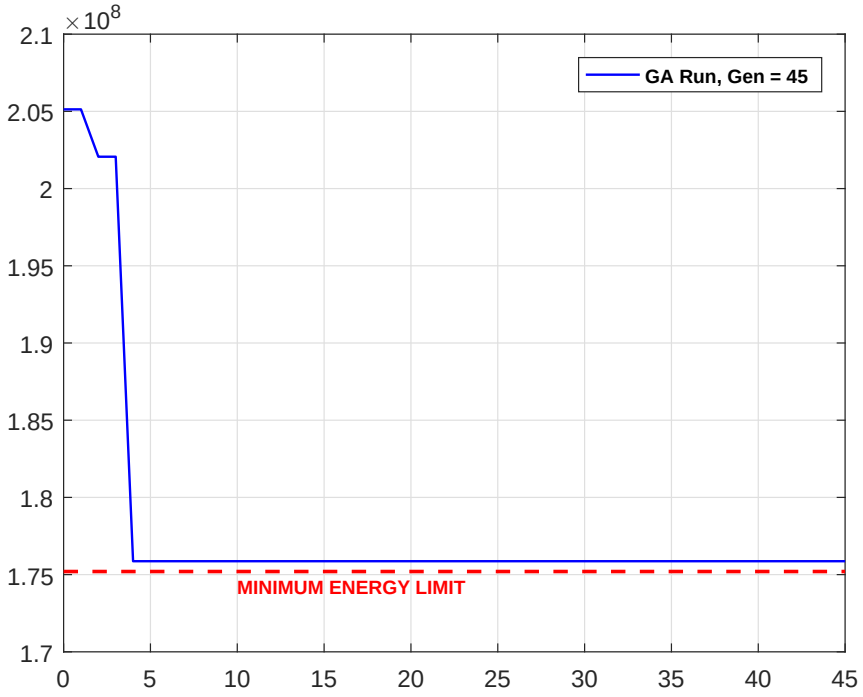


Figure 6.8: Minimum energy threshold - GA optimisation 45 runs.

Table 6.2: Receiver aircraft controller gains and bounds within energy limits

Gain	**Value**	**LB**	**UB**	**Optimised**
Ke_z	-197	-197	-1	-41.029
Ke_{zI}	-50	-50	-1	-18.544
$Ke_{\dot{z}}$	-0.2	-1	-0.2	-0.385
Ka_{ϕ}	-10	-100	-10	-99.493
$Ka_{\phi I}$	10	10	20	11.148
$Kr_{\dot{\phi}}$	50	-50	-1	-39.923
Kt_x	-40	-109	-40	-47.144
Kt_{xI}	-99	-305	-34	-114.848
$Kt_{\dot{x}}$	-600	-1000	-550	-590.325
Kr_y	44	10	100	57.551
Kr_{yI}	100	-400	100	49.984
$Kr_{\dot{y}}$	-10	-10	10	-6.141
K	diag[1 1 1 1]	diag[0.96]; $[4 \times 4]$	diag[1 1 1 1]	diag[0.989]; $[4 \times 4]$
k_1	diag[1 1 1 1]	diag[0.96]; $[4 \times 4]$	diag[1 1 1 1]	diag[0.994]; $[4 \times 4]$
J	2.051e8			1.759e8

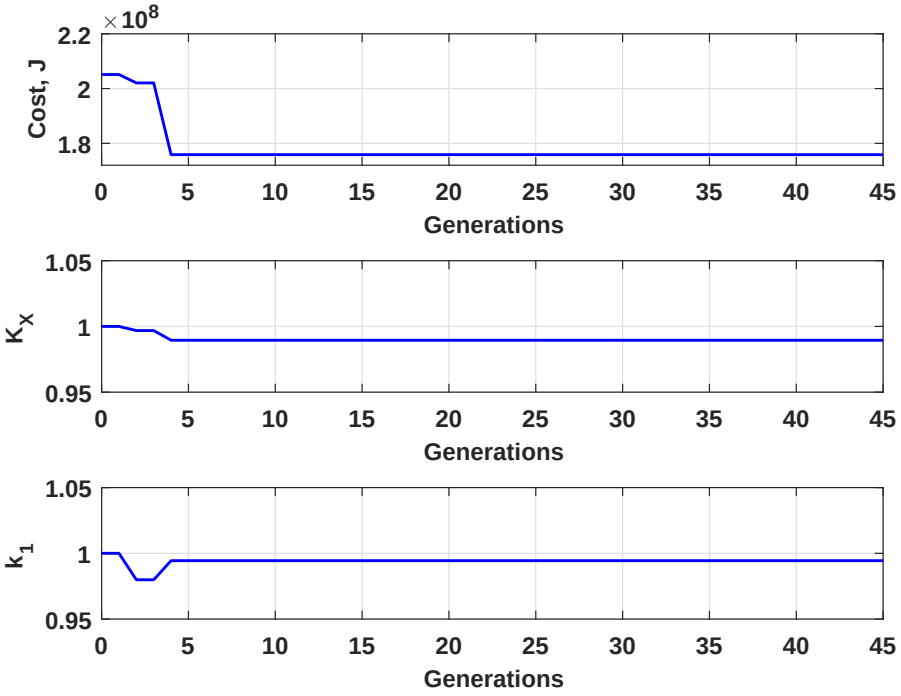


Figure 6.9: Cost and feedback linearisation controller gains.

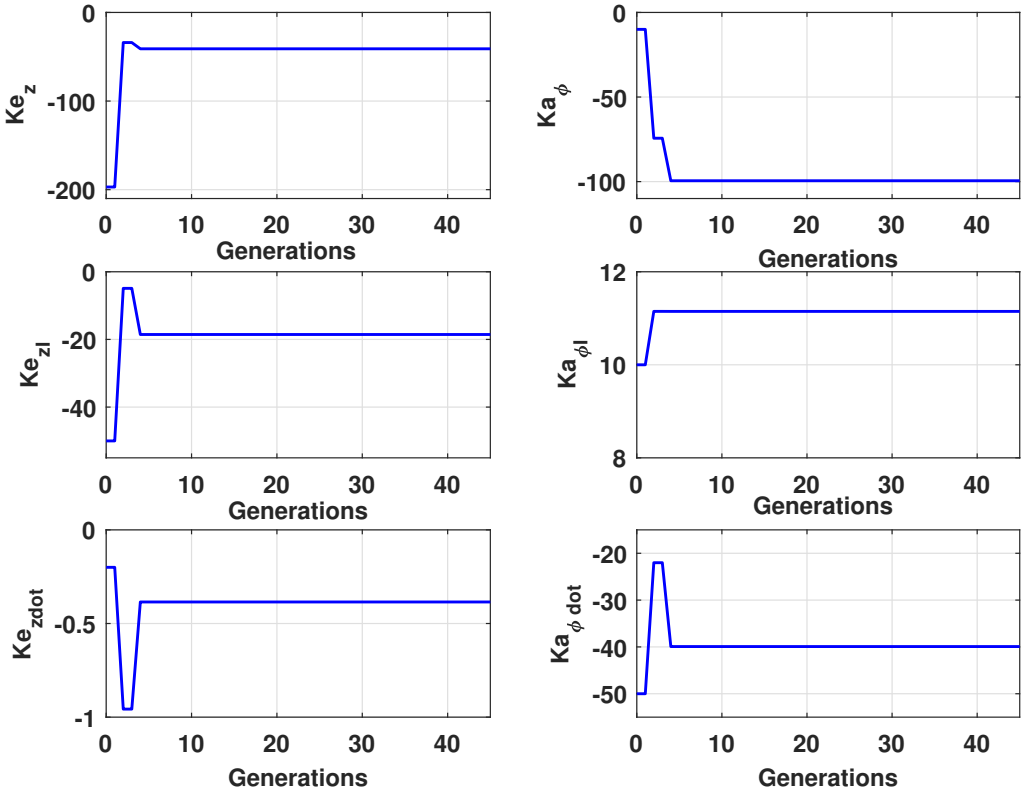


Figure 6.10: Feedback linearisation controller: K_e and K_a controller gains.

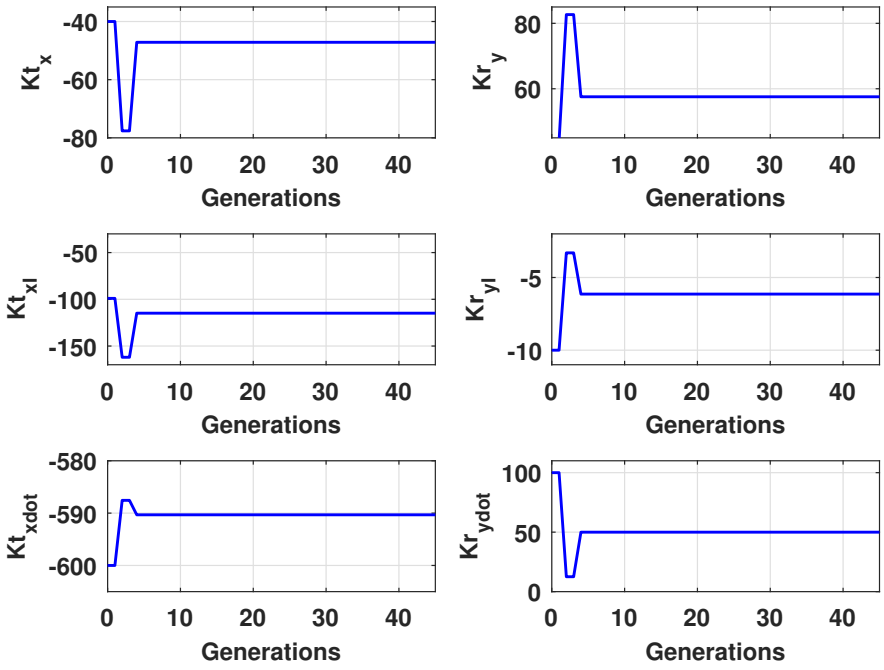


Figure 6.11: Feedback linearisation controller: K_t and K_r controller gains.

6.7.3 Simulation results

The cost function J and $\dot{J}$ for the manually-tuned and optimised controller gains are shown for the baseline, and two disturbance cases in Figure 6.12. As expected, since the mass flow rate is reduced in the defined mass disturbance, cost function J which is also a measure of system energy, is appropriately decreased compared to the baseline. The effect of tanker turbulence on the system is thus to add mechanical energy, since J is larger than that of the baseline case. The difference in J for the baseline and turbulence case becomes more prominent when examining the case where GA-optimised gains have been applied. Since the GA was applied to the baseline non-disturbed case, when the optimised controller gains are then subjected to tanker disturbance, it can be seen that J is distinctly higher than the baseline case. This is attributed to how the cost function J was formulated - as a representation of system energy. Whilst the baseline case was subject to energy being shed through optimisation, the turbulence acted to increase mechanical energy of the system that has not been shed, therefore, the case of the GA-optimised results is indeed larger than the baseline.

The inner-loop rotational rates are shown in Figure 6.13. The lateral-directional roll and yaw rates were sensitive to the addition of fuel to the aft tanks for the manually-tuned system. Upon application of the GA-optimised controller gains, this sensitivity was no longer manifested. The yaw rate was most sensitive to the disturbances applied, however, steady

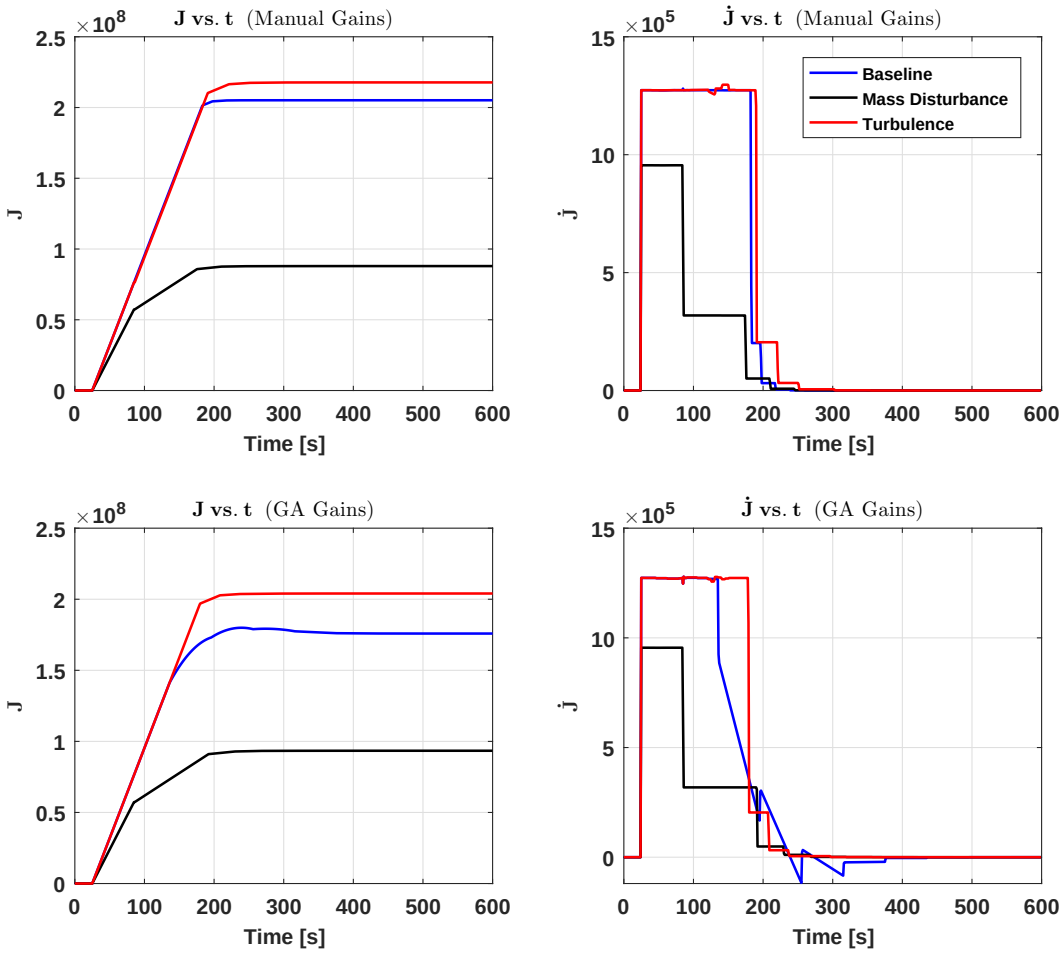


Figure 6.12: Lyapunov cost function and its derivative versus time - baseline + disturbances, manually-tuned and GA-optimised controller gains.

behaviour was attained as refuelling completed and the receiver aircraft remained on station. Additional pitch rate developed due to the tanker turbulence when introduced, and this settled back to zero once transient behaviour at the end of fuelling had dissipated. Although small, the additional pitch rate developed due to tanker turbulence will in turn affect the other longitudinal state variables.

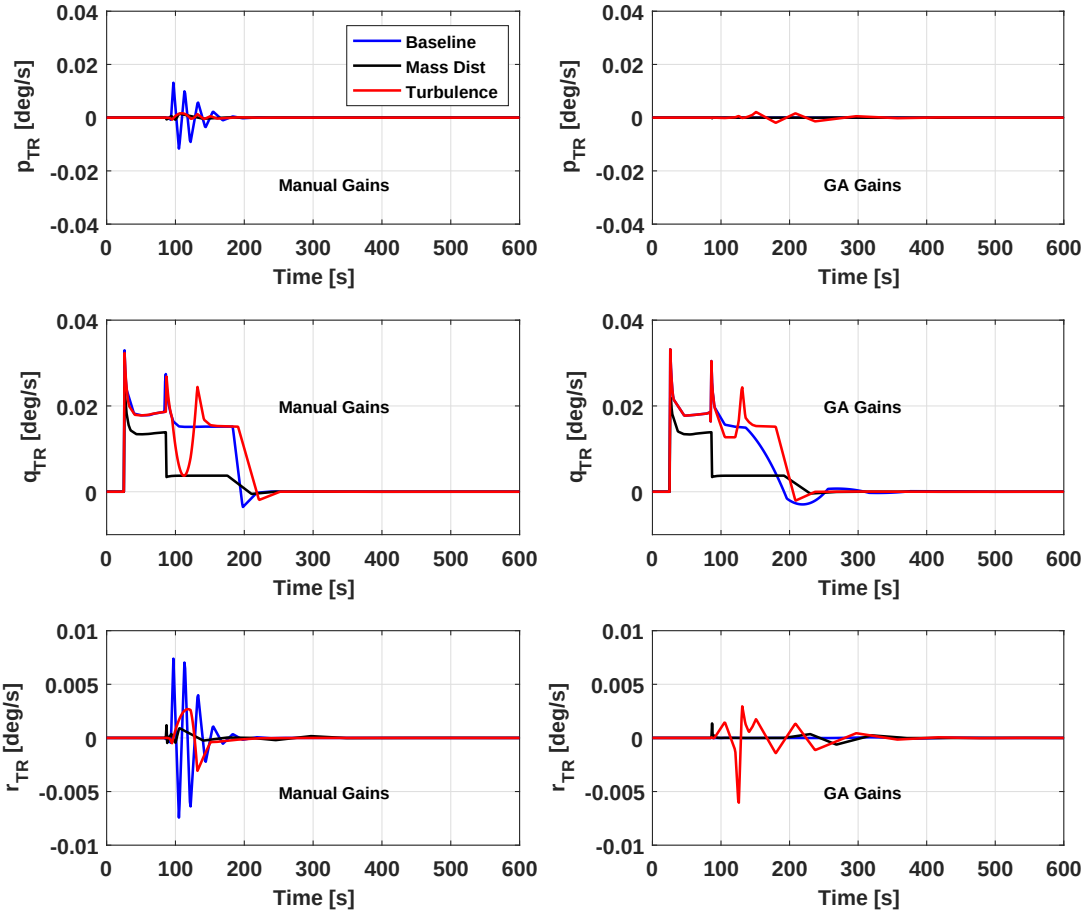


Figure 6.13: Receiver rotational rates versus time - baseline + disturbances, manually-tuned and GA-optimised controller gains.

The airspeeds, sideslip angle and angle of attack are shown in Figure 6.14. Yet again, sensitivity in the lateral-directional parameters to addition of fuel to the aft tanks can be seen in the sideslip angle time history. The angle of attack and airspeed showed steady behaviour, even with disturbances applied. An interesting observation to note is that while the results for the tanker disturbance angle of attack is steady, the value is higher than the baseline case with no disturbance. This corroborates with the trends observed in Figure 6.12 for the system energy. The airspeed showed transient behaviour when the tanker was affected

by turbulence. However, all state variables demonstrated steady behaviour as the transient effects diminished.

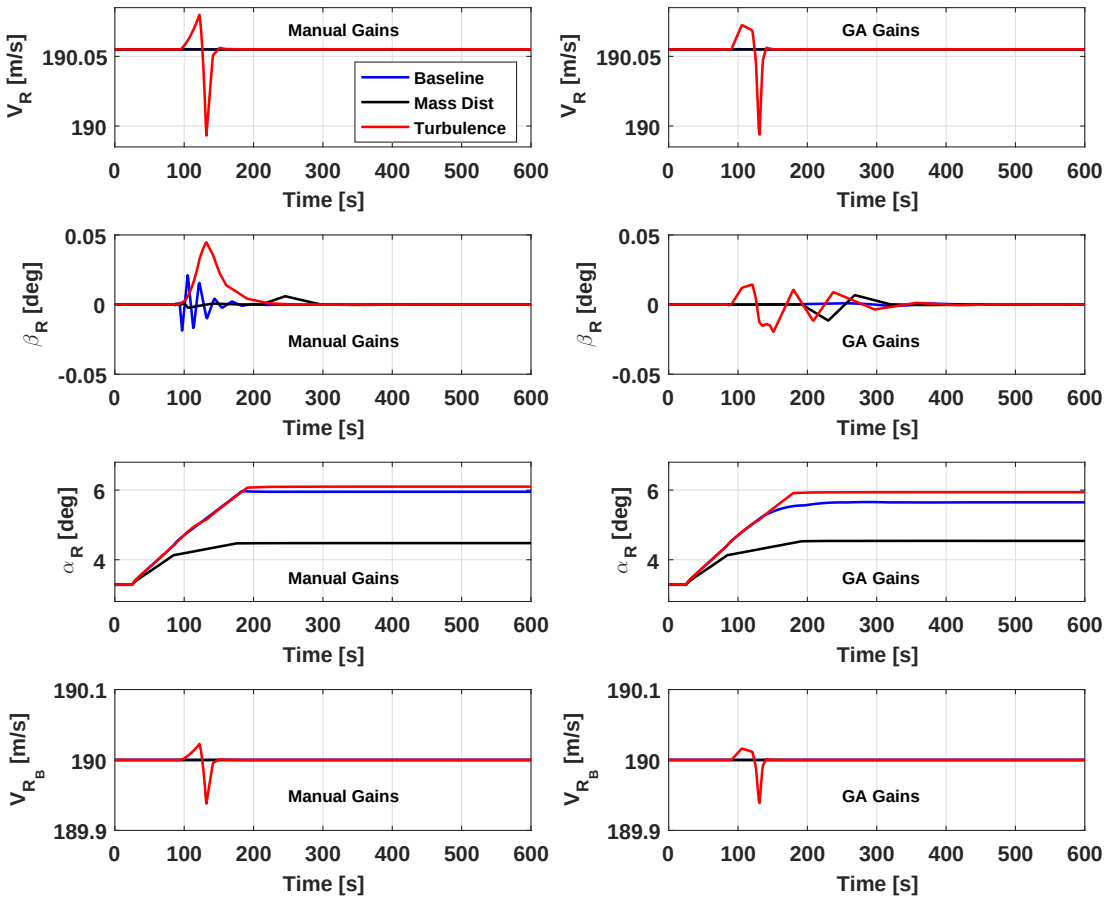


Figure 6.14: Receiver speeds and aerodynamic angles versus time - baseline + disturbances, manually-tuned and GA-optimised controller gains.

The receiver Euler angles relative to the tanker are shown in Figure 6.15. Roll and yaw angles showed similar trends to roll and yaw rates described earlier. The effects of the tanker turbulence disturbance on the roll and yaw angles are still prominent, even when the optimised controller gains are applied. However, the values return to their steady/nominal values as the manoeuvre is completed. Pitch orientation trends are similar to that of the angle of attack and are due to the effects of turbulence bringing additional energy into the system.

The receiver position relative to the tanker is shown in Figure 6.16. The x-separation showed most sensitivity to disturbances.

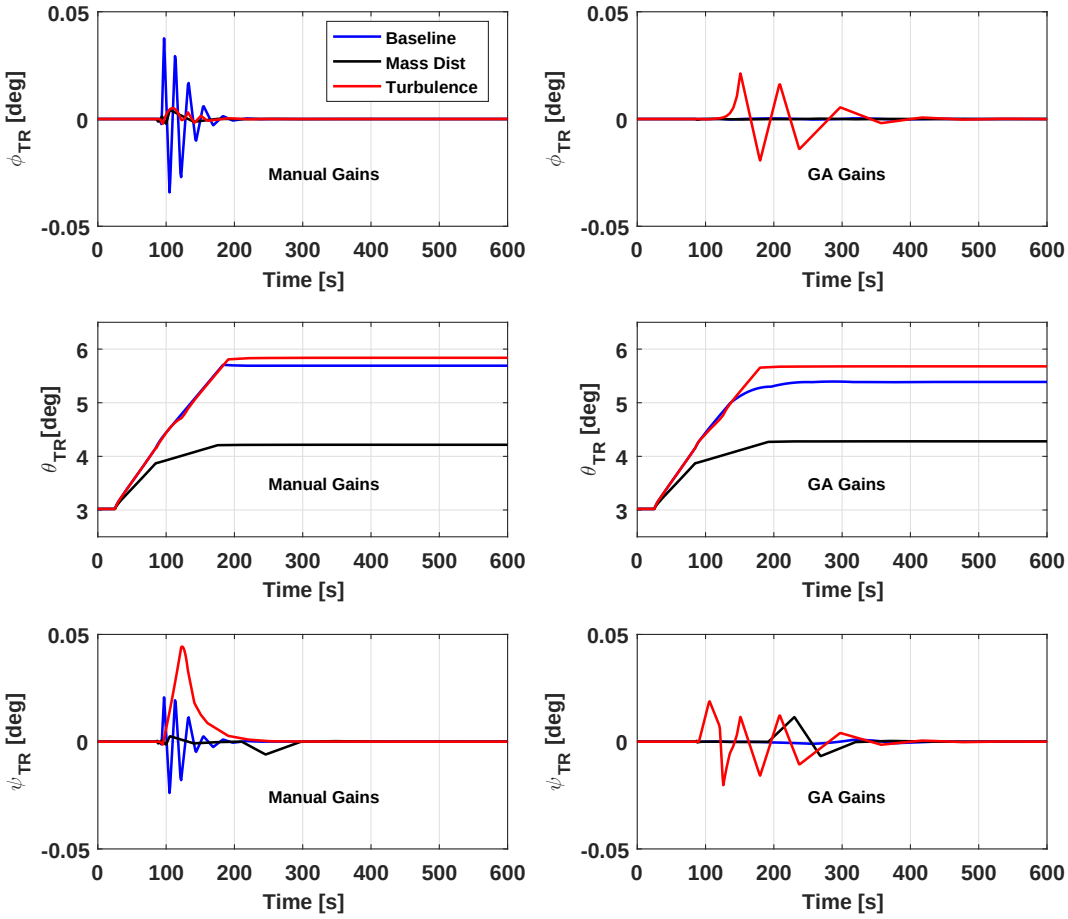


Figure 6.15: Receiver Euler angles versus time - baseline + disturbances, manually-tuned and GA-optimised controller gains.

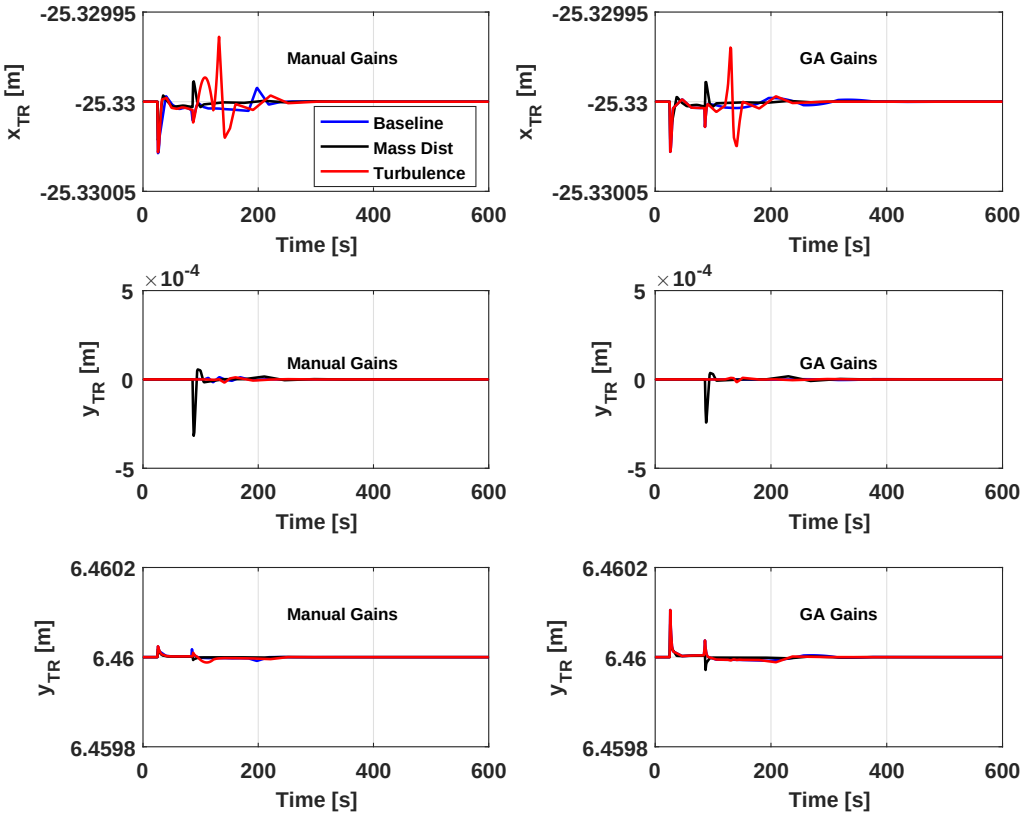


Figure 6.16: Receiver x-, y- and z-separation versus time - baseline + disturbances, manually-tuned and GA-optimised controller gains.

Receiver controller deflections for the manoeuvre are shown in Figure 6.17. The trends in elevator and throttle deflections are in line with that described earlier for other longitudinal state variables. The aileron and rudder deflections are non-zero for the asymmetry produced by the altered mass flow rate profile for the mass disturbance case.

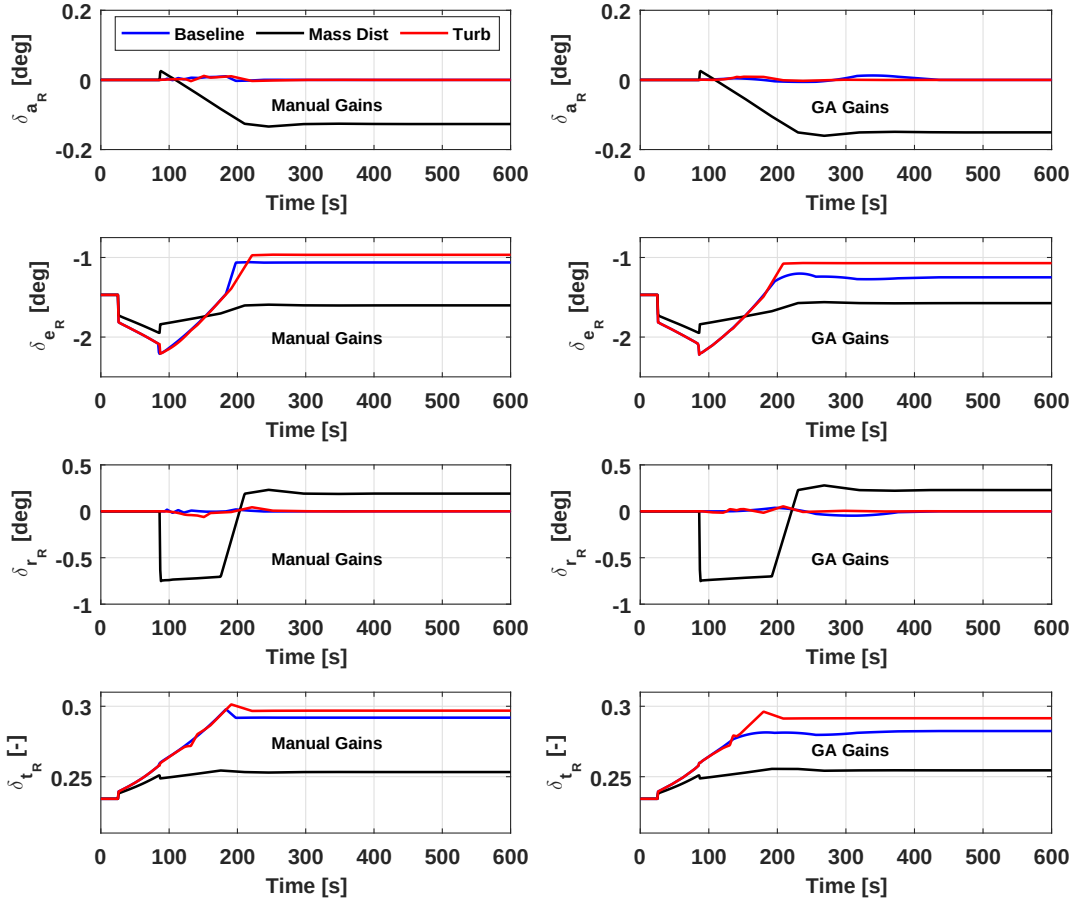


Figure 6.17: Receiver control surfaces' deflections versus time - baseline + disturbances, manually-tuned and GA-optimised controller gains.

The tanker aircraft state and control variables are shown in Figures 6.18 to 6.20

A benchmark control design was conceived in Chapter 3, to which the Lyapunov-based optimisation function was applied to the PSO and GA optimisation techniques in Chapter 5. The dynamic simulation was extended to $600s$ to ascertain the system stability. Thus, the nonlinear controller developed in this chapter will be compared to the results attained in Chapter 5.

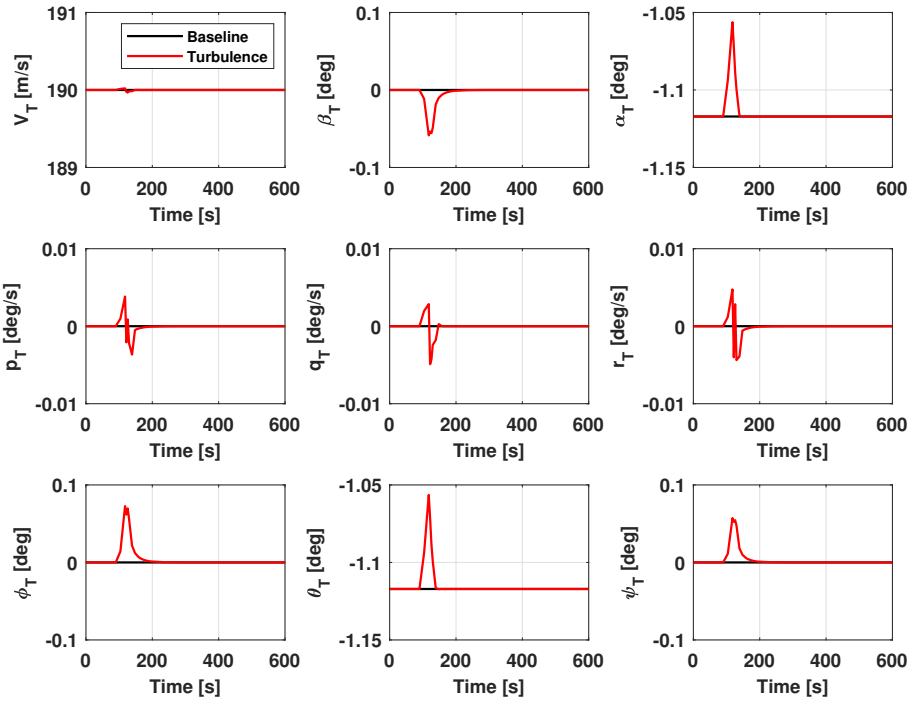


Figure 6.18: Tanker aircraft state variables.

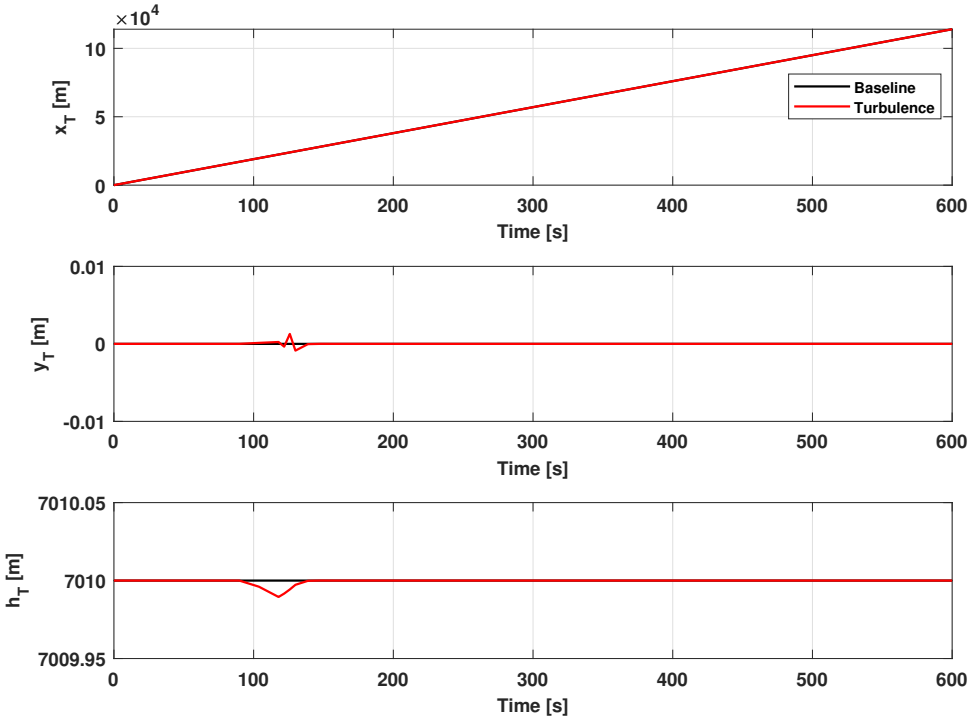


Figure 6.19: Tanker aircraft x- y- and z-positions along flight path.

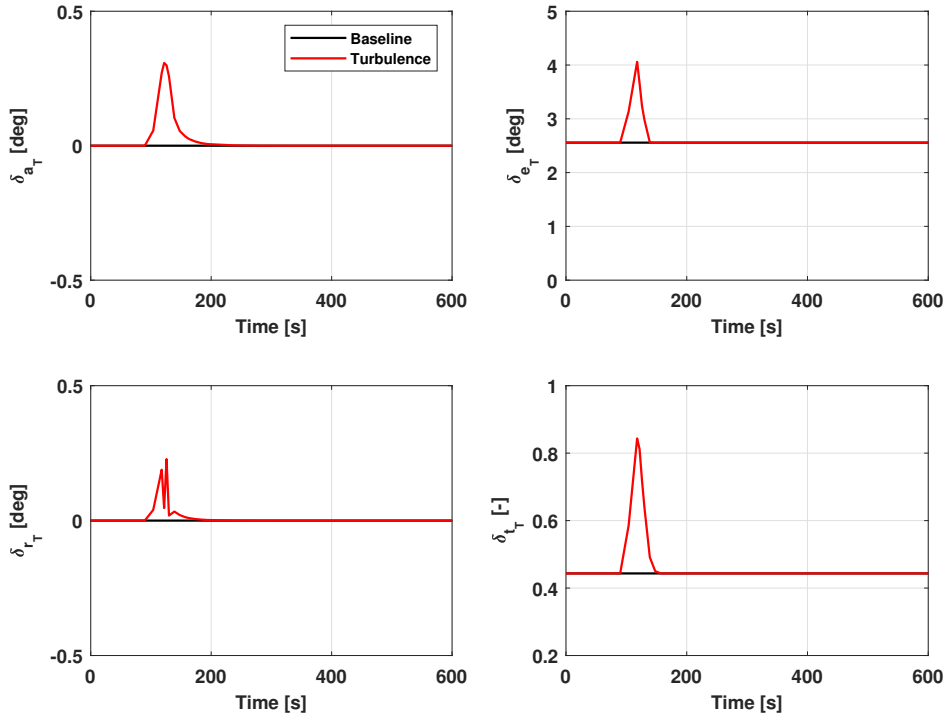


Figure 6.20: Tanker aircraft control surfaces' deflections.

The GA-optimised J for the nonlinear controller is $1.76e8$ compared to that obtained in Chapter 5 $J = 2.14e8$. However, the effect of the tanker turbulence disturbance on the receiver was in effect the addition of extra energy, whose presence was accounted for by the relevant longitudinal state and control variables.

Also, the magnitude of sideslip disturbance due to turbulence is decreased (1 degree for the PID controller to 0.05 degrees for the nonlinear controller). The magnitude of roll rate disturbance improved with the nonlinear controller, as well as the roll and yaw rate transient behaviour when subject to disturbances. The y-deviation magnitude reduced from 0.4m to –4e–4m and the transient behaviour due to turublence in the x-deviation improved was not as sharp as the PID controller. The unsteady behaviour in control surfaces' deflections was also improved. Most notable was the aileron and rudder deflections which minimally disturbed by the tanker turbulence.

6.8 Chapter Summary

This chapter introduced the theory of feedback linearisation and extended its application to a MIMO AAR system. A controller was designed using feedback linearisation in the inner loop, while employing a pseudo-backstepping scheme in the command inversion loop to convert the reference command signals into desired dynamics. PID tracking control was used to close the outer loop to give effect to controller tracking objectives. Manual tuning of controller gains was performed and the Lyapunov-based optimisation routine developed earlier was used to optimise the controller gains using the GA algorithm.

It was again shown that as the GA routine advanced through successive generations, too much energy was shed from the system impacting system stability as the states and controls were minimised in optimisation. The subsequent dynamic simulation results were not desirable when too much of energy was shed during optimisation. It was found that if the GA was run to 45 generations, then the parameters α and β were within the limits of the lower energy limit for optimisation. Disturbances were applied to the system to ascertain performance of the designed controller.

The FBL-based controller performed well compared to the benchmark case defined in Chapter 3 and Chapter 5. Improvements in tracking of the outer loop variables were observed as well as reductions in transient behaviours due to the addition of fuel during the manoeuvre. However, the sensitivity in the lateral-directional channel remained, with damped osciallatory behavior manifesting in the baseline case. Application of the Lyapunov-based GA-optimised controller gains eradicated this behaviour in the baseline case. The designed controller was also robust to disturbances. The same set of manually-tuned and GA-optimised controller gains were applied to both disturbance cases. No divergent or unstable behaviour was observed. The effect of the tanker turbulence on the system was to introduce additional mechanical energy and the values of angle of attack, pitch angle, elevator and throttle deflections were higher than the baseline case to keep the receiver aircraft steady relative to the tanker.

7 Application of Dynamic Neural Networks in Automated Aerial Refuelling System Modelling

7.1 Introduction

Many nonlinear control techniques require the use of a dynamical model. Nonlinear system models can be derived from physical principles/the laws of nature. Since nonlinear systems can exhibit complex behaviours, physical models give insight into its behaviour in varied operational circumstances. Challenges in developing these models (eg., cost or complexity) has led to alternative means of obtaining system models. Using measured input-output data, typically obtained from practical experimentation with the system, the required model can be identified. Neural networks have found a wide variety of applications, including system identification where nonlinear empirical models can be found (Nϕrgaard et al., (2000), Garces et al., (2003)).

Dynamic neural networks are represented by differential equations, as the introduction of feedback into a feedforward neural network architecture produces a state-space dynamic model of the form already presented in this study. One of the aims of this Chapter is to present the DNN in its dynamic model form (section 7.2), thus showing that the basis of analysis is the same as that presented in Chapter 6 for nonlinear systems. The DNN training and validation is addressed in section 7.3, where the parameters of the trained neural networks will be given.

7.2 Ordinary Differential Equation Representation of DNNs - Theoretical Overview

The nonlinear system given by:

$$\dot{x} = f(x) + g(x)u \tag{7.1}$$

$$y = h(x) \tag{7.2}$$

$$x \in \mathbf{R}^n,\ u \in \mathbf{R}^m,\ y \in \mathbf{R}^m,\ f(x) \in \mathbf{R}^n,\ g(x) \in \mathbf{R}^{n\times m},\ h(x) \in \mathbf{R}^{m\times n}$$

can be approximated by a neural network model of the form (Garces et al., (2003), Naimi et al., (2020), Fu et al., (2022)):

$$\dot{x}_n = -\beta x_n + \omega\sigma(x_n) + \gamma u \tag{7.3}$$

$$y_n = C_n x_n \tag{7.4}$$

$$x_n \in \mathbf{R}^N,\ u \in \mathbf{R}^p,\ y \in \mathbf{R}^p,\ \sigma(x_n) = \left[\ \sigma(x_1),\ \ \ldots,\ \ \sigma(x_n)\ \right]^T, \tag{7.5}$$

$$\gamma \in \mathbf{R}^{N\times p},\ C_n = \left[I_{p\times N} 0_{p\times(N-p)}\right],\ \beta \in \mathbf{R}^{N\times N},\ \beta = \operatorname{diag}\{\beta_1 \ldots \beta_N\}$$

Eqs. 7.3 and 7.4 represent a state-space dynamical model. Thus a DNN is said to be a neural network that includes recurrent or feedback elements, and uses differential equations to describe its behaviour.

A neural unit (see Figure 7.1) comprises of a dynamic transfer function $G(s)$ and activation function $\sigma(x)$. The neural unit is a first-order differential equation with a time constant β.

$$G(s) = \frac{1}{s+\beta_i} \tag{7.6}$$

$$\sigma(x_j) = \tanh(x_j) \tag{7.7}$$

When state feedback is introduced, the transfer function $G(s)$ will represent a dynamic system and not a static gain. An inside view of the DNN is shown in Figure 7.2. The first p states in vector x_n are the neural network output states (x^0). The remaining $N-p$ states are hidden (x^h). Thus Eq. 7.3 can be partitioned:

$$x_n = \begin{bmatrix} x^0 \\ x^h \end{bmatrix}, \quad x^0 \in \mathbf{R}^p, \quad x^h \in \mathbf{R}^{n-p} \tag{7.8}$$

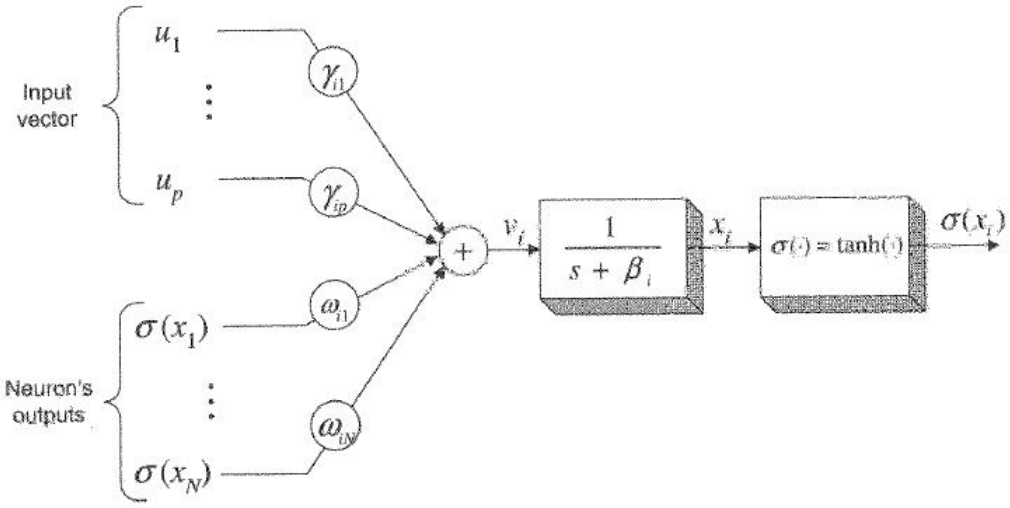


Figure 7.1: Neural unit (Garces et al., (2003)).

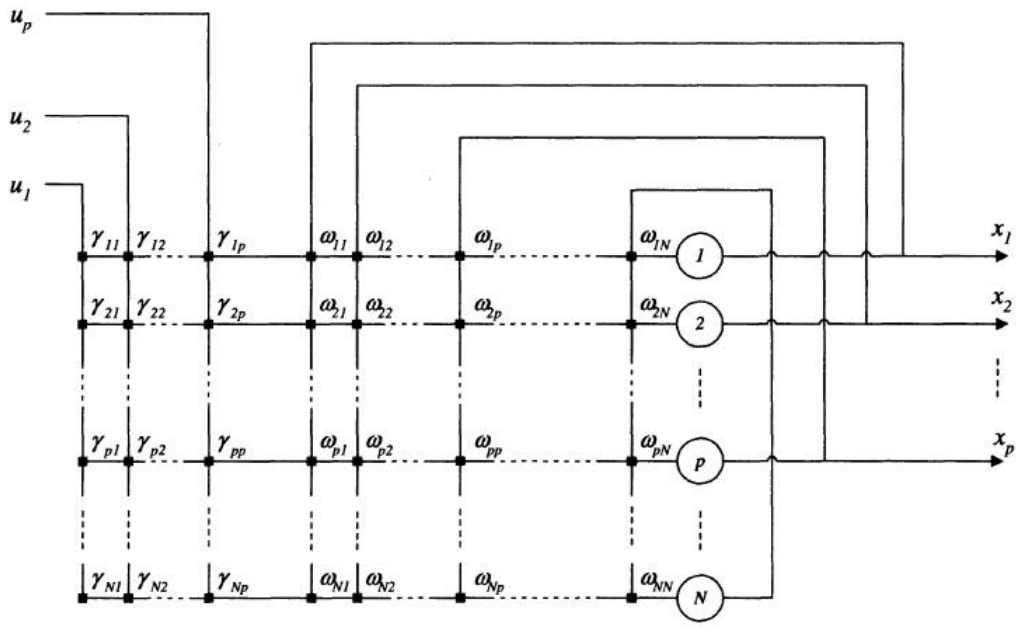


Figure 7.2: Inside view of neural unit (Garces et al., (2003)).

Since the DNN is analogous to the nolinear dynamical system studied in the previous chapter, it can be analysed using the same concepts developed earlier. The DNN also has a vector relative degree and characteristic matrix.

$$C(x) = \begin{bmatrix} L_{\gamma_1} L_f^{r_1-1} x_1 & L_{\gamma_2} L_f^{r_1-1} x_1 & ... & L_{\gamma_m} L_f^{r_1-1} x_1 \\ L_{\gamma_1} L_f^{r_2-1} x_2 & L_{\gamma_2} L_f^{r_2-1} x_2 & ... & L_{\gamma_m} L_f^{r_2-1} x_2 \\ ... & ... & ... & ... \\ L_{\gamma_1} L_f^{r_p-1} x_p & L_{\gamma_2} L_f^{r_p-1} x_p & ... & L_{\gamma_m} L_f^{r_p-1} x_p \end{bmatrix} \tag{7.9}$$

The relative degree given earlier in definition 6.2 can be extended to the DNN as well. The structure of the DNN, defined by values N and p, together with parameters β, ω and γ determine the relative degree. In particular, the first p states of x_n are the output states, and $y_n = C_n(x_n)$. When differentiating y in the manner outlined previously, the explicit emergence of u will depend on whether or not there are non-zero elements in γ related to the output y.

The stability of the neural network has to be ascertained prior to developing a controller. DNN stability is treated in the same way described in Chapter 6 earlier. A rigorous treatment of stability can be found in Chapter 3 of Leondes (1998), Chapters 4 and 5 of Garces et al., (2003), and Chapters 8 to 12 of Gupta et al., (2003). Pedro et al., (2014) has summarised that network stability is ensured if the following conditions hold:

1. The activation function $\sigma(\mathbf{x})$ is continuously differentiable.
2. $\sigma(\mathbf{x})$ is bounded to $0 \leq \sigma(\mathbf{x}) \leq 1$
3. Given $u_t \epsilon \mathbb{R}_+$, there is a symmetric and positive solution P to Eq. 7.10

$$\beta^{\mathbf{T}}\mathbf{P} - \mathbf{P}\beta = -\mu\mathbf{I} \tag{7.10}$$

   where $\mathbf{I}$ is an identity matrix and μ is a scaling factor, which Garces et al., (2003) argued should have a value of 1.

4. the inequality of Eq. 7.11 must be satisfied:

$$||\mathbf{W}||^2 \leq \frac{\mu - 2||P||}{||P||} \tag{7.11}$$

   where $||.||$ signifies the Euclidean norm of the specified matrix.

As the activation function $\sigma(\mathbf{x})$ is the hyperbolic tangent function, conditions 1. and 2. are fulfilled. Conditions 3. and 4. (Eq. 7.10 and the inequality of Eq. 7.11) are shown to hold in Theorem 4.5.3 of Garces et al., (2003). Hence, it may be concluded that the DNN described in Eq. 7.3 is stable.

7.3 Dynamic Neural Networks Training and Validation

Since system identification is meant to provide a neural nonlinear dynamic model approximation of the system to be later used in a controller design, it is important to understand the methodology adopted for the training process. The DNN training is framed as a nonlinear unconstrained optimisation problem. The cost function

$$\frac{1}{2M}\sum_{k=1}^{M}\|y(t_k)-\hat{y}(t_k|\theta)\|^2 \tag{7.12}$$

is minimised, where M represents the number of input-output pairs, $y(t_k)$ is the output data vector, $\hat{y}(t_k|\theta)$ is the output vector of the neural network model at time t_k given a decision vector θ and $\|\quad\|$ is the Euclidian norm. The decision vector θ contains the matrix coefficients in Eq. 7.3, whose values will generate the neural network model output $\hat{y}(t_k)$. The DNN is initialised by setting the DNN output states (x^0) at time t_1 as follows: $x^0(t_1)=y(t_1)$. The hidden states, $x^h(t_1)$ are initialised by solving the optimisation problem:

$$x^h(t_1)=arg\min_{x^h(t_1)}\|\dot{y}(t_1)-\dot{x}^o(t_1)\|^2 \tag{7.13}$$

where $\dot{y}(t_1)$ is calculated from the data using finite differences and $\dot{x}^o(t_1)$ is calculated from the DNN system equation, with β, ω and γ initialised with random values. Training can then be concluded by applying the minimisation in Eq. 7.3. Validation is performed using the same methodology, where the data for initialisation and comparison to predicted outputs is obtained from the validation data-set, which is different to the training data-set.

The nonlinear system described in Chapter 6 in Eqs. 6.67 - 6.68 was decoupled into four SISO systems. Each of these four systems were now approximated by the DNN system defined in Eqs. 7.3 - 7.4. The roll dynamics were related through p_{TR} and δ_{a_R} - this system will be referred to as **PDA**. The pitch dynamics were related through q_{TR} and δ_{e_R} - this system will be referred to as **QDE**. The yaw dynamics were related through r_{TR} and δ_{r_R} - this system will be referred to as **RDR**. Lastly, speed and thrust were related through V_R and δ_{t_R} - this system will be referred to as **VDT**.

7.3.1 Input-output data profile

In system identification, it is essential to select appropriate model data that describes the system behaviour over the expected operating range. A range of input data will ensure that

the output data captures the required amount of dynamics or trends that the estimation needs to be accurate.

The input u can be varied using the sum of sinusoids (Garces et al., (2003)):

$$u(t) = \sum_{j=1}^{M} a_j sin(\omega_j t + \phi_j) \tag{7.14}$$

where a_j is the amplitude, ω_j represents angular frequencies and ϕ_j denotes phase shifts.

The AAR system is unstable in the open-loop, that is, a bounded input would produce an unbounded output in the absence of the control system. Closed-loop system identification is therefore necessary in this case. The manually-tuned FBL-controlled system was used to generate the input and output data. Since DNNs are known for their superior ability to map complex systems, the non-optimised FBL was used for training. Also, in order to test the broader estimation ability of the DNN, the training and validation was limited to only the refuelling phase and not the station-keeping phase once fuel transfer had been completed.

In AAR, the dynamic simulation results from previous chapters show that the states and controls followed a very defined trajectory over time, so application of the parameters a_j (amplitude), ω_j (angular frequencies) and ϕ_j (phase shifts) could also destabilise the system. Through trial-and-error, a suitable u was parametrised and is given in Figure 7.3. When this input data was applied to the system model with FBL control, the output data shown in Figure 7.4 was generated. These data-sets were used in the DNN system identification. The data-set was split into a training data-set and a validation data-set.

7.3.2 Trained and validated models

Table 7.1 summarised the outcome of the training process for each of the four subsystems. The airspeed was the most intense to estimate, and 7 states were required to describe its behaviour with a neural network model. The airspeed included the effects of the tanker vortex wake and mapping required a greater number of neurons to estimate. The pitch dynamics was the second most complex relationship to map as it is complicated by the distinct phases in aerial refuelling, which in order to keep the receiver aircraft steady behind the tanker required q_{TR} to vary. The roll and yaw dynamics were easier to estimate, with 2 states each found to be adequate. This result can be attributed to the symmetric refuelling engagement, thus a lower level of complexity than the longitudinal dynamics was inherently present. All four of the estimated DNN models had relative degree of 1. This is the same as the relative degree of the original system described earlier in Chapter 6. Table 7.2 shows the training and validation mean-squared error (MSE) for each DNN.

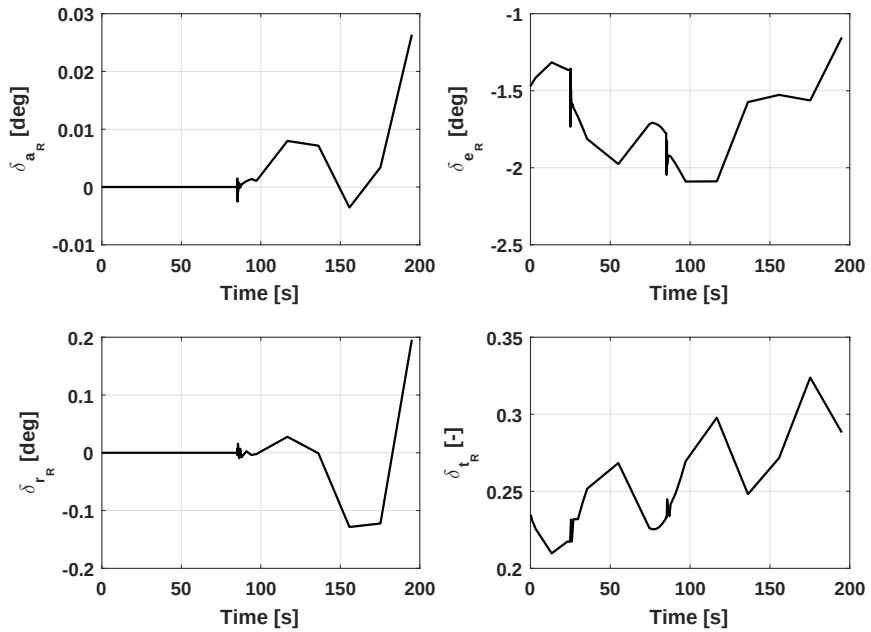


Figure 7.3: System identification receiver input data.

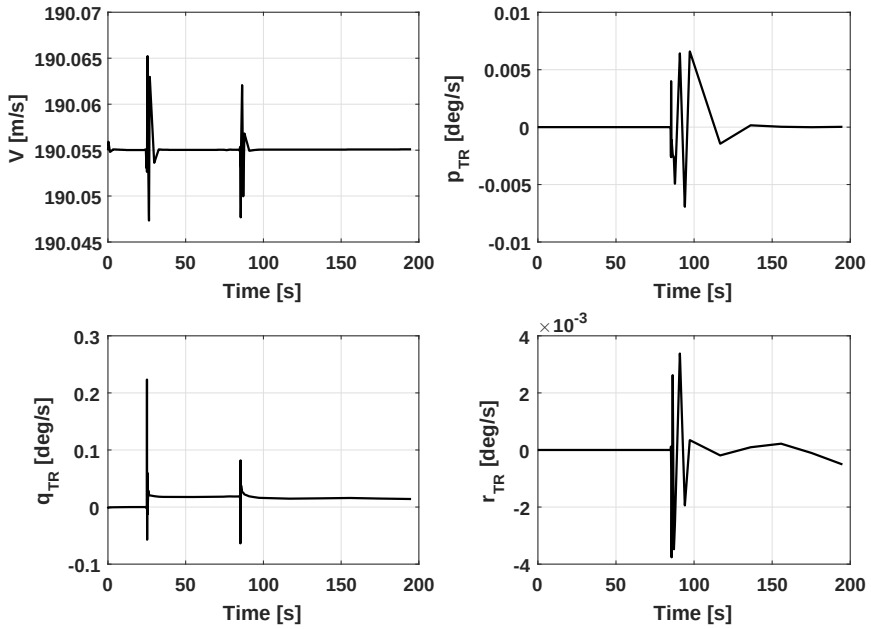


Figure 7.4: System identification - receiver output data.

Table 7.1: Trained DNNs information

Parameter	PDA	QDE	RDR	VDT
Number of inputs	1	1	1	1
Number of DNN states	2	3	2	7
Number of outputs	1	1	1	1
Number of hidden states	1	2	1	6
Relative degree/DNN System order	1	1	1	1

Table 7.2: Mean-squared error at optimal DNN state

Neural Model	Training MSE	Validation MSE
PDA	4.2335e-06	6.6874e-10
QDE	1.7915e-04	4.9322e-06
RDR	7.3865e-06	3.4406e-06
VDT	1.0397e-04	7.1266e-05

Figure 7.5 shows both the training and validation output data of the estimated **PDA** system compared to the original/measured system. In Figure 7.6, the MSE for training and validation vs. the number of possible system states is shown.

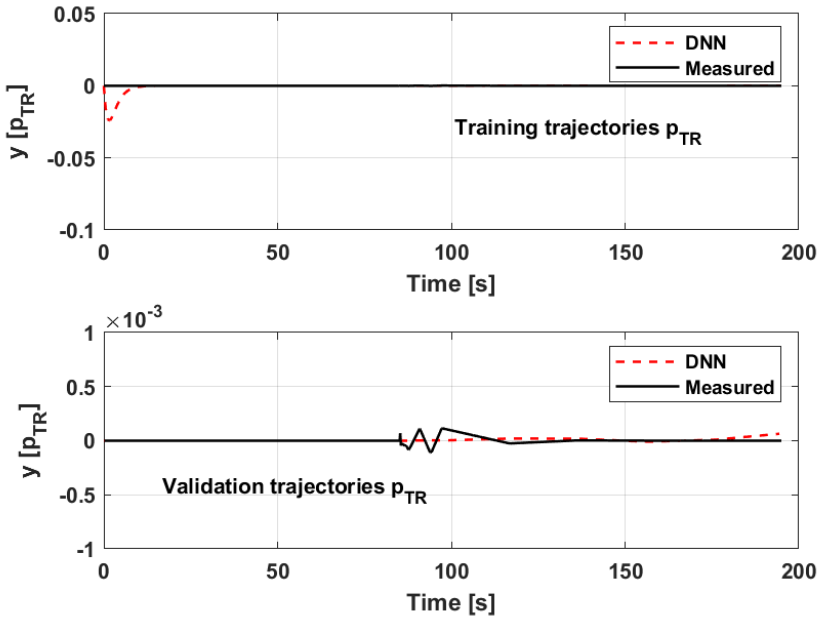


Figure 7.5: PDA training and validation trajectories.

The generated DNN for the PDA system is given by:

$$\dot{x}_P = -\boldsymbol{\beta}_P x_P + \boldsymbol{\omega}_P \sigma(x_P) + \boldsymbol{\gamma}_P u_P \tag{7.15}$$

with:

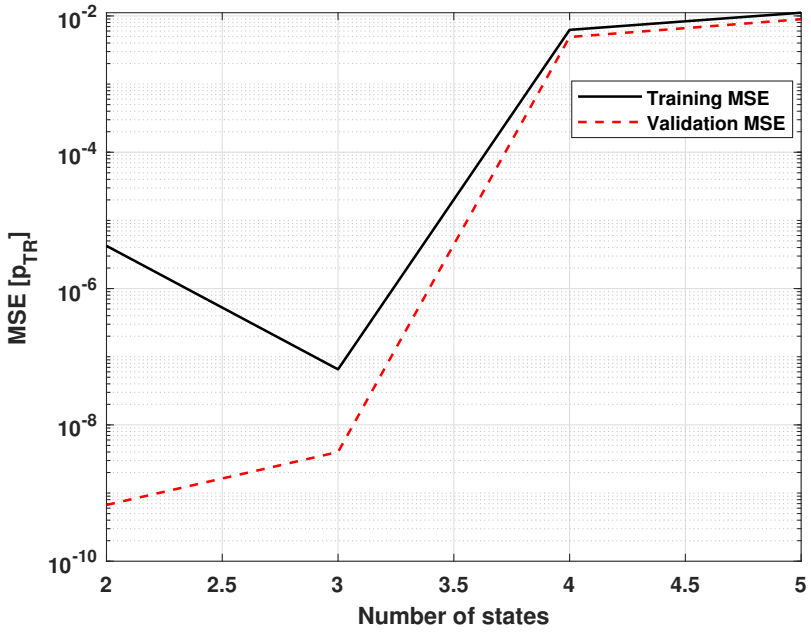


Figure 7.6: PDA MSE.

$$\beta_P = \begin{bmatrix} 1.3131 & 0 \\ 0 & 0.5879 \end{bmatrix} \tag{7.16}$$

$$\gamma_P = \begin{bmatrix} 0.1776 \\ 0.2536 \end{bmatrix} \tag{7.17}$$

$$\omega_P = \begin{bmatrix} 0.3301 & -0.0582 \\ 0.1644 & 0.1077 \end{bmatrix} \tag{7.18}$$

The initial values for the states, including the hidden layer is given by:

$$x_{0_{HIDDEN_P}} = \begin{bmatrix} 0 & 0.9282 \end{bmatrix} \tag{7.19}$$

Figure 7.7 shows both the training and validation output data of the estimated **QDE** system compared to the original/measured system. In Figure 7.8, the MSE for training and validation vs. the number of possible system states is shown.

$$\beta_Q = \begin{bmatrix} 1.7891 & 0 & 00 \\ 0 & 0.9413 & 0 \\ 0 & 0 & 0.8842 \end{bmatrix} \tag{7.20}$$

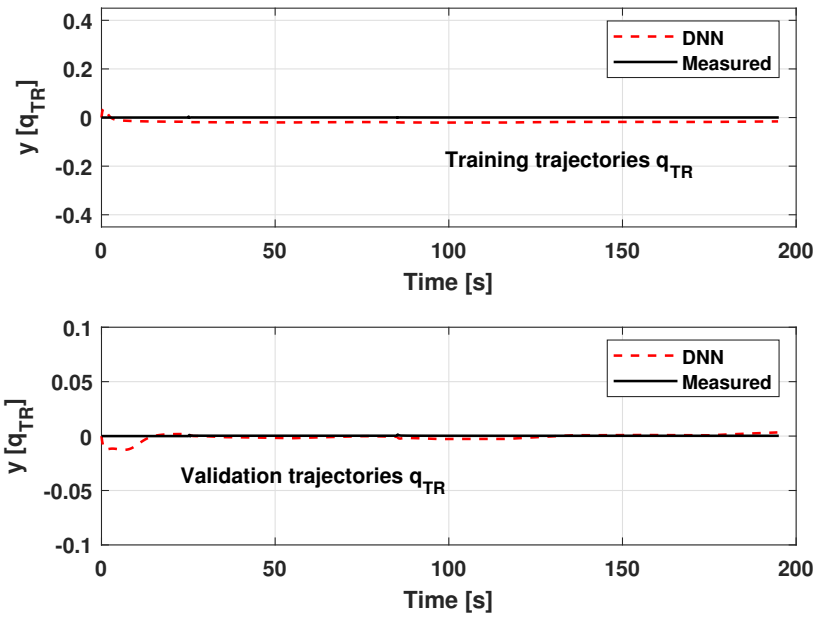


Figure 7.7: QDE training and validation trajectories.

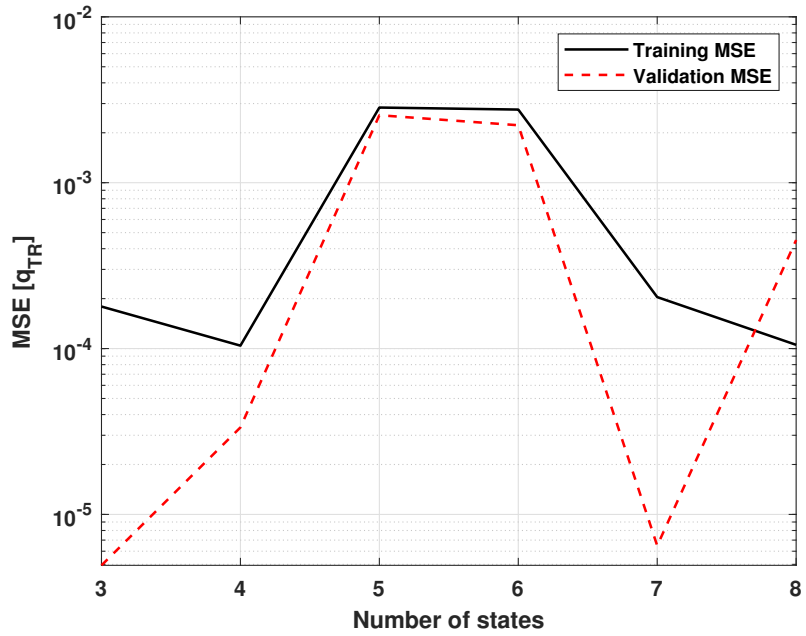


Figure 7.8: QDE MSE.

$$\gamma_Q = \begin{bmatrix} 1.1457 \\ 0.9025 \\ 0.4087 \end{bmatrix} \tag{7.21}$$

$$\omega_Q = \begin{bmatrix} 0.0383 & -0.4392 & 0.2629 \\ 0.8245 & 0.5129 & 0.3528 \\ 0.1708 & 0.9835 & 0.5630 \end{bmatrix} \tag{7.22}$$

$$x_{0_{HIDDEN_Q}} = \begin{bmatrix} 0 & 0.0228 & 0.8760 \end{bmatrix} \tag{7.23}$$

Figure 7.9 shows both the training and validation output data of the estimated **RDR** system compared to the original/measured system. In Figure 7.10, the MSE for training and validation vs. the number of possible system states is shown.

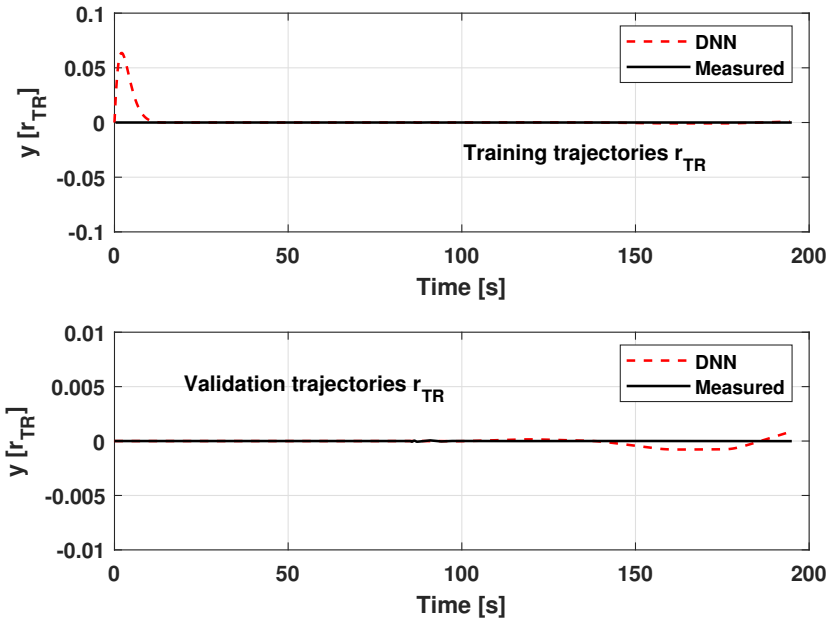


Figure 7.9: RDR training and validation trajectories.

$$\beta_R = \begin{bmatrix} 0.9174 & 0 \\ 0 & 0.6577 \end{bmatrix} \tag{7.24}$$

$$\gamma_R = \begin{bmatrix} 0.0174 \\ 0.9850 \end{bmatrix} \tag{7.25}$$

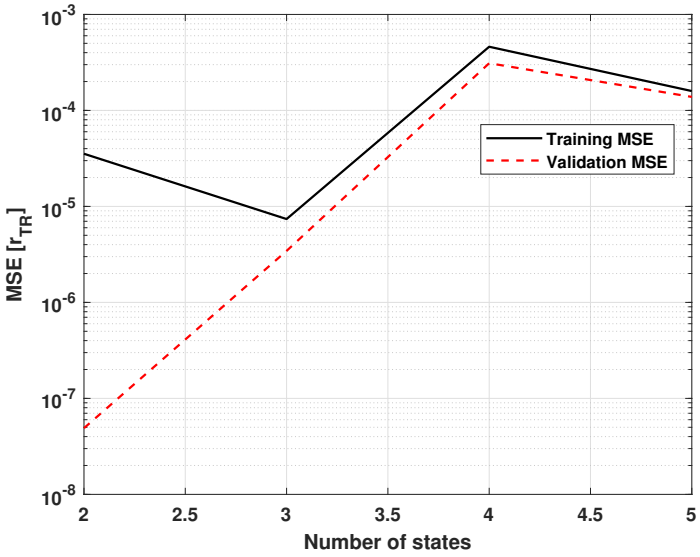


Figure 7.10: RDR MSE.

$$\omega_R = \begin{bmatrix} 0.4259 & 0.0983 \\ -0.5580 & 0.1596 \end{bmatrix} \tag{7.26}$$

$$x_{0_{HIDDEN_R}} = \begin{bmatrix} 0 & 1.0536 \end{bmatrix} \tag{7.27}$$

Figure 7.11 shows both the training and validation output data of the estimated **VDT** system compared to the original/measured system. In Figure 7.12, the MSE for training and validation vs. the number of possible system states is shown.

$$\beta_V = \begin{bmatrix} 1.2776 & 0 & 0 & 0 & 0 & 0 & 0 \\ 0 & 0.6201 & 0 & 0 & 0 & 0 & 0 \\ 0 & 0 & 0.5627 & 0 & 0 & 0 & 0 \\ 0 & 0 & 0 & 0.4793 & 0 & 0 & 0 \\ 0 & 0 & 0 & 0 & 0.8696 & 0 & 0 \\ 0 & 0 & 0 & 0 & 0 & 0.4288 & 0 \\ 0 & 0 & 0 & 0 & 0 & 0 & 0.8244 \end{bmatrix} \tag{7.28}$$

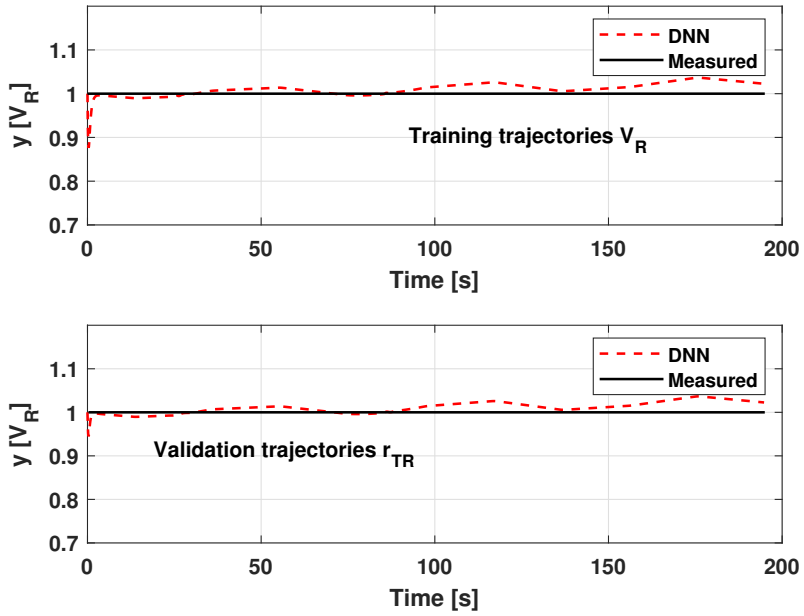


Figure 7.11: VDT training and validation trajectories.

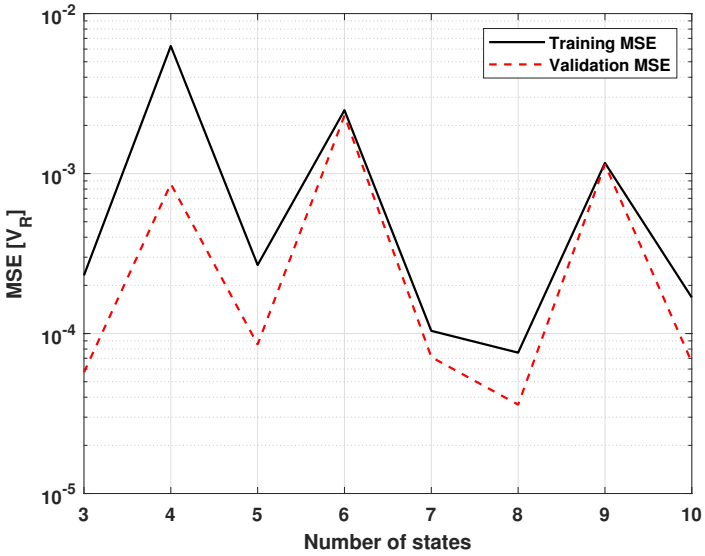


Figure 7.12: VDT MSE.

$$\gamma_V = \begin{bmatrix} 0.2136 \\ 0.0091 \\ 0.0359 \\ 0.9056 \\ 0.0643 \\ 0.0859 \\ 0.8252 \end{bmatrix} \tag{7.29}$$

$$\omega_V = \begin{bmatrix} 0.6789 & -0.0767 & 0.3515 & -0.1165 & -0.0443 & -0.1419 & 0.7386 \\ 0.1865 & 0.0624 & 0.2293 & 0.9284 & 0.7573 & 0.4945 & 0.7335 \\ 0.5166 & 0.0726 & 0.9164 & 0.8001 & 0.0671 & 0.5591 & 0.9955 \\ 0.0895 & 0.5148 & 0.2298 & 0.5612 & 0.4787 & 0.6572 & 0.3947 \\ 0.6860 & 0.9368 & 0.8953 & 0.2358 & 0.9294 & 0.5413 & 0.7309 \\ 0.6127 & 0.2043 & 0.3835 & 0.7622 & 0.6369 & 0.0615 & 0.9758 \\ 0.8954 & 0.4375 & 0.3589 & 0.6135 & 0.9257 & 0.0454 & 0.5464 \end{bmatrix} \tag{7.30}$$

$$x_{0_{HIDDEN_V}} = \begin{bmatrix} 1 & 0.5323 & 0.7618 & 0.4306 & 0.0701 & 0.5558 & 0.7688 \end{bmatrix} \tag{7.31}$$

7.4 Chapter Summary

In this chapter, the DNN was presented as a differential equation, analogous to the nonlinear system that has been studied in previous chapters. The incorporation of feedback into the neural network structure makes the network superior in its ability to map complex relationships. As the DNN was constructed as a nonlinear dynamical system, concepts such as relative degree, the characteristic matrix were the same as previously presented for nonlinear systems in general. Stability was also a pertinent issue and was dealt with extensively in a number of cited sources, with this chapter presenting only a summary of conditions that are to hold for DNN stability to be ensured.

System identification was performed with input-output data sets for training and validation. The input data was generated using the sum of sinusoids approach. Four SISO subsystems were obtained. Each of the 4 DNN systems had system order of 1. The most complex neural mapping was the airspeed, followed by the pitch dynamics. Mean squared errors and training/validation trajectories were presented and the numeric values of parameters β, ω and γ for each trained DNN were given.

8 Dynamic Neural Network-Based Feedback Linearisation Controller

8.1 Introduction

In earlier chapters, the theoretical foundations were laid in order to synthesise techniques in nonlinear and intelligent control to form a DNN-based FBL controller that guarantees system stability while meeting performance specifications and robustness when subject to disturbances. This chapter will provide the final portion required for this synthesis - the development of an input-output feedback linearising control law based on the identified neural models. Section 8.2 presents the theory as applied to the DNN dynamical system model, while showing how the state feedback law is developed for the DNN. The controller structure is outlined in section 8.3, including the depiction of the Lyapunov-based optimisation within the structure. Simulation results based on manually-tuned and GA-optimised controller gains are presented in section 8.4. The PID and FBL controllers are compared with the DNN-based controller in section 8.5.

8.2 Dynamic Neural Network-Based Feedback Linearisation

It was stated in Chapter 7 that the nonlinear system given by:

$$\dot{x} = f(x) + g(x)u \tag{8.1}$$

$$y = h(x) \tag{8.2}$$

$$x \in \mathbf{R}^n,\ u \in \mathbf{R}^m,\ y \in \mathbf{R}^m,\ f(x) \in \mathbf{R}^n,\ g(x) \in \mathbf{R}^{n\times m},\ h(x) \in \mathbf{R}^{m\times n}$$

could be approximated by a neural network model in state-space dynamical form (Garces et al., (2003), Naimi et al., (2020), Fu et al., (2022)):

$$\dot{x}_n = -\beta x_n + \omega\sigma(x_n) + \gamma u \tag{8.3}$$

$$y_n = C_n x_n \tag{8.4}$$

$$x_n \in \mathbf{R}^N,\ u \in \mathbf{R}^p,\ y \in \mathbf{R}^p,\ \sigma(x_n) = \left[\ \sigma(x_1),\quad \ldots,\quad \sigma(x_n)\ \right]^T, \tag{8.5}$$

$$\gamma \in \mathbf{R}^{N\times p},\ C_n = \left[I_{p\times N} 0_{p\times(N-p)}\right],\ \beta \in \mathbf{R}^{N\times N},\ \beta = \text{diag}\left\{\beta_1 \ldots \beta_N\right\}$$

The control law was formulated using the same approach used in Chapter 6. For a dynamic neural network given in Eq. 8.3, whose parameters β, ω and γ have been computed as described in Chapter 7, the relative degree can be obtained. As the neural network model is a nonlinear dynamical system, definition 6.2 in Chapter 6 applies, with Eq. 6.10 applicable for SISO systems and Eq. 6.50 for MIMO systems. Rewriting in the notation used for the DNN, the relative degree is obtained when the following relationship is reached, after successive differentiation has been applied to each output $h_i(x)$:

$$L_{g_j} L_f^k h_i(x) = 0,\ i = 1, 2, \cdots, r-1;\ L_g L_f^{r-1} h(x) \neq 0 \tag{8.6}$$

The vector relative degree will be $\left\{\ r_1,\quad r_2,\quad \ldots\quad r_p\ \right\}$. The resulting characteristic matrix is given below and is similar to Eq. 6.51

$$C(x) = \begin{bmatrix} \sum_{i=1}^{N} \gamma_{ij} \frac{\partial L_f^{r_1-1} x_1}{\partial x_i} & \cdots & \sum_{i=1}^{N} \gamma_{ip} \frac{\partial L_f^{r_1-1} x_1}{\partial x_i} \\ \vdots & \ddots & \vdots \\ \sum_{i=1}^{N} \gamma_{ij} \frac{\partial L_f^{r_p-1} x_p}{\partial x_i} & \cdots & \sum_{i=1}^{N} \gamma_{ip} \frac{\partial L_f^{r_p-1} x_p}{\partial x_i} \end{bmatrix}_{p\times p} \tag{8.7}$$

The parameter λ_{ik} defined earlier in Eq. 6.55 is now written as $\hat{\lambda}_{ik}$, to denote its incorporation into the neural model.

Then, a state feedback law with

$$u = P(x_n) + Q(x_n) v \tag{8.8}$$

produces a linearised-decoupled system that obeys

$$\sum_{k=0}^{r_i} \hat{\lambda}_{ik} \frac{d^k y_{n_i}}{dt^k} = v_i,\ i = 1 \ldots p \tag{8.9}$$

with r_i, the relative degree of the ith output y_{n_i}, being well defined, $A(x_n)$ invertible, and

$$\det\left[\text{diag}\left(\begin{array}{cccc}\hat{\lambda}_{1_{r1}} & \hat{\lambda}_{2_{r2}} & \ldots & \hat{\lambda}_{p_{rp}}\end{array}\right)\right] \neq 0 \tag{8.10}$$

This is the equivalent of Eq. 6.62, with the neural network parameters being used in this case. Also,

$$P(x_n) = -A(x_n)^{-1}B(x_n) \tag{8.11}$$

$$Q(x_n) = A(x_n)^{-1} \tag{8.12}$$

where

$$A(x_n) = \begin{bmatrix} \hat{\lambda}_{1r_1}L_{g_1}L_f^{r_1-1}x_{n_1} & \ldots & \hat{\lambda}_{1r_1}L_{g_p}L_f^{r_1-1}x_{n_1} \\ \ldots & \ldots & \ldots \\ \hat{\lambda}_{pr_p}L_{g_1}L_f^{r_p-1}x_{n_p} & \ldots & \hat{\lambda}_{pr_p}L_{g_p}L_f^{r_p-1}x_{n_p} \end{bmatrix}_{p\times p} \tag{8.13}$$

and

$$B(x_n) = \begin{bmatrix} \sum_{k=0}^{r_1}\hat{\lambda}_{1k}L_f^k x_{n_1} \\ \ldots \\ \sum_{k=0}^{r_p}\hat{\lambda}_{pk}L_f^k x_{n_p} \end{bmatrix}_{p\times 1} \tag{8.14}$$

When the control law in Eq. 8.8 is applied to the system in Eq. 8.1, then its dynamics are approximately input-output linearised and decoupled, and obeys the following equations:

$$\sum_{k=0}^{r_i}\hat{\lambda}_{ik}\frac{d^k y_i}{dt^k} = v_i + \sum_{k=0}^{r_i}\hat{\lambda}_{ik}\frac{d^k e_i}{dt^k},\ i = 1,\ldots,p \tag{8.15}$$

where e_i is the model error corresponding to the ith output:

$$e_i = y_i - y_{n_i} \tag{8.16}$$

Expressed in the Laplace domain:

$$y_i(s) = \frac{1}{\hat{\lambda}_{ir_i}s^r + \ldots\hat{\lambda}_{i0}}v(s) + e_i(s) \tag{8.17}$$

The model error can be seen as an output disturbance on output $y_i(s)$, but this error is dealt with within the DNN training algorithm. Any linear method can be used to design the synthetic input v_i.

8.3 Controller Structure

The controller structure is shown in Figure 8.1. The DNN was incorporated in the inner loop where the feedback linearisation control portion of the overall controller was situated. The DNN was used to estimate the parameters of the system from input-output data and, which was then used as the basis of the FBL, where the identified neural network model was used to produce the linearising feedback law. The DNN also included a weight-updating algorithm to address the approximation error between the neural network model and the actual system. This indirect adaptive control scheme in the inner-loop was closed using the same outer-loop structure and parameters described in Chapter 6. The inner-loop synthetic control v_i was constructed as shown in Eqs. 6.78 - 6.81 using the neural network model output y_n. Figure 8.2 shows the control block diagram with the Lyapunov-based optimisation routine incorporated.

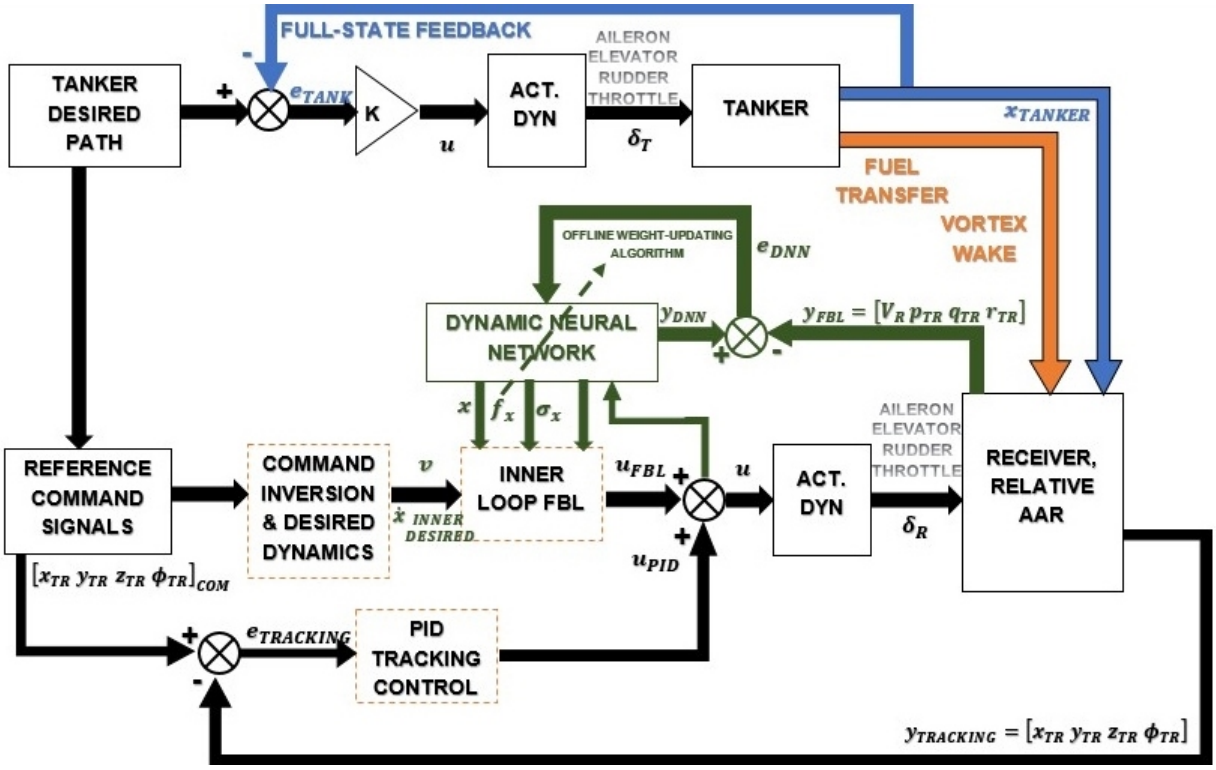


Figure 8.1: Controller block diagram - DNN-based FBL controller

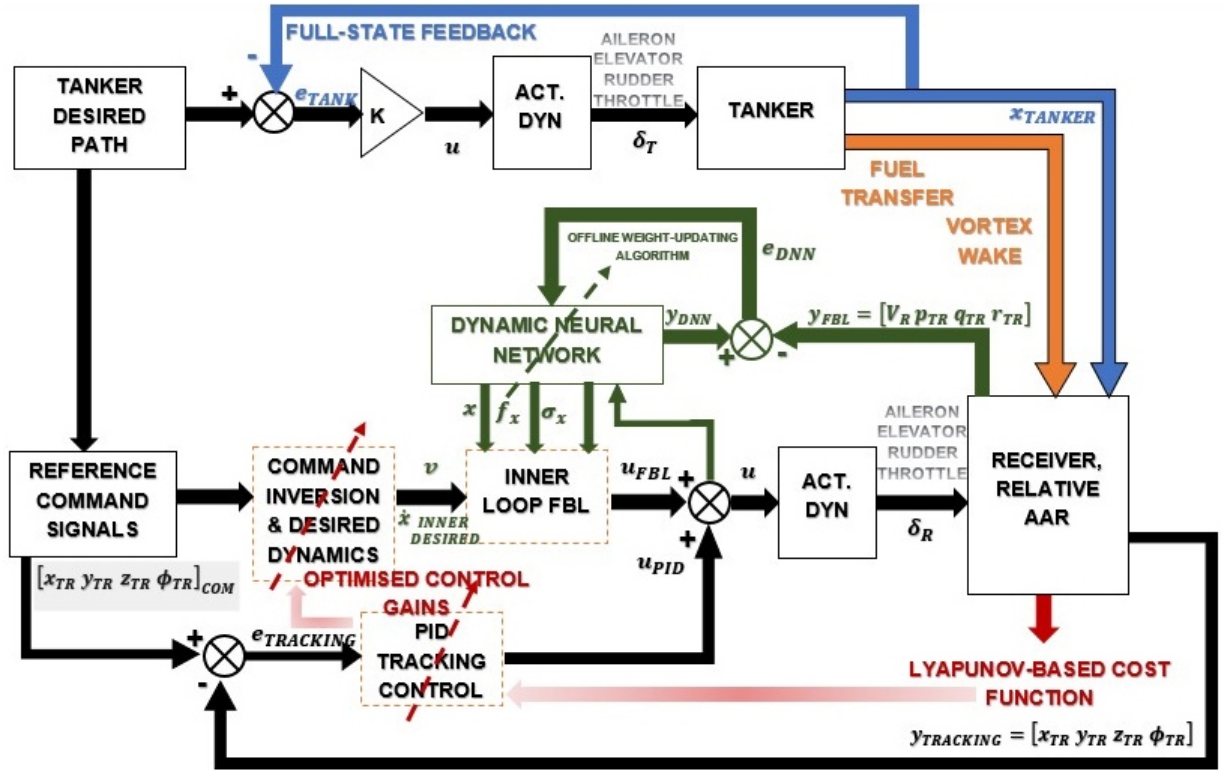


Figure 8.2: Controller block diagram - DNN-based FBL controller with Lyapunov-based GA-optimisation

8.4 Dynamic Simulation of Automated Aerial Refuelling

8.4.1 Controller gains selection and optimisation

The approach used in Chapter 3 was again adopted in the case of the DNN-based controller gains were manually tuned in order to gain an understanding of the system response, and also to develop a bounded search space for the GA optimisation. It was earlier determined (Chapters 5 and 6) that a minimum energy in cost J must be maintained when optimising the controller gains, hence this investigation was not replicated in this chapter. Instead, the outcome from Chapter 6, viz., that the number of generations should be limited to 45, was used directly in the optimisation algorithm. Table 8.1 shows the manually-tuned gains, the upper and lower bounds, the optimised controller gain values, as well as the final cost function.

Table 8.1: Receiver aircraft DNN-FBL-based controller gains and bounds

Gain	**Value**	**LB**	**UB**	**Optimised**
Ke_z	-2.1	-5	-2.1	-2.892
Ke_{zI}	-1000	-1800	-1000	-1125.736
$Ke_{\dot{z}}$	-2	-2.6	-0.3	-1.586
Ka_{ϕ}	-1000	-1203	-980	-1153.579
$Ka_{\phi I}$	-1	-1	-0.9	-0.936
$Ka_{\dot{\phi}}$	32	-10	32	9.419
Kt_x	1.7	1.7	2.72	2.457
Kt_{xI}	-1000	-1040	-700	-812.316
$Kt_{\dot{x}}$	-100	-155	-97	-122.930
Kr_y	4400	4400	7900	6581.273
Kr_{yI}	1	-15	1	-4.901
$Kr_{\dot{y}}$	-500	-504	-495	-496.993
K	diag[1 1 1 1]	diag[0.95]; $[4 \times 4]$	diag[1 1 1 1]	diag[0.993]; $[4 \times 4]$
k_1	diag[1 1 1 1]	diag[0.2]; $[4 \times 4]$	diag[1 1 1 1]	diag[0.634]; $[4 \times 4]$
J	2.430e8			2.070e8

In order to verify that the GA, when run to 45 generations for the DNN-based FBL controller was within the energy threshold established earlier, the parameters α and β were computed:

$$\alpha = \frac{2.430e8}{2.070e8} = 1.1174 \tag{8.18}$$

$$\beta = \frac{2.070e8}{2.430e8} = 0.8519 \tag{8.19}$$

Since α and β were found to be within the determined range for this AAR system given in Chapter 5, it can be expected that the system will exhibit stable behaviour when using the optimised controller gains. Figures 8.3 to 8.5 shows the evolution of the GA cost function and controller gains. In Figure 8.3, the minimum energy limit is superimposed, and it can be seen that the final value of J at the 45th generation still remains within the limit.

8.4.2 Simulation results

In Figure 8.6, J for the manually-tuned baseline case was seen to be greater than the J for the manually-tuned case where turbulence was introduced into the system once refuelling has been completed and the receiver aircraft remains on station. This is in contrast to the results obtained for the FBL controller without the DNN. When subjected to the Lyapunov-based optimisation algorithm, the baseline J was then less than the J when disturbed by turbulence. The difference here is that J now incorporates the estimated states detailed in

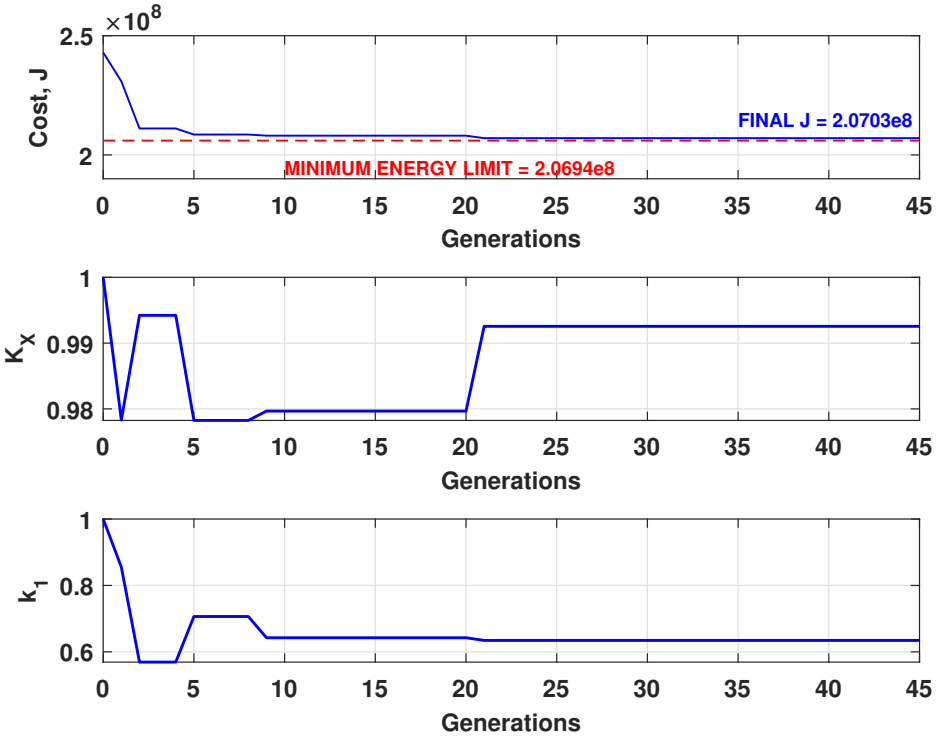


Figure 8.3: Evolution of cost function J and K_x and k_1 controller gains.

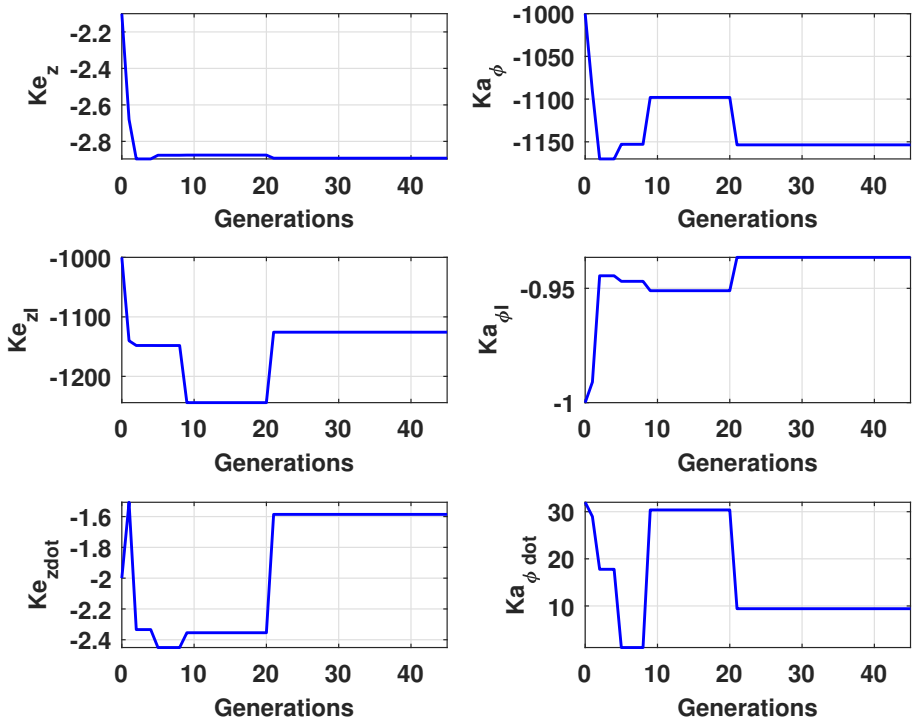


Figure 8.4: Evolution of K_e and K_a controller gains.

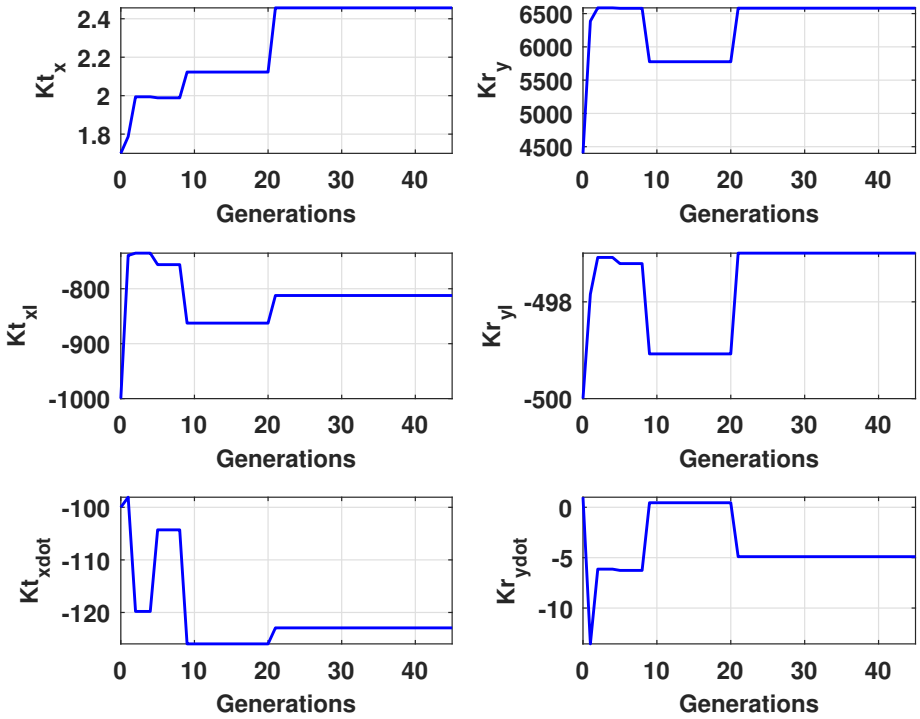


Figure 8.5: Evolution of K_t and K_r controller gains.

Chapter 7, whereas the turbulence has been applied to the actual system model. From this result, it is expected that the GA-optimised results will bring noticeable improvements in the overall performance compared to the manually-tuned case.

The receiver aircraft rotational rates are shown in Figure 8.7. These states were estimated by the DNN in the inner-loop. As mentioned in Chapter 7, the DNN was trained using the un-optimised FBL data which displayed oscillatory behaviour. The simulation results show that the performance in the DNN-based controller was superior to that of the FBL case from which the training data was generated. The damped oscillatory behaviour had not manifested, and proves the capability of the DNN to map the rotational dynamics even with un-optimised training data. The disturbances did introduce transient behaviour on the rotational rates, but when the GA-optimised gains were used, these transients were significantly diminished. In Figure 8.8, this trend is repeated, where the GA-optimised controller gains are seen to improve the system response when subjected to disturbances. Specifically, the effects of disturbances on aerodynamic angle β_R is reduced by an order of magnitude, although it does take time for β_R to settle to its nominal value of 0 deg in the mass disturbance case.

The time history of the receiver aircraft relative Euler angles is shown in Figure 8.9. Once refuelling was completed and the receiver aircraft remained on station in the tanker vortex

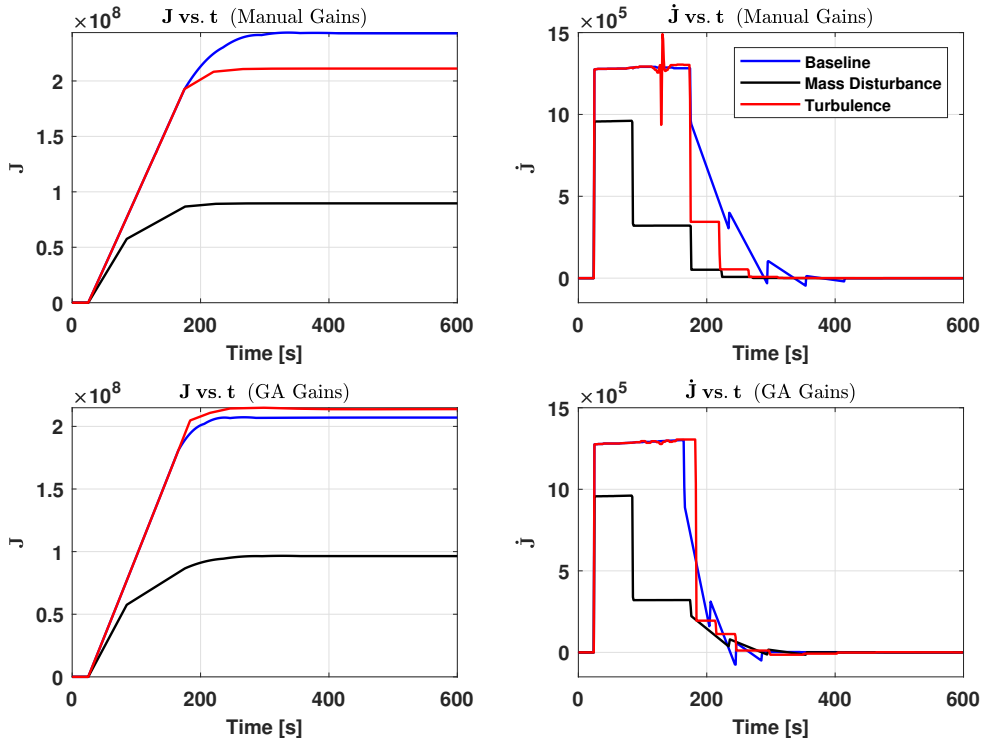


Figure 8.6: J and $\dot{J}$ versus time for manually-tuned and GA-tuned controller gains - baseline + disturbances

wake, the bank angle ϕ_{TR} showed slow-varying transient behaviour. At the instant when $\dot{m} = 0$ at 195s, ϕ_{TR} was disturbed from its nominal value of 0 deg and gradually returned to this. Its maximum deviation from nominal was computed to be 0.003 deg, however, considering the level of accuracy required in aerial refuelling, the maximum deviation would not be experienced as a noticeable variation in orientation. When the GA-optimised controller gains were applied, this behaviour was no longer present. The manually-tuned baseline case yaw angle ψ_{TR} also experienced transient behaviour of a small magnitude (maximum deviation was 0.004 deg, with same earlier comment on its ability to be noticed in real refuelling conditions being applicable), and this behaviour was eliminated once the GA-optimised gains were applied. The disturbances did not destabilise the system and in each instance, the transient behaviour due to the mass and turbulence disturbances was eventually able to be dissipated and steady-state was achieved. The yaw angle ψ_{TR} displayed a similar trend to angle β_R when the mass disturbance was in effect. The pitch angle θ_{TR} was well controlled by the DNN-based controller, with no manifestation of transient behaviour in the station-keeping phase.

For both the x- and z-separation of the receiver aircraft from the tanker aircraft (Figure 8.10), transient behaviour was observed prior to the commencement of fuel transfer. The maximum deviation of x_{TR} from its setpoint was 0.003%. For the z-separation, z_{TR}, the maximum

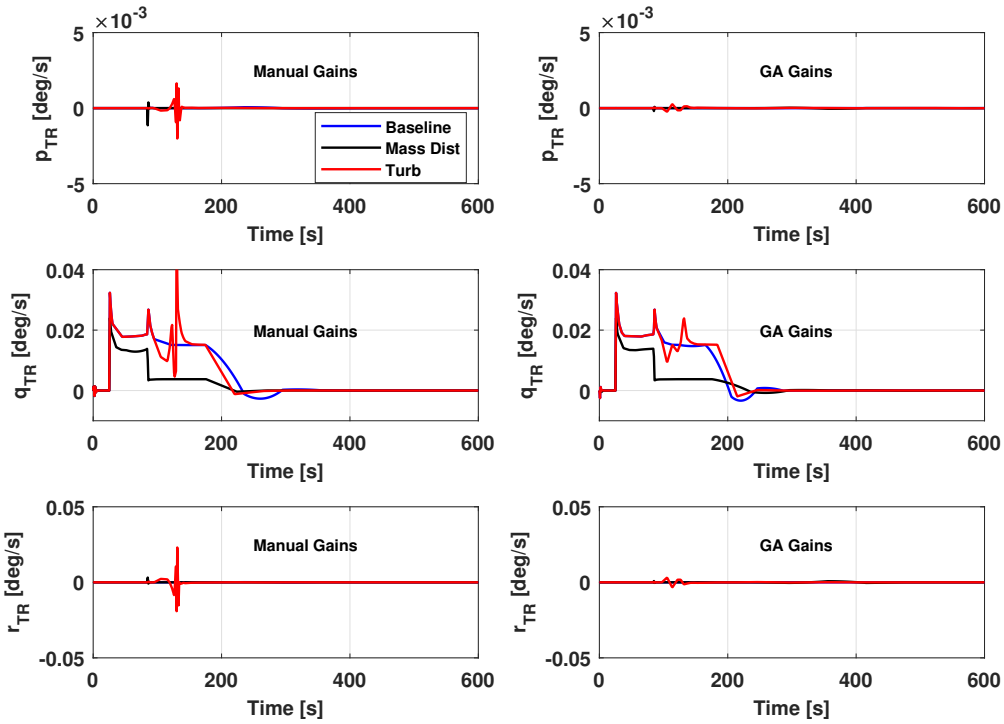


Figure 8.7: Receiver rotational rates for manually-tuned and GA-tuned controller gains - baseline + disturbances.

deviation was 0.004%. These were settled once refuelling commenced, and the controller was able to maintain the receiver aircraft's fixed position with respect to the tanker. There was no unsteady behaviour observed in the station-keeping phase from 195s to 600s.

Figure 8.11 shows the receiver aircraft control surfaces' deflections. In the baseline manually-tuned case, the rudder deflection (δ_{r_R}) showed the same transient trend as that was observed earlier in the Euler angles - manifestation occurred once fuel transfer had been completed, the magnitude of deviation for δ_{r_R} was 0.15 deg, which returned to steady state 0 deg within 100s. This behaviour was improved when the GA-optimised controller gains were applied. Due to the asymmetric refuelling scenario in the case of the mass disturbance (from 85s to 195s fuel tank 3 fills to 50% capacity while tank 4 does not fill), the aileron δ_{a_R} and rudder δ_{r_R} deflections are non-zero. Once refuelling is completed, these deflections remain non-zero to compensate for the asymmetric weight distribution. The elevator δ_{e_R} and throttle δ_{t_R} deflections showed steady behaviour in both the manually-tuned and GA-optimised baseline case. Transient behaviour in δ_{t_R} was manifest when turbulence was introduced when the manually-tuned controller gains were applied. The controller optimisation led to this transient behaviour being eliminated when the GA-optimised controller gains were applied. The tanker aircraft state and control variables time histories are shown in Figures 8.12 to 8.14.

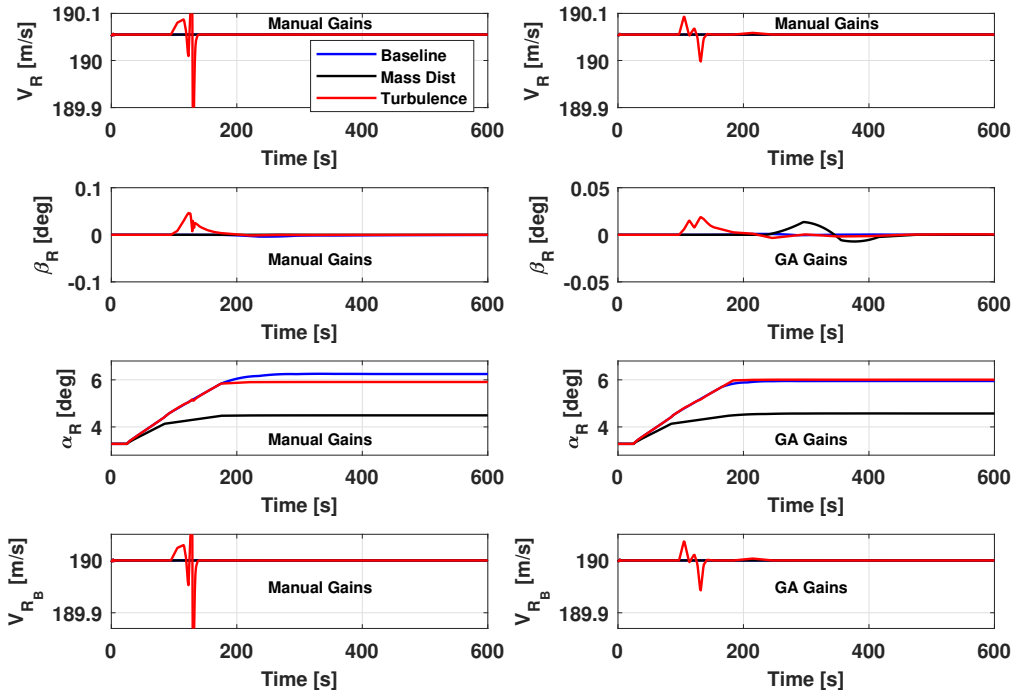


Figure 8.8: Receiver speeds and aerodynamic angles for manually-tuned and GA-tuned controller gains - baseline + disturbances.

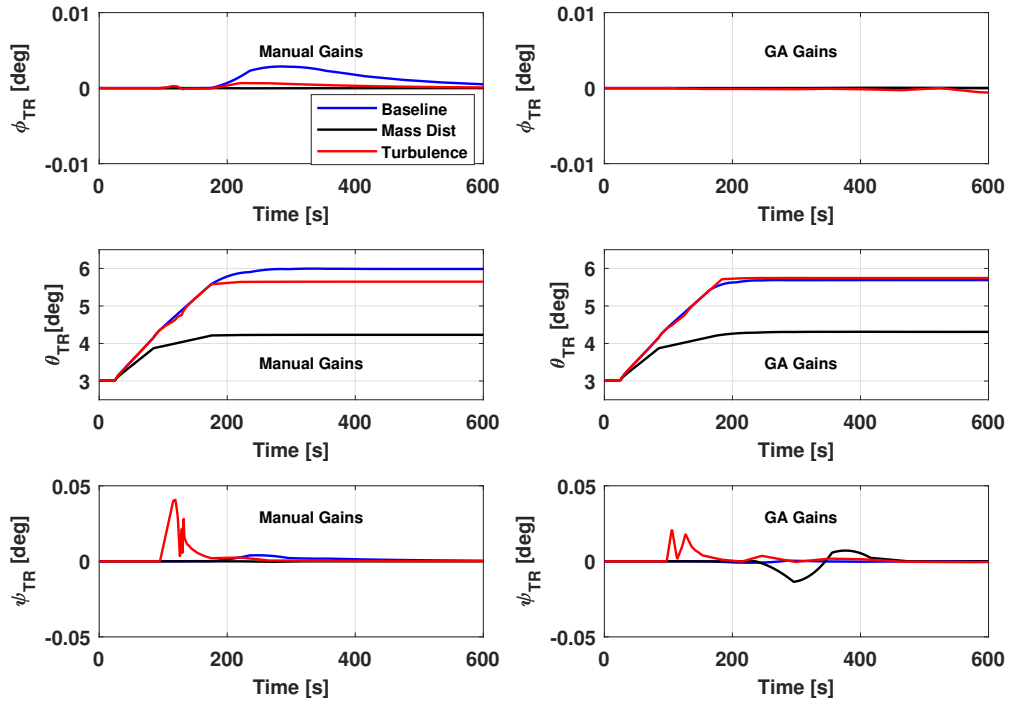


Figure 8.9: Receiver Euler angles for manually-tuned and GA-tuned controller gains - baseline + disturbances.

8.5 Comparison of PID and FBL Controllers During Aerial Refuelling

The performance of the PID and FBL controllers was compared with that of the DNN-based controller. The state and control variables where significant differences in performance were selected for comparison. These were mainly the lateral-directional state variables, as it was earlier established that these state variables were sensitive to disturbances introduced during the refuelling process.

Figures 8.15 to 8.20 show the time histories of the lateral-directional state variables ϕ_{TR}, ψ_{TR}, p_{TR}, r_{TR}, β_{TR}, and y_{TR} for each controller, comparing the manually-tuned and GA-optimised controller performance for the baseline and disturbance cases. The manually-tuned FBL controller in Chapter 6 performed the worst in the baseline case in the refuelling period 25s to 195s for ϕ_{TR}, ψ_{TR}, p_{TR}, r_{TR}, and β_{TR}. In all of these cases, introduction of fuel into tanks 3 and 4, aft of the CG resulted in oscillatory behaviour for each of these state variables, which was damped out as the refuelling was completed at 195s. The GA-optimised FBL controller gains removed this behaviour from the system. The PID controller on the other hand exhibited transient behaviour in the station-keeping phase, when the fuel transfer

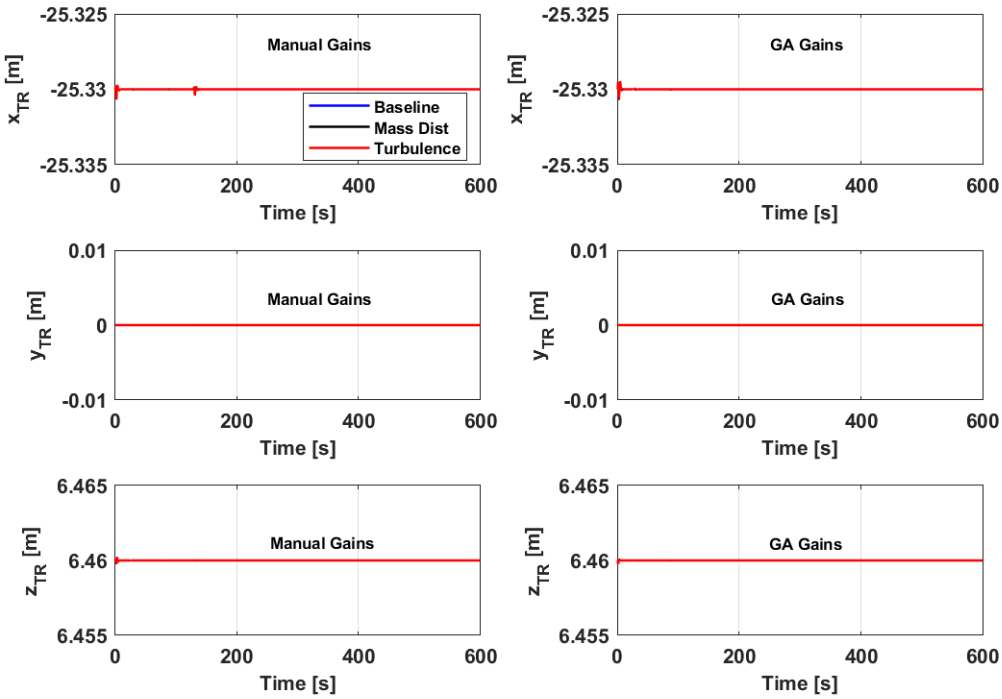


Figure 8.10: Receiver x- y- and z-separation for manually-tuned and GA-tuned controller gains - baseline + disturbances.

rate was 0 kg/s. The DNN-based controller had the best overall performance, however, while the DNN-based controller did show some transient behaviour in the station-keeping phase, it was an order of magnitude lower than that of the FBL and PID controllers. For instance, for ϕ_{TR}, the manually-tuned PID controller had a maximum deviation of 0.05 deg from its nominal value of 0 deg, whereas the DNN-based controller transient behaviour resulted in a deviations of an order of magnitude lower than that of the PID and FBL controllers. When the disturbances were introduced, the PID controller showed the poorest performance of the three controllers. Under the effect of the asymmetric mass disturbance, the manually-tuned PID controller was not able to return the angle ϕ_{TR}, ψ_{TR} and β_{TR} back to its nominal value of 0 deg. Instead, in each case, these angles were offset to a constant value for the duration of the station-keeping phase. The FBL and DNN-based controllers did not exhibit this undesirable behaviour, and while the FBL controller did show transient behaviour for the manually-tuned gains, this was improved when the GA-optimised controller gains were used in the dynamic simulation. In the y-separation y_{TR} (Figure 8.20), the PID controller was not able to return y_{TR} back to 0m once disturbed through asymmetric refuelling at 85s to 195s. The PID controller displayed the worst performance when subject to disturbances, and also experienced transient behaviour in the lateral-directional state variables in the baseline case when refuelling had been concluded and the receiver aircraft remained on station. Any poor

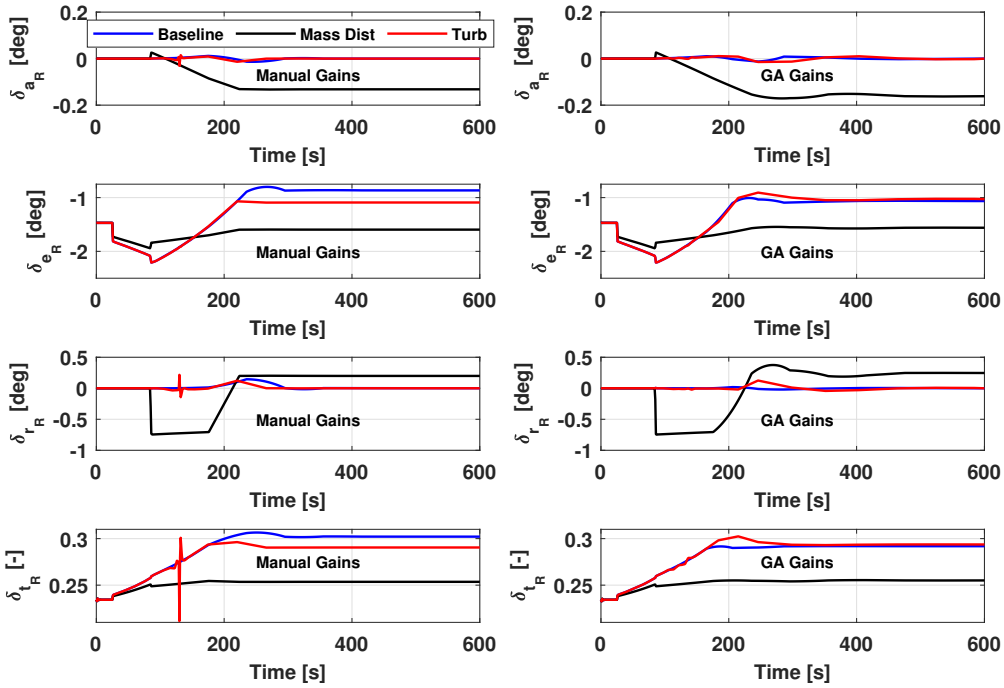


Figure 8.11: Receiver control surfaces deflection for manually-tuned and GA-tuned controller gains - baseline + disturbances.

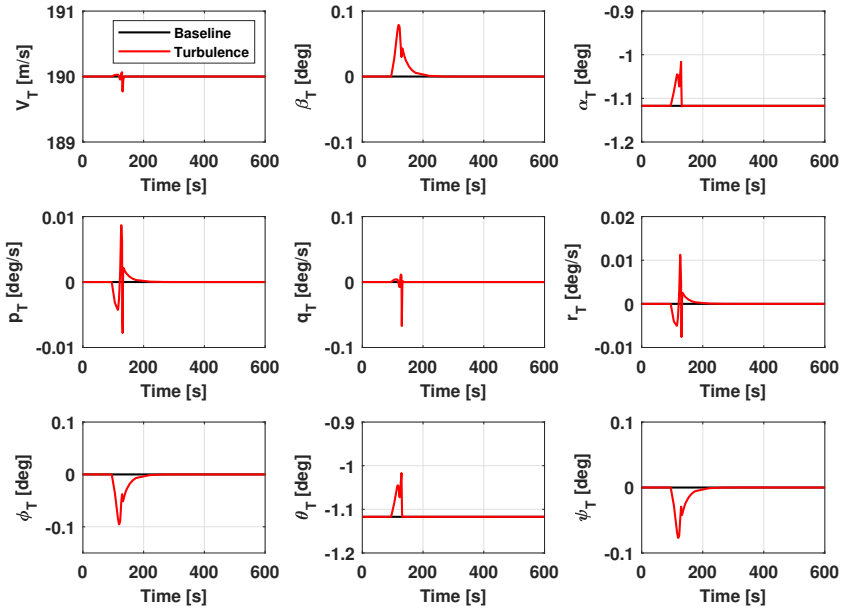


Figure 8.12: Tanker aircraft state variables - baseline + disturbances.

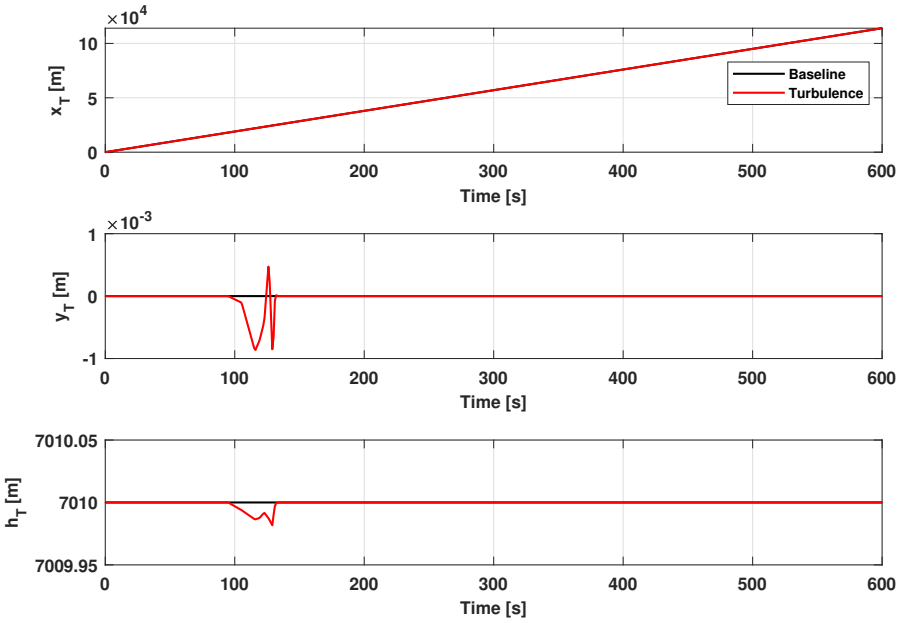


Figure 8.13: Tanker aircraft x- y- and z-positions along flight path - baseline + disturbances.

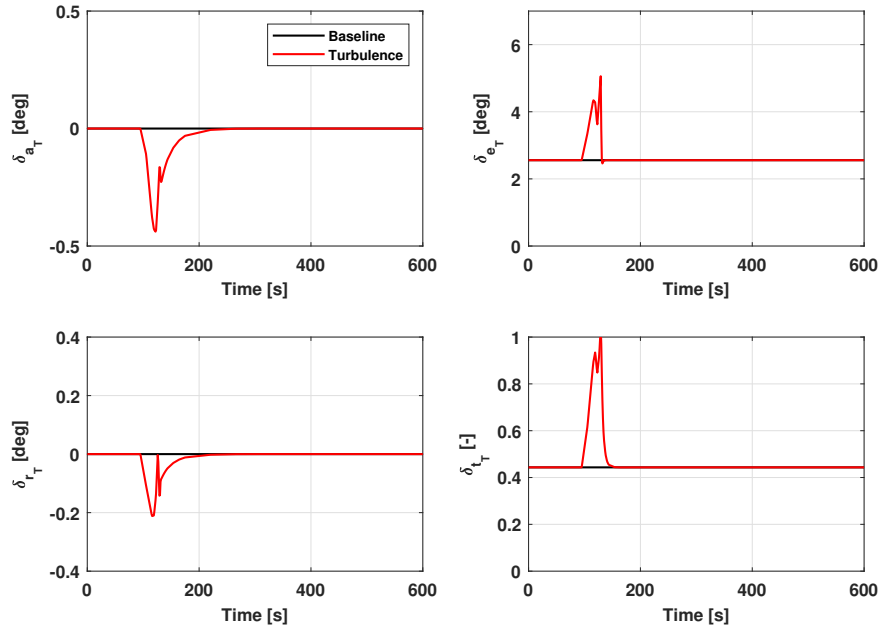


Figure 8.14: Tanker aircraft control surfaces' deflections - baseline + disturbances.

behaviour exhibited by the manually-tuned gains for the FBL and DNN-based controllers was eliminated or diminished by an order of magnitude when the GA-optimised controller gains were applied.

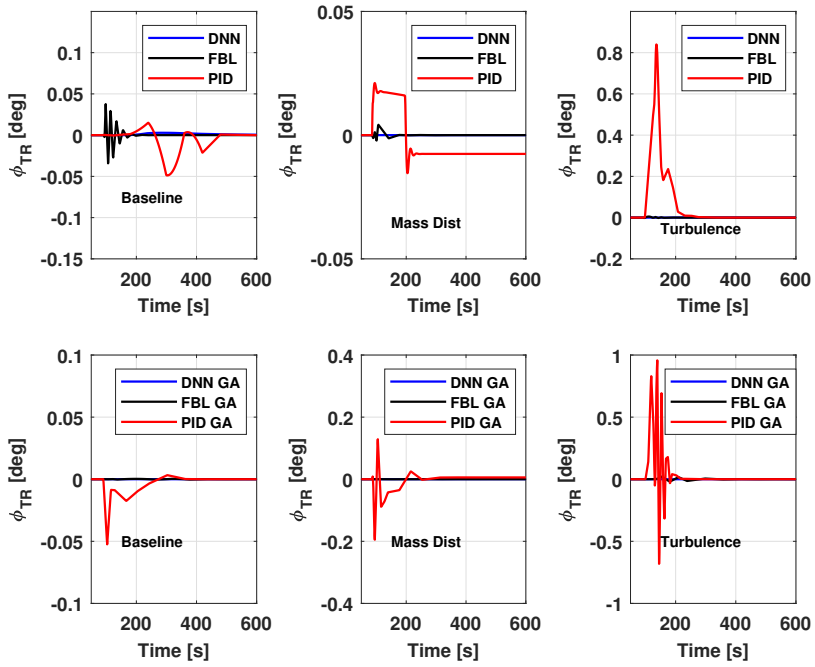


Figure 8.15: ϕ_{TR} vs time from PID, FBL and DNN controllers - baseline + disturbances.

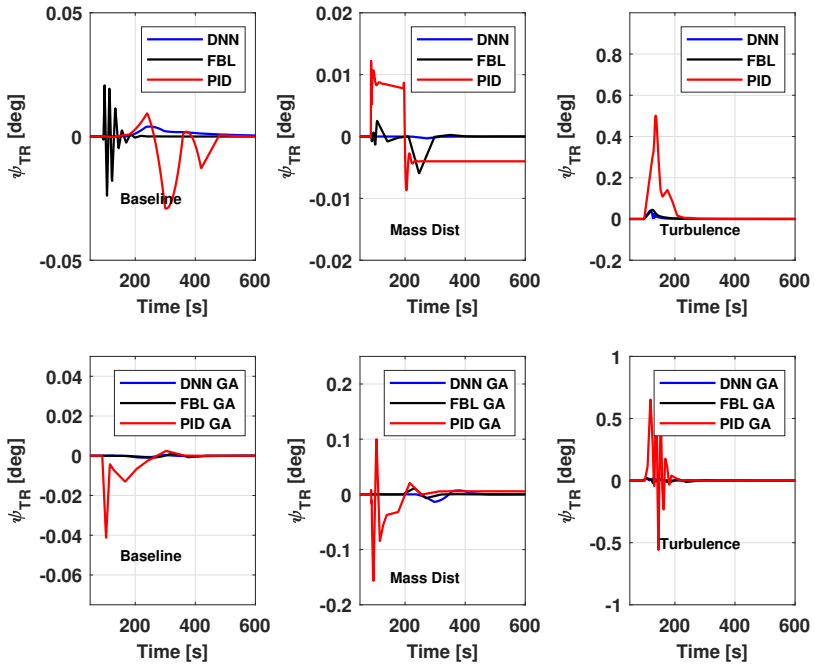


Figure 8.16: ψ_{TR} vs time from PID, FBL and DNN controllers - baseline + disturbances.

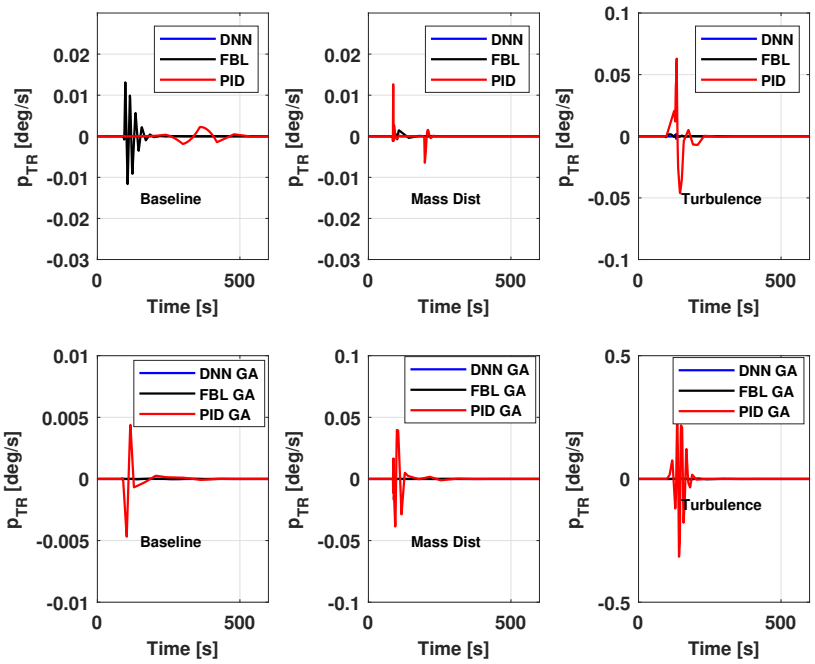


Figure 8.17: p_{TR} vs time from PID, FBL and DNN controllers - baseline + disturbances.

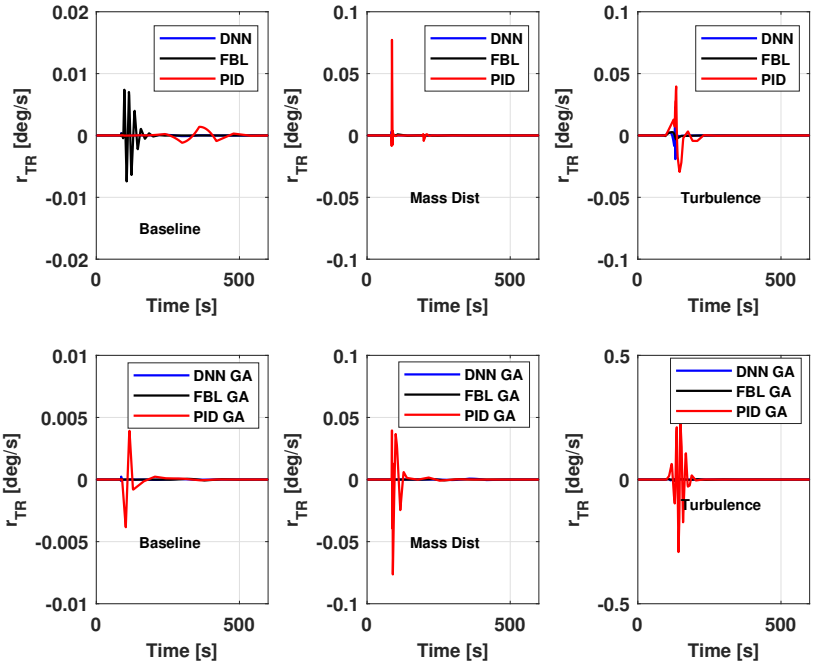


Figure 8.18: r_{TR} vs time from PID, FBL and DNN controllers - baseline + disturbances.

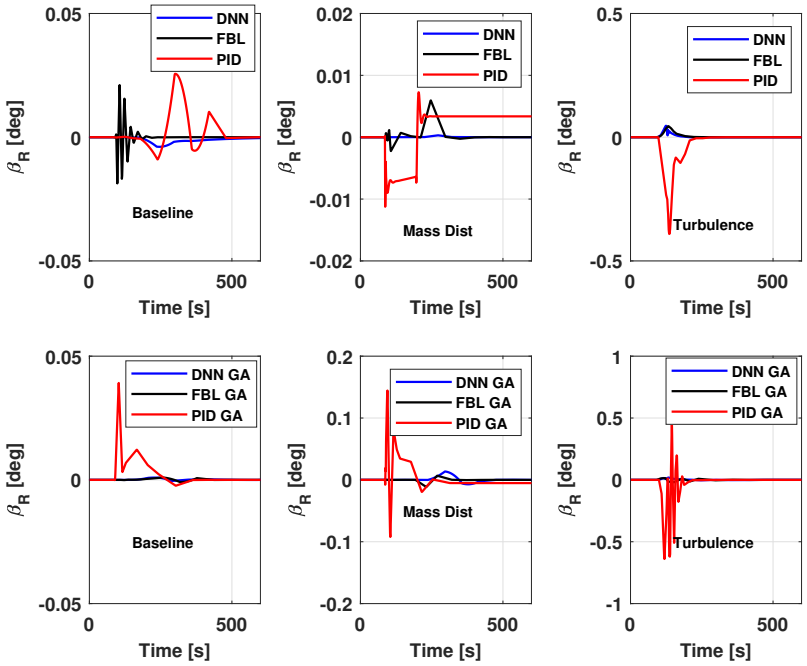


Figure 8.19: β_R vs time from PID, FBL and DNN controllers - baseline + disturbances.

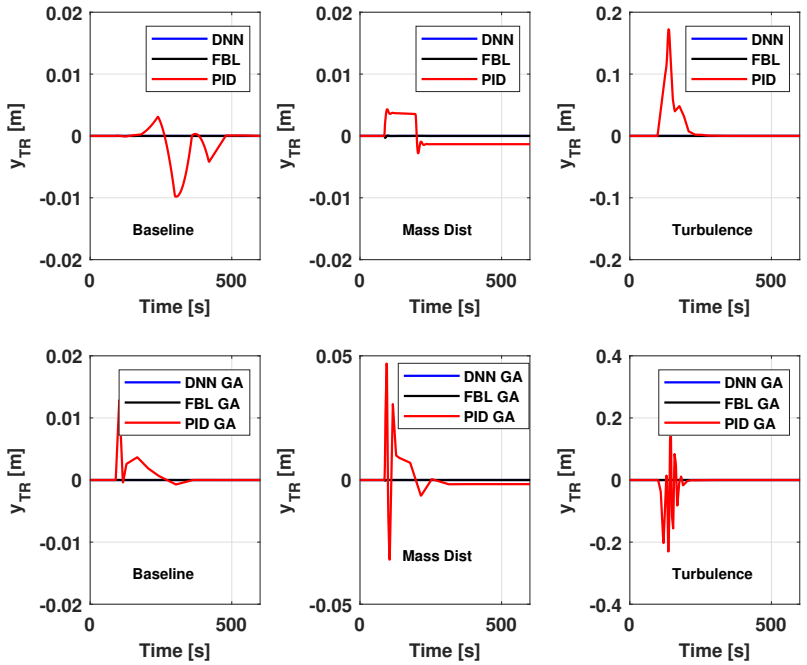


Figure 8.20: y_{TR} vs time from PID, FBL and DNN controllers - baseline + disturbances.

The time histories of the longitudinal state variables pitch orientation θ_{TR}, airspeed V_R and z-separation z_{TR} for each controller, comparing the manually-tuned and GA-optimised controller performance for the baseline and disturbance cases are presented in Figures 8.21 to 8.23. The control of the pitch orientation θ_{TR} was consistently the same in all cases. There were no undesirable behaviours at any phase of the refuelling manoeuvre. PID control using both the manually-tuned and GA-optimised controller gains showed the least favourable performance for the airspeed V_R. Figure 8.23 zooms in on the period 45s to 250s. While the trend shows that the DNN-based controller was superior to the PID controller in maintaining the z-separation of the receiver from the tanker aircraft, when considering the actual deviation, it was found that at 240s, under PID control, the deviation from the setpoint of 6.46m is 6.459998m, which is essentially a negligible difference.

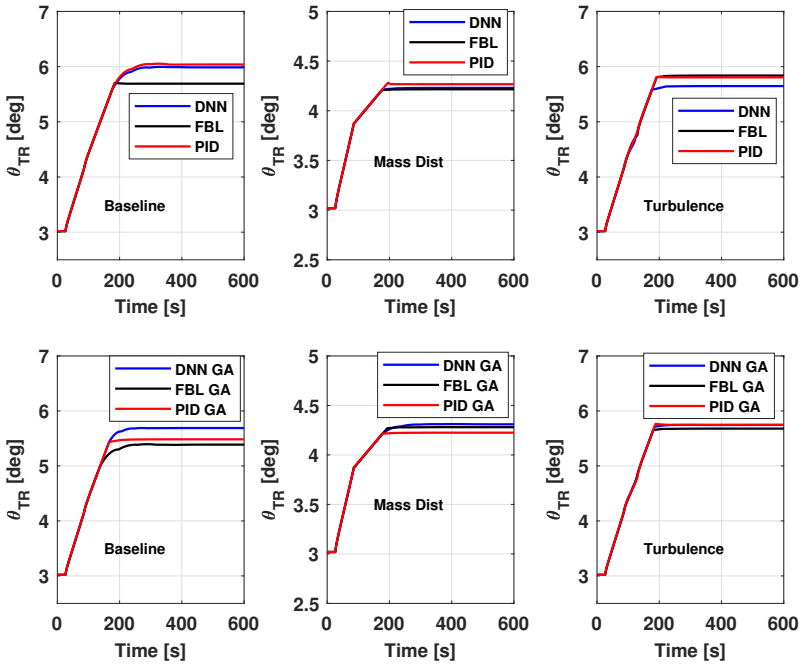


Figure 8.21: θ_{TR} vs time from PID, FBL and DNN-based controllers - baseline + disturbances.

Lastly, the control surfaces' deflections δ_{a_R} and δ_{r_R} in Figures 8.24 and 8.25 show that the PID controller had the least desirable performance when subject to disturbances, even after optimisation. The elevator and throttle deflections follow the trend shown in Figure 8.21 for θ_{TR} and are not presented here.

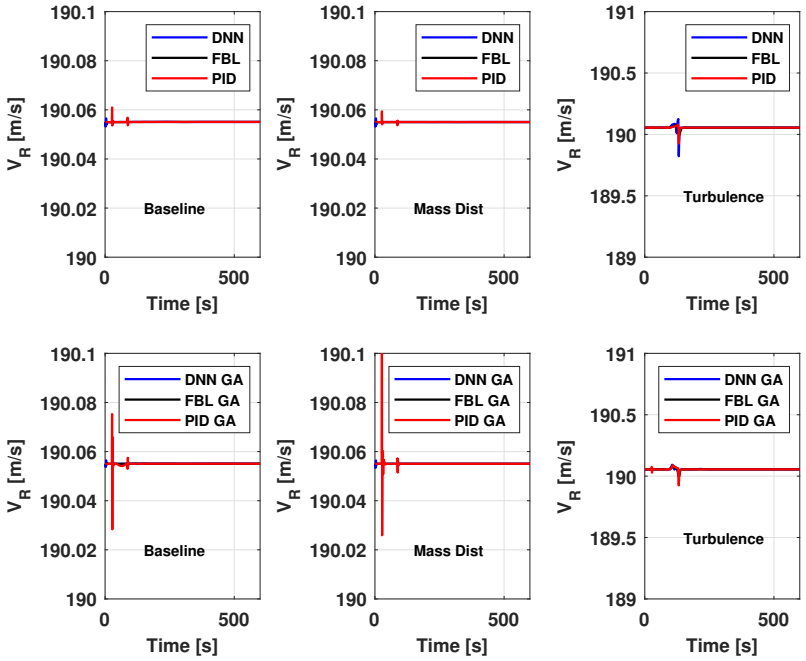


Figure 8.22: V_R vs time from PID, FBL and DNN-based controllers - baseline + disturbances.

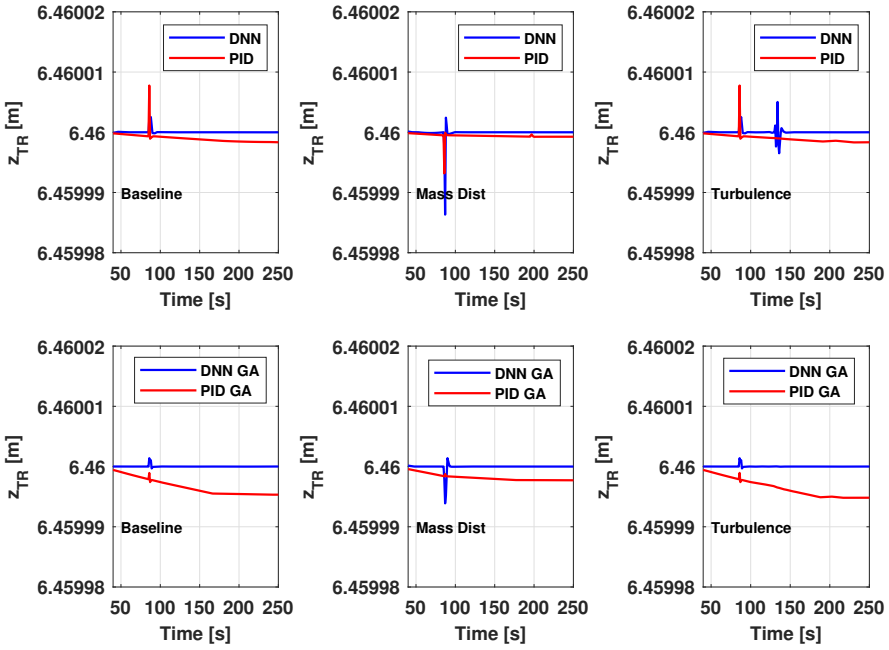


Figure 8.23: z_{TR} vs time from PID and DNN-based controllers - baseline + disturbances.

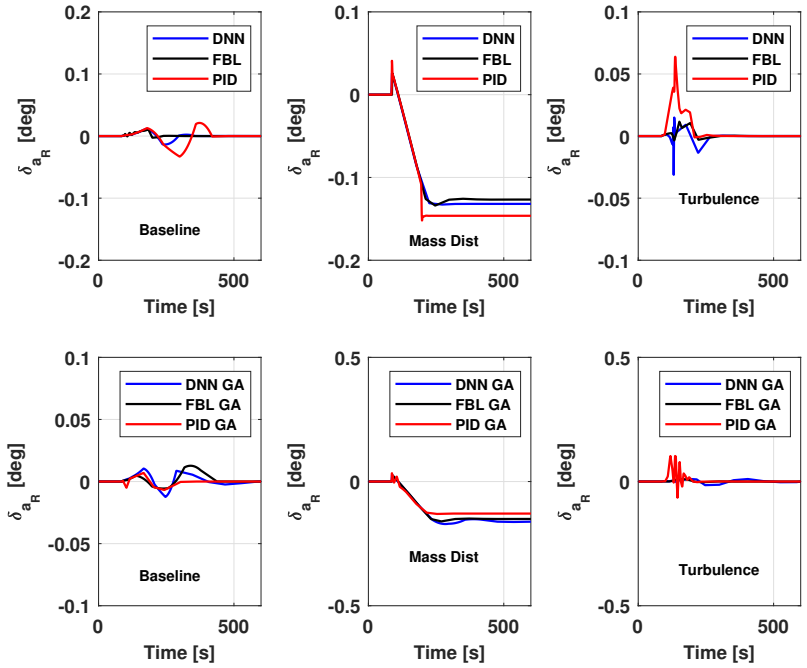


Figure 8.24: δ_{a_R} vs time from PID, FBL and DNN-based controllers - baseline + disturbances.

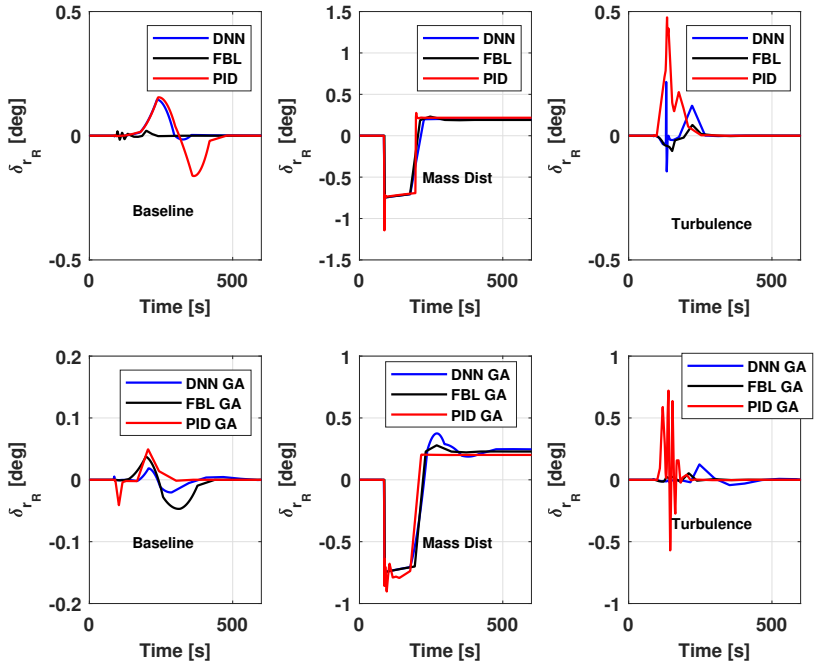


Figure 8.25: δ_{r_R} vs time from PID, FBL and DNN-based controllers - baseline + disturbances.

8.6 Chapter Summary

The dynamic neural networks trained in Chapter 7 were used in a DNN-based indirect adaptive feedback linearisation controller - the synthesis of intelligent and nonlinear control. The controller structure included the trained DNNs in the inner-loop, where the identified neural network model was used to produce the linearising feedback law. The outer-loop command inversion and tracking control structure remained the same as for the FBL case without the DNN. Manual tuning of controller gains was performed and the Lyapunov-based optimisation routine developed earlier was used to optimise controller gains using the GA algorithm. The final value of the cost function J after 45 generations was found to be within the minimum energy threshold. The DNN-based GA-optimised controller was the best performing controller from all the control strategies implemented. Oscillatory behaviour that was observed in the lateral-directional state variables time histories under the FBL controller was eliminated when the DNN was used in the inner-loop control. The DNN-based controller however, did display some slight transient behaviour, however when the GA gains were applied, these transient behaviours were eliminated.

9 Conclusions and Recommendations for Future Work

9.1 Conclusions

Unmanned aerial vehicles are strongly sought-after, and are considered a key technological advancement that can expand operational roles in both military and civilian applications. The need for autonomous aerial refuelling has been established in the context of unmanned aerial systems mirroring the capabilities of their manned counterparts. The receiver aircraft must maintain an accurate position relative to the tanker aircraft in an aerial refuelling manoeuvre, whilst subject to a number of effects inherent to the refuelling process, leading to highly complex engagement dynamics that are nonlinear in nature and strongly cross-coupled. Against this background, the formulated research question, *"Can a stable control law be constructed by synthesising techniques in intelligent control for a receiver-tanker refuelling problem?"* has been addressed comprehensively in this study.

This study has shown that stable control laws can indeed be formulated for the aerial refuelling problem by synthesising techniques in intelligent control. In order to have arrived at this answer, a number of research sub-objectives were defined in Chapter 1, which laid out the investigation in a stepwise and structured manner, leading ultimately to the final stage where the various elements were synthesised to develop the indirect adaptive DNN-based FBL controller. Each sub-objective has been addressed.

To develop the system mathematical model taking all dynamic effects into account

An aerial refuelling system model was developed, inclusive of the tanker-receiver engagement, where the receiver aircraft dynamics was framed as a variable-mass system subject to a wind field as inherent to the process. In framing the model in this manner, this work is differentiated from other works, where, the effects of changing mass, centre of gravity, inertia and vortex wake effects were considered as external disturbances. Additionally, this was an

important factor in the the system stability framework that was developed after the system model was constructed.

To numerically simulate the behaviour of the system based on the developed model

The behaviour of the receiver aircraft during AAR was compared to the case when there was no refuelling at the same flight condition. It was found that in order for the receiver aircraft to hold a fixed position relative to the tanker while mass and inertia properties were changing during the manoeuvre, the pitch rate q_{TR} increases twice; first at the time fuel is introduced into the forward tanks, and then again when fuel is transferred to the aft tanks. As the pitch rate is affected by the fuel transfer, these effects were translated to other longitudinal state variables. The receiver aircraft angle of attack, α_R and relative pitch orientation, θ_{TR} increased in response to fuel being added to the tanks. The receiver aircraft airpseeds in body and wind axes were maintained at constant values. As the fuel transfer into individual tanks was symmetric, only the receiver elevator and throttle deflections would experience deviations from their nominal values at the start of the manoeuvre to maintain the receiver aircraft in its required position throughout the period of fuel transfer. When fuel is transferred to the forward tanks, the elevator deflection adjusts constantly, increasing the magnitude of its negative deflection. Then at the time of the aft tanks refuelling, the elevator reverses its negative deflection trajectory in line with the need to meet system performance specifications. The throttle deflection continuously increases as fuel is increased. These control surfaces remain within their physical limits throughout the AAR manoeuvre.

To develop a baseline PID controller

A PID controller was developed for the receiver aircraft, while LQR control was applied to the tanker aircraft. The receiver aircraft control laws were constructed so that elevator deflection was responsible for the vertical separation control (i.e., height-hold), while speed and x-separation were controlled with the throttle deflection. The lateral-directional control used a combination of aileron and rudder in the outer loop for the y-channel control. Twenty three controller gains were manually tuned. A quadratic cost function, J, was constructed for manual checking of the tuning outcomes. The 23 controller gains constituted a single set of gains that were applied at all three phases defined for the manoeuvre, eliminating the need for gain scheduling across the different phases of the refuelling manoeuvre. When subject to the asymmetric refuelling disturbance, the PID controller could not bring the lateral-directional states back to nominal values, while in the turbulence case, both the longitundinal and lateral-directional states were disturbed, but eventually reached their nominal values. All controller states and control deflections were within acceptable bounds throughout the manoeuvre, even when subject to disturbances.

To develop a framework to address system stability using Lyapunov theory

As mass transfer in an inherent feature of the aerial refuelling process, the receiver aircraft could therefore be considered as a system where mechanical energy is introduced in a specifically-defined manner, for a limited period of time. Due to the fact that the aircraft fuel tanks are finite in capacity, mechanical energy will eventually converge to a fixed value when fuel transfer has ceased. The system and state-space could then be described by a ball of radius R, for which, when additional energy is introduced through [finite] fuel transfer as described above, the radius R will increase from R to R_{final} as fuel is transferred between time t_0 and t_{end}. The growth of radius R will be bounded at a maximum value imposed by the physical system limits itself, with the static margin and allowable CG range also playing a role in the aircraft stability. Since the system states change with time as fuel is introduced, the system was considered non-autonomous. A Lyapunov function which included mass as a proxy for system energy was constructed, whose derivative, when minimised could be used to select controller gains that ensure uniform stability.

In order to show that the manually-tuned benchmark PID controller met the conditions for stability, a Lyapunov-like energy function was constructed to analyse the data generated for the manoeuvre from 0s to 600s. Using control effort away from the initial values ($|\triangle \mathbf{u}|$) as a substitute for system state $\mathbf{x}$, a qualitative assessment of the system energy was performed which revealed that addition of mass increased the system energy and that when the fuel transfer was completed, the mechanical energy of the system was increased compared to the initial state and was conserved following completion of fuel transfer. The aircraft CG variation remained within upper and lower bounds during the refuelling manoeuvre.

To combine an evolutionary algorithm EA with PID thereby developing a PID-EA controller

It was found that when optimisation techniques were applied with a cost function, the aircraft states and control surfaces' deflections were minimised and this had the effect of reducing the system energy reflected in the cost function J. Moreover, the minimisation routine moved the nominal motion trajectory away from the original equilibrium point found through manual tuning. However, for stability, a minimum level of system energy must be maintained when migrating from R to R_{final} and thus R_{final} is limited to R_{opt} when manually-tuned controller gains are optimised. It was shown, that for an AAR system, it is possible to determine what this threshold is, relative to the cost function of the manually-tuned system, through the parameters α and β. The ratio of the additional mass to the total mass at the end of refuelling was the parameter that fixed the minimum energy bound for the AAR system in this study. Both numerical determination and trial-and-error based on the number of optimisation iterations/generations confirmed the minimum system energy that must be available in order for the system at its new optimised equilibrium point to still display good

stability and performance characteristics. When the gains obtained from this process was applied to the controller, the performance of the PID controller still showed the same trends in behaviour as in the manual-tuned case, but the deviations from setpoints of nominal values were improved and/or eliminated. The single set of 23 controller gains was able to be used across the timeframe of the extended manoeuvre, which also included station-keeping after refuelling, i.e., from 0s to 600s, with each phase being different to the once preceding it, without degradation in performance and control.

To apply feedback linearisation to the AAR system to design a controller

A controller was designed using feedback linearisation in the inner-loop, while employing a pseudo-backstepping scheme in the command inversion loop to convert the reference command signals into desired dynamics. PID tracking control was used to close the outer-loop to give effect to controller tracking objectives. Twenty controller gains were manually tuned in this control scheme. The FBL controller displayed damped oscillatory behaviour in lateral-directional state variables during refuelling when no disturbances were applied. Disturbances introduced transient behaviour in the state variables, but the system states were able to return to nominal from these upsets. The single set of twenty controller gains was used from 0s to 600s, and like with the PID controller, there was no need for gain scheduling across the manoeuvre phases.

To optimise the FBL controller gains using the Lyapunov-based EA algorithm

The Lyapunov-based optimisation yielded controller gains that noticeably improved the system behaviour displayed in the baseline case. The damped oscillatory behaviour observed in the manually-tuned case was eradicated when the GA-optimised controller gains were applied. The system behaviour with the GA-optimised controller gains still showed lateral-directional sensitivity in the turbulence disturbance case, however the transient behaviour was smaller in magnitude compared to when the manually-tuned gains were applied.

To identify a system model using dynamic neural networks

Dynamic neural networks were presented as differential equations, analogous to the nonlinear system that had been studied in previous chapters. The incorporation of feedback into the neural network structure makes the network's approximation ability superior to static networks. Since the AAR system would be unstable without control, closed-loop system identification was performed using an input-output data-set generated from the un-optimised FBL controller designed in Chapter 6. Since the application of FBL led to input-output linearisation and decoupling, the system identification was performed on 4 SISO systems. The most complex neural network mappings were the longitudinal states. The pitch dynamics

were complicated by the distinct phases in aerial refuelling, which, in order to keep the receiver aircraft steady behind the tanker, the pitch rate, q_{TR}, varied when fuel was transferred into the fore and aft tanks. The airspeed was most influenced by the tanker-generated wind field over the duration of the manoeuvre. The roll and yaw dynamics were easier dealt with since the refuelling engagement was symmetric. The mean-squared errors ranged from 10^{-4} to 10^{-10} in the training and validation processes.

To use the DNN model in an indirect adaptive feedback linearisation controller using the Lyapunov-based optimisation framework developed previously

The 4 trained DNN models were incorporated in the inner-loop, where the FBL control portion of the overall controller was executed. The DNN models were used to estimate the parameters of the system from input-output data and were then used as the basis of the feedback linearisation, where the identified neural network models were used to produce the linearising feedback law. The DNNs also included a weight-updating algorithm to address the approximation error between the neural network models and the actual system. This indirect adaptive control scheme in the inner-loop was closed using the same outer-loop structure for the command inversion and tracking control described in the case where no DNN was applied to FBL. The sensitivity in the lateral-directional channel did manifest again in the baseline manually-tuned case; however, with the DNN-based controller, this was significantly reduced in magnitude compared to the PID and FBL controllers. The DNN-based GA-optimised controller showed the best performance compared to the other developed controllers, both in the baseline and disturbance cases. The synthesis of nonlinear control and techniques in intelligent control (EAs and DNNs) did yield a stable control scheme that met performance specifications and was robust to disturbances. A single set of controller gains was applied across all phases of the manoeuvre and the addition of the station-keeping phase, thereby extending the duration of the entire manoeuvre.

To test the robustness and performance of the developed controllers by applying system disturbances

Two disturbance cases were defined that were applied to the system at each stage when the controllers were designed. As mentioned in the previous discussions, it was found that the application of the optimised controller gains improved the system performance when the disturbances were applied compared to when the manually-tuned gains were applied. Stability and performance specifications were met due to the application of the Lyapunov-based cost function and limiting the iterations such that the cost function, J, remained within the minimum energy threshold. Controller optimisation under the Lyapunov-based cost function minimisation produced controller gains that guaranteed system stability while having met performance specifications and robustness when subject to disturbances. The least robust controller was the PID controller with manually-tuned gains, while the performance of the

DNN-based GA-optimised controller surpassed that of the other developed controllers in terms of its ability to return the system states to nominal values and minimise the magnitude of transient effects.

9.2 Recommendations for Future Work

Since this study has shown the ability of the DNN to estimate the complex nonlinear aerial refuelling dynamics, future work can focus on an increase in system model complexity as follows:

- Incorporation of the refuelling boom into the system model
- Extension of the manoeuvre from the straight-leg portion to the complete racetrack manoeuvre
- Expansion of disturbance cases to include non-stationary atmosphere and various turbulence profiles within the range of refuelling altitudes

The optimisation algorithms were limited to 50 or 45 iterations based on the cost function J having approached the established minimum bound at this point in the minimisation routine. While this number was determined through a trial-and-error approach, primarily to have understood the system behaviour within and outside of the minimum energy threshold, the minimum value of J relative to the manually-tuned cost function was able to have been determined directly. A multi-objective optimisation approach can form part of future refinement of the Lyapunov-based optimisation methodology presented in this study. Other optimisation techniques such as simulated annealing, differential evolution and pigeon-inspired optimisation can be explored and compared to the genetic algorithm and particle swarm optimisation methods used in this study.

Direct adaptive control could also be considered and compared to the indirect adaptive controller designed in this study. The robustness of the DNN-based FBL control scheme was tested by applying disturbances in refuelling rates and turbulence. While the DNN-based FBL controller performed well when disturbances were applied, the problem can also be addressed using sliding mode control. In the literature, this method was used extensively for probe-drogue docking and can be used in BRR refuelling once the system complexity issue mentioned above is incorporated into the system model.

Interest in AAR followed as a natural progression from research in close formation flight in the early 2000's. While this is an active area of research and has generated a significant body

of research outputs in the subsequent two decades, AAR is yet to be fully operationalised alongside manned aerial refuelling. The available literature has revealed a number of enabling factors that are currently being explored in order for unmanned refuelling to become fully operationalised. Some of these include the development of machine vision systems, hardware requirements, manoeuvre safety considerations and others. However, these are beyond the scope of this study and would not form the basis for additional work to be added to this study. Attention is drawn to this only to illustrate the long lead times involved in new technology development, from inception to technology qualification and operational adoption.

References

Abeyratne, R and Khan, A (2014) "State use of unmanned military aircraft: a new international order?" Journal of Transportation Security vol. 7, no. 1, pp. 83–98.

An, S and Yuan, S (2018) "Relative position control design of receiver UAV in flying-boom aerial refueling phase." ISA Transactions vol. 73, no. February 2018, pp. 40–53.

Behera, L and Kar, I (2010) Intelligent Systems and control principles and applications. New York, NY, USA: Oxford University Press, Inc., 2nd edn.

Belmonte, LM, Morales, R, and Fernández-Caballero, A (2019) "Computer vision in autonomous unmanned aerial vehicles—a systematic mapping study." Applied Sciences vol. 9, no. 15, pp. 1–34.

Bloy, A and Khan, M (2001) "Modeling of the receiver aircraft in air-to-air refueling." Journal of Aircraft vol. 38, no. 2, pp. 393–396.

Bloy, A and Khan, M (2002) "Modelling of the hose and drogue in air-to-air refuelling." Aeronautical Journal vol. 106, no. 1055, pp. 17–26.

Bloy, A, Lamont, P, Abu-Assaf, H, and Ali, K (1986) "Lateral dynamic stability and control of a large receiver aircraft during air-to-air refuelling." Aeronautical Journal vol. 90, no. 896, pp. 237–243.

Bolien, M, Iravani, P, and Du Bois, JL (2017) "Toward robotic pseudodynamic testing for hybrid simulations of air-to-air refueling." IEEE/ASME Transactions on Mechatronics vol. 22, no. 2, pp. 1004–1013.

Bowers, RE (2005) Estimation algorithm for autonomous aerial refueling using a vision based relative navigation system. Phd thesis, Texas A&M University.

Cao, H, Wang, L, and Yue, T (2017) "An nonlinear feedback control for radial constrained force of flying boom after contact with receiver." In "Proceedings of 2017 8th International Conference on Mechanical and Aerospace Engineering," pp. 714 – 718. IEEE.

Chai, R, Tsourdos, A, Savvaris, A, Chai, S, Xia, Y, and Chen, CP (2021) "Review of advanced guidance and control algorithms for space/aerospace vehicles." Progress in Aerospace Sciences vol. 122, pp. 1–21.

Chang, WD and Shih, SP (2010) "PID controller design of nonlinear systems using an improved particle swarm optimization approach." Communications in Nonlinear Science and Numerical Simulation vol. 15, no. 11, pp. 3632–3639.

Chen, B, Dong, X, Xu, Y, and Lin, Q (2007) "Disturbance analysis and flight control law design for aerial refueling." In "Proceedings of the Proceedings of the 2007 IEEE International Conference on Mechatronics and Automation," pp. 2997–3002. Harbin, Heilongjiang, China.

Choi, AJ, Yang, HH, and Han, JH (2021) "Study on robust aerial docking mechanism with deep learning based drogue detection and docking." Mechanical Systems and Signal Processing vol. 154, pp. 1–17.

Choi, YT and Wereley, NM (2013) "Semi-active magnetorheological refueling probe systems for aerial refueling events." Smart Materials and Structures vol. 22, no. 9, pp. 1–10.

Clouet, LM (2012) "Drones as future air power assets: The dawn of aviation 2.0?" In "Power in the 21st century," pp. 177–192. Springer.

Cohen, RS, Scheinmann, GM, and Ph, D (2014) "Can Europe Fill the Void in U.S. Military Leadership?" Orbis vol. 58, no. 1, pp. 39–54.

Cveticanin, L (2016) Dynamics of bodies with time-variable mass. Switzerland: Springer, 1st edn.

Dai, X, Wei, Z, and Quan, Q (2016) "Modeling and simulation of bow wave effect in probe and drogue aerial refueling." Chinese Journal of Aeronautics vol. 29, no. 2, pp. 448–461.

Dangor, M, Dahunsi, OA, Pedro, JO, and Ali, MM (2014) "Evolutionary algorithm-based PID controller tuning for nonlinear quarter-car electrohydraulic vehicle suspensions." Nonlinear Dynamics vol. 78, no. 4, pp. 2795–2810.

DeVries, L and Paley, DA (2013) "Wake estimation and optimal control for autonomous aircraft in formation flight." In "AIAA Guidance, Navigation, and Control (GNC) Conference," pp. 1–20. Boston, MA, USA.

Dogan, A, Blake, W, and Haag, C (2013) "Bow wave effect in aerial refueling: computational analysis and modeling." Journal of Aircraft vol. 50, no. 6, pp. 1856–1868.

Dogan, A, Kim, E, and Blake, W (2007) "Control and simulation of relative motion for aerial refueling in racetrack maneuvers." Journal of Guidance, Control, and Dynamics vol. 30, no. 5, pp. 1551–1557.

Dogan, A, Lewis, TA, and Blake, W (2008) "Flight data analysis and simulation of wind effects during aerial refueling." Journal of Aircraft vol. 45, no. 6, pp. 2036–2048.

Dogan, A, Sato, S, and Blake, WB (2005a) "Flight control and simulation for aerial refueling." In "Proceedings of the AIAA Guidance, Navigation, and Control Conference and Exhibit," August, pp. 1–16. San Francisco, California.

Dogan, A, Venkataramanan, S, and Blake, W (2005b) "Modeling of aerodynamic coupling between aircraft in close proximity." Journal of Aircraft vol. 42, no. 4, pp. 941–955.

Dorsett, KM and Mehl, DR (1996) Innovative Control Effectors (ICE). Tech. Rep. WL-TR-96-3043, Flight Dynamics Directorate, Wright Laboratory.

Elliot, C and Dogan, A (2010) "Investigating nonlinear control architecture options for aerial refueling." In "AIAA Atmospheric Flight Mechanics Conference," pp. 1–10. Toronto, Ontario Canada.

Etkin, B and Reid, LD (1996) Dynamics of flight : stability and control. New York ; Brisbane: Wiley, 3rd edn.

Fu, Z, Lu, Y, Zhou, F, Guo, Y, Guo, P, and Feng, H (2022) "Parametric neural network-based model free adaptive tracking control method and its application to AFS/DYC system." Computational Intelligence and Neuroscience vol. 2022, pp. 1–9.

Garces, F, Becerra, V, Kambhampati, C, and Warwick, K (2003) Strategies for Feedback Linearization A Dynamic Neural Network Approach. London: Oxford Higher Education, 1st edn.

Giancoli, DC (2009) Physics for Scientists and Engineers. New Jersey: Pearson Education Inc., 4th edn.

Gupta, A, Afrin, T, Scully, E, and Yodo, N (2021) "Advances of UAVs toward Future Transportation: The State-of-the-Art, Challenges, and Opportunities." Future Transportation vol. 1, no. 2, pp. 326–350.

Gupta, MM, Jin, L, and Homma, N (2003) Static and Dynamic Neural Networks, From Fundmamentals to Advanced Theory, vol. 143. Hoboken, New Jersey, USA: John Wiley & Sons, Inc.

Haddad, WM and Chellaboina, V (2008) Nonlinear dynamical systems and control. Princeton: Princeton University Press, 1st edn.

Haitao, W, Xinmin, D, Jianping, X, and Jiaolong, L (2014) "Dynamic modeling of a hose-drogue aerial refueling system and integral sliding mode backstepping control for the hose whipping phenomenon." Chinese Journal of Aeronautics vol. 27, no. 4, pp. 930–946.

Haitao, W, Xinmin, D, Jianping, X, Jiaolong, L, and Jian, W (2016) "Modeling and simulation of a time-varying inertia aircraft in aerial refueling." Chinese Journal of Aeronautics vol. 29, no. 2, pp. 335–345.

Han, Y, Huang, G, Song, S, Yang, L, Wang, H, and Wang, Y (2021) "Dynamic neural networks: A Survey." IEEE Transactions on Pattern Analysis and Machine Intelligence pp. 1–20.

Hansen, JL, Murray, JE, and Campos, NV (2004) "The NASA Dryden AAR Project : A Flight Test Approach to an Aerial Refueling System." In "AIAA Atmospheric Flight Mechanics Conference and Exhibit, Providence, Rhode Island," pp. 1–19. Providence, Rhode Island: AIAA.

Hanson, C, Ryan, J, Allen, M, and Jacobson, S (2002) An overview of flight test results for a formation flight autopilot. Technical Memorandum NASA/TM-2002-210729, NASA Dryden Flight Research Center, Edwards, California.

Haupt, R and Haupt, S (2004) Practical Genetic Algorithms. Hoboken, New Jersey: John Wiley & Sons, Inc., 1st edn.

Hedrick, JK and Girard, A (2015) "*Control of nonlinear dynamic systems: Theory and applications*." lecture notes, Control of Nonlinear Dynamic Systems ME237, University of California, Berkeley, delivered Spring 2015 .

Isidori, A (1995) Nonlinear Control Systems. Berlin; New York: Springer, 3rd edn.

Jayachitra, A and Vinodha, R (2014) "Genetic algorithm based PID controller tuning approach for continuous stirred tank reactor." vol. 2014, no. 791230, pp. 1–8.

Johnson, DT, Nykl, SL, and Raquet, JF (2017) "Combining stereo vision and inertial navigation for automated aerial refueling." Journal of Guidance, Control, and Dynamics vol. 40, no. 9, pp. 2250–2259.

Khalil, HK (2015) Nonlinear Systems. Essex: Pearson Education Limited, global edn.

Kramer, O (2017) Genetic Algorithm Essentials. Switzerland: Springer International Publishing AG, 1st edn.

Kriel, S, Engelbrecht, J, and Jones, T (2013) "Receptacle normal position control for automated aerial refueling." Aerospace Science and Technology vol. 29, no. 1, pp. 296–304.

Kuk, T, Ro, K, and Kamman, JW (2011) "Design, test and evaluation of an actively stabilized drogue refueling system." In "Infotech@ Aerospace 2011 conference and exhibit, St. Louis, MI, USA," pp. 1–13. AIAA.

Lee, A, Dallmann, W, Nykl, S, Taylor, C, and Borghetti, B (2020) "Long-range pose estimation for aerial refueling approaches using deep neural networks." Journal of Aerospace Information Systems vol. 17, no. 11, pp. 634–646.

Lee, AT (2020) "Object Detection with Deep Learning to Accelerate Pose Estimation for Automated Aerial Refueling". Masters thesis, Air Force Institute of Technology, Dayton, Ohio.

Lee, J, Dogan, A, and Hullender, D (2011) "Estimation of aircraft states and wind exposure in aerial refueling." In "AIAA Atmospheric Flight Mechanics Conference," pp. 1 – 23. Portland, USA: AIAA.

Leondes, CT (1998) Neural network systems techniques and applications: Advances in theory and applications. Cambridge, Massachusetts: Academic Press, 1st edn.

Li, B, Mu, C, and Wu, B (2012) "A survey of vision based autonomous aerial refueling for unmanned aerial vehicles." In "2012 Third International Conference on Intelligent Control and Information Processing," pp. 1–6. Dalian, China.

Li, Y, Sundararajan, N, and Saratchandran, P (2001) "Neuro-controller design for nonlinear fighter aircraft maneuver using fully tuned RBF networks." Automatica vol. 37, no. 8, pp. 1293–1301.

Liu, Z, Zhu, M, and Tan, F (2014) "Control system design and simulation for UAV during aerial refueling." In "The 26th Chinese Control and Decision Conference (2014 CCDC)," pp. 3482–3486. IEEE.

Lou, JM and Zhang, K (2013) "Design of active disturbance rejection controller for autonomous aerial refueling UAV." In "TENCON 2013-2013 IEEE Region 10 Conference (31194)," pp. 1–4. Xi'an, China.

Lynn, N, Ali, MZ, and Suganthan, PN (2018) "Population topologies for particle swarm optimization and differential evolution." Swarm and Evolutionary Computation vol. 39, pp. 24–35.

Ma, Y, Yuan, D, Yan, J, and Qu, Y (2018) "Predictive guidance scheme with nar neural network for autonomous aerial refueling." In "2018 IEEE CSAA Guidance, Navigation and Control Conference (CGNCC)," pp. 1–6. Xiamen, China.

Mao, W (2008) Effect of mass variation on the dynamics of receiver aircraft during aerial refueling. Phd thesis, University of California Davis.

Mao, W and Eke, FO (2008) "A survey of the dynamics and control of aircraft during aerial refueling." Nonlinear Dynamics and Systems Theory vol. 8, no. 4, pp. 375–388.

Marquez, HJ (2003) Nonlinear control systems: analysis and design. Hoboken: John Wiley & Sons, 1st edn.

Mash, RL (2017) "Toward Automated Aerial Refueling: Auotmated Visual Aircraft Identification with Convolutional Neural Networks". Masters thesis, Air Force Institute of Technology, Dayton, Ohio.

Mavrovouniotis, M, Li, C, and Yang, S (2017) "A survey of swarm intelligence for dynamic optimization: Algorithms and applications." Swarm and Evolutionary Computation vol. 33, pp. 1–17.

McAndrew, IR, Navarro, E, and Witcher, K (2015) "Drogue deflections in low speed unmanned aerial refueling." International Journal of research in Aeronautical Engineering & Mechanical Engineering, IJRAME vol. 3, no. 1, pp. 119–127.

McAndrew, IR and Witcher, K (2013) "Design considerations and requirements for in-flight refueling of unmanned vehicles." Journal of Aeronautics & Aerospace Engineering vol. 2013.

McFarlane, C, Richardson, T, and Jones, C (2007) "Cooperative control during boom air-to-air refueling." In "AIAA Guidance, Navigation and Control Conference and Exhibit," pp. 1–17. Hilton Head, South Carolina, USA.

Michailidis, MG, Rutherford, MJ, and Valavanis, KP (2020) "A survey of controller designs for new generation uavs: The challenge of uncertain aerodynamic parameters." International Journal of Control, Automation and Systems vol. 18, no. 4, pp. 801–816.

Moorhouse, DJ and Woodcock, RJ (1982) Background information and user guide for MIL-F-8785C, military specification-flying qualities of piloted airplanes. Tech. Rep. AFWAL-TR-81-3109, Air Force Wright Aeronautical Labs Wright-Patterson AFB OH.

Naimi, A, Deng, J, Shimjith, SR, and Arul, AJ (2020) "Dynamic neural network-based feedback linearization control of a pressurized water reactor." In "2020 13th International Conference on Developments in eSystems Engineering (DeSE)," pp. 228–232. Liverpool, United Kingdom.

Nikravesh, SKY (2013) Nonlinear systems stability analysis: Lyapunov-based approach. Boca Raton: CRC Press, 1st edn.

Nϕrgaard, M., Ravn, O., Poulsen, N.K., Hansen, and L.K. (2000) Neural Networks for Modelling and Control of Dynamic Systems . London: Springer, 1st edn.

Pachter, M, Houpis, CH, and Trosen, DW (1997) "Design of an air-to-air automatic refueling flight control system using quantitative feedback theory." International Journal of Robust and Nonlinear Control vol. 7, no. 6, pp. 561–580.

Panday, A and Pedro, J (2013) "An overview of aerial refueling control systems applied to UAVs." In "AFRICON Conference," pp. 1 – 5. Pointe-Aux Piments, Mauritius: IEEE.

Panday, A and Pedro, JO (2007) "Neural network control of a UCAV during in-flight refuelling." In "International Conference on Modelling and Optimisation of Structures, Processes and Systems," pp. 1–7. Durban, South Africa.

Pedro, JO, Dangor, M, Dahunsi, OA, and Ali, MM (2014) "Intelligent feedback linearization control of nonlinear electrohydraulic suspension systems using particle swarm optimization." Applied Soft Computing vol. 24, pp. 50–62.

Pedro, JO, Panday, A, and Dala, L (2013) "A nonlinear dynamic inversion-based neurocontroller for unmanned combat aerial vehicles during aerial refuelling." vol. 23, no. 1, pp. 75–90.

Plastino, AR and Muzzio, JC (1992) "On the use and abuse of Newton's second law for variable mass problems." Celestial Mechanics and Dynamical Astronomy vol. 53, no. 3, pp. 227–232.

Qu, Y, Chen, L, and Qiu, J (2009) "Application of non-cancellation decoupling in boom refueling control." In "2009 International Conference on Mechatronics and Automation," pp. 4203–4207. Changchun, Jilin, China: IEEE.

Qu, Y, Yu, Z, and Zhang, Y (2015) "Automatic load alleviation simulation during boom refueling for UAV." In "In Proceedings of International Conference on Intelligent Unmanned Systems," pp. 1–6. Bali, Indonesia.

Quintana, E, Heidenkamp, H, and Codner, M (2014) "Europe's Air Transport and Air-to-Air Refuelling Capability: Examining the Collaborative Imperative." Royal United Services Institute pp. 1–32.

Rezaee Jordehi, A and Jasni, J (2013) "Parameter selection in particle swarm optimisation: a survey." Journal of Experimental & Theoretical Artificial Intelligence vol. 25, no. 4, pp. 527–542.

Ro, K, Basaran, E, and Kamman, JW (2007) "Aerodynamic characteristics of paradrogue assembly in an aerial refueling system." Journal of Aircraft vol. 44, no. 3, pp. 963–970.

Ro, K, Kuk, T, and Kamman, JW (2010) "Active control of aerial refueling hose-drogue systems." In "AIAA Guidance, Navigation and Control Conference," pp. 1–12. Toronto, Ontario, Canada: AIAA.

Roblin, S (2022) "The U.S. Air Force Needs to Fix Its Air Refueling Tankers." URL `https://nationalinterest.org/blog/reboot/`

us-air-force-needs-fix-its-air-refueling-tankers-199773. Last Accessed: 20 March 2022.

Ross, SM, Pachter, M, Jacques, DR, Kish, BA, and Millman, DR (2006) "Autonomous aerial refueling based on the tanker reference frame." In "2006 IEEE Aerospace Conference," pp. 1–22. Big Sky, MT, USA.

Saban, D, Whidborne, JF, and Cooke, A (2009) "Simulation of wake vortex effects for UAVs in close formation flight." The Aeronautical Journal vol. 113, no. 1149, p. 727–738.

Sindhuja, P, Ramamoorthy, P, and Suresh Kumar, M (2018) "A brief survey on nature inspired algorithms: Clever Algorithms for Optimization." Asian Journal of Computer Science and Technology vol. 7, no. 1, pp. 27–32.

Slotine, J and Weiping, L (1991) Applied Nonlinear Control. Englewood Cliffs, New Jersey: Prentice Hall, 1st edn.

Smith, AL and Kunz, DL (2007) "Dynamic coupling of the KC-135 tanker and boom for modeling and simulation." Journal of Aircraft vol. 44, no. 3, pp. 1034–1039.

Soares, F, Burken, J, and Marwala, T (2006) "Neural network applications in advanced aircraft flight control system, a hybrid system, a flight test demonstration." In "International Conference on Neural Information Processing," pp. 684–691. Vancouver, B.C., Canada: Springer.

Stengel, R (2004) Flight Dynamics. Oxfordshire, United Kingdom: Princeton University Press, 1st edn.

Stepanyan, V, Lavretsky, E, and Hovakimyan, N (2003) "A differential game approach to aerial refueling autopilot design." In "Proceedings of the 42nd IEEE Conference on Decision and Control, Maui, Hawaii, USA," pp. 4920–4925.

Stevens, BL, Lewis, FL, and Johnson, EN (2016) Aircraft control and simulation : dynamics, controls design, and autonomous systems. Hoboken, New Jersey: Wiley, 3rd edn.

Su, Z, Wang, H, Li, N, Yu, Y, and Wu, J (2018) "Exact docking flight controller for autonomous aerial refueling with back-stepping based high order sliding mode." Mechanical Systems and Signal Processing vol. 101, pp. 338–360.

Terrell, WJ (2009) Stability and stabilization. Princeton: Princeton University Press, 1st edn.

Thomas, PR, Bhandari, U, Bullock, S, Richardson, TS, and Du Bois, JL (2014) "Advances in air to air refuelling." Progress in Aerospace Sciences vol. 71, pp. 14–35.

Thomas, PR, Bullock, S, Richardson, TS, and Whidborne, JF (2015) "Collaborative control in a flying-boom aerial refueling simulation." Journal of Guidance Control and Dynamics vol. 38, no. 7, pp. 1274–1289.

Venkataramanan, S, Dogan, A, and Blake, W (2003) "Vortex effect modelling in aircraft formation flight." In "AIAA Atmospheric Flight Mechanics Conference and Exhibit," pp. 11–14. Austin, Texas.

Venter, G and Sobieszczanski-Sobieski, J (2003) "Particle swarm optimization." AIAA Journal vol. 41, no. 8, pp. 1583–1589.

Waishek, J (2007) Derivation of the dynamics equations of receiver aircraft in aerial refueling. Master's thesis, University of Texas at Arlington.

Waishek, J, Dogan, A, and Blake, W (2009) "Derivation of the dynamics equations of receiver aircraft in aerial refueling." Journal of Guidance, Control, and Dynamics vol. 32, no. 2, pp. 586–598.

Walton, TA and Clark, B (2021) "Resilient aerial refueling: Safeguarding the US military's global reach." Hudson Institute, Washington D.C.

Wang, J, Cao, C, Hovakimyan, N, and Lavretsky, E (2006) "Novel L1 adaptive control approach to autonomous aerial refueling with guaranteed transient performance." In "Proceedings of the 2006 American control conference, Minneapolis, Minnesota," pp. 14–16.

Wang, J, Patel, VV, Cao, C, Hovakimyan, N, and Lavretsky, E (2008) "Novel L1 adaptive control methodology for aerial refueling with guaranteed transient performance." Journal of Guidance, Control, and Dynamics vol. 31, no. 1, pp. 182–193.

Wang, L, Cao, H, and Yue, T (2017) "Attitude control design for flying boom during air-to-air refuelling." Journal of Systems and Control Engineering vol. 231, no. 1, pp. 812–826.

Wei, ZB, Dai, X, Quan, Q, and Cai, KY (2016) "Drogue dynamic model under bow wave in probe-and-drogue refueling." IEEE Transactions on Aerospace and Electronic Systems vol. 52, no. 4, pp. 1728–1742.

Williamson, WR, Reed, E, Glenn, GJ, Stecko, SM, Musgrave, J, and Takacs, JM (2010) "Controllable drogue for automated aerial refueling." Journal of Aircraft vol. 47, no. 2, pp. 515–527.

Wilson, J (2013) "UAV Roundup 2013." Aerospace America vol. 51, no. 7, pp. 1–32.

Wise, K, Lavretsky, E, Hovakimyan, N, Cao, C, and Wang, J (2008) "Verifiable adaptive flight control: UCAV and aerial refueling." In "AIAA Guidance, Navigation, and Control Conference, AIAA," vol. 6658, pp. 1–26. Honolulu, Hawaii, USA.

Wu, S, Zhang, L, Xu, W, Zhou, T, and Luo, D (2013) "Docking control of autonomous aerial refueling for UAV based on LQR." In "2013 10th IEEE International Conference on Control and Automation (ICCA)," pp. 1819–1823. Hangzhou, China: IEEE.

Yan, L, Yuan, D, Yan, J, and Qu, Y (2016) "Design on automatic alignment control law for aerial boom refuelling." In "Proceedings of 2016 IEEE Chinese Guidance, Navigation and Control Conference," pp. 2094 – 2098. Nanjing, China: IEEE.

Yang, C, Liu, Y, and Lu, Y (2014) "Flying qualities evaluation of aerial refueling boom with stability augmentation system." In "Guidance, Navigation and Control Conference (CGNCC), 2014 IEEE Chinese," pp. 855–860. National Harbor, Maryland, USA: IEEE.

Yaohong, Q, Jizhi, W, Qichuan, T, and Jing, W (2013) "Autonomous alleviating loads of boom air refueling." In "Proceedings of the 32nd Chinese Control Conference," pp. 2407–2410. Xi'an, China.

Yu, Z, Qu, Y, and Zhang, Y (2017) "Robust adaptive dynamic surface control for receiver UAV during boom refueling in the presence of vortex." In "Proceedings of 2017 29th Chinese Control and Decision Conference (CCDC)," pp. 1798 – 1803. IEEE.

Yu, Z, Zhang, Y, and Qu, Y (2018) "Fault-tolerant control for autonomous aerial refueling against actuator fault in receiver UAV." IFAC-PapersOnLine vol. 51, no. 24, pp. 274–279.

Yuan, D, Whidborne, JF, and Xun, Y (2014) "A study on a multi-controller design of the drawtube for aerial boom refueling." In "2014 20th International Conference on Automation and Computing (ICAC)," pp. 128–133. Cranfield, UK: IEEE.

Zhang, S, Liao, F, Cheng, YQ, and He, KF (2020) "Aircraft trajectory control with feedback linearization for general nonlinear systems." In "2020 Chinese Control And Decision Conference (CCDC)," pp. 3937–3944. Hefei, China.

Zipfel, P (2000) Modeling and simulation of aerospace vehicle dynamics. AIAA Education Series. Reston, Virginia: American Institute of Aeronautics and Astronautics, 1st edn.

Appendix A Appendix A - Parameter Specification and Model Validation

A.1 System Parameters

The receiver and tanker aircraft data have been extracted from Dogan et al., (2005b), Waishek et al., (2009) and Dogan et al., (2007).

Parameter	Unit	Tanker	Receiver
Mass (m)	kg	2.5493e5	1.1281e4
Wing area (S)	m^2	511	75.12
Wingspan (b)	m	59.74	11.43
Chord (c)	m	8.32	8.763
Max thrust (T)	N	9.3e5	120e3
Δ_z	m	3.7184	0
α_{ref}	deg	13	0
δ	deg	1	0
I_x	N	1.86e7	3.186e4
I_y	N	4.14e7	8.757e4
I_z	N	5.83e7	1.223e5
I_{xz}	N	1.13e6	-546.394

Parameter	Tanker	Receiver
Cd_0	0.0751	0.023
Cd_α	0	0
Cd_{α^2}	3.7642	0.7
Cd_{δ_e}	0	0
$Cd_{\delta_e^2}$	0	0.25
Cs_0	0	0
Cs_{δ_a}	0	0
Cs_β	-1.08	-0.031
Cs_{δ_r}	0.179	0
Cl_0	0.92	0.062
Cl_α	5.67	2.09
Cl_{α^2}	-5.95	0
Cl_q	5.65	1.53
Cl_{δ_e}	0.36	0.594
Clm_0	0	0
Clm_{δ_a}	0.053	-0.13
Clm_{δ_r}	0.0	-0.004
Clm_β	-0.281	-0.022
Clm_p	-0.502	-0.163
Clm_r	0.195	0.012
Cm_0	0	-0.003
Cm_α	-1.45	-0.024
Cm_q	-21.4	-0.4
Cm_{δ_e}	-1.4	-0.169
Cn_0	0	0
Cn_{δ_a}	0.0083	-0.017
Cn_{δ_r}	-0.113	-0.018
Cn_β	0.184	-0.021
Cn_p	-0.222	-0.023
Cn_r	-0.36	-0.009

A.2 Vortex Model Validation

Figures A.1 to A.6 can be compared with those in Venkataramanan et al., (2003) as a basis of validation of the wake model used in this research.

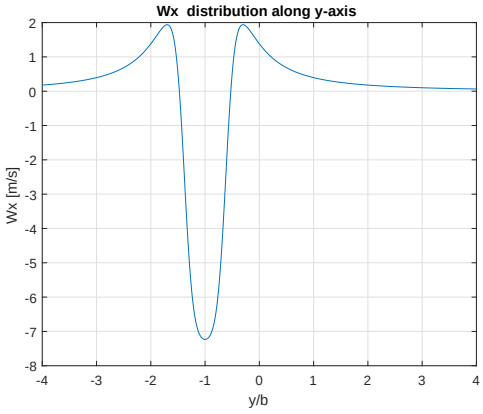


Figure A.1: Distribution of vortex induced velocity W_x along wing

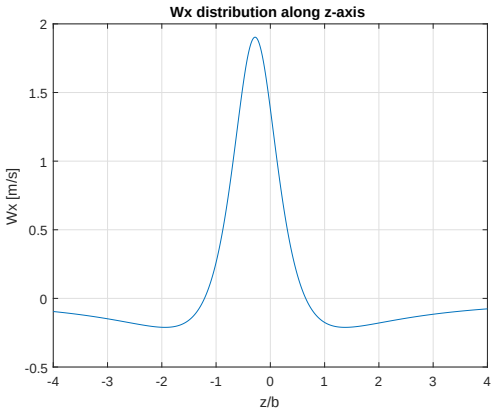


Figure A.2: Distribution of vortex induced velocity W_x along z-axis

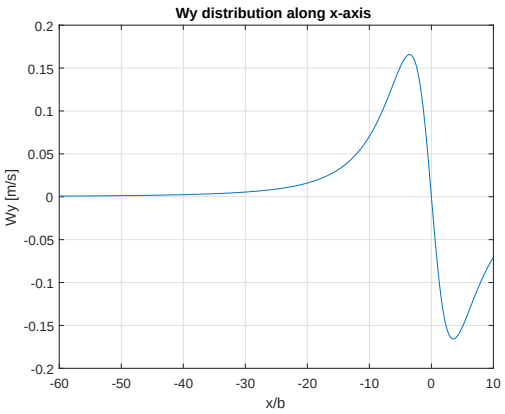


Figure A.3: Distribution of vortex induced velocity W_y along x axis

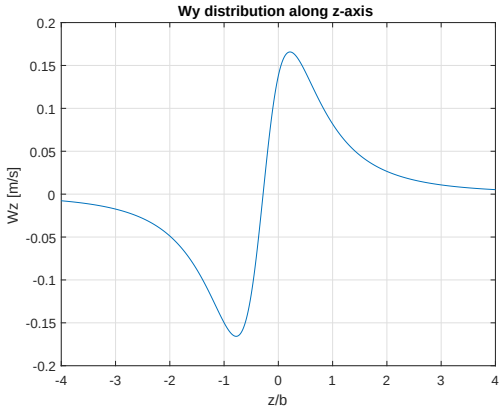


Figure A.4: Distribution of vortex induced velocity W_y along z axis

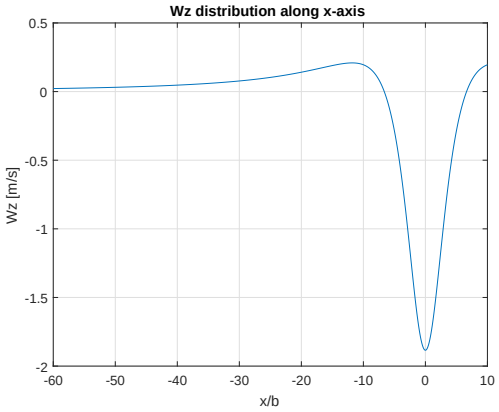


Figure A.5: Distribution of vortex induced velocity W_z along x axis

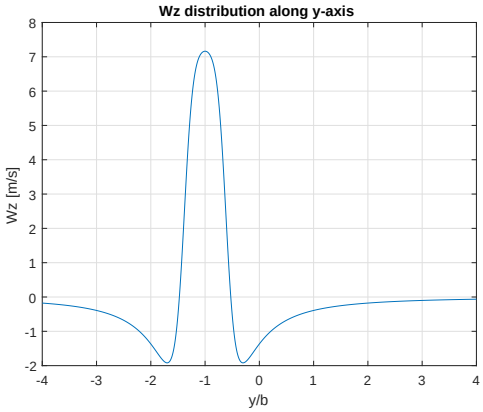


Figure A.6: Distribution of vortex induced velocity W_z along wing

A.3 Inner Loop in Nonlinear Affine Form

$$f_{\mathcal{X}} = F11 + (D1 * E1 * F1 * G1 * A1) \tag{A.1}$$

$$g_{\mathcal{X}} = (D1 * E1 * F1 * G1 * B1) + (D1 * E1 * F1 * C1) \tag{A.2}$$

and

$$f_\omega = F2 + \underline{\underline{\mathbf{I}}}_{\mathbf{t}}^{-1} A2 \tag{A.3}$$

$$g_\omega = \underline{\underline{\mathbf{I}}}_{\mathbf{t}}^{-1} B2 \tag{A.4}$$

$$\begin{aligned}
F2 &= \underline{\underline{\mathbf{I}}}_{\mathbf{t}}^{-1} \mathbf{S}\left(\omega_{\mathbf{B_R B_T}} + \mathbf{R}_{\mathbf{B_R B_T}} \omega_{\mathbf{B_T}}\right) \underline{\underline{\mathbf{I}}}_{\mathbf{M}} \left(\omega_{B_R B_T} + \mathbf{R}_{\mathbf{B_R B_T}} \omega_{B_T}\right) \\
&+ \underline{\underline{\mathbf{I}}}_{\mathbf{t}}^{-1} \mathbf{\Sigma}^{\star} \left[m_j \left(\omega_{B_R B_T}^T + \omega_{B_T}^T \mathbf{R}_{\mathbf{B_R B_T}}^{\mathbf{T}} \right) \rho_{m_j} \left(\omega_{\mathbf{B_R B_T}} + \mathbf{R}_{\mathbf{B_R B_T}} \omega_{\mathbf{B_T}} \right) + m_j \ddot{\rho}_{m_j} + \dot{m}_j \dot{\rho}_{m_j} \right] \\
&+ \underline{\underline{\mathbf{I}}}_{\mathbf{t}}^{-1} \left[\mathbf{\Sigma}_{mj}^{\star} \right] \left\{ - \left[\mathbf{S}\left(\omega_{\mathbf{B_R B_T}}\right) + \mathbf{S}\left(\mathbf{R}_{\mathbf{B_R B_T}} \omega_{\mathbf{B_T}}\right) \right] \left(\mathbf{R}_{\mathbf{B_R W_R}} U + W \right) + \dot{W} \right\} \\
&+ \underline{\underline{\mathbf{I}}}_{\mathbf{t}}^{-1} \left[\sum_{j=1}^{k} \mathbf{S}\left(\rho_{\mathbf{m_j}}\right) \dot{m}_j \right] \left(\mathbf{R}_{\mathbf{B_R W_R}} U + W \right) \\
&- 2 \underline{\underline{\mathbf{I}}}_{\mathbf{t}}^{-1} \sum_{j=1}^{k} m_j \left[\left(\rho_{m_j}^T \dot{\rho}_{m_j} \right) \mathbf{I}_{\mathbf{3\times 3}} - \dot{\rho}_{m_j} \rho_{m_j}^T \right] \left(\omega_{B_R B_T + \mathbf{R}_{\mathbf{B_R B_T}}} \omega_{B_T} \right) \\
&- \underline{\underline{\mathbf{I}}}_{\mathbf{t}}^{-1} \sum_{j=1}^{k} \dot{m}_j \left[\left(\rho_{m_j}^T \dot{\rho}_{m_j} \right) \mathbf{I}_{\mathbf{3\times 3}} - \dot{\rho}_{m_j} \rho_{m_j}^T \right] \left(\omega_{B_R B_T + \mathbf{R}_{\mathbf{B_R B_T}}} \omega_{B_T} \right) \\
&- \mathbf{S}\left(\omega_{B_R B_T}\right) \mathbf{R}_{\mathbf{B_R B_T}} \omega_{B_T} - \mathbf{R}_{\mathbf{B_R B_T}} \dot{\omega}_{B_T} \\
&- \underline{\underline{\mathbf{I}}}_{\mathbf{t}}^{-1} \dot{m} \mathbf{S}\left(\rho_R\right) \left(\mathbf{R}_{\mathbf{B_R B_T}} \mathbf{R}_{\mathbf{B_T I}} \dot{r}_{B_T} + \mathbf{R}_{\mathbf{B_R B_T}} V_{\dot{m}} \right)
\end{aligned} \tag{A.5}$$

$$F3 = \mathbf{f_1} \tag{A.6}$$

$$F4 = \mathbf{f_2} \tag{A.7}$$

$$Q = 0.5 \rho V_{bb} V_{bb} S \tag{A.8}$$

$$C1 = [0,\ 0,\ 0,\ T_{max}; 0,\ 0,\ 0,\ 0; 0,\ 0,\ 0,\ 0] \tag{A.9}$$

$$D1 = \frac{1}{(M+m)} * \mathcal{E}_{\mathbf{R}}^{-\mathbf{1}} \tag{A.10}$$

$$E1 = \mathbf{R}_{\mathbf{B_R B_T}} \mathbf{R}_{\mathbf{B_T I}} \tag{A.11}$$

$$F1 = \mathbf{R}_{\mathbf{B_R I}}^{\mathbf{T}} \tag{A.12}$$

$$G1 = \mathbf{R}_{\mathbf{B_R W_R}} \tag{A.13}$$

$$\tag{A.14}$$

$$
\begin{aligned}
F11 &= \mathcal{E}_{\mathbf{R}}^{-\mathbf{1}}\left[\mathbf{S}\left(\omega_{B_R B_T}\right)+\mathbf{S}\left(\mathbf{R}_{\mathbf{B_R B_T}}\omega_{\mathbf{B_T}}\right)\right]\left(\mathbf{R}_{\mathbf{B_{B_R} W_R}}U+W\right)-\mathcal{E}_{\mathbf{R}}^{-\mathbf{1}} \\
&+ \frac{1}{(M+m)}\mathcal{E}_{\mathbf{R}}^{-\mathbf{1}}\left[\mathbf{R}_{\mathbf{B_R B_T I}}\left(M_R+\dot{m}\dot{r}_{B_T}\right)-\dot{m}\left(\mathbf{R}_{\mathbf{B_R W_R}}U+W-\mathbf{R}_{\mathbf{B_R B_T}}V_{\dot{m}}\right)\right] \\
&- \frac{1}{(M+m)}\mathcal{E}_{\mathbf{R}}^{-\mathbf{1}}\sum_{j=1}^{k}\left(\dot{m}_j\left\{\dot{\rho}_{m_j}-\left[\mathbf{S}\left(\omega_{\mathbf{B_R B_T}}\right)+\mathbf{S}\left(\mathbf{R}_{\mathbf{B_R}}\omega_{\mathbf{B_T}}\right)\right]\rho_{m_j}\right\}\right) \\
&+ m_j\{\ddot{\rho}_{m_j}-\left[\mathbf{S}\left(\omega_{\mathbf{B_R B_T}}\right)\rho_{m_j}-2\dot{\rho}_{m_j}\right] \\
&+ 2\mathbf{S}\left(\mathbf{R}_{\mathbf{B_R B_T}}\omega_{\mathbf{B_T}}\right)\left[\mathbf{S}\left(\omega_{\mathbf{B_R B_T}}\right)\rho_{m_j}-\dot{\rho}_{m_j}\right] \\
&+ +\left[\mathbf{S}^2\left(\mathbf{R}_{\mathbf{B_R B_T}}\omega_{\mathbf{B_T}}\right)-\mathbf{S}\left(\mathbf{R}_{\mathbf{B_R B_T}}\dot{\omega}_{\mathbf{B_T}}\right)\right]\rho_{m_j}\}
\end{aligned}
\tag{A.15}
$$

$$
A2=\begin{bmatrix}
Qb\left(C_{\mathcal{L}0}+C_{\mathcal{L}_p}\dfrac{b}{2V_{bb}}p_{rel}+C_{\mathcal{L}_r}\dfrac{b}{2V_{bb}}r_{rel}+C_{\mathcal{L}\beta}\beta\right) \\
Qc\left(C_{\mathcal{M}0}+C_{\mathcal{M}\alpha}\alpha+C_{\mathcal{M}_q}\dfrac{\bar{c}}{2V_{bb}}q_{rel}\right) \\
Qb\left(C_{\mathcal{N}0}+C_{\mathcal{N}_p}\dfrac{b}{2V_{bb}}p_{rel}+C_{\mathcal{N}_r}\dfrac{b}{2V_{bb}}r_{rel}+C_{\mathcal{N}\beta}\beta\right)
\end{bmatrix}
\tag{A.16}
$$

$$
B2=\begin{bmatrix}
QbC_{\mathcal{L}\delta_a} & 0 & QbC_{\mathcal{L}\delta_r} & 0 \\
0 & QcC_{\mathcal{M}\delta_e} & 0 & 0 \\
QbC_{\mathcal{N}\delta_a} & 0 & QbC_{\mathcal{N}\delta_r} & 0
\end{bmatrix}
\tag{A.17}
$$

$$
A1=\begin{bmatrix}
Q\left(C_{D_0}+C_{D\alpha^2}\alpha^2\right) \\
Q\left(C_{S_0}+C_{S\beta}\beta\right) \\
Q\left(C_{L0}+C_{L\alpha}\alpha+C_{L^2_\alpha}(\alpha-\alpha_{ref})^2+C_{L_q}\dfrac{\bar{c}}{2V_{bb}}q_{rel}\right)
\end{bmatrix}
\tag{A.18}
$$

$$
B1=\begin{bmatrix}
0 & -QC_{L\delta_e 2} & 0 & 0 \\
-QC_{S\delta_a} & 0 & +-QC_{S\delta_r} & 0 \\
0 & -QC_{L\delta_e} & 0 & 0
\end{bmatrix}
\tag{A.19}
$$

$$
K1=\left(\mathbf{I_{3\times 3}}-F3*F4\right)^{-1} \tag{A.20}
$$

$$
K3=K1*F3*f_\omega+K1*f_{\mathcal{X}} \tag{A.21}
$$

$$
K2=F4*\left(\mathbf{I_{3\times 3}}-F3*F4\right)^{-1} \tag{A.22}
$$

$$
K4=(K2*F3*f_\omega)+(K2*f_{\mathcal{X}})+f_\omega \tag{A.23}
$$

$F2$ in Eq. A.5 is similar to c_2 in Eq. 2.69 with moments omitted. $F11$ in Eq. A.15 is similar to c_1 in Eq. 2.66 with forces due to control surfaces removed.

A.4 Outer Loop in Nonlinear Affine Form

$$F_O = \mathbf{R}^{\mathbf{T}}_{\mathbf{B_R B_T}} W_{BR} - \mathbf{R}_{\mathbf{B_T I}} \dot{r}_{B_T} - \mathbf{S}(\xi) \mathbf{R}^{\mathbf{T}}_{\mathbf{B_R B_T}} \omega_{B_R} \tag{A.24}$$

$$G_{O1} = \mathbf{R}^{\mathbf{T}}_{\mathbf{B_R B_T}} \mathbf{R}_{\mathbf{B_R W_R}} \tag{A.25}$$

$$G_{O234} = \mathbf{S}(\xi) \mathbf{R}^{\mathbf{T}}_{\mathbf{B_R B_T}} \tag{A.26}$$

$$f_{outer}(\mathbf{x}) = \begin{bmatrix} F_O(1) \\ (q_{TR} \sin \phi_{TR} + r_{TR} \cos \phi_{TR}) \tan \theta_{TR} \\ F_O(2) \\ F_O(3) \end{bmatrix} \tag{A.27}$$

$$g_{outer}(\mathbf{x}) = \begin{bmatrix} G_{O1}(1,1) & G_{O234}(1,1) & G_{O234}(1,2) & G_{O234}(1,3) \\ 0 & 1 & 0 & 0 \\ G_{O1}(2,1) & G_{O234}(2,1) & G_{O234}(2,2) & G_{O234}(2,3) \\ G_{O1}(3,1) & G_{O234}(3,1) & G_{O234}(3,2) & G_{O234}(3,3) \end{bmatrix} \tag{A.28}$$